

ACOUSTIC TRANSDUCTION – MATERIALS AND DEVICES

Period 1 January 1998 to 31 December 1998

Annual Report

VOLUME V

**OFFICE OF NAVAL RESEARCH
Contract No: N00014-96-1-1173**

**APPROVED FOR PUBLIC RELEASE –
DISTRIBUTION UNLIMITED**

19990427 045

**Reproduction in whole or in part is permitted for any
purpose of the United States Government**

Kenji Uchino

PENNSTATE



**THE MATERIALS RESEARCH LABORATORY
UNIVERSITY PARK, PA**

**Reproduced From
Best Available Copy**

REPORT DOCUMENTATION PAGE

Form Approved
OMB No. 0704-0188

Public reporting burden for this collection of information is estimated to average 1 hour per response, including the time for reviewing instructions, searching existing data sources, gathering and maintaining the data needed, and completing and reviewing the collection of information. Send comments regarding this burden estimate or any other aspect of this collection of information, including suggestions for reducing this burden, to Washington Headquarters Services, Directorate for Information Operations and Reports, 1215 Jefferson Davis Highway, Suite 1204, Arlington, VA 22202-4302, and to the Office of Management and Budget, Paperwork Reduction Project (0704-0188), Washington, DC 20503.

1. AGENCY USE ONLY (Leave blank)	2. REPORT DATE 04/05/99	3. REPORT TYPE AND DATES COVERED ANNUAL REPORT 01/01/98-12/31/98
4. TITLE AND SUBTITLE ACOUSTIC TRANSDUCTION -- MATERIALS AND DEVICES		5. FUNDING NUMBERS ONR CONTRACT NO: N00014-96-1-11173
6. AUTHOR(S) KENJI UCHINO		
7. PERFORMING ORGANIZATION NAME(S) AND ADDRESS(ES) Materials Research Laboratory The Pennsylvania State University University Park PA 16802		8. PERFORMING ORGANIZATION REPORT NUMBER
9. SPONSORING/MONITORING AGENCY NAME(S) AND ADDRESS(ES) Office of Naval Research ONR 321SS Ballston Centre Tower One 800 N Quincy Street Arlington VA 22217-5660		10. SPONSORING/MONITORING AGENCY REPORT NUMBER Office of Naval Research Regional Office Chicago 536 S Clark Str., RM 208 Chicago IL 60605-1588
11. SUPPLEMENTARY NOTES		
12a. DISTRIBUTION/AVAILABILITY STATEMENT		12b. DISTRIBUTION CODE
13. ABSTRACT (Maximum 200 words)		
14. SUBJECT TERMS		15. NUMBER OF PAGES
		16. PRICE CODE
17. SECURITY CLASSIFICATION OF REPORT	18. SECURITY CLASSIFICATION OF THIS PAGE	19. SECURITY CLASSIFICATION OF ABSTRACT
20. LIMITATION OF ABSTRACT		

ABSTRACT

This report documents work performed over the period 1 January 1998 to 31 December 1998 on a MURI under the Office of Naval Research Contract N00014-96-1-1173. The topic "Acoustic Transduction Materials and Devices" brings together groups in the Materials Research Laboratory (MRL), the Applied Research Laboratory (ARL), and the Center for Acoustics and Vibrations (CAV) at Penn State.

Research on the program is adequately represented in the 80 technical appendices.

Outstanding accomplishments include:

Exploration of several new relaxor ferroelectric perovskite solid solution with morphotropic phase boundaries. New evidence of the onset of nonlinearity in soft donor doped PZTs at surprisingly low (1V/cm) fields. Confirmation of the relaxor phase induced by electron irradiation in PVDF:TrFE copolymers, and a processing method which permits very high (4%) electrostrictive strain in the transverse direction, vital for the practical use in actuator systems. In composite transducer, "first fruits" of the cooperative program are cymbal arrays which form most effective acoustic projectors, and a new "dog bone" design which permits deeper submergence for the cymbal. Agile transducers, the 3-D acoustic intensity probe and high force high strain torsional and step and repeat systems continue to make excellent progress. In actuator studies true acoustic emission is proving to be an excellent tool in reliability studies and a new design of small-scale (mini) piezoelectric motor shows outstanding performance. Thick thin film studies and are now "gearing up" for the development of the mini tonpilz arrays. New combinations of ultrasonic and resonance methods appear to offer unique capability for complete characterization of ferroelectric piezoelectric materials.

The mode of presentation of the report emphasizes the outstanding progress made in published research. It is important to also document that the slower and more painstaking development of practical transducer systems in the cymbal and mini tonpilz arrays is progressing very favorably.

APPENDICES

VOLUME I

GENERAL SUMMARY PAPERS

1. Cross, L.E., "Recent Developments in Piezoelectric Ferroelectric Materials and Composites," Proceedings of the 4th European Conference on Smart Structures and Materials in Conjunction with the 2nd International Conference on Micromechanics, Intelligent Materials and Robotics, Harrogate, UK (6-8 July 1998).
2. Newnham R.E., "Functional Composites for Sensors and Actuators," Chapter in *The Era of Materials*, edited by S. Majumdar, R. Tressler, and E. Miller, 259-275, Pennsylvania Academy of Science (1998).
3. Uchino, K., "Piezoelectric Ultrasonic Motors: Overview," *Smart Mater. Struct.* **7**, 273-285 (1998).
4. Newnham, R.E., "Phase Transformations in Smart Materials," *Acta Cryst. A* **54**, 729-737 (1998).

2.0 MATERIALS STUDIES

2.1 *Polycrystal Perovskite Ceramics*

5. Liu, S.F., I.R. Abothu, S. Komarneni, P. Poosanaas, D.S. Paik, Y. Ito, and K. Uchino, "PLZT Ceramics from Conventional and Microwave Hydrothermal Powders," Proceedings in Asian Meeting on Ferroelectrics (AMF2), Singapore (December 8-11, 1998).
6. Abothu, I.R., P. Poosanaas, S. Komarneni, Y. Ito, and K. Uchino, "Nanocomposite Versus Monophasic Sol-Gel Processing of PLZT Ceramics," Proceedings in Asian Meeting on Ferroelectrics (AMF2), Singapore (December 8-11, 1998).
7. Kim, J.S., Y.H. Chen, and K. Uchino, "Dielectric and Piezoelectric Properties of Fe_2O_3 -Doped 0.57PSN-0.43PT Ceramics," *J. Korean Phys. Soc.* **32** [2], S1248-1250 (1998).
8. Alberta, E.F. and A.S. Bhalla, "Electrical Property Diagram and Morphotropic Phase Boundary in the $Pb(In_{1/2}Ta_{1/2})O_3$ - $PbTiO_3$ Solid Solution System," *Ferroelectric Letters* (1998). [accepted]
9. Meng, J.F., Z-Y. Cheng, B.K. Rai, R.S. Katiyar, E. Alberta, R. Guo, and A.S. Bhalla, "Photoluminescence in $PbMg_{1/3}Nb_{2/3}O_3$ - $PbIn_{1/2}Nb_{1/2}O_3$ Systems," *J. Mater. Res.* **13** (7), 1861 (1998).
10. Alberta, E.F. and A.S. Bhalla, "Investigation of the Lead Indium Niobate-Lead Magnesium Niobate Solid Solution," *Materials Letters* (1998). [accepted]
11. Alberta, E.F., A.S. Bhalla, and T. Takenaka, "Large Hydrostatic Piezoelectric Constant and Temperature Dependence of the Piezoelectric Properties of $Bi(NiTi)_{1/2}O_3$: $PbTiO_3$ Ceramics," *Ferroelectrics Letters* (1998). [accepted]
12. Zhang, Q.M. and J. Zhao, "Electromechanical Properties of Lead Zirconate Titanate Piezoceramics Under the Influence of Mechanical Stress, IEEE Trans. UFFFC (accepted).
13. Kugel, V.D. and L.E. Cross, "Behavior of soft Piezoelectric Ceramics under High Sinusoidal Electric Fields," *J. Appl. Phys.* **84** (5), 2815-2830 (1998).

VOLUME II

2.0 MATERIALS STUDIES

2.1 *Polycrystal Perovskite Ceramics* (continued)

14. Du, X-H., Q.M. Wang, U. Belegundu, and K. Uchino, "Piezoelectric Property Enhancement in Polycrystalline Lead Zirconate Titanate by Changing Cutting Angle," *J. Ceram. Soc. Jpn.* (1999). [accepted]
15. Mueller, V. and Q.M. Zhang, "Nonlinearity and Scaling Behavior in Donor Doped Lead Zirconate Titanate Piezoceramic," *Appl. Phys. Lett.* **72**, 2692 (1998).
16. Uchino, K and H. Aburatani, "Field Induced Acoustic Emission in Ferroelectric Ceramics," *Proc. IEEE Ultrasonic Symp.*, Sendai, Japan (October 1998). [in press]
17. Newnham, R.E. and S. Trolier-McKinstry, "Size Effects in Ferroics" *Integrated Ferroelectrics* **20**, 1-13, Gordon & Breach Science Publishers (March 1998).

2.2 *Relaxor Ferroelectric Single Crystal Systems*

18. Uchino, K., "High Electromechanical Coupling Piezoelectrics: Relaxor and Normal Ferroelectric Solid Solutions," *Solid State Ionics* **108**, 43-52 (1998).
19. Wada, S. S.E. Park, L.E. Cross, and T.R. Shrout, "Domain Configuration and Ferroelectric Related Properties of Relaxor Based Single Crystals," *J. Korean Phys. Soc.* **32**, S1290-S1293 (1998).
20. Belegundu, U., X. H. Du, and K. Uchino, "In-Situ Observation of Domain Orientation in $Pb(Zn_{1/3}Nb_{2/3})O_3$ - $PbTiO_3$ Single Crystals," *Proc. 5th Intl. Symp. Ferroic Domains and Mesoscopic Structures*, University Park, PA (April 1998).
21. Du, X.H., J. Zheng, U. Belegundu, and K. Uchino, "Crystal Orientation Dependence of Piezoelectric Properties of Lead Zirconate Titanate Near the Morphotropic Phase Boundary," *J. Appl. Phys. Ltrs.* **72** (19), 2421-2423 (1998).
22. Rehrig, P.W., S.-E. Park, S. Trolier-McKinstry, G.L. Messing, B. Jones, and T.R. Shrout, "Piezoelectric Properties of Zirconium-Doped Barium Titanate Single Crystals Grown by Tempered Grain Growth," submitted to *J. Appl. Phys.*
23. Du, X., Q.M. Wang, U. Belegundu, A. Bhalla, and K. Uchino, "Crystal Orientation Dependence of Piezoelectric Properties of Single Crystal Barium Titanate," *Mat. Ltr.* (1999) [accepted].
24. Guo, R., H.T. Evans, Jr., and A.S. Bhalla, "Crystal Structure Analysis and Polarization Mechanisms of Ferroelectric Tetragonal Tungsten Bronze Lead Barium Niobate," *Ferroelectrics* **206/207**, 123-132 (1998).

2.3 *New High Strain Polymer Materials*

25. Zhao, X., V. Bharti, Q.M. Zhang, T. Ramotowski, F. Tito, and R. Ting, "Electromechanical Properties of Electrostrictive P(VDF-TrFE) Copolymer," *Appl. Phys. Ltrs.* **73**, 2054 (1998).
26. Bharti, V., G. Shanthi, H. Xu, Q.M. Zhang, and K. Liang, "Evolution of Transitional Behavior and Structure of Electron Irradiated Poly(vinylidene fluoride-trifluoroethylene) Copolymer Films," *Appl. Phys. Ltrs.* [accepted].
27. Cheng, Z.-Y., V. Bharti, T.B. Xu, S. Wang, and Q.M. Zhang, "Transverse Strain Responses in Electrostrictive Poly (vinylidene fluoride-trifluoroethylene) Films and Development of a Dilatometer for the Measurement," *J. Appl. Phys.* [accepted]

VOLUME III

2.0 MATERIALS STUDIES

2.3 *New High Strain Polymer Materials* (continued)

28. Bharti, V., X.Z. Zhao, Q.M. Zhang, T. Ramotowski, F. Tito, and R. Ting, "Ultrahigh Field Induced Strain and Polarized Response in Electron Irradiated Poly(vinylidene fluoride-trifluoroethylene) Copolymer," *Mat. Res. Innovat.* **2**, 57-63 (1998).
29. Su, J., P. Moses, and Q.M. Zhang, "A Bimorph Based Dilatometer for Field Induced Strain Measurement in Soft and Thin Free Standing Polymer Films," *Rev. Sci. Instruments* **69** (6), 2480 (1998).

3.0 TRANSDUCER STUDIES

3.1 *Composite Structures*

30. Hughes, W.J., "Transducers, Underwater Acoustic," *Encyclopedia of Applied Physics*, Vol. 22, 67 (1998).
31. Tressler, J.F., W.J. Hughes, W. Cao, K. Uchino, and R.E. Newnham, "Capped Ceramic Underwater Sound Projector."
32. Zhang, J., W.J. Hughes, A.C. Hladky-Hennion, and R.E. Newnham, "Concave Cymbal Transducers."
33. Wang, Q.M., X.-H. Du, B. Xu, and L.E. Cross, "Theoretical Analysis of the Sensor Effect of Cantilever Piezoelectric Benders," *J. Appl. Phys.* **85** (3), 1702-1712 (1998).
34. Fernandez, J.F., A. Dogan, J.T. Fielding, K. Uchino, and R.E. Newnham, "Tailoring the Performance of Ceramic-Metal Piezocomposite Actuators, 'Cymbals,'" *Sensors and Actuator A* **65**, 228-237 (1998).
35. Wang, Q.M. and L.E. Cross, "A Piezoelectric Pseudoshear Multilayer Actuator," *Appl. Phys. Ltrs.* **72** (18), 2238 (1998).
36. Geng, X. and Q.M. Zhang, "Resonance Modes and Losses in 1-3 Composites for Ultrasonic Transducer Applications," *J. Appl. Phys.* **85** (3), 1342 (1999).

3.2 *Frequency Agile Transducers*

37. Hebert, C.A. and G. A. Lesieutre, "Flexural Piezoelectric Transducers with Frequency Agility Obtained Via Membrane Loads," *J. Intel. Mat. Sys. & Str.* (1998). [accepted].
38. Davis, C.L. and G.A. Lesieutre, "An Actively Tuned Solid State Vibration Absorber Using Capacitive Shunting of Piezoelectric Stiffness," *J. Sound & Vibration* (1998). [accepted]
39. Bernard, J., G.A. Lesieutre, and G.H. Koopmann, "Active Broadband Force Isolation using a Flexural Piezoelectric Inertial Actuator," *J. Sound & Vibration* (1999). [submitted]

VOLUME IV

3.0 TRANSDUCER STUDIES

3.3 *3-D Acoustic Intensity Probes* (continued)

40. Lauchle, G.C. and A.R. Jones, "Unsteady Lift Force on a Towed Sphere," *J. Fluids and Structures* **112** (1998).
41. Lauchle, G.C., A.R. Jones, J.J. Dreyer, and J. Wang, "Flow-Induced Lift Forces on a Towed Sphere," *Proc. Of ASME Noise Control and Acoustics Division ASME 1998, NCA-28*, 103-111 (1998).
42. Brungart, T.A. G.C. Lauchle, S. Deutsch, and E. Riggs, "Outer-Flow Effects on Turbulent Boundary Layer Wall Pressure Fluctuations," *J. Acoust. Soc. Am.* **105** (4) (April 1999).
43. Brungart, T.A., G.C. Lauchle, and R.K. Ramanujam, "Installation Effects of Fan Acoustic and Aerodynamic Performance," *Noise Control Eng. J.* **47** (January/February 1999).

4.0 ACTUATOR STUDIES

4.1 *Materials : Designs : Reliability*

44. Uchino, K., "New Trend in Ceramic Actuators," *Proc. 6th Intl. Aerospace Symp. '98*, Nagoya, Japan, p. S1-2, 1-10 (July 14-15, 1998).
45. Uchino, K., "Materials Issues in Design and Performance of Piezoelectric Actuators: An Overview," *Acta. Mater.* **46** (11), 3745-3753 (1998).
46. Yao, K., W. Zhu, K. Uchino, Z. Zhang, and L.C. Lim, "Design and Fabrication of a High Performance Multilayer Piezoelectric Actuator with Bending Deformation."
47. Aburatani, H. and K. Uchino, "Acoustic Emission in Damaged Ferroelectric Lead Zirconate Titanate Ceramics," *Jpn. J. Appl. Phys.* **37**, L553-L555 (1998).
48. Atherton, P.D. and K. Uchino, "New Developments in Piezo Motors and Mechanisms," *Proc. 6th Intl. Conf. On New Actuators (Actuator 98)*, Bremen, Germany, p. 164-169 (June 17-19, 1998).
49. Uchino, K. and B. Koc, "Compact Piezoelectric Ultrasonic Motors," *2nd Asian Meeting on Ferroelectrics (AMF-2)*, Singapore (December 7-11, 1998).
50. Koc, B., Y. Xu, and K. Uchino, "Ceramic/Metal Composite Piezoelectric Motors," *IEEE Ultrasonic Symposium*, Sendai, Japan (October 1998).
51. Koc, B., Y. Xu, and K. Uchino, "Roto-Linear Ultrasonic Motors," *Proc. 6th Intl. Conf. On New Actuators (Actuator 98)*, Bremen, Germany, p. 349-352 (June 17-19, 1998).
52. Koc, B., A. Dogan, Y. Xu, R.E. Newnham, and K. Uchino, "An Ultrasonic Motor Using a Metal-Ceramic Composite Actuator Generating Torsional Displacement," *Jpn. J. Appl. Phys.* **37**, 5659-5662 (1998).

4.2 *Photostrictive Actuators*

53. Poosanaas, P. and K. Uchino, "Photostrictive Effect in Lanthanum-Modified Lead Zirconate Titanate Ceramics Near The Morphotropic Phase Boundary," *J. Mat. Chem. & Phys.* (October 1998). [submitted]
54. Uchino, K. and P. Poosanaas, "Photostriction in PLZT and Its Applications," *Proc. CIMTEC '98*, Florence, Italy (June 14-19, 1998).

VOLUME V

4.0 ACTUATOR STUDIES

4.3 *Torsional and High Force Actuators* (continued)

55. Glazounov, A.E., Q.M. Zhang, and C. Kim, "Torsional Actuator Based on Mechanically Amplified Shear Piezoelectric Response," Sensors and Actuators (1998). [submitted]
56. Frank, J., G.H. Koopmann, W. Chen, and G.A. Lesieutre, "Design and Performance of a High Force Piezoelectric Inchworm Motor."

5.0 MODELING and CHARACTERIZATION

5.1 *Finite Element and Other Methods*

57. Qi, W. and W. Cao, "Finite Element and Experimental Study of Composite and 1-D Array Transducers," SPIE **3341** (1998).
58. Wang, H., W. Jiang, and W. Cao, "Characterization of Lead Zirconate Titanate Piezoceramic Using High Frequency Ultrasonic Spectroscopy," J. Appl. Phys. (1998). [accepted]
59. Zhu, S.N., B. Jiang, and W. Cao, "Characterization of Piezoelectric Materials Using Ultrasonic and Resonant Techniques," Proceedings of SPIE Imaging '98, **3341**, 154-162 (1998).
60. Cao, W., "Virtual Design of Medical Transducers," Proceedings of SPIE Imaging '98, **3341**, 56-63 (1998).
61. Cao, W., "Elastic Property Characterization in Thin Samples of Sub-Wavelength in Thickness," Ferroelectrics **206/207**, 355-363 (1998).
62. Cao, W., S.N. Zhu, and B. Jiang, "Analysis of Shear Modes in A Piezoelectric Resonator," J. Appl. Phys. **83**, 4415-4420 (1998).

5.2 *Relaxor Ferroelectrics*

63. Giniewicz, J.R., A.S. Bhalla, and L.E. Cross, "Variable Structural Ordering in Lead Scandium Tantalate-Lead Titanate Materials," Ferroelectrics **211**, 281-297 (1998).
64. Pan, X., W.D. Kaplan, M. Rühle, and R.E. Newnham, "Quantitative Comparison of Transmission Electron Microscopy Techniques for the Study of Localized Ordering on a Nanoscale," J. Am. Ceram. Soc. **81** (3), 597-605 (1998).
65. Zhao, J., A.E. Glazounov, and Q.M. Zhang, "Change in Electromechanical Properties of 0.9PMN:0.1PT Relaxor Ferroelectric Induced by Uniaxial Compressive Stress Directed Perpendicular to the Electric Field," Appl. Phys. Ltrs. **74**, 436 (1999).
66. Zhao, J., V. Mueller, and Q.M. Zhang, "The Influence of the External Stress on the Electromechanical Response of Electrostrictive $0.9\text{Pb}(\text{Mg}_{1/3}\text{Nb}_{2/3})\text{O}_3\text{-}0.1\text{PbTiO}_3$ in the dc Electrical Field Biased State," J. Mat. Res. **14**, 3 (1999).

VOLUME VI

5.0 MODELING and CHARACTERIZATION

5.3 *Thin and Thick Thin Films*

67. Maria, J.P., W. Hackenberger, and S. Trolier-McKinstry, "Phase Development and Electrical Property Analysis of Pulsed Laser Deposited $\text{Pb}(\text{Mg}_{1/3}\text{Nb}_{2/3})\text{O}_3\text{-PbTiO}_3$ (70/30) Epitaxial Films," *J. Appl. Phys.* **84** (9), 5147-5154 (1998).
68. Shepard, J.F., Jr., P.J. Moses, and S. Trolier-McKinstry, "The Wafer Flexure Technique for the Determination of the Transverse Piezoelectric Coefficient (d_{31}) of PZT Thin Films," *Sensors and Actuators A* **71**, 133-138 (1998).
69. Zavala, G. J.H. Fendler, and S. Trolier-McKinstry, "Stress Dependent Piezoelectric Properties of Ferroelectric Lead Zirconate Titanate Thin Films by Atomic Force Microscopy," *J. Korean Phys. Soc.* **32**, S1464-S1467 (1998).
70. Wasa, K., Y. Haneda, T. Satoh, H. Adachi, I. Kanno, K. Setsune, D.G. Schlom, S. Trolier-McKinstry, C.-B. Eom, "Continuous Single Crystal PbTiO_3 Thin Films Epitaxially Grown on Miscut (001) SrTiO_3 ," *J. Korean Phys. Soc.* **32**, S1344-S1348 (1998).
71. Xu, B., Y. Ye, L.E. Cross, J.J. Bernstein, and R. Miller, "Dielectric Hysteresis from Transverse Electric Fields in Lead Zirconate Titanate Thin Films," *Appl. Phys. Ltrs.* (1998). [submitted]
72. Xu, B., N.G. Pai, Q.-M. Wang, and L.E. Cross, "Antiferroelectric Thin and Thick Films for High Strain Microactuators," *Integrated Ferroelectrics* **22**, 545-557 (1998).

5.4 *Domain Studies*

73. Erhart, J. and W. Cao, "Effective Material Properties in Twinned Ferroelectric Crystals," *J. Appl. Phys.* (1999). [submitted]
74. Belegundu, U., M. Pastor, X.H. Du, L.E. Cross, and K. Uchino, "Domain Formation in 0.90 $\text{Pb}(\text{Zn}_{1/3}\text{Nb}_{2/3})\text{O}_3$ -0.10 PbTiO_3 Single Crystals under Electric Field along [111] Direction," *IEEE '98*, Sendai, Japan (1998).
75. Zhu, S.N. and W. Cao, "Pyroelectric and Piezoelectric Imaging of Ferroelectric Domains in LiTaO_3 by Scanning Electron Microscopy," *Phys. Status Solidi* (1998). [submitted]
76. Hatch, D.M. and W. Cao., "Determination of Domain and Domain Wall Formation at Ferroic Transitions," *Ferroelectric* (1998). [submitted]
77. Mueller, V. and Q.M. Zhang, "Threshold of Irreversible Domain Wall Motion in Soft PZT-Piezoceramic. Ferroelectrics" **206/207**, 113-122 (1998).
78. Aburatani, H., J.P. Witham, and K. Uchino, "A Fractal Analysis on Domain Related Electric Field Induced Acoustic Emission in Ferroelectric Ceramics," *Jpn. J. Appl. Phys.* **37**, 602-605 (1998).

5.5 *Electrostriction*

79. Newnham, R.E., V. Sundar, R. Yimnirun, J. Su, and Q.M. Zhang, "Electrostriction in Dielectric Materials," in *Advances in Dielectric Ceramic Materials*, eds. K. Nair and A. Bhalla. Ceramic Trans. **88**, 154-39 (1998).
80. Sundar, V., R. Yimnirun, B.G. Aitken, and R.E. Newnham, "Structure Property Relationships in the Electrostriction Response of Low Dielectric Permittivity Silicate Glasses," Mat. Res. Bull. **33**, 1307-1314 (1998).

ACTUATOR STUDIES

**Torsional and High Force
Actuators**

APPENDIX 55

Torsional actuator based on mechanically amplified shear piezoelectric response

A. E. Glazounov and Q. M. Zhang

Materials Research Laboratory, The Pennsylvania State University, University Park,
PA 16802

C. Kim

Naval Research Laboratory, Washington DC 20375

Abstract

A torsional actuator, based on the concept of mechanical amplification of piezoelectric shear strain and capable of generating large angular displacement, was proposed and studied experimentally. The actuator is a tube consisting of an even number of the segments poled along the length, which are adhesively bonded together, and the joints act as electrodes to apply the driving voltage. The experimental data measured on the prototype actuators (i) prove the proposed concept of mechanical amplification of small piezoelectric shear strain to generate large torsional motion, (ii) show that the actuator functions well both without load and under the torque load and (iii) demonstrate that the actuator can operate continuously for a long period of time without drop in its performance. Also, the results demonstrated that the proposed torsional actuator is capable of producing both large torque and large angular displacement in a compact package, sufficient to meet many smart structures requirements, and can be tailored for a variety of application requirements. Finally, one of the obvious advantages of the present design of the actuator is its simplicity: the piezoelectric shear strain is transformed directly into the angular displacement, whereas in the previously reported actuators, the conversion mechanism into the torsional motion was rather complicated which thus required a sophisticated design of the whole system.

Keywords: torsional actuator, shear strain, piezoelectric ceramics, nonlinearity, reliability

1. Introduction

Piezoelectric ceramic materials, such as lead zirconate titanate (PZT) are now widely used in solid-state actuators and sensors which were designed for numerous applications, such as precision positioning, noise and vibration sensing and cancellation, linear motors, and many others.^{1,2} In many of those applications, a large torsional displacement is required, for example, in robotics to achieve the micropositioning,^{3,4} in CD drivers,⁵ in helicopters to control the trailing edge flaps of rotor blades,^{6,7,8} etc. To meet this demands, many works have recently been devoted to the development of actuators capable of generating a large angular displacement with a large torque output³⁻⁹ from the piezoelectric strain.

Recently, a novel type of torsional actuator has been proposed.¹⁰ Its concept is to use shear piezoelectric effect and tubular geometry in order to generate the angular displacement. The advantages of this design include (i) the possibility to obtain large angular displacement by using the geometrical amplification, L/R (where L and R are the length and the radius of the tube, respectively). Also, (ii) in most piezoelectric materials the shear piezoelectric coefficient, d_{15} , has the highest value among piezoelectric coefficients, which also contributes to developing large values of torsional angle and torque output. Finally, (iii) the design is simple, because the piezoelectric shear strain is transformed directly into the angular displacement (whereas in the previously reported actuators, the conversion mechanism into the torsional motion was rather complicated, including the use of hinges, which thus required a sophisticated design of the whole system⁴⁻⁹).

It is the purpose of this paper to continue the study of the proposed torsional actuator and report the results of the detailed tests of its performance, which addresses both the device and material issues. The former include operation of the actuator in different conditions, such as without load, under the torque load, and at electromechanical resonance. Material issues are related with the utilization in this actuator of piezoelectric shear response of PZT ceramics, which has not yet received a broad use in the actuator applications. They include fatigue behavior, mechanical strength and nonlinear shear piezoelectric response of PZT ceramics.

2. Actuator design

An idea of the torsional actuator proposed recently¹⁰ and studied in this work is to use the shear piezoelectric effect, where the external electric field is applied perpendicular to the direction of the spontaneous polarization, P_s , Fig.1(a), in order to produce the angular displacement. A schematic view of the actuator is shown in Fig.1(b). The actuator is a tube consisting of an even number of piezoelectric ceramic segments which are adhesively bonded together using a conductive epoxy, which acts as electrodes to apply the driving field, E . The segments are poled along the length, where the polarization direction alternates between adjacent segments. Since the segments are electrically connected in parallel, they will exhibit a coherent shear deformation under the applied electric field. The cylindrical symmetry of the actuator will directly transform the shear strain, $S_5 = d_{15} \cdot E$, induced in each segment into the angular displacement, β , of the top of the tube with respect to its bottom, Fig.1(b), which is equal to:

$$\beta = \frac{L}{R_{\text{out}}} \cdot d_{15} \cdot E \quad , \quad (1)$$

where L is the length of the tube and R_{out} is its outer radius. This equation shows that even though the shear strain is usually quite small in the piezoelectric materials, a large torsional displacement β can be achieved by using a tubular structure with a large ratio of L/R_{out} . Using elastic properties of tube-shaped samples,¹¹ the torque, T_{dev} , developed by the actuator can be found as:

$$T_{\text{dev}} = \frac{\pi (R_{\text{out}}^4 - R_{\text{in}}^4)}{2s_{44}R_{\text{out}}} \cdot d_{15} \cdot E \quad , \quad (2)$$

where s_{44} is the shear elastic compliance of the material and R_{in} is the inner radius of the tube. According to Eq.(2), the torque T_{dev} is independent of the length of the tube, even though the angular displacement β increases linearly with L , Eq.(1).

3. Experimental

Prototype torsional actuators were fabricated from the commercial piezoelectric ceramic tubes of composition PZT-5A ("EDO, Inc." USA). Each tube was first cut into 8 segments, which then were poled along the length using a continuous poling technique.¹² Finally, the segments were bonded together using a silver-filled epoxy adhesive MB-10HT/S ("Master Bond, Inc." USA), which was selected because it has both high shear strength, and is easy to process. This adhesive compound was coated on both surfaces of the segments, which were then assembled into the tubular actuator according to the design shown in Fig.1(b), and cured at 125°C for one hour using a vacuum bagging process. Consolidation of the joints by vacuum bagging lead to joints typically 25 μm in thickness and very uniform along their length.¹² The assembled single-tube prototype actuator had the following dimensions: $R_{\text{in}} = 0.96 \text{ cm}$, $R_{\text{out}} = 1.27 \text{ cm}$, and $L = 6.35 \text{ cm}$, so that the aspect ratio in Eq.(1) was equal to $L/R_{\text{out}} = 5$.

According to Eq.(1), in the proposed design of torsional actuator, the angle β increases linearly with the length L of the actuator. To test this hypothesis, two identical tubes with the dimensions described above were joint together lengthwise. The test included the characterization of the tubes before and after the joining them together.

To characterize the actuator, the torsional angle produced by the applied electric field was measured in the following experiments. In the load-free conditions, β was measured as a function of the amplitude and frequency of the ac driving field. Also, electrical fatigue test was performed, where the ac field with a fixed amplitude and frequency was applied to the actuator, and β was monitored as a function of time. Under the torque load, T , the torsional angle was measured as a function of dc and ac electric driving field at different values of T .

In all experiments, the actuator was tightly clamped with its bottom to the optical table, and its top was free to twist due to the applied electric field. In order to measure β , a small mirror was attached on the top of the tube and the distance change between the mirror and the optical fiber probe of a MTI-2000 fotonics sensor was measured. The electrical output signal from the MTI-2000 was monitored using an oscilloscope or SR-830 lock-in amplifier.

The effect of the torque load on the actuator performance was studied using a special set-up, Fig.2, which was developed in Materials Research Laboratory.¹³ Although, there are

commercial torque load test machines available, they are not suitable for the torque load test of torsional actuators. The main reason is that these machines were mainly designed to test the properties of the metals, and therefore deal with the magnitudes of torque and twisting angle which are much larger than those expected for the piezoelectric actuators. Additionally, the commercial machines are very expensive, which does not justify their purchase and the following modification to meet the requirements of experiments with actuators. In the developed set-up, Fig.2, the external torque was produced by applying a force to the lever using springs with different elastic constants.

4. Characteristics of prototype actuator

4.1. Proof of the concept of the torsional actuator

Figure 3 summarizes the data which verify the concept of the proposed torsional actuator. In Fig.3(a), the torsional angle measured at 10 Hz is plotted as a function of the amplitude of the ac driving voltage for two separate tube (open circles), and for the same tubes joint lengthwise (closed circles). For separate tubes, the actuation behavior is almost identical and angular displacement is doubled when the length of the actuator is increased by joining these two tubes. This behavior perfectly agrees with predictions of Eq.(1).

The further proof of the concept of the proposed torsional actuator is illustrated in Fig.3(b). The plot compares the data for the piezoelectric coefficient d_{15} of PZT-5A ceramics derived from the experimentally measured data for $\beta(E_m)$ of a single tube (closed circles) and two tubes joint lengthwise (open circles) using Eq.(1), where the amplitude E_m of the driving field was substituted for E , with d_{15} values measured directly from the cubic ceramic samples of the same composition, PZT-5A ("EDO, Inc.", USA). As one can see, the values of the d_{15} derived from the actuators are nearly the same as those measured on the cubic sample. The small, less than 5%, difference could be attributed to the difference in the aging states of ceramics in segments and cubic samples. To summarize, the results presented in Figs.3(a) and 3(b) prove the concept of the proposed torsional actuator, Eq.(1), that is, to use the shear piezoelectric effect, d_{15} , and the geometrical amplification, L/R_{out} , to generate a large angular displacement, β .

4.2. Evaluation of torsional angle and torque output

The results reported in the previous section demonstrate that knowing the material properties, d_{15} , the magnitude of driving electric field, E , and the tube dimensions, L and R_{out} , the torsional angle produced by the actuator, Fig.1(b), can be calculated using Eq.(1).

In order to evaluate the torque output, T_{out} , developed by the actuator, we studied the effect of the torque load on static response of the prototypes. In these experiments, a static torque, T , was first applied to the actuator, thus producing its initial twisting, β_0 . Afterwards, a dc field was turned on, with the polarity to induce a twisting of the actuator in the direction opposite to β_0 . In Fig.4, the torsional angle β measured on the two joint tubes is plotted as a function of the driving field at different torque loads. The blocking torque of the actuator can be evaluated from the intersection of the curve $\beta(E)$ measured at a fixed torque load, with the dashed line corresponding to $\beta = 0$. The zero torsional angle means that at that value of the electric driving field the absolute value of the torque, T_{dev} , developed by the actuator is equal to the external static torque, T . For example, by using the data from Fig.4, one can estimate that at $E \approx 2.5$ kV/cm, the torque output is equal to $T_{dev} = 6$ N·m.

4.3. Effect of the torque load on actuator performance

The effect of the torque load on the static response of the prototype actuator is illustrated in Fig.4 for the two-tube assembly. This data clearly demonstrates that the torque load almost does not change the response of the actuator to the dc field, because the initial twisting, β_0 , can be completely nullified by the appropriate choice of the magnitude of the electric field, and because the slope of $\beta(E)$ curve, which according to Eq.(1) gives the shear piezoelectric coefficient, $d_{15}(E)$, does not show marked change with increasing T , cf. Fig.4. Similar result was obtained for the single tube actuator.

In the experiment of investigating the effect of external torque on the dynamic response of the prototype actuator, an ac driving field of 10 Hz was applied to the actuator and the torsional angle was measured as a function of the ac field amplitude and the torque load. Figure 5 shows the plot of the ac field dependence of piezoelectric coefficient d_{15}

derived from the data on $\beta(E_m)$ using Eq.(1). Similar to the static response, the external torque does not affect significantly the actuator response to the ac field. Application of the torque results only in a small, less than 10%, change in d_{15} from its value measured under load-free condition, $T = 0$ N·m. With the further increase in T , the d_{15} remains nearly constant, Fig.5.

4.4. Frequency dependence of torsional angle

The frequency dependence of the torsional angle was measured within the frequency range 3 - 600 Hz under a relatively large electric fields, $E_m \approx 2$ kV/cm. Only a minor decrease in β , equal to 3% per decade, with increasing frequency was observed.

For small electric fields, $E_m = 50$ V/cm, the frequency dependence of β was measured over a broad frequency range from 100 Hz to 20 kHz. In Fig.6(a), the solid line shows the frequency dependence of the ratio $\beta(f)/\beta(0)$, where $\beta(0)$ corresponds to the low-frequency value of the torsional angle, given by Eq.(1). A series of the peaks are seen in this curve. A comparison of $\beta(f)$ with the frequency dependence of the electrical admittance of the actuator (dashed line in Fig.6(a)) shows that the peaks occur at resonance and antiresonance frequencies of the tube, which correspond to the maximum and minimum admittance, respectively.

In order to understand the origin of these peaks, we performed a theoretical analysis of the acoustic modes propagating in the tube. The analysis showed that the resonance peaks are related with the shear mode propagating along the axis z of the tube, i.e., along its length. When the bottom, $z = 0$, of the tube is mechanically clamped, and the top, $z = L$, is free, the angular displacement at the top of the tube can be written as:

$$\beta = d_{15} \cdot E \cdot \frac{L}{R_{out}} \cdot \frac{\tan \alpha L}{\alpha L} , \quad (3)$$

and the electrical admittance of the actuator is given by:

$$Y = j 2\pi f C_0^T \cdot \left(1 - k_{15}^2 + k_{15}^2 \frac{\tan \alpha L}{\alpha L} \right) , \quad (4)$$

where $\alpha = 2\pi f \sqrt{\rho s_{44}}$ (ρ is the density of PZT), k_{15} is shear electromechanical coupling coefficient, and C_0^T is the electrical capacitance of the tube in stress-free condition. The resonances occur when $\alpha L = n\pi/2$ (n - is the odd value), which gives the resonance frequency equal to: $f_r = n/4L\sqrt{\rho s_{44}}$. Using Eq.(4), around the first resonance frequency f_r with $n = 1$, we can substitute the tube with the equivalent circuit which is shown in Fig.6(b). In this circuit, $C_0 = C_0^T(1 - k_{15}^2)$, $N = d_{15}(R_{out} - R_{in})/s_{44}$, $C_m = 8Ls_{44}/\pi^3(R_{out}^2 - R_{in}^2)$, $L_m = 1/(2\pi f_r)^2 C_m$, and we took into account mechanical losses in the actuator by introducing $R_m^{-1} = 2\pi f C_m Q_m$, where Q_m is the mechanical quality factor. Using the equivalent circuit, one can show that at resonance frequency, f_r , the time dependence of the torsional angle is given by:

$$\beta = \frac{8Q_m}{\pi^2} \cdot \frac{d_{15} E_m L}{R_{out}} \cdot \sin(2\pi f_r t - 90^\circ) \quad , \quad (5)$$

when the electric driving field changes with time as: $E(t) = E_m \sin(2\pi f_r t)$. Equation (5) shows that at resonance there is a phase shift of -90° between the torsional angle and the driving field, and that the amplitude of the torsional angle should be amplified by the factor of $8Q_m/\pi^2$ compared to the low-frequency value given by Eq.(1).

Inspection of the experimental data showed that the model can fit the data nicely. Using actuator dimensions and material datasheet from "EDO, Inc.", the resonance frequencies corresponding to $n = 1, 3, 5$ were estimated as: 6.2 kHz, 18.6 kHz, and 31 kHz, respectively, and were in a good agreement with the positions of the maxima in electrical admittance in Fig.6(a). Also, from the peak in $\beta(f)/\beta(0)$ corresponding to the first resonance in Fig.6(a), the mechanical quality factor of the actuator can be determined as $Q_m = 22$. This values closely compares with that determined from the half-width of the electrical conductance of the tube, which gave $Q_m \approx 20$. Finally, in direct measurements of the torsional angle, at resonance, $f_r = 6$ kHz, we observed the phase shift between $\beta(t)$ and driving field $E(t)$ very close to -90° . All these data indicate that the torsional actuator performed well also in resonance conditions.

The additional angular amplification of the torsional angle by a factor of $8Q_m/\pi^2$ at resonance frequency is very important for possible application of the torsional actuator in the piezoelectric motors, where the actuators usually operate in a resonance mode. To make the stator of the motor, the tube shown in Fig.1(b) may be combined with another piezoelectric actuator generating longitudinal displacement. The combination of torsional and longitudinal displacements will produce an elliptical motion of the contact surface between the stator and rotor, which may be necessary to spin the rotor.¹⁴

4.5. Reliability test of prototype actuator

At present, most commercially available solid state actuators are fabricated of the ferroelectric ceramics PZT. A common feature of ferroelectric materials is a fatigue, or a degradation of their properties caused by cycling them with the electrical field of large magnitude. In addition, in the tubular assembly of the actuator, Fig.1(b), there is also a possibility of the fatigue caused by bonding layer between segments. Therefore, the reliability test of the actuator should include the study of time variation of actuator performance related with its fatigue under required operation conditions.

In present work, the actuator was driven by an ac field of amplitude $E_m = 1.5$ kV/cm and frequency 20 Hz. The change in the torsional angle with time was monitored using a MTI-2000 fotonics sensor and lock-in amplifier. Figure 7 shows β as a function of the number of the fatigue cycles, N . As one can see, the torsional angle remains nearly constant with N up to $3 \cdot 10^6$ cycles (which corresponds to 2 days of continuous operation). This result indicates that there is no degradation of torsional actuator caused by large ac driving field.

The absence of the fatigue shown in Fig.7 agrees with the results of other studies of the fatigue in ferroelectric ceramics. For example, it was shown¹⁵ that the fatigue in PZT ceramics was observed only when the amplitude of the ac driving field exceeded the coercive field, and, thus, caused the switching of the spontaneous polarization. The fatigue occurred already after 10^4 cycles. At the same time, when the driving field was smaller than the coercive field (even being very close to it), no fatigue was observed, up to 10^6 cycles.¹⁵ A possible interpretation of this phenomenon is based on one of the scenarios of the fatigue in

ferroelectric ceramics, which attributes the electrical fatigue to the mechanical degradation of the material, namely, the growth of cracks in it. As was documented in a number of works,^{16,17} the cracks form at internal defects in ceramics, like pores, and then propagate through the material. The formation and growth of the cracks can be explained as follows. The switching of the polarization in ferroelectric ceramics occurs through the motion of domain walls (180° and 90°) through the bulk of the sample. The moving domain wall creates local stresses because of the difference in the strain in neighboring domains with different orientation of the spontaneous polarization. When the wall meets the internal defects in ceramics, like pores, the local stress will be relieved by the formation of cracks originating from these defects. Therefore, upon the continuous cycling of the material with the field larger than the coercive field, the once formed cracks will continue to grow. On the other hand, when the applied ac field is below the coercive field, no polarization reversal, and hence no propagation of the domain walls through the bulk of the sample occurs in ferroelectric ceramics. This may explain the absence of the fatigue in such an experiment. The same conclusion should be valid in the case of the torsional actuator studied in this work. The principle of its operation is to use the shear piezoelectric effect, where the electric field is applied in the direction perpendicular to the spontaneous polarization, and to drive the material with field lower than the coercive field, in order not to switch the polarization in the direction along the field. Thus, no electrical fatigue should be expected.

For torsional actuators studied in this work, the experiments were limited to the use of the driving field of $E_m = 2 - 3$ kV/cm. This limit was mostly determined by the desire to avoid a possible damage to the actuator due to the electrical short circuit related with the discharge over the surface of the segments, which was observed above approximately 3 - 3.5 kV/cm. If special precautions, related with an electrical insulation of the contacts are made, the electric driving field can be significantly higher. Special test was performed on a cubic sample of PZT-5A immersed into silicone oil, where electric field was applied in the direction perpendicular to the spontaneous polarization, and the shear strain, $S_5(E)$, was measured using MTI-2000 fotonics sensor. With electric fields as high as $E_m = 9$ kV/cm, no evidence for the polarization switching into direction along the electric field was observed: the field dependence of induced strain, $S_5(E)$, had a cigar-like shape and remained fully reversible

upon increase and decrease of the field amplitude, E_m . If the polarization switching occurred, the strain would change from shear to longitudinal one and its field dependence would have a shape of the “butterfly loop”, which characterizes the strain related with the polarization reversal in ferroelectric materials.¹⁸

Another reliability test included the measurements of the mechanical strength of the torsional actuator. The results of this study will be published separately. Here we mention only that the mechanical fracture strength of the actuator was determined by the mechanical strength of PZT ceramics, and not by the joints between ceramic segments. This conclusion was suggested by the inspection of the fragments of the broken prototype actuator, and was supported by the fact that the fracture shear stress of the tube, $\sigma_{fr} = 13$ MPa, almost coincided with that of PZT ceramics of the same composition, $\sigma_{fr} \approx 14$ MPa, which was measured for the cubic ceramic sample.¹⁹

5. Tailoring of the characteristics of the torsional actuator for different applications

The specific values of torsional angle and torque output can be different for each particular application. Using the results obtained in this work, we can evaluate the proposed torsional actuator to its application in helicopter rotor blades in trailing edge flap (TEF), where the actuation should reduce the vibration and improve the lifting power.⁶⁻⁸ The eight seat commercial helicopter¹² requires the following values: $\beta = \pm 4^\circ$ and $T_{dev} = 5 \pm 3$ N·m. The prototype torsional actuators made of PZT-5A ceramics has $d_{15} = 1800$ pm/V at $E = 4$ kV/cm, Fig.3(b), which yields the angular displacement $\beta = \pm 0.4^\circ$ (for $L/R_{out} = 10$), and the torque output $T_{dev} = 40$ N·m. Even though the angular displacement is smaller than the required values, it can be increased for example by increasing ratio L/R_{out} , or by trading off some excess torque output with mechanical displacement amplification, since T_{dev} is much larger than the value required for TEF application.

Each particular application will set the requirements not only for the absolute values of the torsional angle and/or torque developed, but also will limit the actuator dimensions. Based on the result of this study, we can suggest the following ways to improve the characteristics of the proposed torsional actuator. The increase in the magnitude of induced shear strain, $S_5 =$

$d_{15} \cdot E$, will result in the increase of both β and T_{dev} , as predicted by Eqs.(1) and (2). This implies the use of larger values of driving electric field and the development the new piezoelectric materials with higher values of shear piezoelectric coefficient, d_{15} (see next section). From the engineering point of view, the increase in the torque output of the actuator, Eq.(2), can be achieved by using the tube with a larger outer radius, R_{out} , (which gives an increase proportional to R_{out}^3) and with a smaller ratio R_{in}/R_{out} .

At this point, we would like to stress one important advantage of the present tubular design of the torsional actuator. As predicted by Eq.(1), the tube with a larger length L will produce larger torsional angle, whereas the torque output will remain the same, Eq.(2). We can prove this statement using the experimental results for the single tube and for the two tubes joint lengthwise. Figure 3(a) already showed that the joining two identical tubes doubles the torsional angle. To demonstrate that the torque output remains that same, for the same tubes we compare the data for the torsional angle, β , measured as a function of static torque load, T , at different magnitudes of the dc driving voltage. Using Eq.(1), we calculate the shear strain as: $S_5 = \beta \cdot R_{out}/L$, and plot the data for $S_5(T)$ in Fig.8. As one can see, for the same value of the driving field, the data for single tube and two joint tubes agree well. Since according to Eq.(2), the shear strain produces the torque T_{dev} , this result indicates that for tubular actuator, the torque output is independent of the length of the tube.

The last feature represents an important advantage of the present design of torsional actuator over another design based on piezoelectric bimorphs where the displacement of the tip of the bimorph due to its bending under the driving electric field is converted into the torsional motion using the system of levers.⁶ In the bimorph system, the produced torsional angle depends upon the displacement of the tip of the bimorph, η . Since η changes with the length, L_b , of the bimorph, as²⁰ $\eta \propto L_b^2$, the longer the bimorph, the larger should be the torsional angle β . However, the increase in L_b will result simultaneously in the decrease of the force, F , developed by the bimorph, since the force is inversely proportional to the length of the bimorph:²⁰ $F \propto L_b^{-1}$. In contrast, the tubular actuator, Fig.1(b), is free of this drawback, because, as we showed before, its torque output is independent of the length, L , of the tube.

Therefore, by increasing L , one can achieve larger torsional angle, Eq.(1): $\beta \propto L/R_{\text{out}}$, without drop in the produced torque.

Finally, we suggest that instead of increasing the length of the tube, larger values of the torsional angle can be achieved by a slight modification of the actuator geometry. One alternative to the tubular assembly, Fig.1(b), is a conical actuator which is schematically drawn in Fig.9. The advantage of this configuration is that the radius of the end 1 can be made much larger than that of the end 2. If end 1 is fixed at a support and end 2 generates the twisting, this design is quite desirable. For conical geometry, the length, L , of the ceramic segments becomes longer than that in the tubular structure, Fig.1(b), and the effective outer radius of the actuator, R_{out} , becomes smaller, since now it is the radius of the actuator at the end 2. The combined effect will be the increase in the amplification factor, L/R_{out} , in Eq.(1), and, therefore, in the produced torsional angle.

6. Nonlinear piezoelectric effect

In actuator and transducer applications, the piezoelectric ceramics is often subjected to high electric fields where the electric field dependence of induced strain is strongly nonlinear.² It is believed that the nonlinearity of the piezoelectric response of PZT ceramics is controlled by the irreversible displacement of domain walls²¹⁻²³ which separate regions of the material with different orientation of spontaneous polarization, P_s . The domain wall motion may be affected by many factors, including the crystal structure and microstructure of ceramics, the presence of impurities, dopants, defects, and a local variation in the composition of ceramics.^{2,22} Possible mechanisms of domain wall motions have recently been discussed in detail in Refs.[22,23].

Shear piezoelectric response of PZT-5A strongly depends upon the magnitude of the driving electric field. This is evident from Fig.3(b), where one can see that at $E = 3$ kV/cm, the magnitude of piezoelectric shear coefficient, d_{15} , of PZT-5A is doubled compared to the low field value, which is usually reported in manufacturer datasheets. Also, one can see that within the studied range of the ac field amplitude, the data corresponding to both ceramic sample and tubular actuators can be fit to the linear function:

$$d_{15} = d_{15}(0) + a \cdot E_m, \quad (6)$$

where $d_{15}(0)$ is the low-field limit of piezoelectric shear coefficient and a is the parameter. The fit of the data to Eq.(6) is shown in Fig.2(a) with the lines.

This result suggests two conclusions which are important of practical application of PZT. First, the knowledge of how the material response changes with the amplitude of the driving field and its proper mathematical description are important for the modeling of the device performance. The data shown in Fig.2(b) contradicts to a conventional description of strain response of ferroelectrics, where the field induced strain is expressed in terms of the Taylor series expansion in terms of electric field. Using symmetry arguments, one would expect to have the following expression for $d_{15}(E)$:²³

$$d_{15} = d_{15}(0) + b_1 \cdot E_m^2 + b_2 \cdot E_m^4 + \dots \quad . \quad (7)$$

Thus, for the device modeling, Eqs.(1) and (2), one should use the experimentally derived linear dependence of $d_{15}(E)$, Eq.(6), rather than the polynomial expansion, Eq.(7). The second conclusion is important for the materials development for their application in torsional actuator. The strong change in the piezoelectric shear coefficient with electric driving field indicates that one should optimize the entire characteristic $d_{15}(E)$ in order to achieve the highest value of the piezoelectric coefficient, $d_{15}(E)$, as a function of the driving field. The higher the d_{15} , the larger will be the values of the torsional angle and the torque output, according to Eqs.(1) and (2).

7. Summary

In this work, we performed a detailed experimental study of a novel type of the piezoelectric torsional actuator. The data obtained prove the proposed concept of the torsional actuator, show that the actuator functions well both without load and under the torque load, and demonstrate that the actuator can operate continuously for a long period of time without drop in its performance. Comparison of the experimental data obtained on the tube and ceramic samples, such as piezoelectric shear coefficient, d_{15} , and mechanical fracture stress, σ_f , indicates that the material properties determine the performance of the torsional actuator.

Also, the experimental results demonstrated that the proposed torsional actuator is capable of producing both large torque and large angular displacement in a compact package, sufficient to meet many smart structures requirements, and can be tailored for a variety of application requirements. Finally, one of the obvious advantages of the present design of the actuator is its simplicity: the piezoelectric shear strain is transformed directly into the angular displacement.

Acknowledgments

The authors wish to thank Dr. W. Chen (PSU) for his help in designing the torque load set-up, and DARPA for the financial support of this work

References

1. K. Uchino, "Electrostrictive actuators: materials and application," *Bull. Amer. Ceram. Soc.* **65**, 647 (1986).
2. L. E. Cross, "Ferroelectric ceramics: materials and application issues," *Ceramic Trans.* **68**, 15 (1996).
3. Y. Fuda and T. Yoshida, "Piezoelectric torsional actuator," *Ferroelectrics* **160**, 323 (1994).
4. J. Satonobu, N. Torii, K. Nakamura, and S. Ueha, "Construction of megatorque hybrid transducer type ultrasonic motor," *Jpn. J. Appl. Phys.* **35**, 5038 (1996).
5. A. Yabuki, M. Aoyagi, Y. Tomikawa, and T. Takano, "Piezoelectric linear motors for driving head element of CD-ROM," *Jpn. J. Appl. Phys.* **33**, 5365 (1994).
6. D. K. Samak and I. Chopra, "A feasibility to build a smart rotor: trailing edge flap actuation," *Proc. of the 1993 SPIE's North American Symposium on Smart Structures and Materials*, Albuquerque, NM, 1993.
7. I. Chopra, "Status of application of smart structures technology to rotocraft systems," Presented at the Innovation in rotocraft technology, Royal Aeronautical Society, London, June 1997.
8. E. F. Prechtl and S. R. Hall, "Design of a high efficiency discrete servo-flap actuator for helicopter rotor control", *SPIE Conference on Smart Structures and Materials*, SPIE **3041**, 158 (1997).
9. M. Aoyagi, S. Tsuchiya, and Y. Tomikawa, "Trial production of an ultrasonic motor using longitudinal and torsional vibrations of a rod vibrator driven by piezoceramic plates inserted in its axial direction," *Jpn. J. Appl. Phys.* **36**, 6106 (1997).
10. A. E. Glazounov, Q. M. Zhang, and C. Kim, "Piezoelectric actuator generating torsional displacement from piezoelectric d_{15} shear response", *Appl. Phys. Lett.* **72**, 2526 (1998).
11. P. Ch. Chou and N. J. Pagano, "Elasticity: tensor, dyadic, and engineering approaches", pp. 115-144, Dover Publications, New York, 1992.
12. C. Kim, D. Lewis III, C. Cm. Wu, A. E. Glazounov, and Q. M. Zhang, "High authority piezoelectric torsional actuators", Presented at ISAF-98, Montreux, Switzerland, August 1998.

13. A. E. Glazounov, Q. M. Zhang, and C. Kim, "A new torsional actuator based on shear piezoelectric response", SPIE Conference on Smart Structures and Materials, SPIE 3324, 82 (1998).
14. S. Ueha and Y. Tomikawa, "Ultrasonic motors", Clarendon Press, Oxford, 1993.
15. D. Wang, E. Fotinich, and G. Carman, "Influence of temperature on the electromechanical and fatigue behavior of piezoelectric ceramics", *J. Appl. Phys.* **83**, 5342 (1998).
16. Q. Y. Jiang and L. E. Cross, "Effect of porosity on electric fatigue behaviour in PLZT and PZT ferroelectric ceramics" *J. Mater. Sci.* **28**, 4536 (1993).
17. H. Cao and A. Evans, "Electric field-induced fatigue crack growth in piezoelectrics", *J. Amer. Ceram. Soc.* **77**, 1783 (1994).
18. B. Jaffe, W. Cook, H. Jaffe, "Piezoelectric ceramics", Academic Press, London, 1971.
19. A. E. Glazounov, Q. M. Zhang, C. Cm. Wu, and C. Kim, to be published.
20. V. D. Kugel, S. Chadran, and L. E. Cross, "Caterpilar-type piezoelectric d_{33} bimorph transducer," *Appl. Phys. Lett.* **69**, 2021 (1996).
21. Q. M. Zhang, W. Y. Pan, S. J. Jang, and L. E. Cross, "Domain wall excitations and their contributions to the weak-signal response of doped lead zirconate titanate ceramics," *J. Appl. Phys.* **64**, 6445 (1988).
22. D. Damjanovic, "Stress and frequency dependence of the direct piezoelectric effect in ferroelectric ceramics," *J. Appl. Phys.* **82**, 1788 (1997).
23. V. Mueller and Q. M. Zhang, "Shear response of lead zirconate titanate piezoceramics", *J. Appl. Phys.* **83**, 3754 (1998).

Figure captions

Figure 1. (a) In piezoelectric shear effect, electric field, E , is applied perpendicular to the direction of the spontaneous polarization, P_s , thus producing the shear strain, $S_5 = d_{15} \cdot E$, in the sample. Solid and dashed lines show the sample before and after deformation, respectively. (b) The proposed torsional actuator is a tube consisting of an even number of the segments of piezoelectric ceramics which are poled along the length and bonded together using a conductive epoxy. The polarization direction alternates between adjacent segments, as shown with arrows on the left. The electric field, E , is applied perpendicular to P_s , and also has opposite directions in neighboring segments (as shown with arrows on the right). Therefore, depending upon the polarity of applied voltage, the top of the tube will twist on angle β either clockwise or counterclockwise with respect to its bottom.

Figure 2. A photograph of the set-up used for the study of the effect of external static torque on the response of the torsional actuator.

Figure 3. (a) Angular displacement of torsional actuator as a function of the ac driving voltage for two separate tubes and two tubes joint as one assembly. (b) Piezoelectric shear coefficient d_{15} as a function of the amplitude of the ac driving field. Circles correspond to the data calculated from the torsional angle of the actuator, consisting of a single tube (closed circles) and two joint tubes (open circles), using Eq.(1). Plus signs show the data measured directly from the cubic ceramic sample of the same composition, PZT-5A. Symbols show the experimental data and the lines correspond to the fit of the data to the linear function, Eq.(7). In (a) and (b), the frequency of the ac voltage is 10 Hz.

Figure 4. Torsional angle of the two-tube actuator is plotted as a function of applied dc field at different external static torque.

Figure 5. The effect of the static torque on the dynamic response of the torsional actuator. The values of the piezoelectric coefficient d_{15} calculated from the data on the

torsional angle are plotted as a function of the amplitude of the ac driving field. The frequency of the field is 10 Hz. The values of applied torque are given in the legend.

Figure 6. (a) Frequency dependence of the torsional angle normalized over its static value (solid line) and of the electrical admittance of the torsional actuator (dashed line). (b) Equivalent circuit corresponding to the torsional actuator around its resonance frequency, $f_r = 6$ kHz.

Figure 7. Torsional angle is plotted as a function of the number of fatigue cycles.

Figure 8. Shear strain calculated from the experimentally measured values of the torsional angle is plotted as a function of the external static torque at different values of the dc driving voltage (same symbols). Closed symbols correspond to the actuator consisting of two joint tubes and open circles show the data for the single tube.

Figure 9. Schematic drawing of the torsional actuator fabricated in the form of the cone. It is expected, that in the real application, the end 1 is fixed at a support, while the torsional displacement is produced at the end 2.

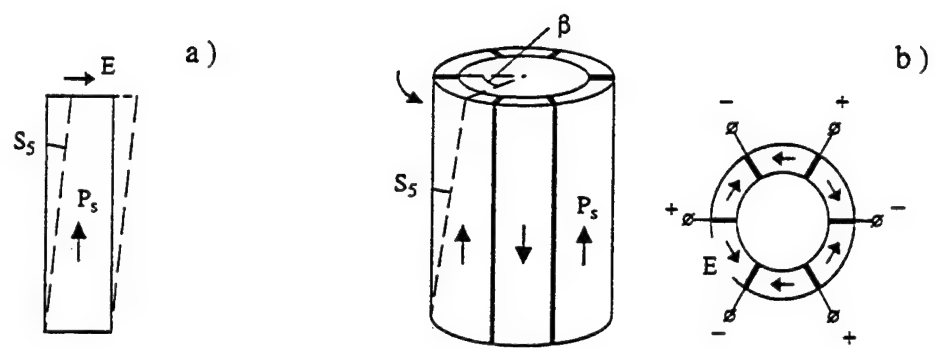


Figure 1

Paper by: A. E. Glazounov, Q. M. Zhang, and C. Kim

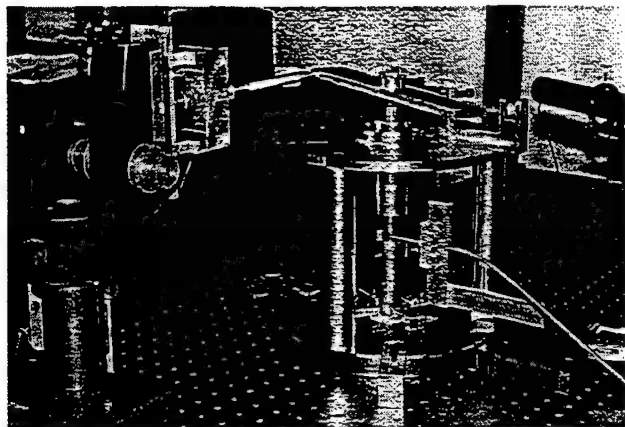


Figure 2

Paper by: A. E. Glazounov, Q. M. Zhang, and C. Kim

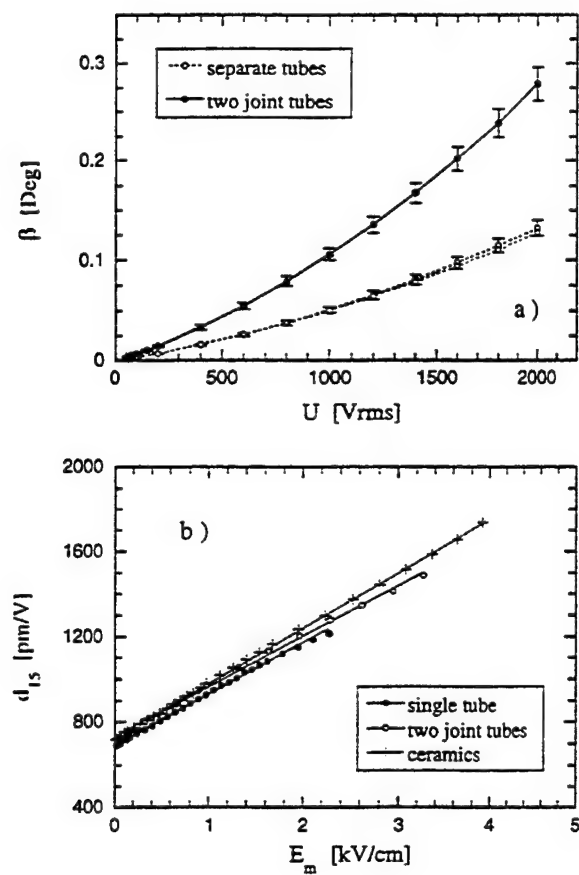


Figure 3

Paper by: A. E. Glazounov, Q. M. Zhang, and C. Kim

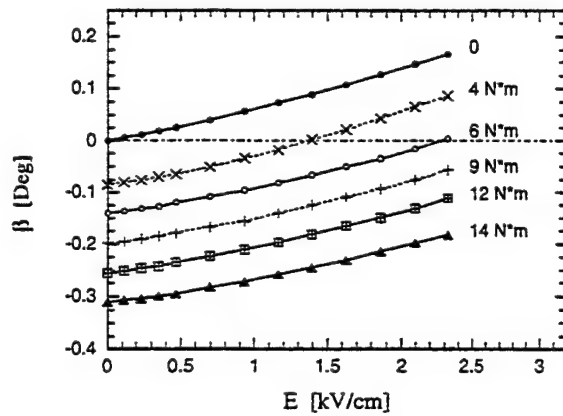


Figure 4

Paper by: A. E. Glazounov, Q. M. Zhang, and C. Kim

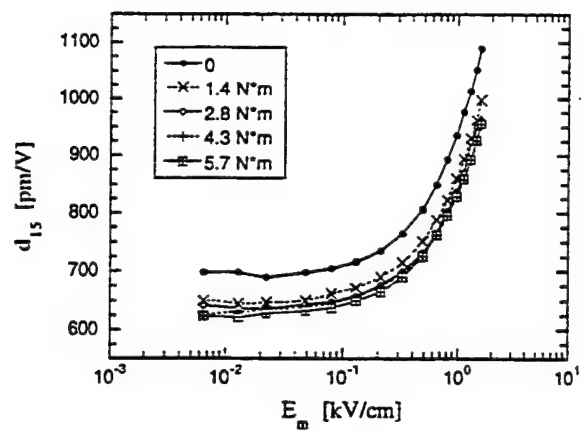


Figure 5

Paper by: A. E. Glazounov, Q. M. Zhang, and C. Kim

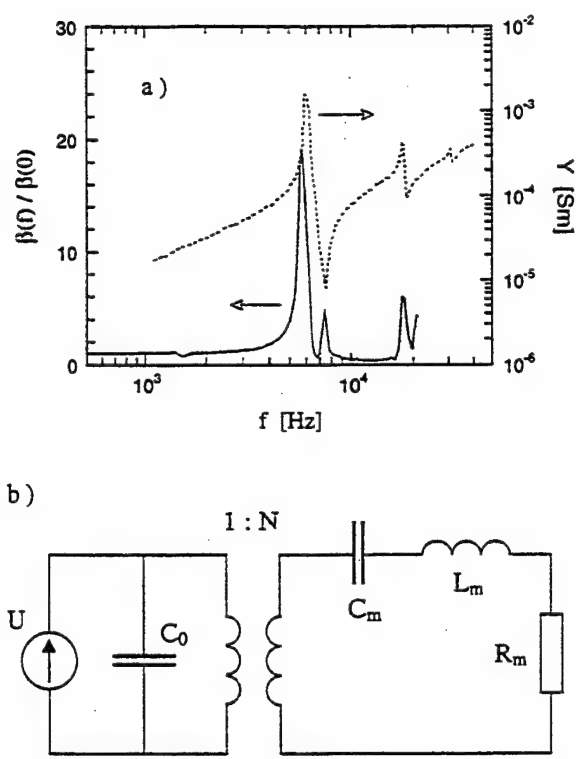


Figure 6

Paper by: A. E. Glazounov, Q. M. Zhang, and C. Kim

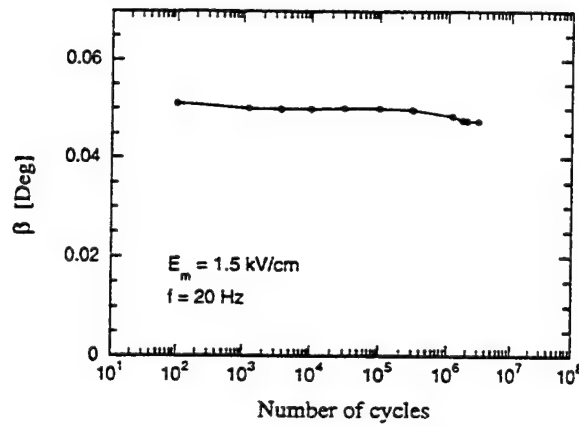


Figure 7

Paper by: A. E. Glazounov, Q. M. Zhang, and C. Kim

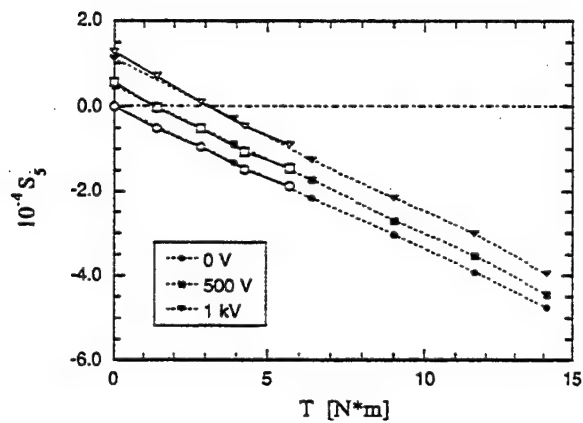


Figure 8

Paper by: A. E. Glazounov, Q. M. Zhang, and C. Kim

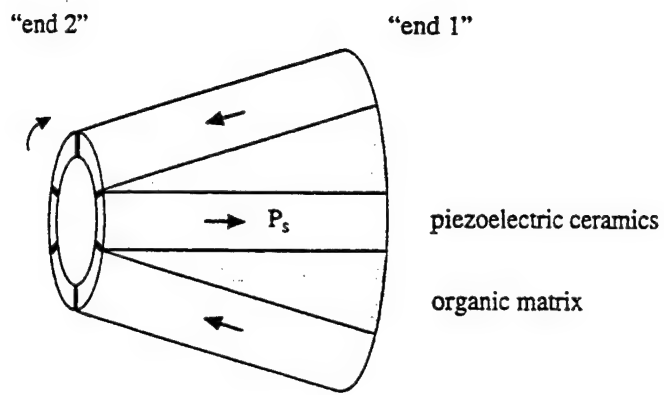


Figure 9

Paper by: A. E. Glazounov, Q. M. Zhang, and C. Kim

APPENDIX 56

Design and Performance of a High Force Piezoelectric Inchworm Motor

Jeremy Frank, Gary H. Koopmann, Weiching Chen, and George A. Lesieutre

Center for Acoustics and Vibration, Penn State University, University Park, PA 16802

ABSTRACT

A linear inchworm motor was developed for applications in adaptive, conformable structures for flow control. The device is compact (82 x 57 x 13 mm), and capable of unlimited displacement and high force actuation (150 N). The static holding force is 350 N. Four piezoceramic stack elements (two for clamping and two for extension) are integrated into the actuator, which is cut from a single block of titanium alloy. Actuation is in the form of a steel shaft pushed through a precision tolerance hole in the device. Unlimited displacements are achieved by repetitively advancing and clamping the steel shaft. Although each step is only on the order of 10 microns, a step rate of 100 Hz results in a speed of 1 mm/s. Since the input voltage can readily control the step size, positioning on the sub-micron level is possible.

Keywords: Inchworm actuator, piezoceramic actuator, piezoelectric actuator

1. INTRODUCTION

The possible applications of a high force, high displacement linear actuator are numerous, and the development of such a device has received considerable attention in recent years, as evidenced by the patents disclosed.¹⁻¹⁶ Two types of linear piezoelectric actuators, 'quasi-static inchworm' and 'ultrasonic travelling wave' have been most common.¹⁷⁻²² With the goal of improving the maximum dynamic actuation force, the quasi-static inchworm actuator was developed to actuate adaptive, conformable structures in flow control systems (Figure 1).

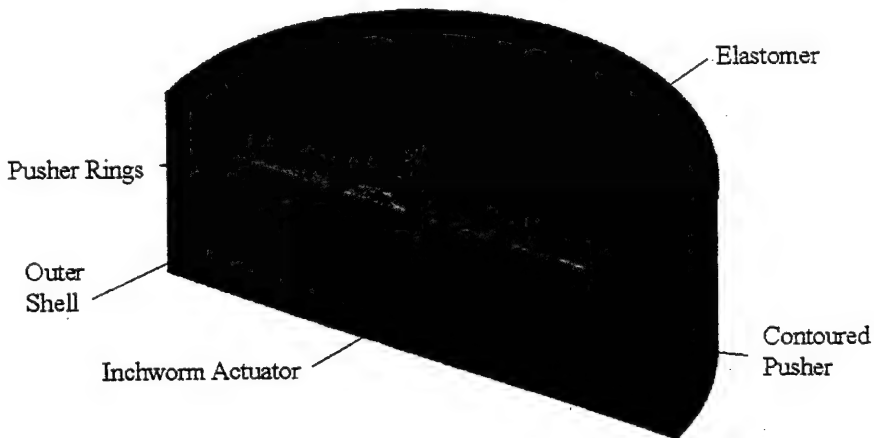


Figure 1 Application of the actuator in a flow control structure

Further author information -

J.F.: Email: jef@kirkof.meche.psu.edu Ph.D. candidate - Correspondence: Telephone: 814-865-7262; Fax: 814-863-4592

G.H.K.: Email: ghk@kirkof.meche.psu.edu Professor, Director of the Center of Acoustics and Vibration

W.C.: Email: chen@kirkof.meche.psu.edu Research Associate

G.A.L.: Email: g-lesieutre@psu.edu Associate Professor, Associate Director, CAV

2. DESIGN OF THE INCHWORM ACTUATOR

In previous designs, the dynamic actuation force has been limited by machining clearance issues and passive clamping schemes. With the current design, similar to a design investigated by Daimler-Benz,²³ we achieve higher forces by using the piezoceramic stacks to directly clamp a shaft, and by minimizing the tolerance between the shaft and the structure. As seen in Figure 2, the design concept consists of four integrated piezoceramic stacks, two for clamping and two for extension. The structure of the actuator consists of an outer frame, and an inner block which is able to move vertically on structural monolithic springs. In step 1, the lower clamping stack is energized, clamping the steel shaft to the inner block. Next, in step 2 the pushing stacks are energized, lifting the inner block and steel shaft a distance of 10 to 15 microns. Finally, the upper clamping stack is energized, clamping the shaft to the outer frame. At the same time, the lower clamping stack and the pushing stacks are de-energized, allowing the spring flexures to return the inner block to its original position, ready for the next step. When this process is repeated at high frequency, motion is achieved.

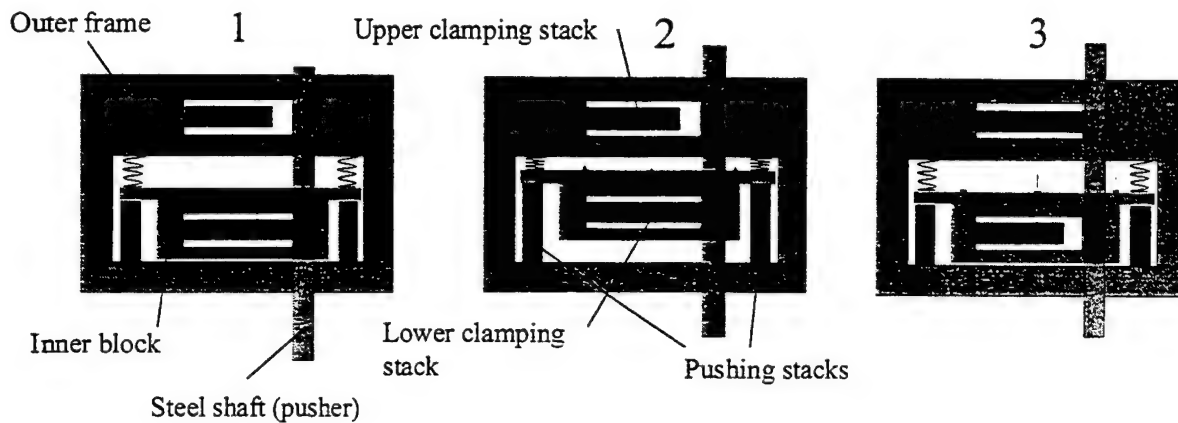


Figure 2 Conceptual schematic of the inchworm actuator

Using 21 mm long PZT stacks, poled in the d_{33} direction, the blocked force is 2000 N with a corresponding free deflection of approximately 20 microns (see Figure 3). Because of the small deflection, any clearance between the clamp and the shaft will result in a significant loss of potential clamping force. For this reason, the hole through which the steel shaft passes is reamed, ground and honed to as precise a tolerance as possible. The shaft is of hardened, precision ground stainless steel, and is chosen specifically to match the machined hole. This procedure reduces the tolerance between the shaft and the hole to about 5 microns, resulting in a minimized loss of clamping force.

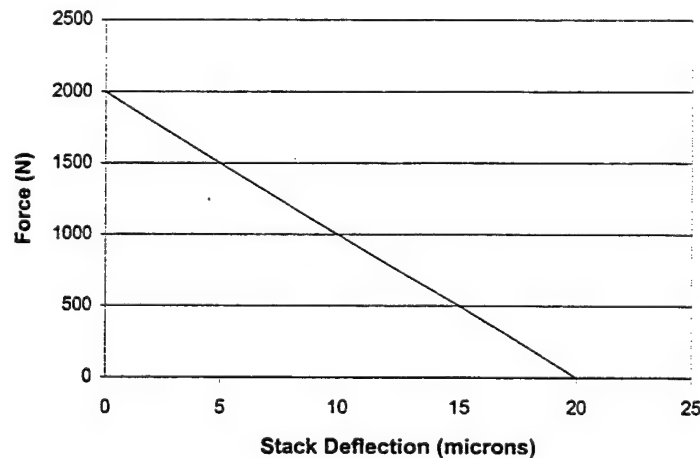


Figure 3 Force/displacement characteristics of the piezoceramic stacks

A picture of the prototype actuator is shown in Figure 4. The structure is cut using an EDM process from a single block of titanium alloy, resulting in a sleek design with no assembly necessary. Of particular interest are the monolithic flexures, also

cut directly out of the material, that allow relative motion of the moving parts. The inner block of the titanium frame, for example, is connected to the outer frame only by four monolithic flexures. These flexures allow vertical motion but not horizontal motion of the inner block, and provide the necessary pre-compression force to the piezoceramic stacks. This force prevents the stacks from receiving a tensile load, which is known to cause failure. The two clamping stacks are also pre-compressed into the frame with monolithic flexures. The flexures support the upper and lower clamp (seen in Figure 4), which provide the clamping force on the shaft when the stacks are energized. The clamp flexures also support the vertical shear load, which must not be supported by the piezoceramics.

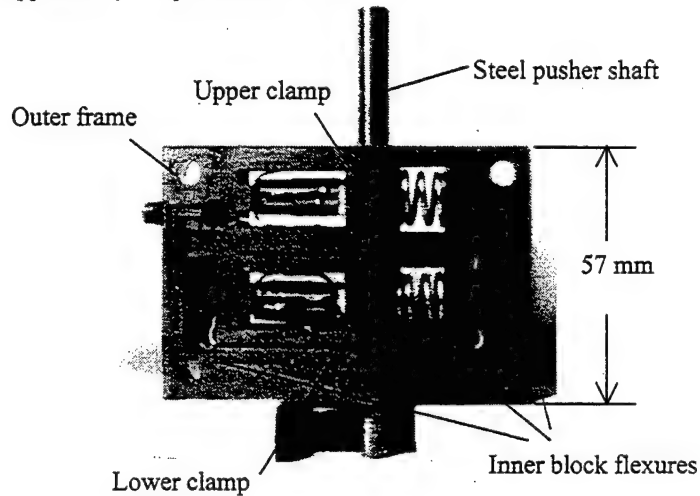


Figure 4 Photograph of the inchworm actuator

3. TESTING THE PROTOTYPE ACTUATOR

The prototype actuator was tested to characterize its performance. The variables of the signals driving the stacks included waveform shape, level, duty cycle and relative phasing. With a need for flexibility in mind, LABVIEW software was used to generate inchworm drive signals through a PC digital to analog output board. A typical set of drive signals, seen in Figure 5, shows that the pusher stacks are driven with a sine wave while the clamping stacks are driven with overlapping square waves. Since the clamping mechanism is only active when the piezoceramics are energized, the overlap in the clamp signals is necessary to prevent backslip when actuating an external force. The use of square waves as drive signals limits the upper range of available drive frequencies by inducing higher order longitudinal resonances in the piezoceramic stacks.²² However, only a square wave can provide the signal overlap that is essential to ensure clamping of the shaft at all times.

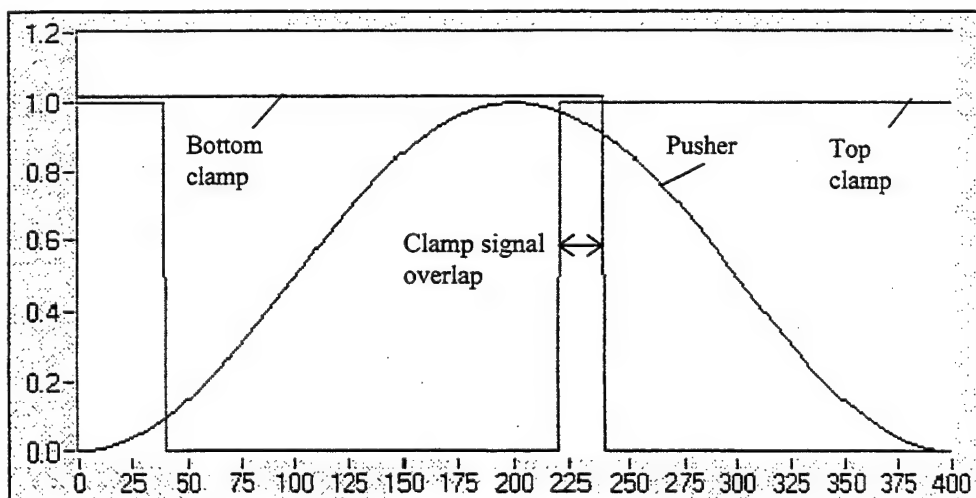


Figure 5 Typical drive signals generated with LABVIEW

A special-purpose calibration fixture is used for characterization of the inchworm, as shown in Figure 6. Its main feature is a stiff beam pivoted on one end in a precision bearing. The fixture is able to selectively drive loads that are primarily inertial in nature, primarily stiffness in nature, or a combination of both. The beam can be driven against a compression spring for a stiffness load, or a mass can be attached to the beam to increase the inertial load. A high-sensitivity strain gauge load cell and an LVDT position transducer are used to measure performance. Further, an analog to digital input board is used to record the output force and velocity in LABVIEW, a feature of the experimental setup that will eventually enable closed-loop operation of the inchworm.

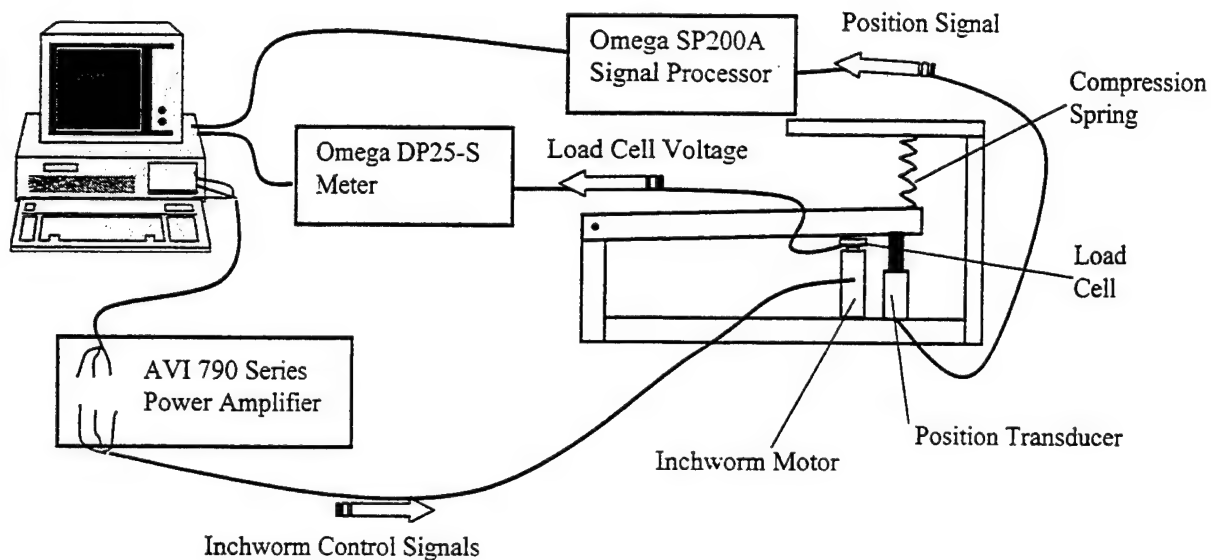


Figure 6 Schematic of the inchworm actuator performance characterization experiment

Three initial experiments were devised to characterize the actuator's speed, holding force and dynamic force. First, the actuator was driven against no load and the velocity was measured as a function of drive frequency. As seen in Figure 7, the behavior was fairly linear up to about 150 Hz, increasing to 1.2 mm/s. Above 150 Hz however, the square clamping signals began to cause problems, and the performance degraded.

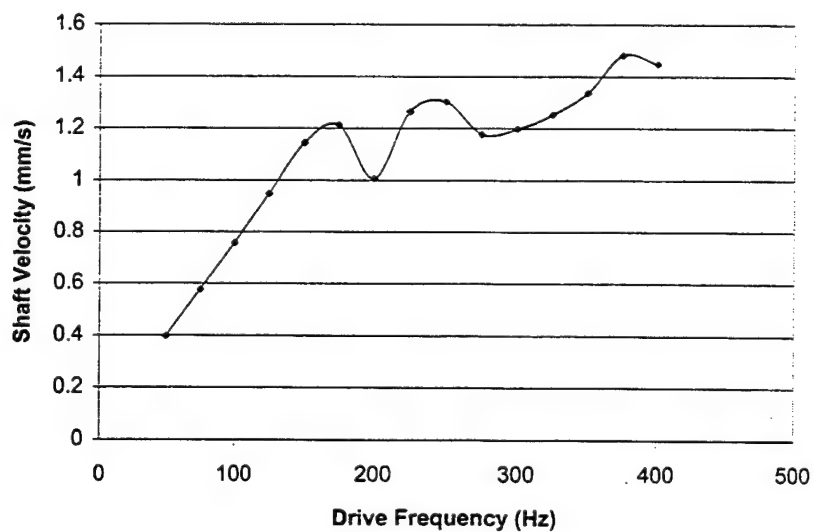


Figure 7 Free velocity of the actuator as a function of drive frequency

Next, the static holding force of the clamps was determined by applying a DC voltage to one clamping stack and measuring the load at which the shaft slips backward. As seen in Figure 8, the voltage was increased up to 100 V and a corresponding increase in holding force was observed. The two clamps were tested independently and displayed similar but not identical performance, probably because of variations in machining tolerance. This indicates that even tiny imperfections in machining can result in a significant loss of performance. The static holding force of the top and bottom clamps are shown to be 275 N and 375 N, respectively.

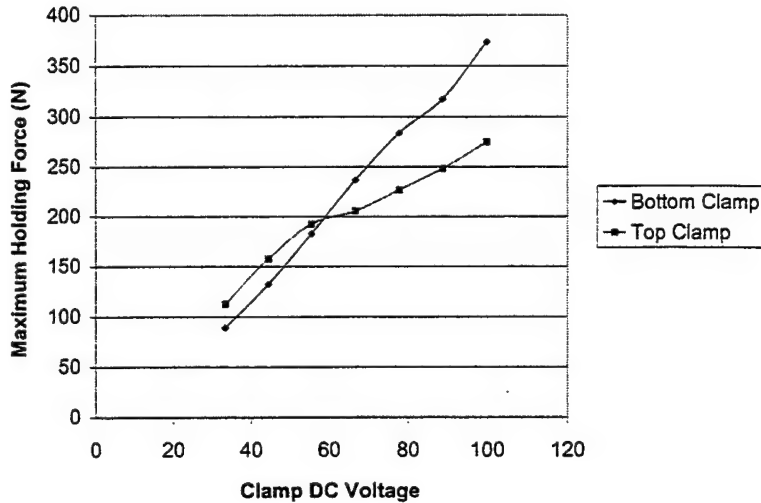


Figure 8 Static holding force of the clamps

Next, the dynamic drive signals were used to actuate the shaft against a spring load to measure the maximum dynamic force, or stall load. The maximum force was measured as a function of the input voltage to both the clamping and pushing stacks, which was increased up to 124 V. As shown in Figure 9, the stall force increased linearly with the voltage input to a maximum value of about 130 N. The power amplifiers were unable to generate square waves at more than 124 V, but for the voltage limitation of the piezoceramics (150 V) the maximum dynamic pushing force can be extrapolated to about 155 N. Although this force is high, it is disappointing in that it is more than 100 N lower than the measured static holding force. The loss in dynamic force is probably a result of unwanted oscillations of the piezoceramics, caused by the square wave excitation.

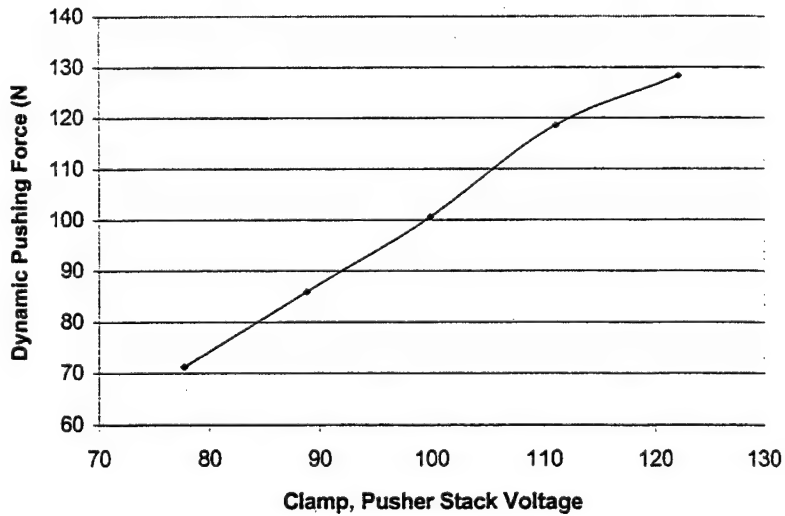


Figure 9 Maximum dynamic pushing force (stall load) as a function of input voltage

With evidence that the square waves were causing limitations in dynamic holding force, we tried alternative signal shapes in order to improve performance. First, sine waves were used to drive both the pushing and the clamping stacks. As expected,

the motion was quieter than with square waves, since the clamps were gradually clamping onto the shaft. However, the driving force was limited to less than 60 N (see Figure 10) because of the lack of overlap in the clamp signals. For applications where high speed but low force is required, sinusoidal signals could be used, since the smoother clamping mechanism allows the actuator to be driven at much higher frequencies. In the next part of the experiment, ramped square waves were used to drive the clamps in order to remove the high frequency problems caused by the square waves. The ramped square signals were really square waves with sine waves spliced in between. The hope was that the ramped waves could provide the necessary overlap between the clamp signals but eliminate the problems caused by the discontinuous square wave. As seen in Figure 10, the ramped waves achieved better stall loads than the sinusoidal signals, but did not perform as well as square waves. From this experiment it was determined that although the square waves reduce the dynamic force capability of the actuator, they are needed to cause the necessary overlap between the clamping signals.

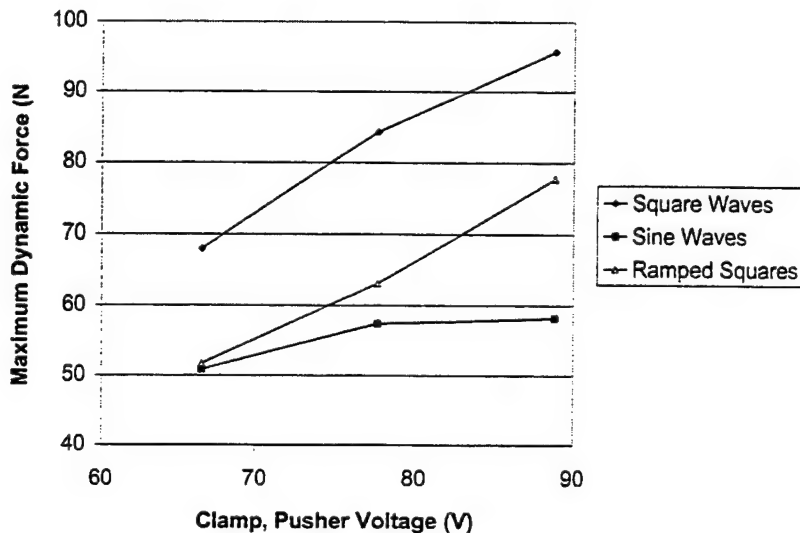


Figure 10 Dynamic force tests for alternative clamping signals

4. CONCLUSIONS

A linear inchworm motor was developed for structural shape control applications. Features of the subject device include small size (82 x 57 x 13 mm), unlimited stroke, speeds of about 1 mm/s, dynamic forces approaching 150 N, and static holding force capability greater than 275 N. The device is machined as one continuous structure with monolithic flexures, and actuates a steel shaft through its center. Large displacements are achieved by repetitively advancing and clamping the shaft. The dynamic actuation force, although high, is limited by the use of square waves in the driving signals. Other types of signals were tried, but did not improve the stall load.

ACKNOWLEDGEMENTS

This work was supported by DARPA under the SAMPSON project, and performed in collaboration with engineers at Boeing St. Louis, General Dynamics, Penn State's Applied Research Laboratory, and PCB Piezotronics.

REFERENCES

1. R. Stibitz, "Incremental Feed Mechanisms", *U.S. Patent: 3,138,749*, 1964.
2. J.T. McNancy, "Piezoelectric transducer force to motion converter", *U.S. Patent: 2,154,700* 1964.
3. K. Hsu, and A. Biatter, "Transducer", *U.S. Patent: 3,292,019*, 1966.
4. G.L. Locher, "Micrometric linear actuator", *U.S. Patent: 3,296,467*, 1967.
5. A.D. Brisbane, "Position control device", *U.S. Patent: 3,377,489*, 1968.
6. G.V. Galutva, "Device for precision displacement of a solid body", *U.S. Patent: 3,684,904* 1972.
7. R.A. Bizzigotti, "Electromechanical translational apparatus", *U.S. Patent: 3,902,085*, 1975.
8. Y. Sakitani, "Stepwise fine adjustment", *U.S. Patent: 3,952,215*, 1976.
9. Ishikawa, and Y. Sakitani, "Two-directional piezoelectric driven fine adjustment device", *U.S. Patent: 4,163,168*, 1979.
10. G. O'Neill, "Electromotive actuator", *U.S. Patent: 4,219,755*, 1980.
11. T. Taniguchi, "Piezoelectric driving apparatus", *U.S. Patent: 4,454,441*, 1984.
12. A. Hara, H. Takao, Y. Kunio, T. Sadayuki, and N. Keiji, "Electromechanical translation device comprising an electrostrictive drive of a stacked ceramic capacitor type", *U.S. Patent: 4,570,096*, 1986.
13. C.W. Staufenberg, Jr., and R.J. Hubbell, "Piezoelectric electromechanical translation apparatus", *U.S. Patent: 4,622,483*, 1986.
14. T. Fujimoto, "Piezo-electric actuator and stepping device using same", *U.S. Patent: 4,714,855* 1987.
15. T. Murata, "Drive apparatus and motor unit using the same", *U.S. Patent: 4,974,077*, 1990.
16. G. Rennex, "Inchworm actuator", *U.S. Patent: 5,3323,942*, 1994.
17. J.E. Meisner and J.P. Teter, "Piezoelectric/magnetostrictive resonant inchworm motor". *SPIE*, Vol. 2190, pp. 520-527, 1994.
18. S.K. Lee and M. Esachi, "Design of the electrostatic linear microactuator based on the inchworm motion", *Mechatronics*. Vol. 5, No. 8, pp. 9653-972, 1995.
19. T. Funakubo, T. Tsubata, Y. Taniguchi, and K. Kumei, "Ultrasonic linear motor using multilayer piezoelectric actuators", *Japanese Journal of Applied Physics*, Vol. 34, Part 1, No. 5B, pp. 2756-2759, May 1995.
20. T. Pandell and E. Garcia, "Design of a piezoelectric caterpillar motor", *Proceedings of the ASME aerospace division*. AD-Vol. 52, pp. 627-648, 1996.
21. T. Galante, "Design and fabrication of a high-force linear piezoceramic actuator", M.S. thesis, Penn State University, August 1997.
22. D. Newton, E. Garcia, and G. C. Horner, "A linear piezoelectric motor", *Smart Materials and Structures*, Vol. 7, No. 3, pp. 295-304, June 1998.
23. W. Martin, Daimler-Benz, Private communication, January 1998.

MODELING
and
CHARACTERIZATION

**Finite Element and
Other Methods**

APPENDIX 57

Finite element and experimental study of composite and 1-D array transducers

Wenkang Qi^a and Wenwu Cao^b

^aDiasonics Vingmed Ultrasound, 2860 De La Cruz Blvd., Santa Clara, CA 95050

^bMaterials Research Laboratory and Department of Mathematics, The Pennsylvania State University, University Park, PA 16802

ABSTRACT

This paper reports a combined finite element and experimental study of composite and 1-D array transducers. The main properties characterized are the electrical impedance and beampattern. In order to calculate the beampattern of a transducer immersed in water, the pressure distribution and the normal velocity at the interface of water and transducer were calculated by using ANSYS®. These results were then input into the Helmholtz integral to calculate the beampattern. The impedance curve was obtained by performing harmonic analysis using ANSYS®. Related experiments were also conducted to verify these calculated results, good agreement was achieved between the experiments and simulations. Because of the similarity between the structures of 2-2 composite and 1-D array, the same FEA modeling procedure for 2-2 composites was extended to study a 1-D array. Particularly, the cross talk level and directivity of each element in an array were studied.

Keywords: FEA, composite, array, beam pattern, impedance, Helmholtz integral, ANSYS®

1. INTRODUCTION

Lateral modes in piezocomposites limit the application of piezocomposites. These lateral modes are caused by the periodic structure of piezocomposites⁽¹⁻⁷⁾. Both the T-matrix and multisource T-matrix studies showed that lateral modes can be suppressed by introducing irregularities into either ceramic phase or polymer phase^{8,9}. In our previous studies, FEA was used to study composite transducers^{10,11}. The beampattern was calculated directly by using FEA, few experiments were conducted at the time. When calculating the beampattern of a transducer directly using FEA (ANSYS®), the model is too large since one needs to include a large volume of water medium. In this paper we report a new way of calculating the beampattern. Considering the similarity of the structures between 2-2 composites and 1-D arrays, this new method is also extended to study 1-D arrays. In array designs, there are still many problems need to be addressed, such as crosstalk and angularity of each element of arrays.

2. BEAMPATTERN CALCULATION

The beampattern is an important factor in transducer design. The lateral resolution (beam width), the resolution in elevation direction (slice thickness), sidelobe level and grating lobe level can all be retrieved from the beampattern. A commonly used method to calculate the beampattern is to take a cosine Fourier transform of the space distribution of the vibrating intensity. For example, the beampattern in the far field of a uniformly vibrating rectangular transducer in an infinite rigid baffle is a sinc function. However, there are limitations to this approach. First, it is valid for farfield only; second, the baffle of the transducer is assumed to be an infinite rigid one, which does not correspond to reality. In ultrasonic imaging, the nearfield is of great interest, but the beampattern in the nearfield cannot be obtained by simply performing a cosine transform. We must calculate the general form of the Helmholtz integral.

Calculating the beampattern in the medium is to find the complex radiated pressure $p(x)$ in the fluid region exterior to a closed vibrating surface S . This problem follows from Green's Theorem that the acoustic pressure, p , and the normal velocity, v , satisfy the integral formula¹²

$$p(x) = \iint_S \left\{ p(\sigma) \frac{\partial G(x, \sigma)}{\partial n_\sigma} + i\omega \rho v(\sigma) G(x, \sigma) \right\} ds(\sigma) \quad (1)$$

where, S is the vibrating surface, x is an arbitrary point exterior to S , σ is a point on surface S , $\frac{\partial}{\partial n}$ denotes differentiation in the outward normal direction, $p(\sigma)$ is the pressure at σ , and $v(\sigma)$ is the normal velocity at point σ . $G(x,\sigma)$ is the green function,

$$G(x,\sigma) = \frac{1}{4\pi} \frac{e^{-ik|x-\sigma|}}{|x-\sigma|} \quad (2)$$

$$k = \frac{\omega}{c} \quad (3)$$

The beampattern may also be directly calculated using FEA by adding the medium to the model. A large volume of water in front of the transducer greatly increases the computation task. Large model may also cause error accumulation. Fig. 1 shows the difference between the two methods. One can see that the two methods agree with each other very well in the region near the transducer; however, the result from FEA oscillates in the medium beyond the focal point. Our new combined method, FEA plus Helmholtz, gives good results in both the near field and the far field.

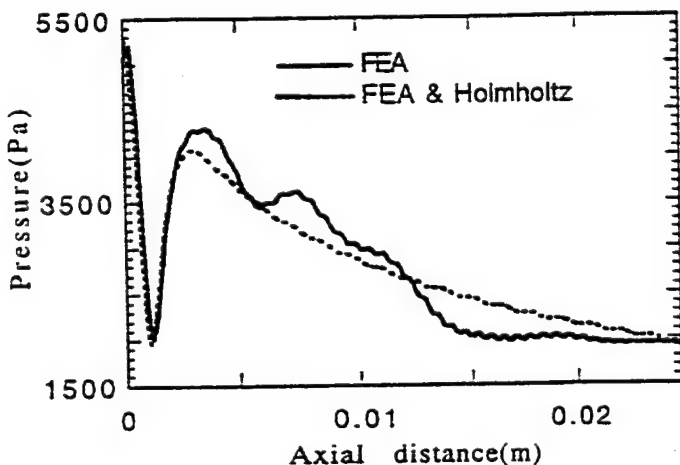


Fig. 1 The axial pressure distribution obtained using FEA and FEA plus Helmholtz integral, respectively.

3. STUDY OF 2-2 COMPOSITE TRANSDUCERS

Finite element analysis (FEA) and experiments have been performed to study 2-2 composites with both low and high ceramic volume percentages. The electrical impedance and the beampattern were measured using an impedance analyzer and a hydrophone water tank system, respectively. Dicing and filling technique was employed to build the designed 2-2 composites. Spurrs epoxy, which has 4 components, was used as the filler for the kerfs and the PZT-5H elements were diced by using a K&S computer controlled diamond saw.

3.1. The electrical impedance

A. Regular 2-2 composites

A few regular periodic 2-2 composites were fabricated. Table I shows the specifications of the four regular composites constructed.

Table I. Specifications of the two regular 2-2 composite transducers

Sample No.	Ceramic volume(%)	kerf(mils)(microns)	Center frequency
1	80	2 (50.8)	3.5MHz
2	40	5 (127.0)	3.5MHz

Fig. 2 is the computed and measured impedance curves for the No.1 sample. The first anti-peak is the thickness mode and the fifth anti-peak is its third harmonic. The second, third and fourth anti-peaks are lateral modes. In this case, the lateral modes are not strongly coupled with the thickness mode. The calculated impedance is almost the same as the measured impedance curve.

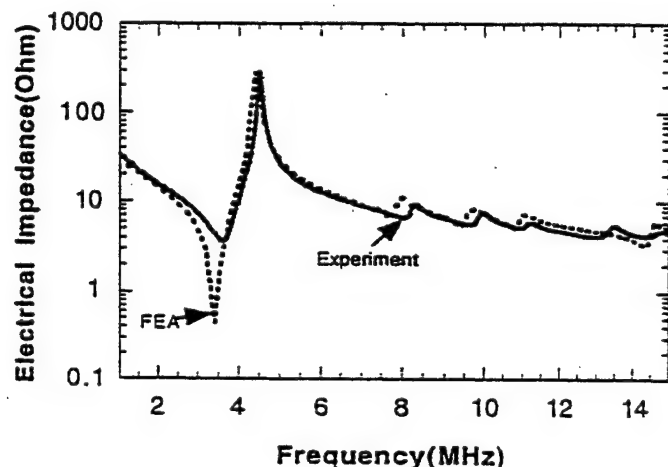


Fig. 2 Impedance spectrum of a regular 2-2 composite with 80% ceramic volume and 2 mil kerfs

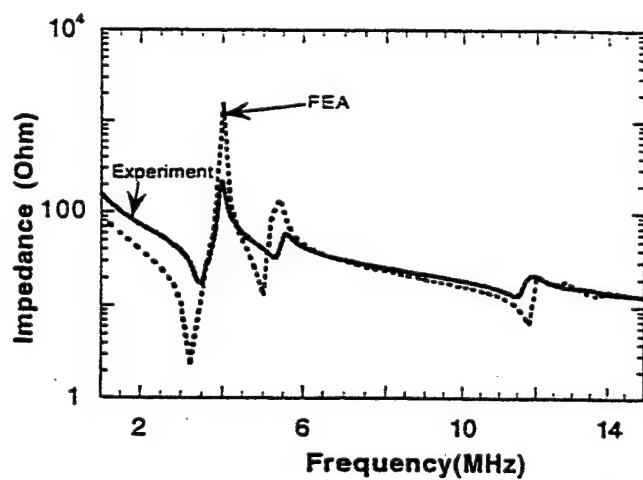


Fig. 3 A Impedance spectrum of a regular 2-2 composite with 5 mil kerfs and 40% ceramic volume.

Fig. 3 is the computed and measured impedance curves for the No.2 sample. The three modes are the thickness mode, lateral mode, and the third harmonics of the thickness mode, respectively. The lateral mode strongly couples to the thickness mode in this case. One can see again that the FEA results match the measured results very well.

B. 2-2 composites with irregular kerfs

A 2-2 composite with three different kerfs have been constructed by dicing the ceramic with three different blades, the widths of the three different blades are 5, 4 and 2 mils, respectively. The spacing data can be programmed into a laptop computer which controls the diamond saw.

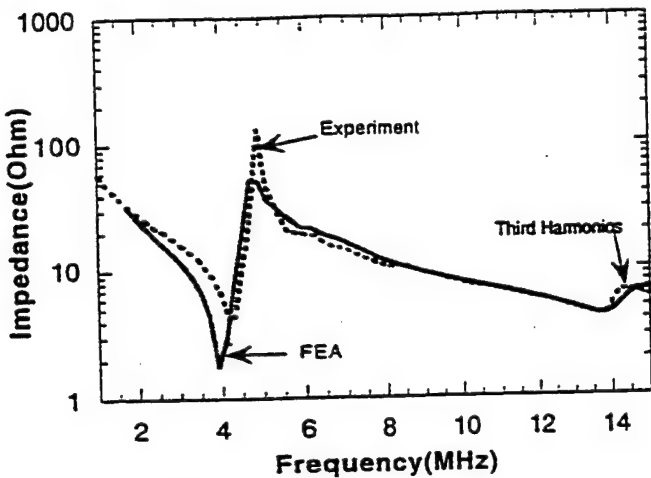


Fig. 4 Impedance spectrum of a sequential irregular 2-2 composite with 40% ceramic volume and 3 different kerfs (5,4,2 mils)

Fig. 4 is the calculated and measured impedance curves of a sequential irregular 2-2 composite with 40% ceramic volume and 3 different sized kerfs. There are basically two major modes shown in Fig. 4. The first is the thickness mode and the second one is its third harmonic. The measured results are almost the same as the calculated result.

Fig. 5 are the impedance curves of a 2-2 composite with 60% ceramic by volume and irregular ceramic width. There is only one major mode, i.e., the thickness resonance mode. One can see two small bumps in both the calculated and the measured results in the vicinity of the thickness mode which could be remnant of lateral mode. Since these two bumps are very small, the interference to the thickness mode is minimal. These two bumps also imply that the ratio of 5:4:2 irregularity may not be sufficient to suppress the lateral mode.

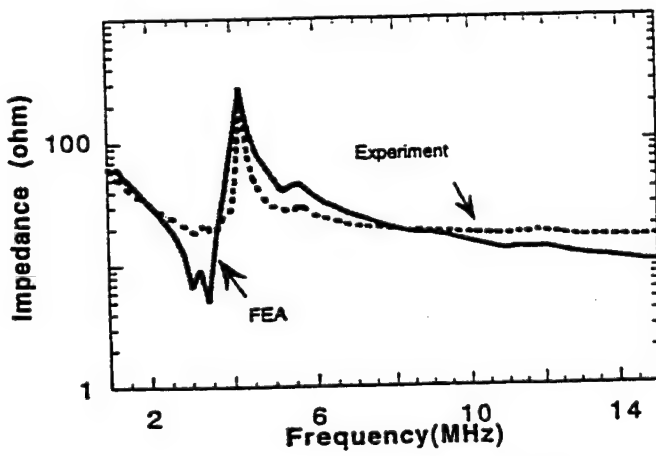


Fig. 5 The impedance of a sequential irregular 2-2 composite with different ceramic width (5,4,2 mil) and 60% ceramic by volume.

From the comparison of the four sets of calculated and experimental measured electrical impedance curves, it can be concluded that the FEA results are very accurate in evaluating the electrical impedance. In other words, the FEA simulation can practically replace the experiments to study the impedance spectrum.

3.2. Beampattern for 2-2 composite trasducers

A hydrophone system was used to measure the transducer beampattern. Both the nearfield and farfield can be measured accurately by using this system.¹³ Fig. 6(a) is the calculated 2-D beampattern of a 2-2 40% ceramic composite transducer with water loading. Fig. 6(b) is the measured result. The shapes of the two results are almost the same, but the calculated beampattern appeared to have much more details which did not show on the measured one due to the low sensitivity of the hydrophone.

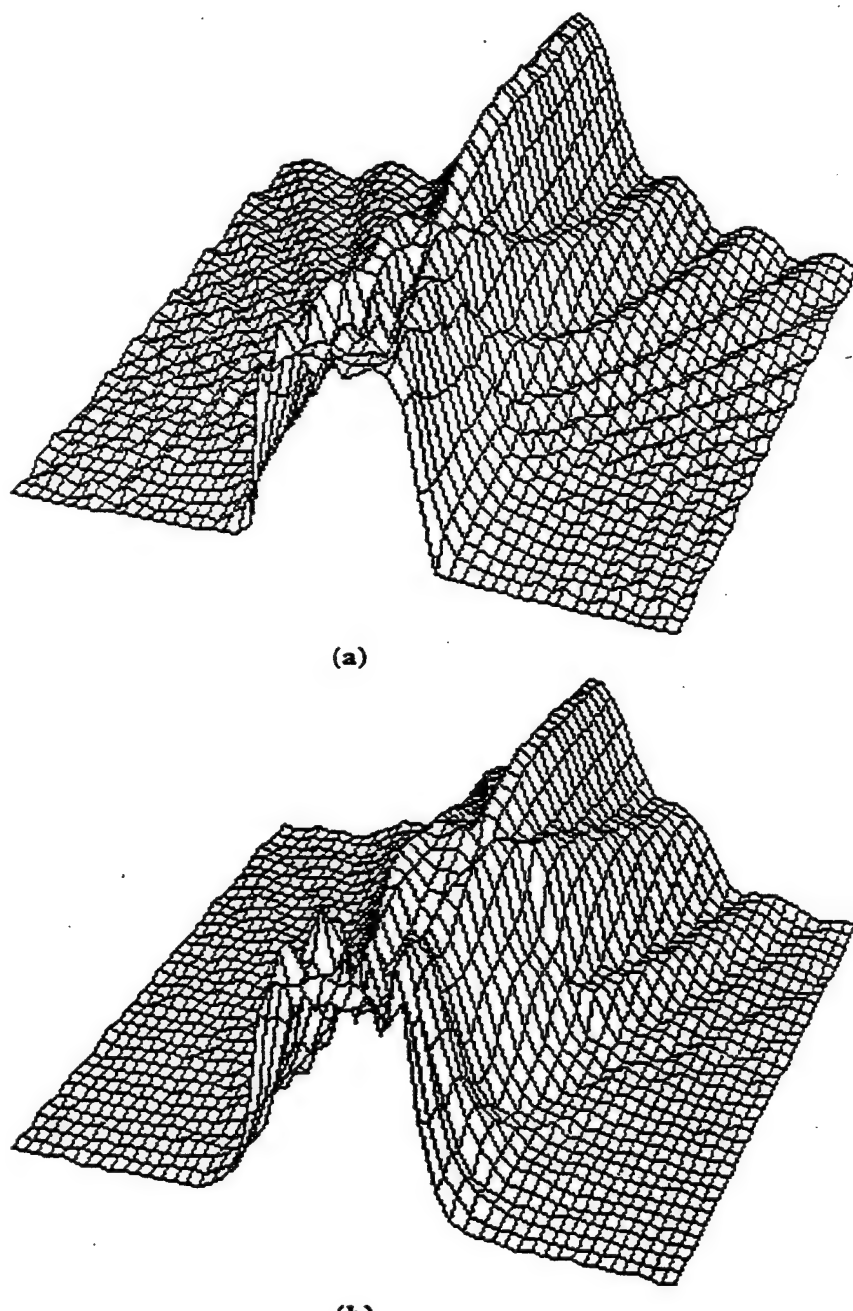


Fig. 6 Beampattern of regular 40% ceramic 2-2 composite transducer immersed in water. (a) Calculated using the combined method; (b) Measured beampattern using a hydrophone system.

Fig. 7 is the directivity pattern of a regular 2-2 composite transducer with 60% ceramic by volume. The kerf of the 2-2 composite is 5 mils. The measured directivity has lower sidelobe level, and the measured directivity is not symmetric. The asymmetry may be caused by the asymmetry of the transducer construction or by the misalignment of the transducer. The calculated directivity pattern showed more details of the sidelobes while the measured one has much lower sidelobe level. This is caused by the low sensitivity of the hydrophone. Fig. 8 is the on-axis pressure distribution comparison. the agreement is satisfactory considering the non-optimized transducer and the sensitivity of the hydrophone.

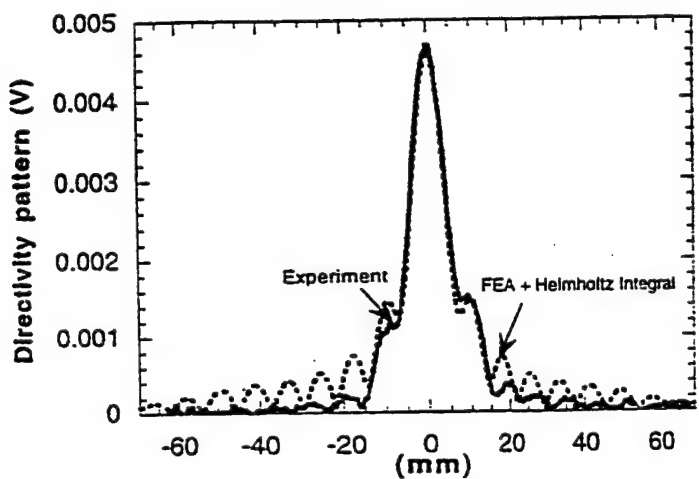


Fig. 7 A regular 2-2 composite with 5 mil kerf and 60% ceramic volume

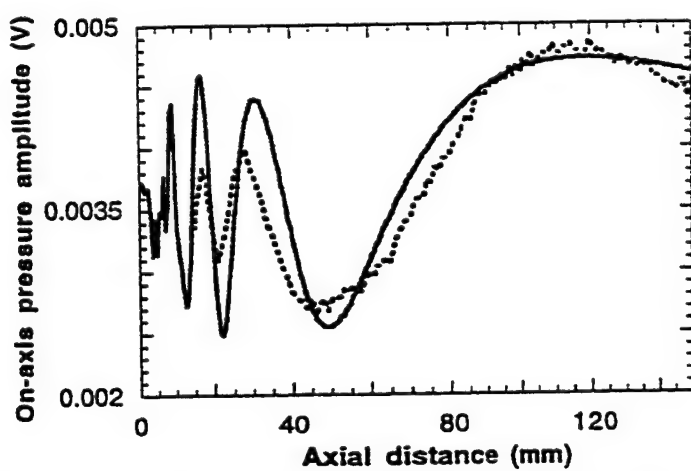


Fig. 8 On-axis pressure of a regular 2-2 composite with 5 mil (127 micron) kerf and 60% ceramic volume. The solid line is from calculation while the dotted line is measured data.

Fig. 9 is the directivity pattern of a sequential irregular 2-2 composite with different ceramic widths. The calculated directivity pattern and the on-axis pressure distribution by FEA and Helmholtz are almost the same as the measured ones as shown in Fig. 10.

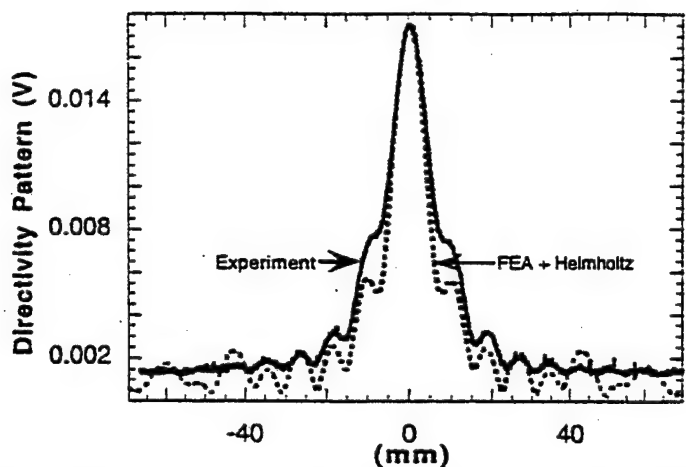


Fig. 9 A sequential irregular 2-2 composite with 3 different ceramic width and 60% ceramic by volume.

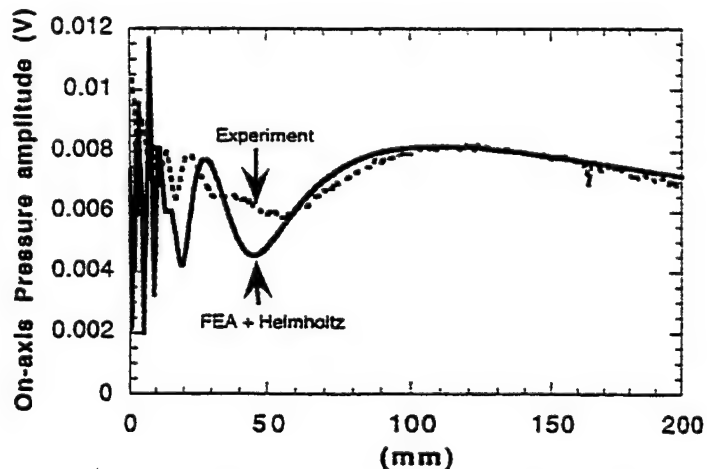


Fig.10. A sequential irregular 2-2 composite with 3 different kerfs and 50% ceramic volume

Three sets of pressure distribution data have been compared in this section. Although some difference were found, the FEA plus Helmholtz results are basically the same as the experimental results. We therefore conclude that the FEA simulation can replace experiment to study the beampattern of transducers with good accuracy.

4. FEA (ANSYS®) STUDY ON 1-D ARRAYS

The crosstalk, subdicing and baffle effects in a transducer array have not been thoroughly studied theoretically up to date. Because of the complexity, the FEA seems to be the only tool which could be employed to address these issues.

4.1 Angularity study of an element embeded in an array

Each element of an array is embeded in a finite dimension array, the baffle effect is neither a cosine function, nor a constant. It always has been assumed to be a cosine function in the transducer industry because of lacking more accurate modeling tools.

Fig. 11. is a 1-D array FEA model, it has a backing, 2 matching layers, Fluid-structure interface and water medium. There are 32 elements in this array model. The kerf is 4 mil. the ceramic volume percentage is 60%, and the thickness of the ceramic is 1.12 mm. With this model, the directivity pattern of an element can be studied by exciting only one element.

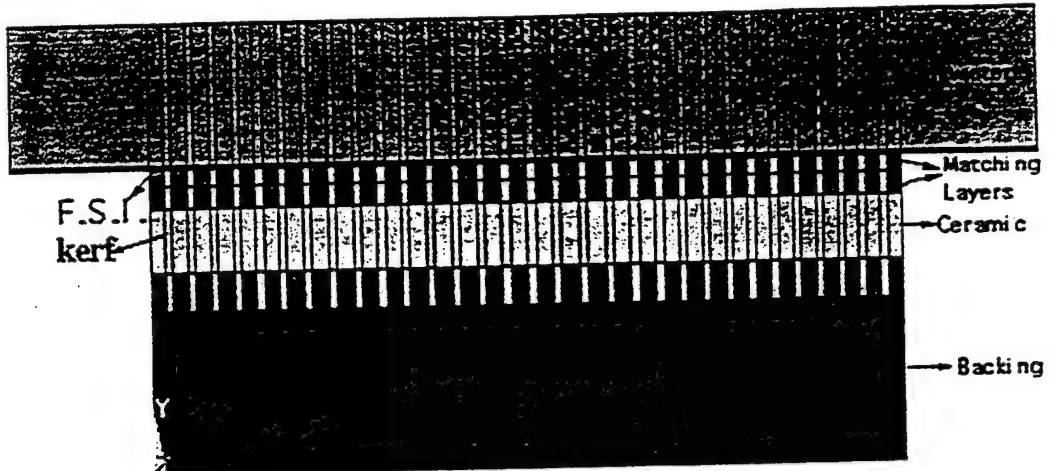


Fig. 11 The FEA model for a 1-D array

If the 16th element in the array is fired, the pressure and normal velocity distribution can be obtained through harmonic analysis in ANSYS®.

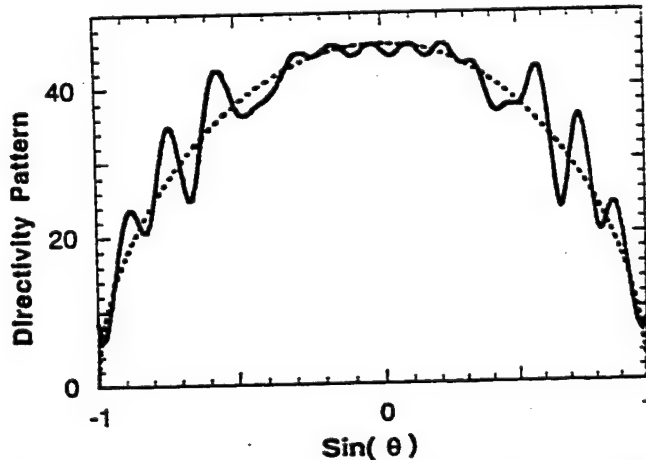


Fig. 12 The directivity pattern of a 1-D array with only one element excited

In Fig. 12, the dashed line represents the $\text{sinc}(\frac{kd}{2} \sin(\theta)) * \cos(\theta)$ the solid line is the FEA result. The directivity pattern obtained from FEA is much more complicated than the simple product of $\text{sinc}(\frac{kd}{2} \sin(\theta)) * \cos(\theta)$. The directivity pattern may also depends on many other factors, such as the properties of the kerf filler and the geometry of the array structure. For example, the hardness of the filler material can have a strong influence on the directivity pattern. As shown in Fig.13, the intensity of the sound field is higher when the kerf is filled with harder material. For a 2-2 composite with soft kerf filler, the kerf is vibrating out of phase with the ceramic, causing the vibrating intensity to become smaller than that of the array filled with harder material. On the other hand, the angular response becomes wider when the backing material is softer although the amplitude of angular response is smaller.

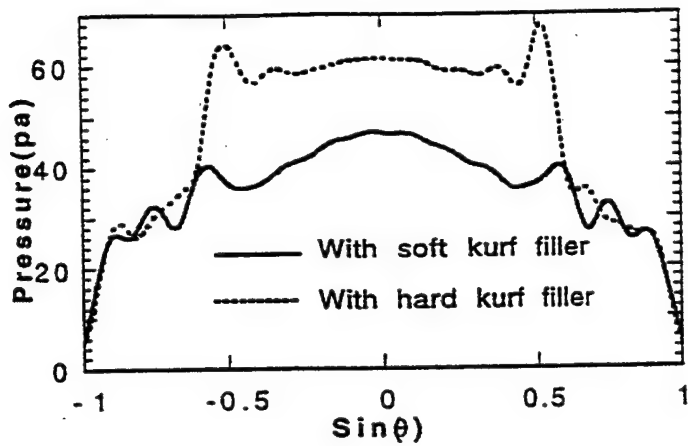


Fig.13 The directivity pattern (acceptance angle) of an array element with soft and hard kerf filler

It is desirable to have a wide angular response for each element in an array, particularly for phased arrays. However, the crosstalk between elements makes the angular response narrower, or strongly angular dependent. As shown in Fig. 14, the amplitude variations are caused by the crosstalk with the neighboring elements. One can also see that when the two matching layers are not diced, the crosstalk is very strong and the angular response of the element is very narrow. If one matching layers is subdivided, the angular response becomes wider. There is a substantial improvement in the angular response when both matching layers are subdivided. This results explains the necessity to cut both the two matching layers.

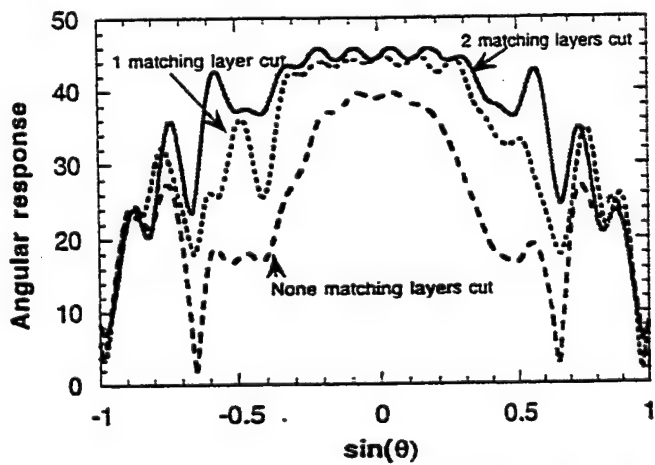


Fig. 14 The angular response of an element in an array with different matching layer configuration

4.2 Crosstalk in 1-D array

The crosstalk in arrays degrades the contrast resolution or cause artifacts, it is of great importance to reduce the crosstalk level in medical imaging. In this section, a new way to define the crosstalk is discussed. We will also discuss how to cut the kerfs in order to reduce the level of crosstalk between elements. The dimensions of this array is the same as the linear array studied above.

If we excite one element at the center of an array using a pulse, then record the impulse response of this element and its neighbors, the ratio of the responses of the neighbor elements to that of the excited element will be defined as the crosstalk level in this study.

The center element of the array shown in Fig. 11 is excited electronically, and the impulse responses of the center element and its four neighbors have been calculated. The outer matching layer was not cut while the inner matching layer was diced. From Fig. 15 (a) to Fig. 15 (c), the amplitude of impulse response of the neighboring elements gradually decreases as they are away from this element. Also the impulse response gradually delays because of the distance which the wave has to travel. Fig. 16 (dashed line) shows how fast the impulse response decreases from one element to its neighbors. The RMS value has been used as the measure for the impulse response. The ratio of the impulse response of the neighbor to the impulse response of the center element was calculated in dB scale.

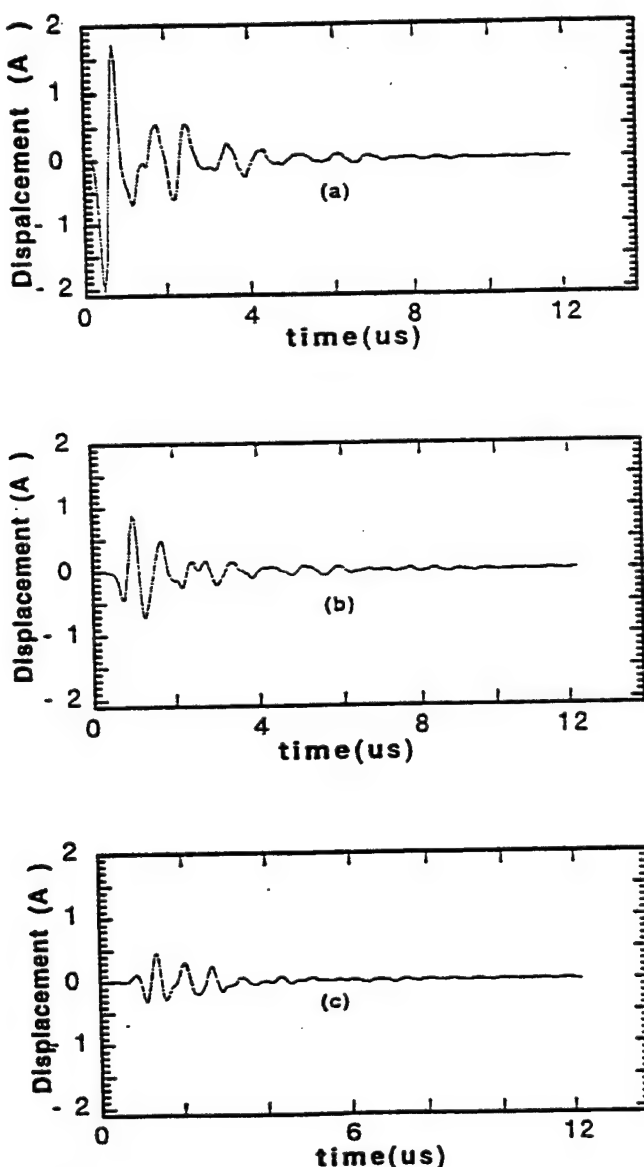


Fig. 15(a) The impulse response of the center element in an array. (b) The impulse response of the second neighbor of the center element in an array. (c) The impulse response of the third neighbor of the center element in an array

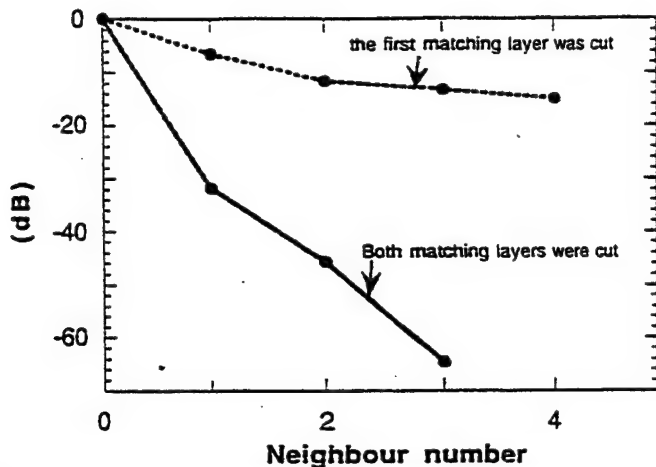


Fig. 16 The crosstalk level of an array with one or two matching layers cut

Fig. 16 shows the results for an array with only the inner matching layer diced and with both matching layers diced. One can see that the crosstalk level is much lower when both of the matching layers are diced. The crosstalk level for the nearest neighbor should be at least -30 dB or lower in order to avoid the artifacts, therefore it is not enough to dice only one matching layer. This is the reason why the current array designs have both matching layers diced.

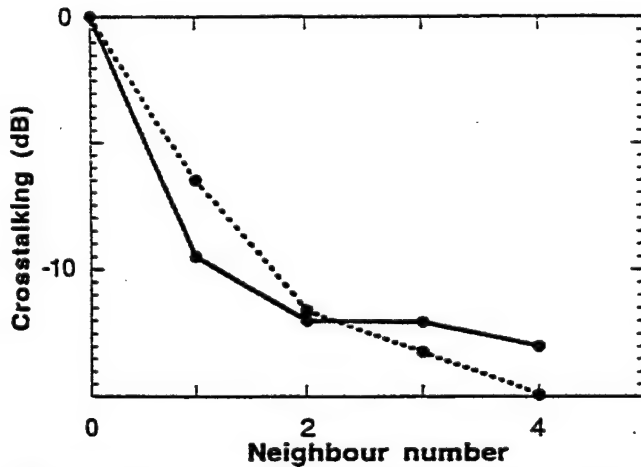


Fig. 17 The crosstalk level of an 1-D array with one matching layer dicing and without dicing.

Fig. 17 shows the comparison of the crosstalk level of an array without dicing on the matching layers (dashed line) and with dicing only on one of the two matching layers (solid line). Interestingly, cutting only one matching layer does not help much in this case. The explanation for this is that one non-diced matching layer can still strongly couple the adjacent elements. A lens is often put on top of the array to change the focus of the transducer. This lens may cause extra crosscoupling unless the lens is made of materials which have very small shear modulus.

5. CONCLUSION

In this paper, we have demonstrated that finite element analysis (FEA) is a powerful numerical tool in ultrasonic transducer and array design. The theoretical results from FEA have been confirmed by related experiments for 2-2 composite transducers. A new way of combining the FEA and Helmholtz integral has been used in our study of the beampattern, which can overcome the difficulty of error accumulation in large size FEA model. The same method used in 2-2 composite transducer study has been extended to study 1-D arrays. The cross talk among adjacent elements in arrays can be coupled through matching layers and the backing. Cutting both matching layers are necessary to reduce the element cross-talk.

6. ACKNOWLEDGEMENTS

This work was supported by the Office of Naval research and the Witaker Foundation under Special Opportunity Award.

7. REFERENCES

1. W. Cao, Q. M. Zhang and L. E. Cross, Theoretical Study on the Static Performance of Piezoelectric Ceramic-Polymer with 2-2 Conductivity, *IEEE Trans. Ultrason., Ferroelec., Freq. Contr.*, **40**, pp. 103-109, 1993.
2. T. R. Gururaja, A. Safari, R. E. Newnham, and L. E. Cross, Piezoelectric Ceramic-Polymer Composites for Transducer Applications, In *Electronic Ceramics*, L. M. Levinson, Ed. New York: Marcel Dekker, 1987, pp. 92-128.
3. W. A. Smith, New Opportunities in Ultrasonic Transducers Emerging from Innovations in Piezoelectric Materials, *SPIE* **1**, pp 733-738, 1992.
4. W. A. Smith, A. A. Shaulov, and B.A. Auld, Design of Piezocomposites for Ultrasonic Transducers, *Ferroelectrics*, **91**, pp. 155-162, 1989.
5. W. A. Smith, The role of piezocomposites in ultrasonic transducers, *Proc. 1989 IEEE Ultrason.Symp.*, pp. 755-766, 1989.
6. B. A. Auld and Y. Wang, Acoustic Wave Vibrations in Periodic Composite Plates, *IEEE 1984 ultrasonics symposium*, pp. 528-532, 1984.
7. B. A. Auld, Y. A. Shui and Y. Wang, Elastic Wave Propagation in Three-Dimensional Periodic Composite Materials, *J. Phys.*, **45**, pp. 159-163, 1984.
8. W. Cao and W. Qi, Plane Wave Propagation in Finite 2-2 Composite, *J. Appl. Phys.*, **78**, pp. 4627-4632, 1995.
9. W. Cao and W. Qi, Multisource Excitations in a Stratified Biplane Structure, *J. Appl. Phys.*, **78**, pp. 4640-4646, 1995.
10. W. Qi and W. Cao, Finite Element Analysis and Experimental Studies on the Thickness Resonance of Piezocomposite Transducers, *Ultrasonic Imaging* **18**, pp. 1-9, 1996.
11. W. Qi and Wenwu Cao, Finite element analysis of periodic and random 2-2 piezoceramic transducers with finite dimensions, *IEEE Transactions on Ultrasonics, Ferroelectrics, and Frequency Control*, **44**, pp.1168-1171, 1997.
12. G. W. Benthien, D. Barach and D. Gillette, *CHIEF Users Manual*, Naval Ocean System Center Technical Report, 1988.
13. M. Draheim, Finite Element Modeling and Experimental Study of Ultrasonic Impedance Matching Layer for Medical Transducers, M.S. Thesis, The Pennsylvania State University, 1997.

APPENDIX 58

Characterization of Lead Zirconate Titanate Piezoceramic Using High Frequency Ultrasonic Spectroscopy

Haifeng Wang, Wenhua Jiang* and Wenwu Cao

Materials Research Laboratory

National Resource Center for Medical Ultrasonic Transducer Engineering

The Pennsylvania State University, University Park, PA 16802

Abstract

Doped piezoceramic lead zirconate titanate (PZT-5H) has been characterized in the frequency range of 20-60 MHz using ultrasonic spectroscopy. Theoretical analyses were performed for the reflection and refraction of acoustic waves at the interface of water-piezoelectric ceramic. The incident directions of the wave were chosen to be appropriate for ultrasonic spectroscopy measurements. Shear wave spectrum was obtained through mode conversion using a pair of longitudinal transducers submerged in water. The phase velocity shows linear dependence on frequency while the attenuation may be described by a second order polynomial of frequency in the frequency range investigated. The Kramers-Kronig relation between ultrasonic phase velocity and attenuation were compared to measured results.

PACS Numbers: 62.20.Dc, 74.25.+k, 78.20.Hp, 43.58.+z, 43.60.+r

I. Introduction

Application of higher frequency broadband ultrasonic transducer results in the improvement of the axial and lateral resolutions in medical imaging. Design high frequency transducer requires better knowledge of material properties since the ultrasonic dispersion becomes important for frequencies above 50 MHz. The dispersions of velocity and attenuation may deform the acoustic pulse and cause inappropriate interpretation of the pulse acoustic signal. Hence, knowing the properties of the transducer materials at high frequencies is important for designing high frequency transducers. Currently, there are very limited experimental data available in the literature on high frequency properties of piezoelectric materials due to many technical difficulties [1]. Reported in this paper are results of velocity and attenuation for doped lead zirconate titanate (PZT-5H) in the frequency range of 20-60 MHz measured by using an ultrasonic spectroscopy method. The experimental results were also used to verify the Kramers-Kronig relations[2].

Ultrasonic spectroscopy method has been widely used in the characterization of solid materials. With angular incidence, mode conversion effect was used to investigate shear wave properties of porous materials and polymeric materials [3-8]. If such method is generalized to characterize piezoelectric materials, one needs to deal with the problem of plane wave propagation through an interface between an isotropic medium and an anisotropic piezoelectric material. Since the propagation velocity of waves varies with propagation direction in an anisotropic material, the refraction becomes complicated when the ultrasonic wave is obliquely incident onto the interface. Generally speaking, the refraction coefficient can not be given in an explicit analytic form. For poled PZT ceramics the symmetry is cm , which has the same number of independent physical constants as that of 6mm symmetry, i.e., 5 independent elastic constants, 3 independent piezoelectric coefficients and 2 independent dielectric permittivity. Because of the reasonably high symmetry, the situation may be simplified in some special incident angles. The present paper is divided into two parts: First, we discuss the refraction of a plane wave at the interface of water-PZT ceramic. Based on the theoretical analysis, an ultrasonic spectroscopy technique suitable for characterization of PZT ceramic was developed and used to characterize PZT-5H samples. Second, the measured results were compared with those predicted by the Kramers-Kronig relations.

II. The reflection and refraction of a longitudinal wave at the water-piezoceramic interface

Based on the principle described by Rokhlin[8], we have derived the reflection/refraction of acoustic wave at the interface of water and a PZT ceramic plate. The poling direction of a plate PZT sample is either perpendicular or parallel to the large surface of the plate. As shown in Fig.1 the plate sample with the poling direction perpendicular to its large surface is referred as PZT_z, whereas the plate with poling direction parallel to its large surface is referred as PZT_x.

II.1 Reflection/refraction of a longitudinal wave at the interface of water and PZT_z

When a longitudinal wave is incident upon the interface of water and PZT_z, we choose the coordinate system to make the incident plane coincident with either the x-z or the y-z plane of PZT since the plane perpendicular to the z-axis is acoustically isotropic for PZT with ∞ m symmetry. If the x-z plane is wave propagation plane as shown in Fig.1 (a). the incident longitudinal wave in water can be expressed as:

$$U_i = U_{0i} \exp[j(\omega t - k_w x_1 \sin \theta_i - k_w x_3 \cos \theta_i)] \quad (i = 1, 2, 3) \quad (1)$$

or

$$U_i = U_{0i} \exp[j\omega(t - m_1^w x_1 - m_3^w x_3)] \quad (1')$$

where $k_w = \omega/v_w$, v_w is sound velocity of water, θ_i is incident angle,

$$m_1^w = \frac{n_1}{v_w} = \frac{\sin \theta_i}{v_w} \quad \text{and} \quad m_3^w = \frac{n_3}{v_w} = \frac{\cos \theta_i}{v_w}.$$

The unit vector \mathbf{n} represents the wave propagation direction.

Similarly, the refractive waves propagating in the PZT sample are expressed as:

$$u_i = u_{0i} \exp[j(\omega t - k n_1 x_1 - k n_3 x_3)] \quad (i = 1, 2, 3, 4) \quad (2)$$

where u_4 stands for electric potential wave with the electric field given by $E_i = \frac{\partial u_4}{\partial x_i}$. For

convention we rewrite Eq.(2) as

$$u_i = u_{0i} \exp[j\omega(t - m_1 x_1 - m_3 x_3)] \quad (2')$$

with $m_i = \frac{n_i}{v}$ ($i = 1$ or 3). Substituting the wave solutions into the equation of motion

$\rho \ddot{u}_i = \frac{\partial T_{ij}}{\partial x_j}$ and considering the constitutive equation $T_{ij} = c_{ijkl} \frac{\partial u_k}{\partial x_l} - e_{mij} E_m$, the amplitude

u_{0i} ($i = 1-4$) in Eq.(2) will be governed by the following equations:

$$\left[\frac{1}{\rho} (c_{11} m_1^2 + c_{44} m_3^2 - 1) u_{01} + \frac{1}{\rho} (c_{13} + c_{44}) m_1 m_3 u_{03} + \frac{1}{\rho} (e_{31} + e_{15}) m_1 m_3 u_{04} \right] = 0 \quad (3a)$$

$$\left\{ \frac{1}{\rho} \left[\frac{1}{2} (c_{11} - c_{12}) m_1^2 + c_{44} m_3^2 \right] - 1 \right\} u_{02} = 0 \quad (3b)$$

$$\frac{1}{\rho} (c_{13} + c_{44}) m_1 m_3 u_{01} + \left[\frac{1}{\rho} (c_{44} m_1^2 + c_{33} m_3^2) - 1 \right] u_{03} + \frac{1}{\rho} (e_{15} m_1^2 + e_{33} m_3^2) u_{04} = 0 \quad (3c)$$

$$(e_{15} + e_{31}) m_1 m_3 u_{01} + (e_{15} m_1^2 + e_{33} m_3^2) u_{03} - (e_{11} m_1^2 + e_{33} m_3^2) u_{04} = 0 \quad (3d)$$

where ρ is the density, c_{ij} are the elastic stiffness constants, $e_{i\lambda}$ are the piezoelectric stress constants and ϵ_{ij} are the dielectric constants for the poled PZT ceramic. Short notation for the elastic constants, \tilde{c} , and the piezoelectric coefficients, \tilde{e} , have been used, their definition could be found in Ref. [9].

From Eq.(3) it is seen that u_{02} representing the amplitude of a shear wave does not couple with u_{01} and u_{03} . Hence, this wave cannot be generated through mode conversion effect in this incidence arrangement. In other words, the particle displacement of the refractive waves in the PZT ceramic has only u_1 and u_3 components.

From Eq.(3d),

$$u_{04} = \frac{(e_{15} + e_{31}) m_1 m_3 u_{01} + (e_{15} m_1^2 + e_{33} m_3^2) u_{03}}{\epsilon_{11} m_1^2 + \epsilon_{33} m_3^2} \quad (4)$$

Substituting Eq.(4) into (3a) and (3c) gives:

$$\begin{aligned} & \left[\frac{1}{\rho} (c_{11} m_1^2 + c_{44} m_3^2 + \frac{(e_{31} + e_{15})^2 m_1^2 m_3^2}{\epsilon_{11} m_1^2 + \epsilon_{33} m_3^2}) - 1 \right] u_{01} \\ & + \frac{1}{\rho} [c_{13} + c_{44} + \frac{(e_{33} m_3^2 + e_{15} m_1^2)(e_{31} + e_{15})}{\epsilon_{11} m_1^2 + \epsilon_{33} m_3^2}] m_1 m_3 u_{03} = 0 \quad (5a) \end{aligned}$$

$$\frac{1}{\rho} [c_{13} + c_{44} + \frac{(e_{33} m_3^2 + e_{15} m_1^2)(e_{31} + e_{15})}{\epsilon_{11} m_1^2 + \epsilon_{33} m_3^2}] m_1 m_3 u_{01}$$

$$+ \left[\frac{1}{\rho} (c_{44}m_1^2 + c_{33}m_3^2 + \frac{(e_{15}m_1^2 + e_{33}m_3^2)^2}{\epsilon_{11}m_1^2 + \epsilon_{33}m_3^2}) - 1 \right] u_{03} = 0 \quad (5b)$$

The propagation directions of the refractive waves allowed in the PZT ceramic are determined by the coefficient determinate of Eq.(5), i.e.,

$$\left| \begin{array}{cc} \frac{1}{\rho} (c_{11}m_1^2 + c_{44}m_3^2 + \frac{(e_{31} + e_{15})^2 m_1^2 m_3^2}{\epsilon_{11}m_1^2 + \epsilon_{33}m_3^2}) - 1 & \frac{1}{\rho} (c_{13} + c_{44} + \frac{(e_{33}m_3^2 + e_{15}m_1^2)(e_{31} + e_{15})}{\epsilon_{11}m_1^2 + \epsilon_{33}m_3^2}) m_1 m_3 \\ \frac{1}{\rho} (c_{13} + c_{44} + \frac{(e_{33}m_3^2 + e_{15}m_1^2)(e_{31} + e_{15})}{\epsilon_{11}m_1^2 + \epsilon_{33}m_3^2}) m_1 m_3 & \frac{1}{\rho} (c_{44}m_1^2 + c_{33}m_3^2 + \frac{(e_{33}m_3^2 + e_{15}m_1^2)^2}{\epsilon_{11}m_1^2 + \epsilon_{33}m_3^2}) - 1 \end{array} \right| = 0 \quad (6)$$

It is known that the phase matching condition at the interface, or the Snell's law, demands

$m_1^{\text{incident}} = m_1^{\text{reflective}} = m_1^{\text{refractive}}$, or $m_1^w = m_1^{\text{PZT}}$. Since m_1^w is known for a given incident wave, one can determine m_3^{PZT} of refractive waves propagating in the PZT from Eq.(6).

There are two solutions of m_3^{PZT} from Eq. (6) corresponding to two refracted waves in PZT. Substituting the two roots of Eq.(6) back into Eq.(5), two eigenvectors with two components can be obtained, which provides the polarization directions of the two refracted waves. In more general cases, one of them is quasilongitudinal wave and the other is a quasishear waves. Thus, when a longitudinal wave is incident from water upon PZT ceramic, there are incident and refracted waves in the water medium: both are longitudinal waves with amplitudes by u_0 and u_r , respectively. In the PZT ceramic there are refracted quasilongitudinal and quasishear waves. Their propagation direction and polarization direction are determined by Eqs.(5) and (6) to be \mathbf{m}^L , \mathbf{l}^L and \mathbf{m}^S , \mathbf{l}^S , respectively. Their amplitudes u_L and u_S are related to that of the incident wave u_0 through the boundary conditions at the interface of $x_3 = 0$:

$$\begin{aligned} u_3(\text{water}) &= u_3(\text{PZT}) \\ T_{13} &= 0 \\ T_{33}(\text{water}) &= T_{33}(\text{PZT}) \end{aligned} \quad (7a-c)$$

The above equations may be re-written as

$$\begin{aligned} u_r \cos \theta + l_3^L u_L + l_3^S u_S &= u_0 \cos \theta \\ ru_L + su_S &= 0 \\ Z_w u_r - pu_L - qu_S &= -Z_w u_0 \end{aligned} \quad (8a-c)$$

where Z_w is acoustic impedance of water and

$$\begin{aligned}
 r &= c_{44}(m_3^L l_1^L + m_1 l_3^L) + e_{15}(A^L l_1^L + B^L l_3^L) \\
 s &= c_{44}(m_3^S l_1^S + m_1 l_3^S) + e_{15}(A^S l_1^S + B^S l_3^S) \\
 p &= c_{13}m_1 l_1^L + c_{33}m_3^L l_1^L + e_{33}m_3^L (A^L l_1^L + B^L l_3^L) \\
 q &= c_{13}m_1 l_1^S + c_{33}m_3^S l_1^S + e_{33}m_3^S (A^S l_1^S + B^S l_3^S) \\
 A^{L,S} &= \frac{(e_{15} + e_{31})m_1 m_3^{L,S}}{\varepsilon_{11}m_1^{L,S} + \varepsilon_{33}m_3^{L,S}} \quad B^{L,S} = \frac{e_{15}m_1 + e_{33}m_3^{L,S}}{\varepsilon_{11}m_1^{L,S} + \varepsilon_{33}m_3^{L,S}}
 \end{aligned} \tag{9a-d}$$

From Eq.(8) the ratios of u_r/u_0 , u_L/u_0 and u_S/u_0 , i.e., the reflection and refraction coefficients can be determined. Using this procedure one can determine the amplitude and propagation direction of the refractive waves.

In ultrasonic spectroscopy technique, however, one can use slightly different way to solve the problem. As mentioned above, m_1^w is known for a given incident wave. i.e..

$$m_1^w = \frac{n_1}{v_w} = \frac{\sin \theta_i}{v_w}$$

From the Snell's law it is given that $m_1^{PZT} = \frac{\sin \theta_i}{v_w} = \frac{\sin \theta_p}{v_p}$, where θ_p and v_p ($p = L$ or S)

are the refractive angle and velocity of longitudinal(L) or shear(S) wave. If the velocity v_p has been determined by spectroscopy method, one can simply calculate θ_p through the Snell's law. Obviously, m_3^{PZT} can be found by the relation of $m_3^{PZT} = \frac{\cos \theta_p}{v_p}$.

Using Eq.(6) the longitudinal and shear velocities can be correlated to appropriate elastic constants. In what follows we discuss three special cases to illustrate the procedure.

Case 1. Normal incidence

In this case $m_1^{water} = 0$, therefore, $m_1^{PZT} = 0$, $\theta_p = 0$ and

$$m_3^S = \frac{1}{v_S} \tag{10a}$$

or

$$m_3^L = \frac{1}{v_L} \tag{10b}$$

Substituting these results into Eq.(5) results in the following simple relations,

$$v_s = \sqrt{\frac{c_{44}}{\rho}} \quad \text{and} \quad v_L = \sqrt{\frac{c_{33}^D}{\rho}} = \sqrt{\frac{c_{33} + \frac{e_{33}^2}{\epsilon_{33}}}{\rho}} \quad (10, c,d)$$

which are the velocity of the shear wave and the stiffened longitudinal wave, respectively.

From Eq.(6), two eigenvectors are obtained:

$$I^S = [1,0,0] \quad \text{and} \quad I^L = [0,0,1] \quad (11a,b)$$

This means that one of the possible refracted waves is a pure shear wave with polarization direction along the x-axis and another is a pure longitudinal wave. Substituting these results into Eqs.(8) and (9), one can obtain the reflection and refraction ratios:

$$R = \frac{u_r}{u_0} = \frac{Z_L - Z_w}{Z_L + Z_w} \quad (12a)$$

$$T = \frac{u_L}{u_0} = \frac{2Z_L}{Z_L + Z_w} \quad (12b)$$

$$u_s = 0 \quad (12c)$$

Eq.(12c) implies that mode conversion does not exist in normal incidence, reflection coefficient R and transmission coefficient T of the longitudinal wave are the same as for an interface of water and an isotropic solid. In the expressions Eq.(12a,b), Z_L is the acoustic impedance of the longitudinal wave in PZT.

Case 2. Incidence at the critical angle of the longitudinal wave.

When a longitudinal wave is obliquely incident from water upon PZT_z, mode conversion takes place. In PZT medium there are, in general, refractive quasilongitudinal and quasishear waves. If the wave is incident at the critical angle of longitudinal wave, the refractive longitudinal wave becomes an evanescent wave. This means that m_3^L equals to zero (θ_i =critical angle) or complex (θ_i >critical angle). The vector m^S representing the propagation direction of the refractive quasishear wave can be determined by the following expressions:

$$m_1^S = \frac{\sin \theta_i}{v_w} = \frac{\sin \theta_s}{v_s} \quad (13a)$$

$$m_3^s = \frac{\cos \theta_s}{v_s} \quad (13b)$$

If the velocity v_s is determined from the ultrasonic spectroscopy method, θ_s can be calculated from Eq.(13a), therefore m^s is totally determined. Knowing m^s , the polarization direction can be determined by Eq.(5) and the transmission coefficient can be calculated from Eq. (8). The velocity of the quasimode wave is related to a combination of elastic constants of PZT by

$$v_s = \sqrt{\frac{c^*}{\rho}} \quad (14)$$

where

$$2c^* = c_{11} \sin^2 \theta_s + c_{33} \cos^2 \theta_s + c_{44} + p_1 + p_2 + \{[(c_{11} - c_{44}) \sin^2 \theta_s + (c_{44} - c_{33}) \cos^2 \theta_s + p_1 - p_2]^2 + (c_{13} + c_{44} + p_3)^2 \sin^2 2\theta_s\}^{1/2} \quad (15a)$$

and

$$p_1 = \frac{(e_{31} + e_{15})^2 \sin^2 \theta_s \cos^2 \theta_s}{\varepsilon_{11} \sin^2 \theta_s + \varepsilon_{33} \cos^2 \theta_s} \quad (15b)$$

$$p_2 = \frac{(e_{33} \cos^2 \theta_s + e_{15} \sin^2 \theta_s)^2}{\varepsilon_{11} \sin^2 \theta_s + \varepsilon_{33} \cos^2 \theta_s} \quad (15c)$$

$$p_3 = \frac{(e_{33} \cos^2 \theta_s + e_{15} \sin^2 \theta_s)(e_{31} + e_{15})}{\varepsilon_{11} \sin^2 \theta_s + \varepsilon_{33} \cos^2 \theta_s} \quad (15d)$$

are terms associated with piezoelectric coupling. θ_s is the refractive angle of the quasimode wave in PZT ceramic.

II.2 Reflection/refraction of a longitudinal wave at the interface of water and PZT_x

Assuming the plate normal direction is along x-axis and the poling direction is parallel to the z direction of the PZT plate as shown in Fig.(1b), the incident plane of the ultrasonic wave has three independent orientations: 1)x-y plane; 2)y-z plane; and 3) incident in a plane that rotates around y-axis at an arbitrary angle. Since the last case makes the problem much complicated, it will not be discussed here. The second option is actually

equivalent to the Case 2 of Sec.II.1, therefore, we only need to discuss the first option which we call it Case 3 as described below.

The plane perpendicular to the z-axis of PZT is an acoustically isotropic plane as mentioned above. When an incident wave is in the x-y plane, as shown in Fig.(1b), the reflection/refraction of a longitudinal wave at the interface of water and PZT ceramic is the same as at the interface of water and an isotropic solid. In this case the particle displacement \mathbf{u} of the refractive waves has only components in the x and y directions. When a wave is normally incident, the only refractive wave is a pure longitudinal wave with the velocity given by

$$v_L = \sqrt{\frac{c_{11}}{\rho}} \quad (17a)$$

When a wave is obliquely incident, one of the two refractive waves is a pure longitudinal wave with the same velocity as Eq.(17a), another refractive wave is a pure shear wave with the velocity of

$$v_S = \sqrt{\frac{\frac{1}{2}(c_{11} - c_{12})}{\rho}} = \sqrt{\frac{c_{66}}{\rho}} \quad (17b)$$

This shear wave polarizes in the x-y plane.

Other cases of reflection/refraction of a plane wave at the interface of PZT ceramic-water can be discussed by using the same procedure. However, pure modes do not exist for general cases.

In summary, by using angular incidence of a longitudinal wave from water to two PZT plates we can determine the elastic constants and their dispersion from dispersion of velocity and attenuation in the following acoustic modes:

A). For a PZT_z sample:

1. Longitudinal wave propagating along the poling direction with the wave normal incident upon the plate. From the velocity dispersion of this wave, the frequency dependence of elastic constant c_{33}^D can be determined.
2. Quasishear wave propagating in the x-z plane with the wave obliquely incident at the critical angle of the longitudinal wave. From its velocity dispersion one can determine an elastic constant combination c^* and its frequency dependence.

B). For a PZT_x sample:

1. Longitudinal wave propagating perpendicular to the poling direction. From its velocity dispersion one can determine the elastic constant c_{11} and its frequency dependence.
2. Shear wave with directions of propagation and polarization normal to the poling direction when the wave is incident at the critical angle of the longitudinal wave. From the velocity dispersion of this wave one can determine the elastic constant c_{66} and its frequency dependence.

III. Principles of measurements

The basic principle of the ultrasonic spectroscopy method used to determine the velocity and attenuation of materials is shown in Figure 2. A pair of aligned transmitting and receiving transducers are immersed in water with an adjustable separation between them. When the transmitting transducer is driven by an electric pulse signal, an acoustic broadband signal is produced at $x=0$, noted as $u(t)$. Its Fourier transform is $\tilde{u}(f)$. For a linear and causal acoustic system shown in Fig. (2a), the transfer function of the medium for the wave to propagate can be expressed as:

$$H(f) = \exp[-\alpha_w(f)L] \exp[-j(2\pi f L / v_w(f))] \quad (18)$$

where L is the distance between the transmitting and receiving transducers, v_w and α_w are the wave velocity and attenuation of water, respectively. When the medium is considered to be dispersive and dissipative, both α_w and v_w are frequency dependent. The spectrum of the output signal from the receiving transducer is

$$\tilde{u}_w(f) = \tilde{u}(f) \exp[-\alpha_w(f)L] \exp[-j(2\pi f L / v_w(f))] \tilde{u}'(f) \quad (19)$$

where $\tilde{u}'(f)$ is the transfer function of the receiving transducer. Thus, the amplitude and phase spectra of the output signal can be expressed as

$$A_w(f) = |\tilde{u}(f)| \exp[-\alpha_w(f)L] |\tilde{u}'(f)| \quad (20a)$$

$$\Phi_w(f) = 2\pi f L / v_w(f) + \phi_u + \phi_{u'} \quad (20b)$$

where ϕ_u and $\phi_{u'}$ are the phase angles of the two transducers, respectively. They will not enter the calculations below since the spectroscopic method depends only on the relative phase shift.

When the sample to be measured is inserted between the transmitting and receiving transducers, the transfer function of the system as shown in Fig.(2b) becomes

$$\begin{aligned}
 H_s(f) = & T\tilde{u}(f) \exp\left\{-\alpha_w(f)\left[L - \frac{d}{\cos\theta_i} - d(\tan\theta - \tan\theta_i)\sin\theta_i\right]\right\} \exp\left[-\alpha(f)\frac{d}{\cos\theta}\right] \\
 & \cdot \exp\left\{-j[2\pi f\left(L - \frac{d}{\cos\theta_i} - d(\tan\theta - \tan\theta_i)\sin\theta_i\right)/v_w(f) + 2\pi f\frac{d}{\cos\theta}/v(f)]\right\} \tilde{u}'(f)
 \end{aligned} \tag{21}$$

where d is the thickness of the sample, α and v are attenuation coefficient and phase velocity in the sample, respectively, θ_i and θ are the incident and the refractive angles of the wave at the interface, respectively, T is the total transmission coefficient which is equal to the product of the transmission coefficients of the wave from water to sample and from sample to water.

Thus, the amplitude and phase spectra of the output signal for the system shown in Fig.(2b) can be written as:

$$A(f) = T|\tilde{u}(f)| \exp\left\{-\alpha_w(f)\left[L - \frac{d}{\cos\theta_i} - d(\tan\theta - \tan\theta_i)\sin\theta_i\right]\right\} \exp\left[-\alpha(f)\frac{d}{\cos\theta}\right] |\tilde{u}'(f)| \tag{22a}$$

and

$$\varphi = 2\pi f\left[L - \frac{d}{\cos\theta_i} - d(\tan\theta - \tan\theta_i)\sin\theta_i\right]/v_w(f) + \frac{2\pi f d}{v(f)\cos\theta} + \phi_u + \phi_w \tag{22b}$$

From Eqs.(20) and (22) the phase velocity and attenuation coefficients in the sample are given by

$$v = \frac{v_w}{\sqrt{\sin^2\theta_i + \left[\frac{(\varphi - \varphi_w)v_w}{2\pi f d} + \cos\theta_i\right]^2}} \tag{23}$$

$$\alpha = \alpha_w \cos(\theta - \theta_i) + \left(\ln \frac{T A_w}{A}\right) \cos\theta/d \tag{24}$$

If the values of A_w , A , φ_w , and φ can be measured, the attenuation and phase velocity dispersion of the sample can be determined.

When the wave is normally incident to the sample, $\theta_i = \theta = 0$, the above equations give the velocity and attenuation of the longitudinal wave in the case discussed in Sec.II for the

longitudinal wave propagating in either x-z plane or x-y plane as shown in Fig.(1a) and Fig.(1b), respectively.

$$v_L = \frac{v_w}{1 + \frac{(\varphi - \varphi_w)v_w}{2\pi fd}} \quad (25)$$

and

$$\alpha_L = \alpha_w + \ln\left(\frac{T_L A_w}{A}\right)/d \quad (26)$$

where

$$T_L = \frac{4\rho_0 v_w \rho v_L}{(\rho_0 v_w + \rho v_L)^2} = \frac{4z_w z_L}{(z_L + z_w)^2} \quad (27)$$

ρ_0 and ρ are mass density of water and sample, respectively, and v_L is longitudinal wave velocity in the sample.

If the wave is obliquely incident at the critical angle of the longitudinal wave, shear wave will be generated through mode conversion effect. The velocity and attenuation of the shear wave can be calculated by the following expressions:

$$v_s = \frac{v_w}{\sqrt{\sin^2 \theta_i + \left[\frac{(\varphi - \varphi_w)v_w}{2\pi fd} + \cos \theta_i\right]^2}} \quad (28)$$

$$\alpha_s = \alpha_w \cos(\theta_s - \theta_i) + \left(\ln \frac{T_s A_w}{A}\right) \cos \theta_s / d \quad (29)$$

where T_s and θ_s are transmission coefficient and refractive angle of the shear wave. The transmission coefficients for fluid- isotropic solid interface are simply given by

$$T_1 = -\left(\frac{\rho_0}{\rho}\right) \frac{2z_{sn} \sin(2\theta_s)}{z_{Ln} \cos^2(2\theta_s) + z_{sn} \sin^2(2\theta_s) + z_{wn}} \quad (30a)$$

$$T_2 = \frac{\tan \theta_i}{2 \sin^2 \theta_s} \left(1 - \frac{z_{Ln} \cos^2(2\theta_s) - z_{sn} \sin^2(2\theta_s) + z_{wn}}{z_{Ln} \cos^2(2\theta_s) + z_{sn} \sin^2(2\theta_s) + z_{wn}}\right) \quad (30b)$$

$$T_s = T_1 T_2 \quad (30c)$$

where T_{12} and T_{21} stand for the transmission coefficients of a wave from water to PZT and

from PZT to water, respectively; $z_{wn} = \frac{z_w}{\cos \theta_i}$, $z_{Ln} = \frac{z_L}{\cos \theta_L}$, $z_{sn} = \frac{z_s}{\cos \theta_s}$, and v_s is the

shear wave velocity in the sample. The refractive angles θ_L and θ_S are calculated from Snell's law,

$$\frac{\sin \theta_i}{v_w} = \frac{\sin \theta_L}{v_L} = \frac{\sin \theta_S}{v_S} \quad (31)$$

where the incident angle θ_i is controlled by a computerized rotating table in our experiments. For the quasimode wave propagating in the x-z plane of a PZT ceramic, the transmission coefficient can be calculated from Eq.(8).

IV. Experiment Results for PZT-5H and Discussions

The experimental setup is shown in Fig.3. A pair of transducers with a center frequency of 50MHz and bandwidth of 80% were used. Without sample, the spectra of the output signal from the receiving transducer are shown in Fig.4. Since the ultrasonic attenuation of water is about 6 dB/cm at 50MHz, the high frequency components of the Fourier spectrum are decayed when the distance between the transmitter and receiver increases, as indicated in Fig.4. The interval between transmitter and receiver should be selected in such a way that the high frequency components are preserved as much as possible, and at the same time leaving enough room for the sample to be rotated. In our experiments, the distance L is set at about 3 cm.

The output waveform was sampled by a digital oscilloscope (Tektronix TDS 460A) at a sampling rate of 10Gs/sec. The data were transferred into computer via a GPIB interface. The total recording length for a waveform was 2500 points. The amplitude A_w and the phase spectra ϕ_w were obtained through FFT of the output signal from the configuration in Fig.(2a). When the sample was put in place, the trigger delay time was adjusted so that the shifting of the waveform caused by putting in the sample can be compensated. Using the same procedure, the amplitude A and the phase ϕ of the output signal from the configuration Fig.(2b) were obtained. Note: the velocity calculation must take into account the trigger time delay, τ ,

$$v_L = \frac{v_w}{1 + \frac{(\phi - \phi_w + 2\pi f\tau)v_w}{2\pi f d}} \quad (32a)$$

$$v_s = \frac{v_w}{\sqrt{\sin^2 \theta_i + \left[\frac{(\varphi - \varphi_w + 2\pi f \tau) v_w}{2\pi f d} + \cos \theta_i \right]^2}} \quad (32b)$$

The attenuation of the longitudinal and shear waves can be calculated from Eqs.(24) and (26), respectively. Here the attenuation of water was given by $0.00271f^2$ (dB/mm), (f in MHz). The measured velocity and attenuation for piezoceramic PZT-5H are given in Fig.5-8. It was observed that velocity dispersion exists for both the longitudinal and shear waves in the frequency range of the measurement and it is nearly linear, but the attenuation exhibits nonlinear frequency dependence. The attenuation of the shear wave is an order of magnitude higher than that of longitudinal wave.

Usually, the wavenumber of a decay wave is considered to be a complex number. Therefore, if the frequency is taken as real, the velocity becomes complex and is associated with the complex elastic modulus in the following fashion,

$$\tilde{v} = \sqrt{\frac{\tilde{C}}{\rho}} = \sqrt{\frac{C + jC'}{\rho}} \quad (33)$$

In general, it is true that $|C'|/|C| \ll 1$, we may write the above equation as

$$\tilde{v} \approx \sqrt{\frac{C}{\rho}} \left(1 + j \frac{C'}{2C} \right) \quad (34)$$

The complex wavenumber can be expressed as

$$\tilde{k} = k - j\alpha \quad (35)$$

where $k = \omega/v$ and α is the attenuation coefficient. Thus, the real and imaginary parts of the elastic modulus can be derived from the phase velocity and attenuation measurements:

$$C = \rho v^2 \quad (36a)$$

$$\tan \delta = \frac{C'}{C} = \frac{2\alpha v}{\omega} \quad (36b)$$

If a medium in which an acoustic wave propagates can be considered as linear and causal system, its attenuation, which is associated with the imaginary part of the elastic modulus, and velocity dispersion, which is associated with the real part of elastic modulus, are related by the Kramers-Kronig relations. The approximation forms of the nearly local relationships can be expressed as [9,10]:

$$v(\omega) = v(\omega_0) + \frac{2v^2(\omega_0)}{\pi} \int_{\omega_0}^{\omega} \frac{\alpha(\omega)}{\omega^2} d\omega \quad (37a)$$

$$\alpha(\omega) = \frac{\pi\omega^2}{2v^2(\omega_0)} \frac{dv(\omega)}{d\omega} \quad (37b)$$

where ω_0 is the starting frequency at which $v(\omega_0)$ and $\alpha(\omega_0)$ are known. In our experiment, $\omega_0=2\pi*20\text{MHz}$.

The ultrasonic spectroscopy technique is inherently based on the assumption of linearity. Thus, the velocity dispersion and attenuation obtained from the technique are expected to satisfy the above Kramers-Kronig relations. To verify the validity of these relations, the measured attenuation for the PZT-5H samples was fitted as a polynomial of frequency and the phase velocity dispersion was derived by the first Kramers-Kronig relation Eq.(37a), then these calculated results were compared to measured results. As shown in Figs. 7 and 8 that the agreement is quite acceptable. The maximum deviation is less than .6% and the trend is correct. We have also performed the reverse checking, i.e., using the measured velocity dispersion to calculate the dispersion of the attenuation based on the local approximation Eq. (37b). We found that this relation is extremely sensitive to the curvature of the velocity dispersion. Higher order polynomial fitting of the velocity curve gives unreasonable results. Because the velocity dispersion is fairly small, we decided to use linear approximation to these velocity data, which created error less than the experimental uncertainty for the velocity fitting but gave good agreement to the measured attenuation dispersion. The results are shown in Figs.8 and 9 for the two different cut PZT samples. Owing to this sensitivity, one should be really careful when using the second Kramers-Kronig relation Eq.(37b). One may have problems of using this relation if the velocity dispersion has a downward curvature, such as the shear velocity measured in this work, since it will lead to a decrease of the attenuation at higher frequencies. The measured attenuation seems always increase with frequency. Our experience is that a linear fitting of the velocity dispersion could provide much better prediction of the attenuation dispersion using the Kramers-Kronig relations. This linear fitting of course must be piece-wised since the relationship is not linear in general for all frequency ranges.

V. Conclusion

The dispersions of velocity and attenuation for piezoceramic PZT-5H were investigated by using ultrasonic spectroscopy at the frequency range of 20-60 MHz. In the investigated frequency range, velocity dispersion of 1-3m/s per MHz was observed. The attenuation depends nonlinearly on frequency and the shear wave exhibited an order of magnitude larger attenuation than the longitudinal wave.

We showed that the Kramers-Kronig relations between velocity dispersion and attenuation dispersion are satisfied for the longitudinal waves. However, for the shear waves, the agreement between experiments and theory was not satisfactory, indicating the nonlinear origin of the shear wave attenuation. Based on these results we conclude that the Kramers-Kronig relation may be safely applied to longitudinal waves, which provides us with a convenient way to measure the velocity dispersion. Such measurement is difficult to be accurate using other available techniques since the dispersion is quite small. By using the Kramers-Kronig relations, one can derive the velocity dispersion from the velocity measurement at one frequency plus the attenuation spectrum.

Acknowledgement

This research was sponsored by the NIH under Grant number P41-RR11795-01A1 and the ONR under Grant number N00014-98-1-0527.

References:

*Present address: Institute of Acoustics and State Key Laboratory of Modern Acoustics,
Nanjing University, Nanjing 210093, P.R.China

1. A.R.Selfridge, IEEE Tans. Son. Ult., **SU-32**, 3, 381 (1985).
2. M. O'Donnell, E.T.Jaynes and J.G.Miller, J.Account. Soc., Am., **63**, 1935 (1978).
3. W. Sachse and Y. H. Pao, J. Appl. Phys., **49**, 4320 (1978).
4. R. A. Kline, J. Acoust. Soc. Am., **76**, 499 (1984).
5. S. Baudouin, B. Hosten, Ultrasonics, **34**, 379 (1996).
6. T. J. Plona, R. D'Angelo and D. L. Johnson, Proc. IEEE 1990 Ultrasonics Symposium.
1233 (1990).
7. J. Wu, J. Acoust. Soc. Am., **99**, 2871 (1996).
8. S. I. Rokhlin, T. K. Balland and L. Adler, J. Acoust. Soc. Am., **79**, 906 (1986).
9. J. F. Nye, in *Physical Properties of Crystals*, Clarendon Press, Oxford (1985).
10. M. O'Donnell, E. T. Jaynes and J. G. Miller, J. Acoust. Soc. Am., **69**, 690 (1981).
11. D. Zellouf, Y. Jayet, N. Saint-Pierre, J. Tatibouet and J. C. Baboux, J. Appl. Phys., **80**,
2728(1996).

Figure Captions:

Figure 1. (a) Incidence of a wave in the x-z plane of a PZT sample.

(b) Incidence of a wave in the x-y plane of a PZT sample.

Figure 2. Principle of ultrasonic spectroscopy technique. (a) without sample. (b) with sample placed in a rotated position.

Figure 3. Experiment setup.

Figure 4. The variation of amplitude spectrum with propagation distance in water.

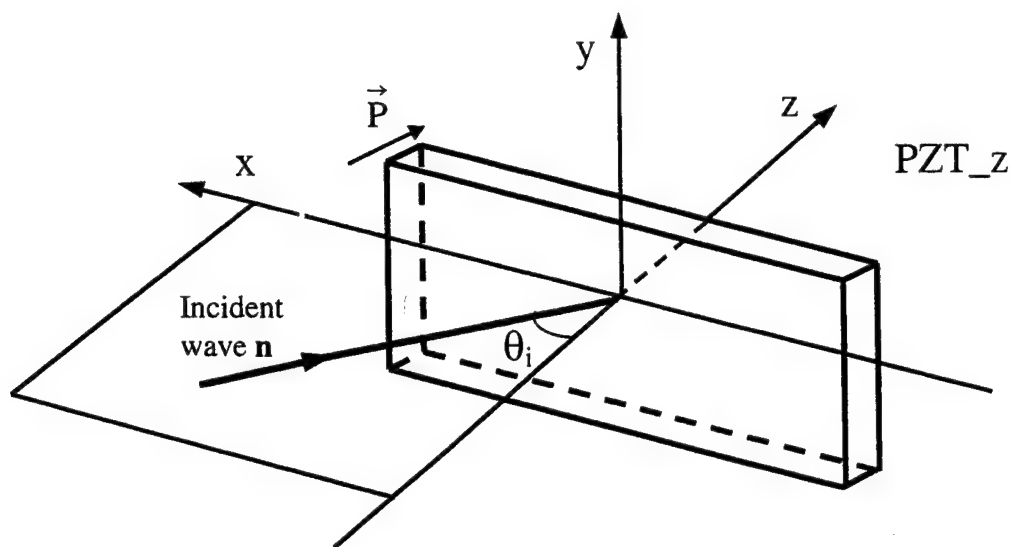
Figure 5. Dispersion relationship of the velocity and attenuation for water.

✓ Figure 6. The phase velocity dispersion measured by experiment and derived by Kramers-Kronig relationship for a wave propagating in the x-z plane of a PZT sample and the corresponding elastic constants.

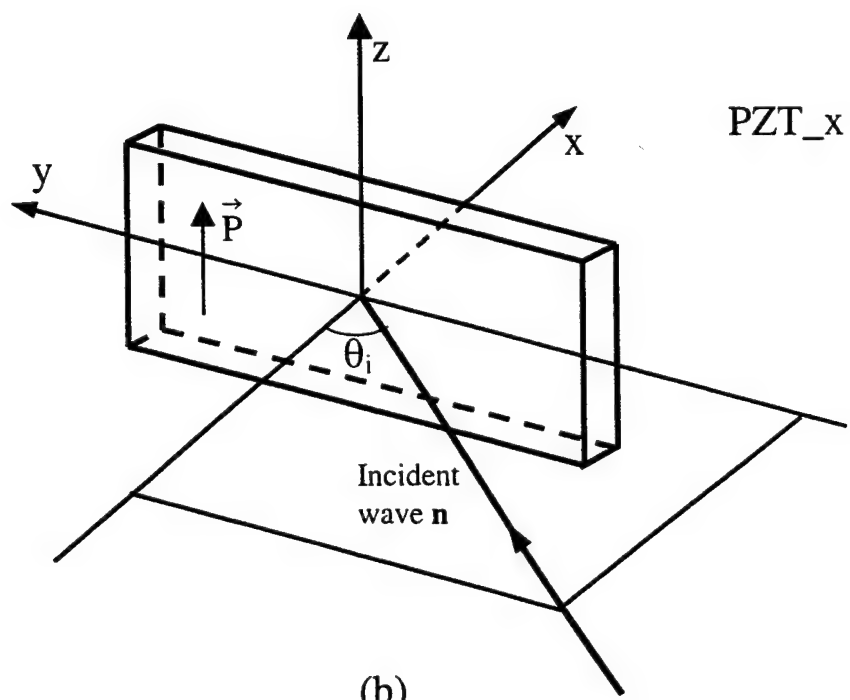
Figure 7. The phase velocity dispersion measured by experiment and derived by Kramers-Kronig relationship for wave propagating in the x-y plane of a PZT sample and the corresponding elastic constants. The longitudinal and shear velocities were fitted to linear curves: $v_L = 3744.4 + 1.00e-6f$ (Hz) and $v_S = 1762.5 + 5.47e-7f$ (Hz).

Figure 8. The attenuation measured by experiment and derived by Kramers-Kronig relationship for a wave propagating in the x-z plane of a PZT sample. The longitudinal and shear velocities were fitted to linear curves: $v_L = 4156.8 + 1.44e-6f$ (Hz) and $v_S = 1597 + 8.67e-7f$ (Hz).

Figure 9. The attenuation measured by experiment and derived by Kramers-Kronig relationship for a wave propagating in the x-y plane of a PZT sample.

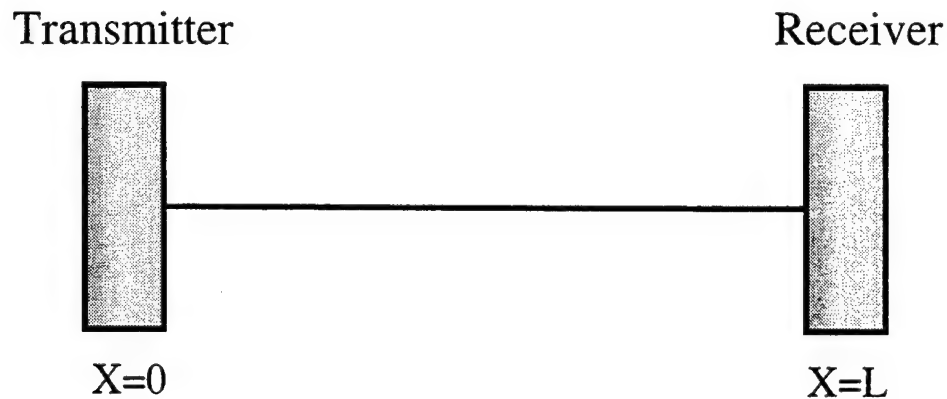


(a)

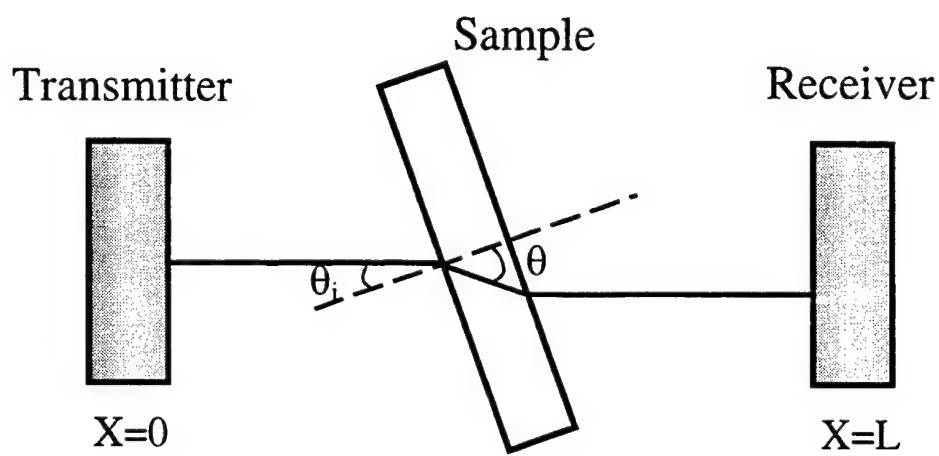


(b)

Fig. 1



(a)



(b)

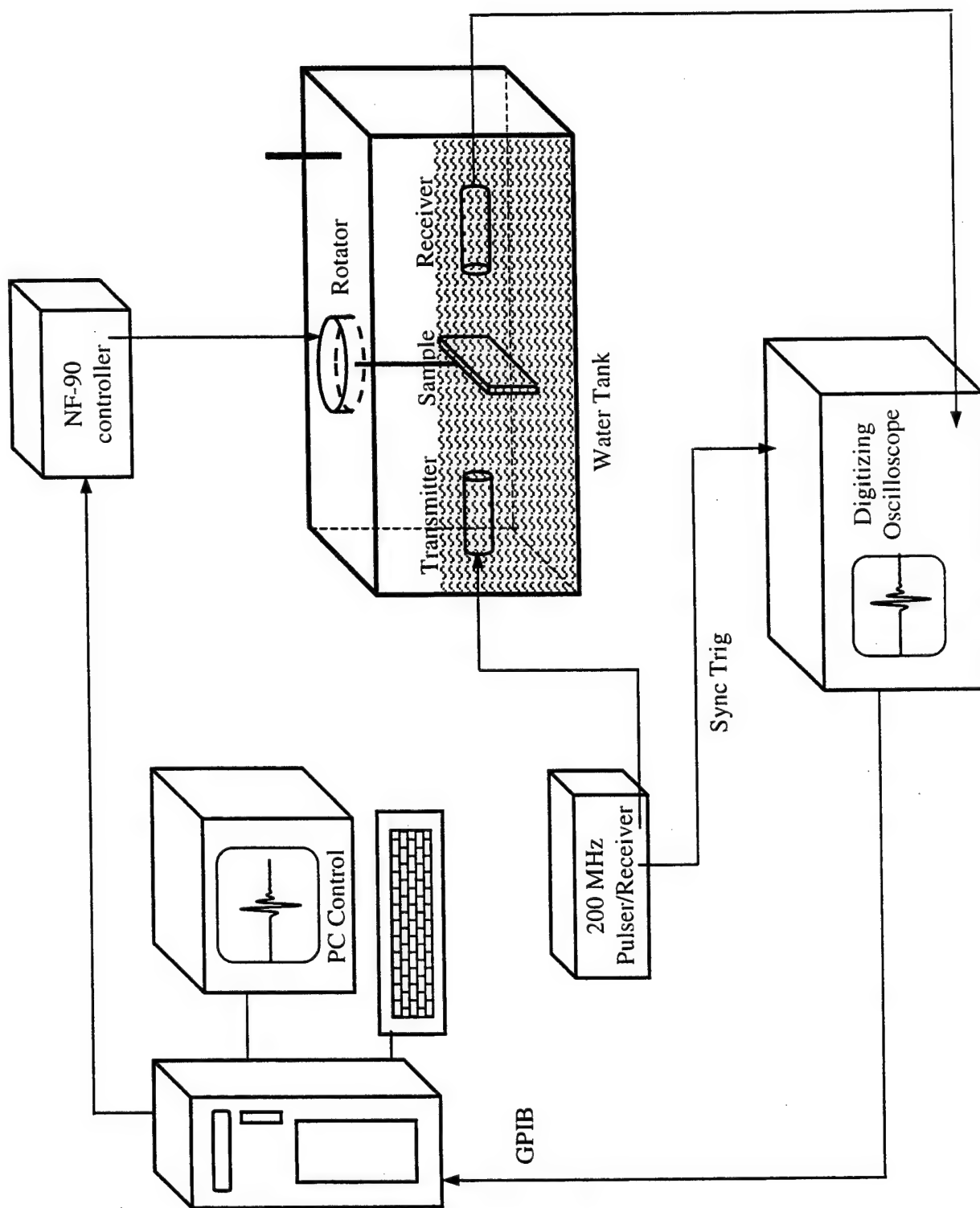


Fig. 3

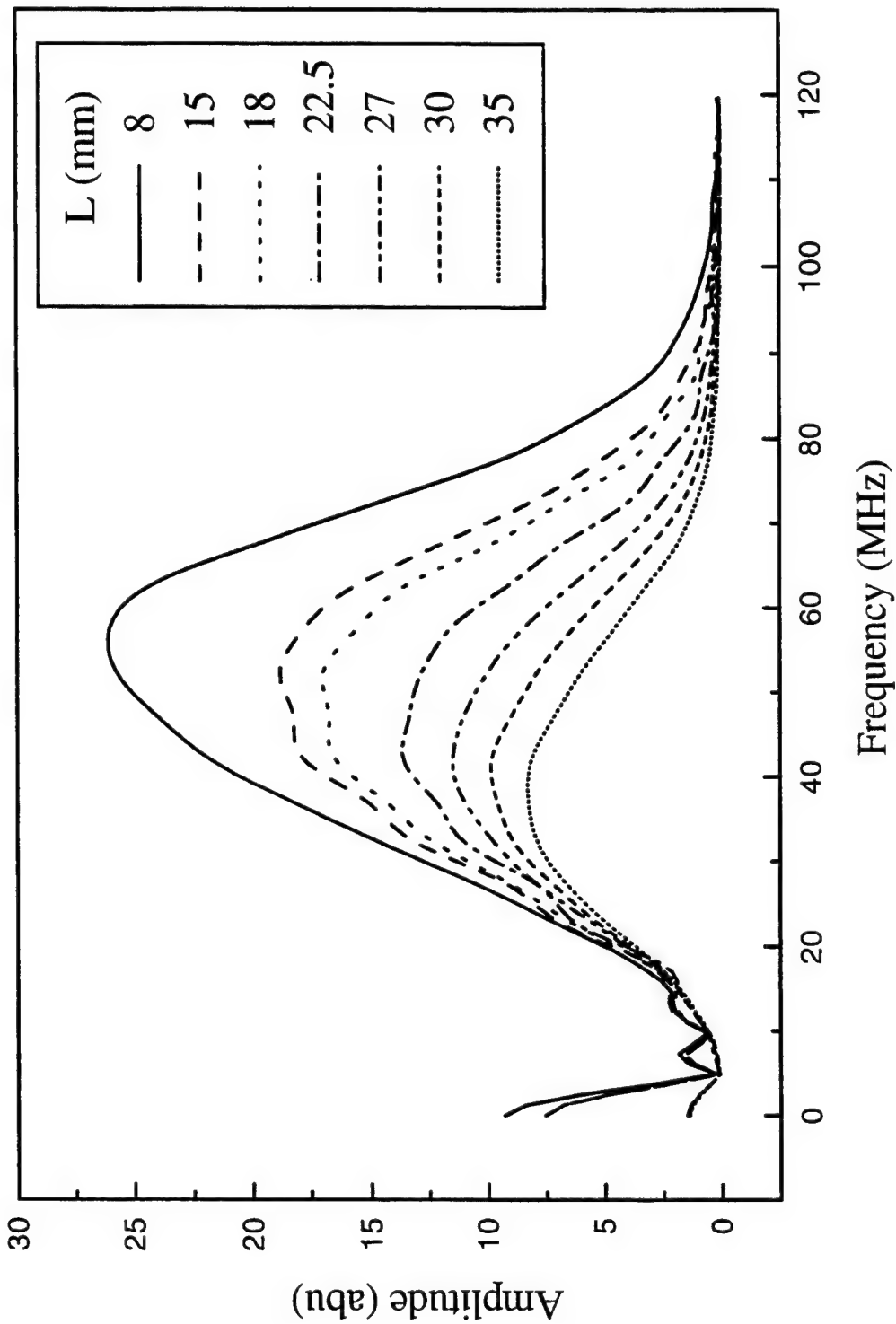


Fig. 4

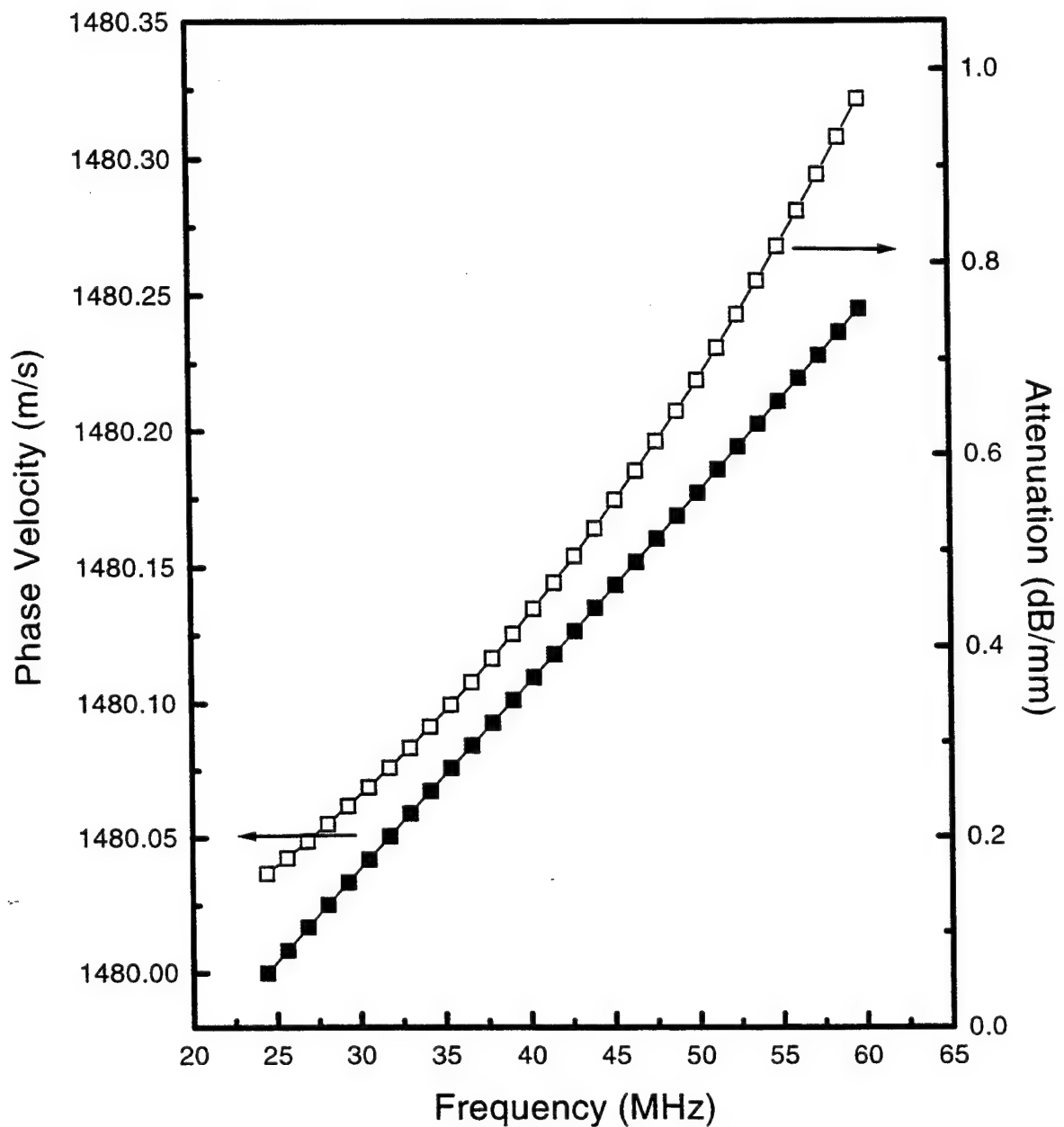


Fig. 5

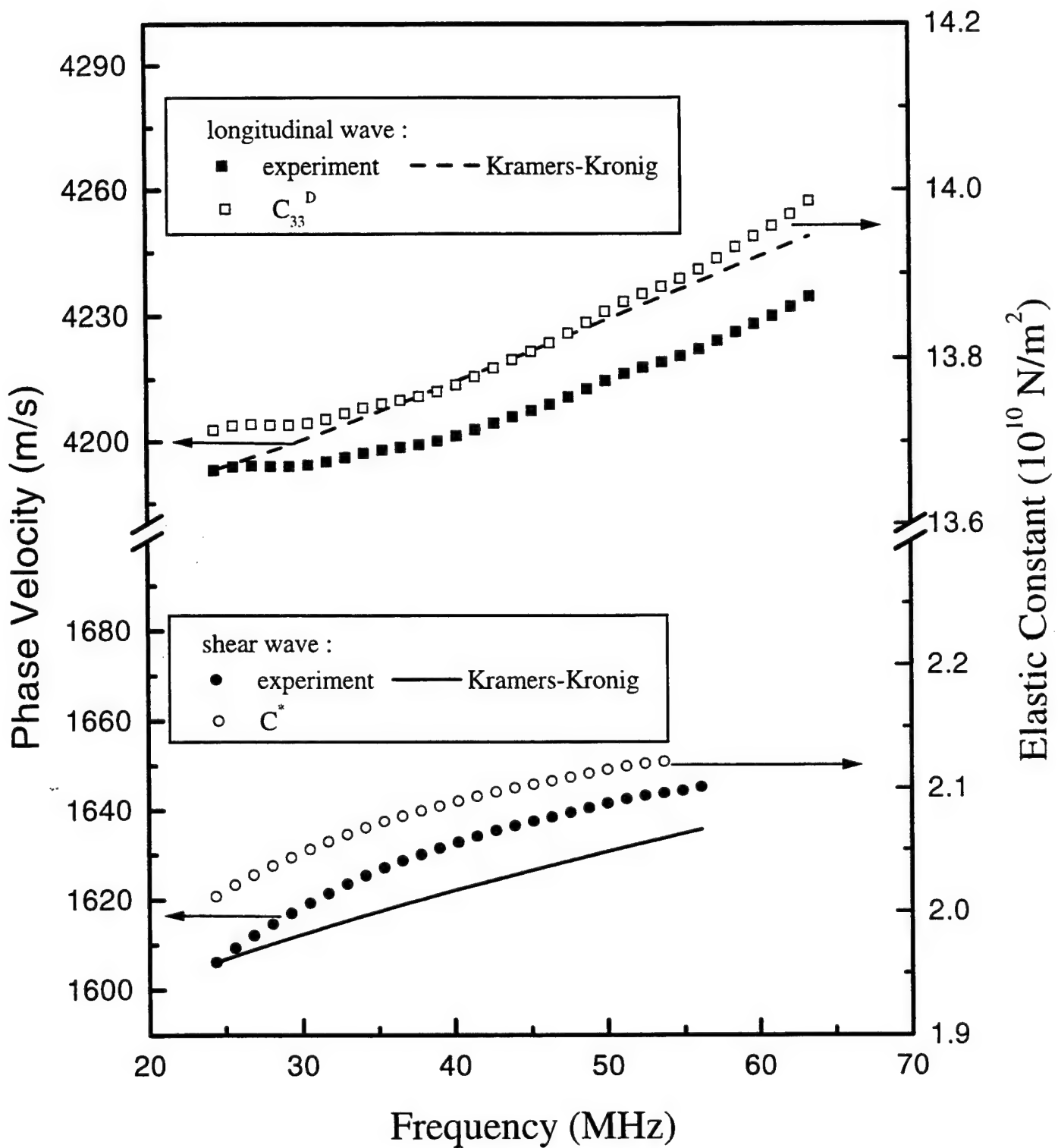


Fig. 6

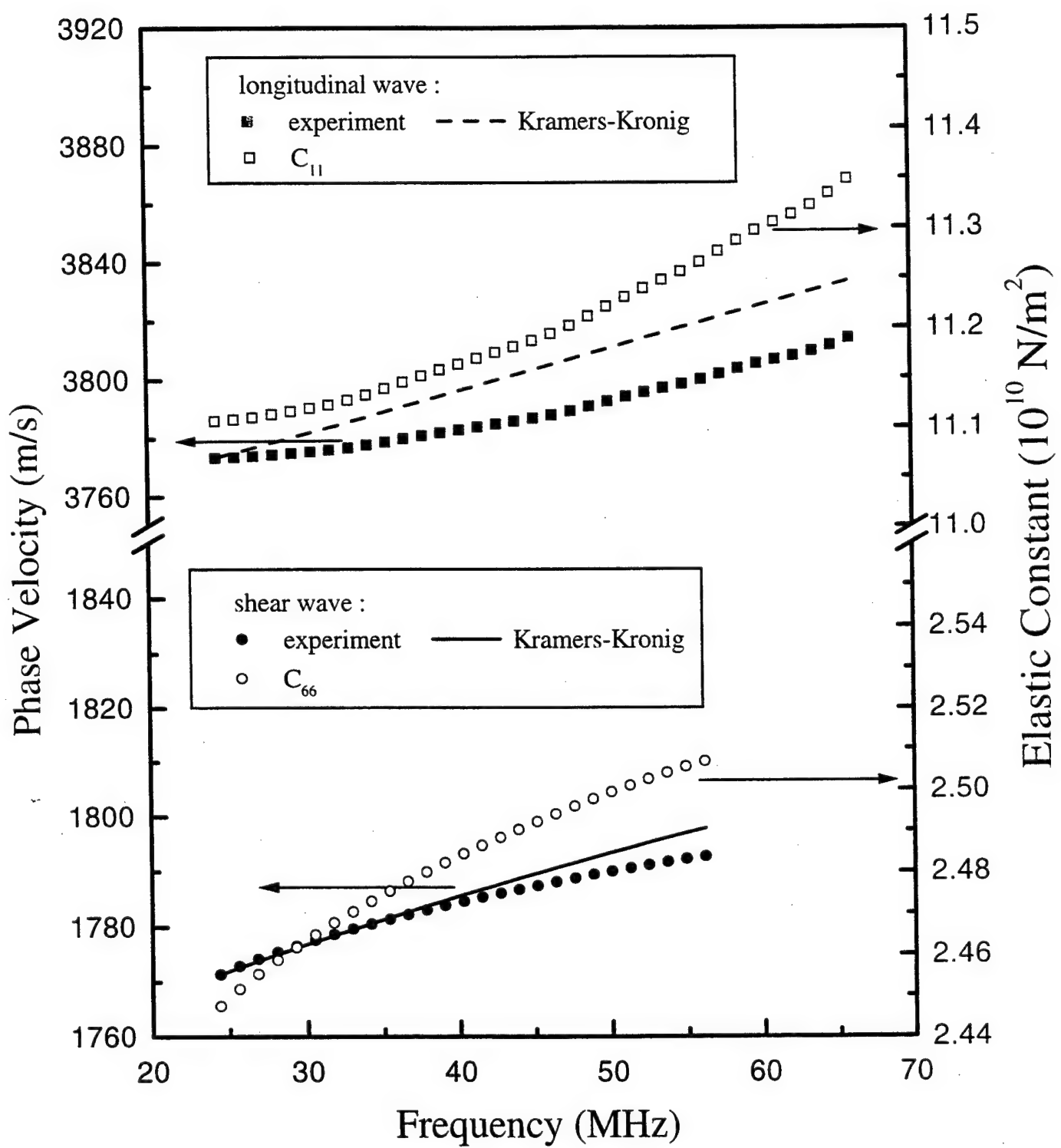


Fig. 7

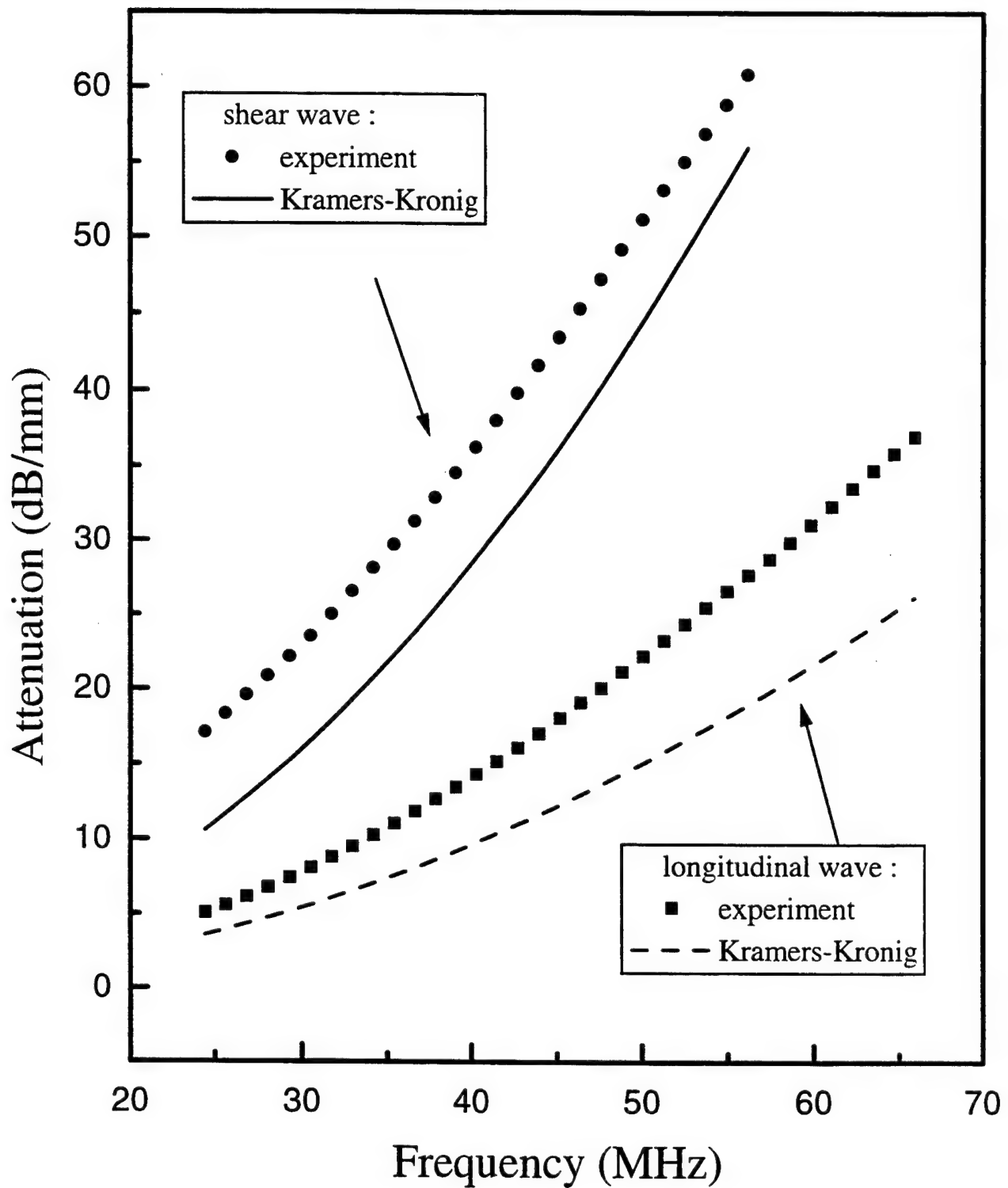


Fig. 8

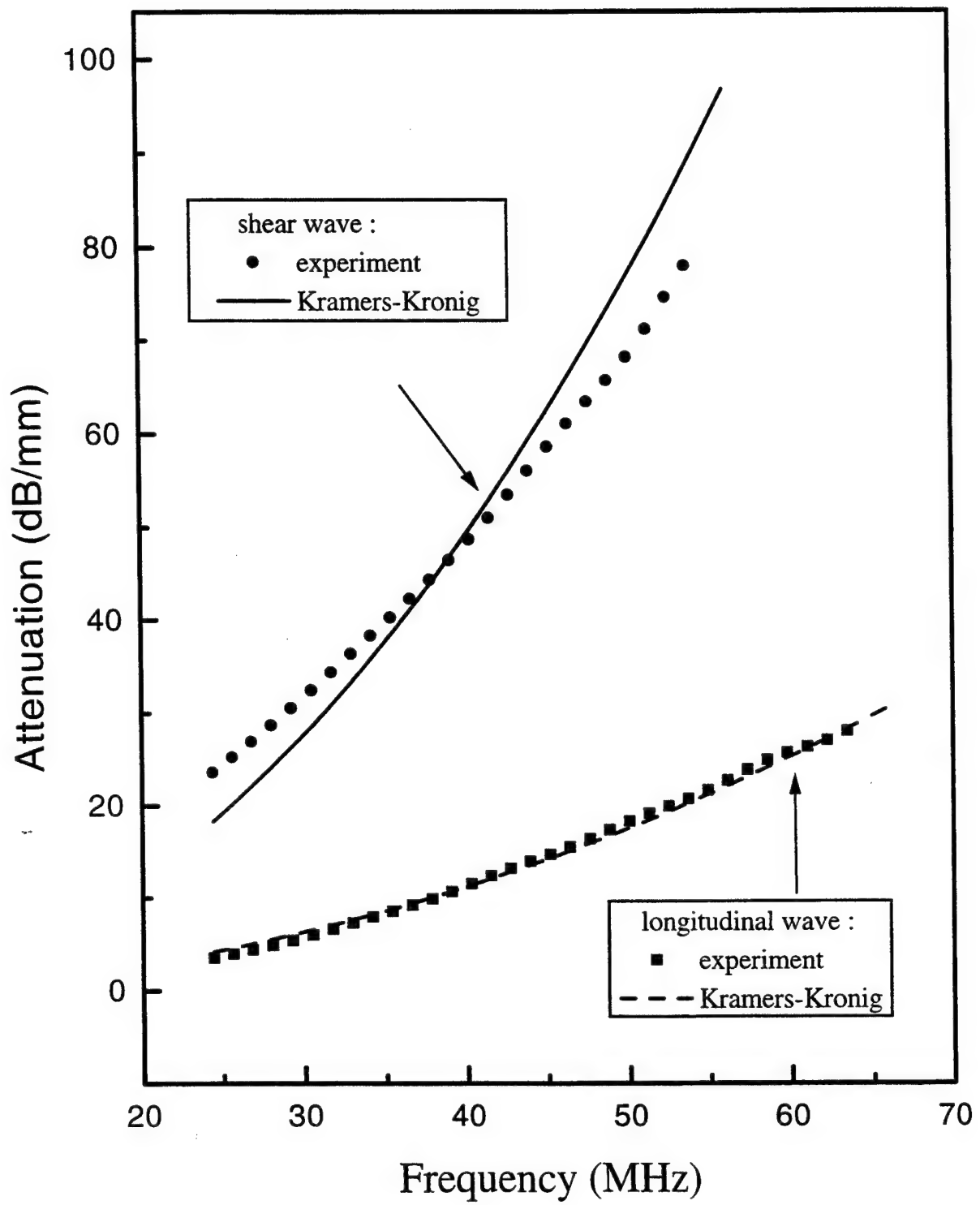


Fig. 9

APPENDIX 59

Characterization of piezoelectric materials using ultrasonic and resonant techniques

Shining Zhu, Bei Jiang and Wenwu Cao

Materials Research Laboratory

The Pennsylvania State University, University Park, PA 16802

ABSTRACT

Resonance technique for determining the physical properties of piezoelectric material can be difficult to implement for some low symmetry systems. Inconstancy may be introduced because several samples are needed and the degree of poling depends on sample geometry. The ultrasonic method on the other hand, allows the determination of a complete set of elastic, piezoelectric, dielectric constants for materials of certain symmetries. However, some of these independent constants can not be directly measured from the phase velocities of pure modes, they need to be derived by solving a complicated coupled Christoffel equation, some relatively large errors may be introduced into these derivations. We found that if an additional length-longitudinal vibrator is used to assist the measurements, the computation would be greatly simplified and the final results became more accurate. As an example, the elastic, piezoelectric, dielectric constants and electromechanical coupling factors have been determined for a PZT-5H piezoelectric ceramic by using the combined method. This method can also be extended to piezoelectric crystals with symmetry point group of 4mm and 3mm.

Keyword: Ultrasonic measurement, resonance, piezoelectric ceramic, PZT-5H, Christoffel equation, elastic constant, piezoelectric constant, dielectric constant, electromechanical coupling factor.

1. INTRODUCTION

Piezoelectric crystals and ceramics have numerous applications including ultrasonic transducers, microphones, delay lines, filters etc.¹⁻³ The qualities of these piezoelectric materials are described in terms of some basic parameters such as piezoelectric, dielectric, elastic constants and electromechanical coupling factors. A number of methods, such as static and quasi-static, resonance and pulse-echo ultrasonic techniques,^{4,5} have been used to measure these constants. In the case of piezoelectric ceramics, the symmetry is ∞ mm after poling, the independent property tensors are the same as those of point group 6mm. The resonance methods for the measurement of ceramic sample are described in IRE and IEEE standards.^{6,7} In the resonance method, some specific resonance modes may be excited by applying a variable frequency a.c. field to piezoelectric samples of a specific shape, aspect ratio and specific polarization orientation. The resonance frequency f_r and anti-resonance frequency f_a corresponding to every sample can be recorded from the frequency spectrum. All physical parameters except dielectric constants, can be calculated from these resonance and anti-resonance frequencies according to the dynamic equations for these piezoelectric vibrators.

The resonance method can also be used to measure piezoelectric single crystals. However, if the symmetry of the crystal is lower than the poled ceramic, the measurement process will become complicated. We must prepare more samples because more independent physical constants need to be measured. Moreover, the resonance method requires the measured sample to have large aspect ratio to avoid the interference effects of different resonance modes. Because only small size crystals are available for some new crystals, it is difficult to meet the large aspect ratio requirement, therefore, the resonance method is not always preferred. For some cases, when the resonance method is no longer applicable, certain alternative or combined method need to be considered to make the measurements more reliable. The measurement results obtained from the alternative or combined method, under normal condition, should be self consistent and comparable to those obtained from resonance method if one could perform such measurements.

The ultrasonic pulse-echo method is frequently used to determine the elastic constants of solid materials of different symmetries.^{5,7-9} By sending shear and longitudinal waves into several plates of specified orientations, all elastic stiffness

constants of the material can be measured. It is often more accurate than other methods, such as the resonance method, there are no mode interference effects, because the method is performed under non-resonance condition. However, the method was not used very often to measure the piezoelectric and dielectric constants. The main reason is that the solution of the Christoffel equation for materials with low symmetry is usually coupled, large errors may be introduced while extracting these constants from mixed modes. In this paper, we analyze this in detail and show that if additional measurements of the electromechanical coupling factor k_{33} and the elastic compliance s_{33}^E from a length longitudinal bar are included, the computations will be greatly simplified and the final results become more accurate. As an example, the elastic, piezoelectric and dielectric constants have been determined for a PZT-5H piezoelectric ceramic (Morgan Matroc. Inc.). These constants were extracted from a combination of six measured ultrasonic phase-velocities, the measured resonant and anti-resonant frequencies of a single length longitudinal bar and the measured low-frequency capacitance. The results are compared with those obtained by using the IEEE resonance method.

2. GENERAL PRINCIPLE OF ULTRASONIC MEASUREMENT

Theoretically, a complete set constants for any materials with the point group symmetries $6mm$, $4mm$ and $3mm$ can be determined from ultrasonic phase velocity measurements and low frequency capacitance measurement alone. The propagation velocities of ultrasonic plane waves measured for various propagation and polarization direction produce a set of effective elastic stiffness constants through the product of the density of material and square of the velocity. These effective elastic stiffness constants are related to the fundamental elastic, piezoelectric and dielectric constants by the general equations of motion for elastic plane wave propagation in a piezoelectric solid.

The equation of motion for particle displacements u_k associated with plane traveling waves may be written as¹⁰

$$(\Gamma_{ik} - \delta_{ik} \rho V^2) u_k = 0, \quad (1)$$

where

$$\Gamma_{ik} = \bar{c}_{ijkl} n_j n_l \quad (2)$$

is the Christoffel stiffness tensor for an arbitrary propagation direction n , and

$$\bar{c}_{ijkl} = c_{ijkl}^E + \frac{e_{pij} e_{qkl} n_p n_q}{\epsilon_{rs}^S n_r n_s} \quad (3)$$

is the effective elastic stiffness tensor of a piezoelectric crystal. The symbol ρ and V denote density of the material and phase velocity of the elastic plane wave, while c_{ijkl}^E , e_{pij} , ϵ_{rs}^S represent the components of the constant field elastic stiffness tensor, piezoelectric stress tensor, and dielectric tensor under constant strain, respectively. For nontrivial solutions, the determinant of the coefficients of u_k must vanish, or

$$|\Gamma_{ik} - \delta_{ik} \rho V^2| = 0. \quad (4)$$

Eq.(4) yields three positive real eigenvalues ρV_j^2 , $j=1,2,3$, for each specified propagation direction n . As an example, we introduce the general procedure of using ultrasonic pulse-echo method to get a full set of independent physical parameters for a tetragonal crystal with point group $4mm$.

There are a number of important piezoelectric materials, such as BaTiO₃, PZT (PT>48%), PZN-PT(PT>10%), belong to point group $4mm$ at room temperature.¹¹ The elastic, piezoelectric and dielectric matrices for tetragonal point group $4mm$ are listed, according to Voigt notation in Table I. These matrices are written assuming that the axes are oriented according the IRE convention as illustrated in Fig.1. A crystal with $4mm$ symmetry has two independent components of dielectric constant: ϵ_{11} and ϵ_{33} , six independent components of elastic stiffness: c_{11}^E , c_{12}^E , c_{13}^E , c_{33}^E , c_{44}^E and c_{66}^E and three independent components of piezoelectric stress constant: e_{31} , e_{33} and e_{15} .

Table I: The elastic, piezoelectric, and dielectric matrices for tetragonal crystal with $4mm$ point group symmetry.

ELASTIC MATRIX	c_{11}	c_{12}	c_{13}	0	0	0
	c_{12}	c_{11}	c_{13}	0	0	0
	c_{13}	c_{13}	c_{33}	0	0	0
	0	0	0	c_{44}	0	0
	0	0	0	0	c_{44}	0
	0	0	0	0	0	c_{66}
PIEZOELECTRIC MATRIX	0	0	0	0	e_{15}	0
	0	0	0	e_{15}	0	0
	e_{31}	e_{31}	e_{33}	0	0	0
DIELECTRIC MATRIX	ϵ_{11}	0	0			
	0	ϵ_{11}	0			
	0	0	ϵ_{33}			

6 INDEPENDENT CONSTANTS

3 INDEPENDENT CONSTANTS

2 INDEPENDENT CONSTANTS

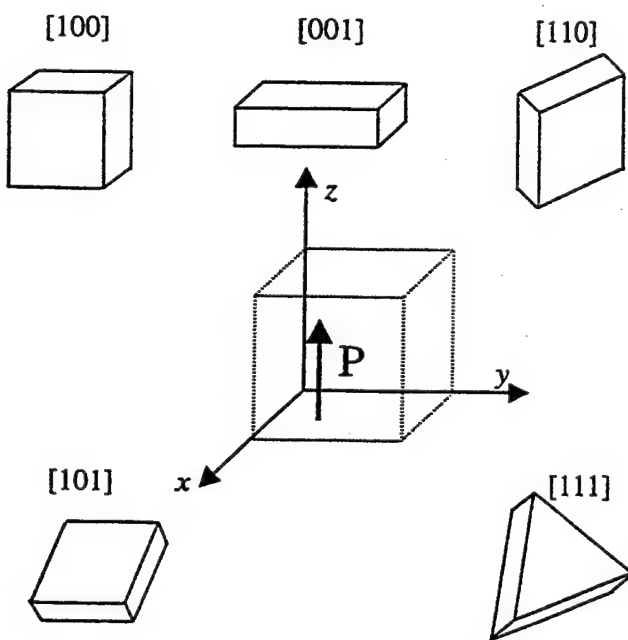


Fig.1. The orientation of test samples for ultrasonic pulse-echo measurement.

Direct measurement of the clamped dielectric constants ϵ_{11}^s and ϵ_{33}^s at very high frequencies is difficult because of the influence of the mechanical resonance and/or their high harmonics. Moreover, many piezoelectric ceramics and crystals also have fairly large capacitance relaxation that also affects high frequency measurements. By contrast, the constant stress dielectric constants ϵ_{11}^r and ϵ_{33}^r may be determined accurately from low-frequency capacitance measurements.

Equation (4) gives the general solution of the wave equation for plane elastic traveling wave propagating along an arbitrary direction n in an infinite piezoelectric medium. For tetragonal crystal with point group $4mm$, a complete set of elastic and piezoelectric constants can, in principle, be extracted from ultrasonic phase velocity measurements along the two principal crystallographic axes [100], [001] and three additional axes in [110], [101] and [111]. There exist two special types of crystallographic directions for propagation of elastic waves. The first allows propagation of one pure longitudinal mode and two pure shear modes, and the second allows propagation of two mixed modes, one quasi-longitudinal and one quasi-shear and one pure shear mode. In the above five crystallographic directions, [100], [001] and [110] belong to the first kind, while [101] and [111] belong to the second kind. Table II lists the effective elastic constants obtained from various modes in these five propagation directions according to Eq. (1), (2) and (3).

Table II: Effective elastic constants $\Lambda_{ik} = \rho V^2$ for class $4mm$ and $6mm$ ($\mathbf{P} = [0, 0, P]$), and measured ultrasonic phase velocities V and \bar{c} for a piezoelectric ceramic PZT-5H

Mode No.	Sample thickness (mm)	Propagation direction	Polarization displacement	Wave type	$\bar{c} = \rho V^2$	Phase velocity (m/sec)	Effective elastic stiffness constant ($\times 10^{10}$ N/m 2)
1	2.13	[100]	[100]	L	c_{11}^E	3922.7	11.3
2			[010]	S	c_{66}^E	1767.6	2.30
3			[001]	S	$c_{44}^D = c_{44}^E + e_{15}^2 / 4\epsilon_{11}^s$	2209.5	3.56
4	3.13	[001]	[100]	S	c_{44}^E	1651.7	2.01
5			[001]	L	$c_{33}^D = c_{33}^E + e_{33}^2 / \epsilon_{33}^s$	4293.6	13.6
6	2.56	[110]	[110]	S	$(c_{11}^E - c_{12}^E) / 2$	1762.1	2.29
7	2.91	[101]	[101]	QS	c_{101}^{qs}	1929.7	2.74
8			[101]	QL	c_{101}^{ql}	4133.5	12.6
9	5.30	[111]	[111]	QL	c_{111}^{ql}	1981.3	12.3
10			[112]	QS	c_{112}^{qs}	4094.2	2.89

where L: longitudinal; S: shear; QL: quasi-longitudinal; QS: quasi-shear, and the new quantities in the table are given by

$$\begin{aligned}
 c_{101}^{qs} &= (c_{11}^E + c_{33}^E + 2c_{44}^E) / 4 + E_{31}^2 + E_{33}^2 - \left\{ [(c_{11}^E - c_{33}^E) / 4 + E_{31}^2 - E_{33}^2] + [(c_{13}^E + c_{44}^E) / 2 + 2 \cdot E_{31} \cdot E_{33}] \right\}^{1/2} \\
 c_{101}^{ql} &= (c_{11}^E + c_{33}^E + 2c_{44}^E) / 4 + E_{31}^2 + E_{33}^2 + \left\{ [(c_{11}^E - c_{33}^E) / 4 + E_{31}^2 - E_{33}^2] + [(c_{13}^E + c_{44}^E) / 2 + 2 \cdot E_{31} \cdot E_{33}] \right\}^{1/2} \\
 c_{111}^{ql} &= (c_{11}^E + c_{12}^E + c_{33}^E + 3c_{44}^E + 2c_{66}^E) / 6 + E_{31}^2 / 12 + E_{33}^2 / 6 + \left\{ [(c_{11}^E + c_{12}^E - c_{33}^E - c_{44}^E + 2c_{66}^E + E_{31}^2 / 2 - E_{33}^2)^2 + 8[(c_{13}^E + c_{44}^E) + E_{31} \cdot E_{33} / 2]] \right\}^{1/2} / 6 \\
 c_{112}^{qs} &= (c_{11}^E + c_{12}^E + c_{33}^E + 3c_{44}^E + 2c_{66}^E) / 6 + E_{31}^2 / 12 + E_{33}^2 / 6 - \left\{ [(c_{11}^E + c_{12}^E - c_{33}^E - c_{44}^E + 2c_{66}^E + E_{31}^2 / 2 - E_{33}^2)^2 + 8[(c_{13}^E + c_{44}^E) + E_{31} \cdot E_{33} / 2]] \right\}^{1/2} / 6 \\
 E_{31} &= \frac{e_{15} + 2e_{31}}{4(\epsilon_1 + \epsilon_3)^{1/2}}; \quad E_{33} = \frac{e_{15} + 2e_{33}}{4(\epsilon_1 + \epsilon_3)^{1/2}}; \quad E_{31}' = \frac{e_{15} + 2e_{31}}{(2\epsilon_1 + \epsilon_3)^{1/2}}; \quad E_{33}' = \frac{e_{15} + 2e_{33}}{(2\epsilon_1 + \epsilon_3)^{1/2}}.
 \end{aligned}$$

It is evident from Table II that the six independent elastic stiffness constants, c_{ij}^E , four independent piezoelectric constants and two clamped dielectric constants must be extracted from the experimental data of phase velocities and the dielectric constants ϵ_{11}^T and ϵ_{33}^T . In the computational procedure, ϵ_{11}^T and ϵ_{33}^T are preferred as input data, while ϵ_{11}^S and ϵ_{33}^S are to be determined along with the elastic stiffness and the piezoelectric stress constants. Four elastic stiffness constants c_{11}^E , c_{12}^E , c_{44}^E and c_{66}^E , one piezoelectric constants e_{15} , and one clamped dielectric constant ϵ_{11}^S may be calculated directly from the measurements of the phase velocities with pure modes along [100], [001] and [110] crystallographic directions, respectively, with the help the measurement of ϵ_{11}^T .

The remaining five constants c_{13}^E , c_{33}^E , e_{13} , e_{33} and ϵ_{33}^S , in principle, may be evaluated from phase velocity measurements along propagation directions of [001], [101] and [111] and the measurement of ϵ_{33}^T . We can construct a set of nonlinear equation according to Table II and the relationship between ϵ_{33}^S and ϵ_{33}^T . These nonlinear equations may be solved numerically using Newtons's method.¹² There are, however, numerical problems, particularly, if the piezoelectric constants are small compared to the elastic properties. Also, the solutions of these equations may have multiple roots, addition examinations are needed to guarantee the reliability of the ultimate results. In this case, piezoelectric constants will be easier to be determined from the measurements of electromechanical coupling factors and the resonance and anti-resonance frequencies of piezoelectric vibrators.

3. THE COMBINED CHARACTERIZATION PROCEDURE

Direct determination of a length extension vibrator may eliminate the need for the ultrasonic measurement along [111] or [101], because one can derive the transverse electromechanical coupling factor k_{31} , the constant electric field elastic compliance constant s_{11}^E and the piezoelectric strain constant d_{31} from measured f_r and f_a ^{6,7},

$$\frac{k_{31}^2}{1-k_{31}^2} = -\frac{\pi f_a}{2f_r} \tan\left(\frac{\pi \Delta f}{2f_r}\right),$$

$$f_r = 1/2l(\rho s_{11}^E)^{1/2},$$

$$k_{31}^2 = \frac{d_{31}^2}{s_{11}^E \epsilon_{33}^T},$$
(5)

where $\Delta f = f_a - f_r$, and l is the length of the vibrator. The constants s_{11}^E and d_{31} are regarded as independent parameters here. In the same manner, a length longitudinal bar can also be used to provide two independent measurements. The longitudinal electromechanical coupling factor k_{33} , s_{33}^E and d_{33} can be derived from the measured f_r and f_a of the length longitudinal bar according to the equations

$$k_{33}^2 = \frac{\pi f_r}{2f_a} \cot\left(\frac{\pi f_r}{2f_a}\right)$$

$$f_a = 1/2l(\rho s_{33}^D)^{1/2}$$

$$s_{33}^E = s_{33}^D / (1 - k_{33}^2)$$

$$k_{33}^2 = d_{33}^2 / s_{33}^E \epsilon_{33}^T,$$
(6)

where s_{33}^D is an elastic compliance under constant electric displacement. In this case, s_{33}^E and d_{33} can serve as two independent parameters instead of c_{33}^E and e_{33} in the ultrasonic method. Thus nine independent components for point group

$4mm$ can be determined by the ultrasonic pulse-echo methods combining with the resonance measurements. Three choices are listed below:

(1). The measurements of [100], [001] and [110] oriented plates in pure longitudinal and pure shear modes determine five independent constants: $c_{11}^E, c_{12}^E, c_{44}^E, c_{66}^E$ and e_{15} . The constants: $s_{11}^E, s_{33}^E, d_{31}$ and d_{33} can be determined by resonance measurements of a length extension bar and a length longitudinal vibrator, respectively.

(2). The measurements of [100], [001], and [110] oriented plates in pure longitudinal and pure shear modes determine the independent constants $c_{11}^E, c_{12}^E, c_{44}^E, c_{66}^E$ and e_{15} , and the measurements of [101] oriented plate in quasi-longitudinal and quasi-share modes determine two independent constants: c_{33}^E and e_{33} . In this case, an additional resonance measurement of a length extension vibrator is need to provide another two independent constants s_{11}^E and d_{31} instead of the constants c_{13}^E and e_{31} extracted from the ultrasonic measurement in [111] oriented plate.

(3). The measurements of [100], [001], and [110] oriented plates in pure longitudinal and pure shear modes determine the independent constants $c_{11}^E, c_{12}^E, c_{44}^E, c_{66}^E$ and e_{15} , and the measurements of [101] oriented plate in quasi-longitudinal and quasi-share modes determine two independent constants: c_{13}^E and e_{31} . The remaining two independent constants s_{33}^E and d_{33} , while s_{33}^E and d_{33} are determined from an additional resonance measurement of a length longitudinal vibrator.

4. EXPERIMENTAL METHOD AND MEASUREMENT RESULTS

Using the nine measured independent constants above and two dielectric constants ϵ_{11}^T and ϵ_{33}^T derived from the low frequency capacitance values of [100] and [001] cut thin plates, a complete set of physical parameters can be derived for a piezoelectric material with tetragonal point group $4mm$. The electromechanical coupling factor k_{15} , k_{31} and k_{33} can also be calculated from these constants. Here we will give an example of the measurement on piezoelectric ceramic PZT-5H using the above combined methods. A set of data obtained only from conventional resonance technique is also listed as comparison. The physical property tensors matrix are the same for point groups $6mm$ and $4mm$, however, there is one less independent constant since the elastic component $c_{66}=(c_{11}-c_{12})/2$ and $s_{66}=2(s_{11}-s_{12})$ in $6mm$ system. Although c_{66} is not an independent constant in the measurement of our ceramic sample, it has been included for completeness since it represents one of the basic measured quantities.

Three kinds of physical quantities are involved in the measurements of these constants, i.e., ultrasonic phase velocity, resonance and anti-resonance frequencies and capacitance, respectively. The most convenient method to measure the ultrasonic phase velocity is the pulse-echo method in which a short pulse trains of plane-wave are sent into the sample with a pair of parallel faces. A 15 MHz longitudinal and a 20 MHz shear transducer were used to measure the longitudinal and transverse waves, respectively. The transducer was affixed to one face of the measured sample to act as a generator and receiver. The phase velocity was computed from the delay time between echoes and the thickness of the sample.

The measurements of resonance and anti-resonance frequencies were performed using an HP-4194A Impedance/Gain-phase analyzer. The resonance and anti-resonance frequencies, locating the minimum and maximum values of impedance, can be found easily from the impedance spectrum. The length extension vibrator has the following dimensions: $l = 14.79$ mm, $w = 3.0$ mm and $t = 0.45$ mm, where l , w and t are length, width and thickness, respectively. The sample was poled in the thickness direction and the electric field applied is parallel to the thickness direction and perpendicular to the length. The length longitudinal vibrator has the following dimensions: $l = 19.16$ mm, $w = 2.50$ mm and $t = 2.45$ mm. Both poling direction and electric field were parallel to the length direction of the sample in this case.

The capacitance measurements were performed using the impedance analyzer, they could use the same sample that were prepared for the ultrasonic measurement. The dielectric constants were calculated based on the parallel plate capacitance formula $\epsilon = Ct/\epsilon_0S$, where C and S are the capacitance of sample and its electrode surface area, and ϵ_0 is the vacuum permittivity. Three complete sets of physical constants of PZT-5H are listed in Table III. The data of the first column (M-1) in the table were derived from the independent constants $c_{11}^E, c_{12}^E, c_{44}^E, c_{66}^E, e_{15}$, determined from three ultrasonic samples,

Table III. The elastic, piezoelectric, dielectric constants and electromechanical coupling factors for poled piezoelectric ceramic PZT-5H measured by the different methods (the density $\rho = 7.36 \times 10^3 \text{ kg/m}^3$).

	M-1	M-2	Resonance		M-1	M-2	Resonance	
Constant electric field	$(\times 10^{10} \text{ N/m}^2)$				$(\times 10^{10} \text{ N/m}^2)$			
Elastic stiffness					Constant electric displacement			
c_{11}^E	11.3	11.3	11.5		c_{11}^D	11.5	11.5	11.7
c_{12}^E	6.73	6.73	6.85		c_{12}^D	6.91	6.88	7.02
c_{13}^E	6.69	6.58	6.89		c_{13}^D	5.87	5.81	6.09
c_{33}^E	9.89	9.79	10.15		c_{33}^D	13.6	13.6	14.1
c_{44}^E	2.01	2.01	2.03		c_{44}^D	3.59	3.59	3.60
c_{66}^E	2.30	2.30	2.33					
Constant electric field	$(\times 10^{-12} \text{ m}^2/\text{N})$				Constant electric displacement	$(\times 10^{-12} \text{ m}^2/\text{N})$		
Elastic compliance					Elastic compliance			
s_{11}^E	16.4	16.3	16.3		s_{11}^D	14.0	14.0	13.9
s_{12}^E	-5.32	-5.43	-5.23		s_{13}^D	-2.69	-2.69	-2.69
s_{13}^E	-7.52	-7.31	-7.51		s_{33}^D	10.8	10.7	10.7
s_{33}^E	20.3	20.5	20.0		s_{44}^D	27.8	27.8	27.8
s_{44}^E	49.8	49.8	49.3					
s_{66}^E	43.5	43.5	43.7					
Piezoelectric stress constant	(C/m^2)				Piezoelectric strain constant	$(\times 10^{-12} \text{ C/N})$		
e_{15}	14.8	14.8	14.7		d_{15}	735	735	726
e_{31}	-5.26	-4.85	-5.01		d_{31}	-263	-253	-262
e_{33}	23.5	23.8	24.0		d_{33}	515	512	518
Piezoelectric voltage constant	$(\times 10^3 \text{ m}^2 \text{ C}^{-1})$				Piezoelectric stiffness constant	$(\times 10^8 \text{ NC}^{-1})$		
g_{15}	29.9	29.9	29.5		h_{15}	10.7	10.7	10.6
g_{31}	-9.36	-9.02	-9.31		h_{31}	-3.52	-3.24	-3.35
g_{33}	18.4	18.3	18.4		h_{33}	15.7	15.9	16.0
Constant stress					Constant strain			
Dielectric constant					Dielectric constant			
ϵ_{11}^T	2778	2778	2778		ϵ_{11}^S	1550	1550	1567
ϵ_{33}^T	3170	3170	3170		ϵ_{33}^S	1691	1691	1691
Electromechanical Coupling factor								
k_{15}	0.664	0.664	0.660					
k_{31}	-0.387	-0.374	-0.386					
k_{33}	0.683	0.683	0.683					

and the constants $s_{11}^E, s_{33}^E, d_{31}, d_{33}$, were determined from resonance technique. The data of the second column (M-2) were derived from the independent constants $c_{11}^E, c_{12}^E, c_{13}^E, c_{44}^E, c_{66}^E, e_{15}, e_{31}$, determined from four ultrasonic samples, and s_{33}^E and d_{33} , determined from a length longitudinal vibrator, which is outlined in method (3) of Sec.3. The data in the third column (M-3) were derived from a set of independent constant totally determined by standard resonance technique from four resonance samples. These samples include a thickness-shear and a disk-extension vibrator in addition to a length-extension and a length-longitudinal vibrator. The technique has been described in detail in many references, therefore, here we only list the measured results as comparison with the results listed in the first and second columns. One can find that the values of the same constant listed in the three columns of Table.III agree well.

5. SUMMARY AND CONCLUSIONS

We have investigated thoroughly the characterization techniques for obtaining reliable material parameters for piezoelectric materials. The results can be summarized below:

- (1). For materials with $6mm$, $4mm$ symmetries, the constants $c_{15}^E, c_{33}^E, e_{31}$ and e_{33} can not be directly measured using pure modes along the principle crystallographic axes. They may be indirectly extracted from some effective elastic stiffness constants of mix modes by solving a coupled Christoffel equation, which may introduce relatively large errors in these measured constants due to the loss of significance in numerical procedure.
- (2). If an additional direct measurement of the constants s_{33}^E and k_{33} or d_{33} can be performed using a length-longitudinal vibrator, it will simplify the calculations and eliminate the problematic quantities in the Christoffel equation and increase the accuracy of the final results.
- (3). The constants c_{44}^E and e_{15} can be directly determined from the ultrasonic measurement on [100] and [001] oriental plates, therefore, are more accurate than the measurements of a thickness-shear vibrator, since the interference effect of two shear modes always exit in a thickness-shear vibrator¹³. Ultrasonic technique is particularly appropriate for the measurements of shear constants of materials.

Our results show that a complete set of fundamental material constant can be accurately determined by using ultrasonic technique assisted with resonance technique. Three option were given which could lead to accurate measurements. The data obtained using this combined method for a PZT-5H is consistent with the data obtained by the IEEE resonance method. The advantage of using the ultrasonic technique is that the measured samples require only one set of precisely aligned faces and no aspect ratio requirement. Moreover, the samples can be the same one as those used in resonance technique and dielectric measurements. Fewer samples used would increase the self-consistency of the material parameters.

6. ACKNOWLEDGEMENTS

This work is supported by the Ben Franklin Partnership of Pennsylvania and the NIH under Grant #P41RR11795-01A1.

7. REFERENCE

1. D. A. Berlincourt, D. R. Curran, H. Jaffe, "Piezoelectric and piezomagnetic materials and their function in transducers", *Physical Acoustics Vol. 1A* (ed. W.P.Mason), *Academic Press*, 1964.
2. T. Ikeda, "Fundamentals of piezoelectricity", *Oxford University Press*, *Oxford*, 1990.

3. W. P. Mason, "Piezoelectric crystals and their application to ultrasonic", *D. Van Nostrand Co., Inc., New York*, 1950.
4. "IRE standards on piezoelectric crystals, 1949", *Proc. IRE*, **37**, pp.1378-1395, 1949.
5. "IRE standards on piezoelectric crystals – the piezoelectric vibrator: definitions and methods of measurement, 1957", *Proc. IRE*, **45**, pp. 353 – 358, 1957.
6. "IRE standards on piezoelectric crystals: determination of the elastic, piezoelectric, and dielectric constants—the electromechanical coupling factor, 1958", *Proc. IRE* **46**, pp.764-778, 1958.
7. "IEEE standard on piezoelectricity, ANSI/IEEE std, 176-1987", *IEEE, New York*, 1987.
8. J. J. Kyame, " Wave Propagation in Piezoelectric Crystals", *J. Acous. Soc. Amer.* **21**, pp. 159-167, 1949.
9. H. J. McSkimin, "Note and references for the measurement of elastic moduli by means of ultrasonic waves", *J. Acous. Soc.* **33**, pp. 606-616, 1961.
10. R. T. Smith and F. S. Welsh, Temperature dependence of the elastic, piezoelectric, and dielectric constants of lithium tantalate and lithium niobate", *J. Appl. Phys.* **42**, pp. 2219-2230, 1971.
11. D. Berlincourt and H. Jaffe, " Elastic and piezoelectric coefficients of single-crystal barium titanate", *Phys. Rev.* **111**, pp. 143-148, 1958.
12. W. H. Press, B. P. Flannery, S. A. Teukolsky, and W. T. Vetterling, " Numerical Recipes", *Cambridge Univ. Press, Cambridge*, pp.240-273, 1986.
13. W. Cao, S. N. Zhu and B. Jiang, "Analysis of shear modes in a piezoelectric vibrator", *J. Appl. Phys.*, (in press) 1998.

APPENDIX 60

Virtual Design of Medical Transducers

Wenwu Cao

National Resource Center for Medical Transducer Engineering
Department of Mathematics and Materials Research Laboratory
The Pennsylvania State University, University Park, PA 16802

ABSTRACT

Computer simulation has been used widely in medical ultrasonic transducer designs. One could now construct and test a transducer entirely on a virtual basis. Such a virtual design and testing procedure not only can save us time and money, but also provide better understanding on design failures and allow us to modify designs more efficiently and economically. This paper is intended to give a brief review on virtual transducer design procedure using a few examples and also list the necessary precautions while using such advanced design tools.

1. INTRODUCTION

More and more transducer manufacturers are using finite element tools to enhance the modeling capability for complex transducer designs. This can substantially reduce the cost and time for innovative transducer research. It is very exciting to see the fast development of this field, but one also must understand the limitations of simulation modeling. It is necessary to follow certain procedure in order to make the simulation modeling more accurate and effective. Such limitations include numerical error accumulation, model size constraints and incompatibility between different software.

For the current modeling capability, a virtual design procedure refers to three basic steps: (1) Model construction; (2) Vibrational analysis of the transducer structure; (3) Radiation field study. The information from vibrational analysis and virtual testing can provide feedback for modification of the model design so that a better performance can be achieved. In other words, these three steps can form a design loop for optimization. It is similar to real experimental procedure for manufacture a transducer except no real transducers need to be built until the simulated design reaches the optimum configuration. While such simulation design has been realized in many fields, it is only in recent years that such methods begin to gain popularity in transducer industry. One of the reasons is that the equivalent circuit models, such as the KLM model,¹ have been working well, particularly for designing single element transducers. There was no real motivation to spend the effort to develop more fancy modeling scheme. Another reason is that the simulated results often not good enough to compare to the experimental results in the past. Such inaccuracy was due to the influence of many factors, for example, inaccurate input material parameters, oversimplified model design, and improper calculation mechanism which leads to large error propagation. With the improvement of computation methodologies and the ever increasing demand for better and higher frequency transducers which are beyond the capability of equivalent circuit models, there is an urgent need to push simulation design. A very important aspect of medical ultrasonic imaging is the lateral resolution which requires the knowledge of 2- and 3-dimensional information. Nonuniform surface vibration is also an area that the equivalent circuit and other 1-D models can not give a proper description.

A lot of progress were made on finite element analysis (FEA) of transducer designs.²⁻⁸ Over the past a few years, we have been concentrated to integrate individual analysis into a more complete virtual design and testing procedure.⁵⁻⁸ Through experimental verifications, we found that many simulation results can be as reliable as experiments if proper modeling procedure is followed. There are, of course, still some limitations in the simulation procedure, some are intrinsic to the numerical methods and some are created by improper model simplification and wrong input parameters. It is easy to detect catastrophic errors, but if the errors do not lead to instability of the solution, they become very difficult to detect. Focusing on this kind of problems, we have performed many experimental verifications on the simulation results and have obtained some first hand experience in performing such simulations. In this review, a brief description will be given for of all the three steps mentioned above. In addition, a summary of the important error sources that must be treated carefully in performing the simulation, will be listed.

2. MODEL CONSTRUCTION

The first important step in simulation is to construct a realistic model which requires the minimum computation time. The main factors that can help this aspect are symmetry and dimensionality. Symmetry could reduce the model size usually by a factor of 2-8. For an axial symmetry system, the system may be simplified from a 3-D to 2-D model, which can save us orders of magnitude in computation time. Reducing the number of computational steps has two effects, one is to make the computation time realistic and the other is to reduce the amount of error accumulation. For this reason, one should try to avoid long time or large dimensions with a very small step size. Although some of the modern algorithms have better convergence and stability, it is always advisable to be frugal in model construction to reduce error accumulation. On the other hand, one should not oversimplify the model so that the fundamental characteristics are lost from the original design.

Showing in Fig. 1(a) is the commonly used 2-D axial symmetry model for a simple single element transducer illustrated in Fig. 1(b). While such approximation can greatly reduce the computation time, one must understand that the simplification has eliminated all nonaxial symmetric modes that exist in the 3-D structure. As a consequence, the spectrum analysis using the model of 1(a) will contain fewer peaks than the situation in 1(b). Such approximation is good enough to analyze a single element transducer since the nonaxial symmetric modes are not relevant. However, if the materials in each of the layers are nonuniform, such as composites transducers, the 2-D model would not be accurate to describe the situation.

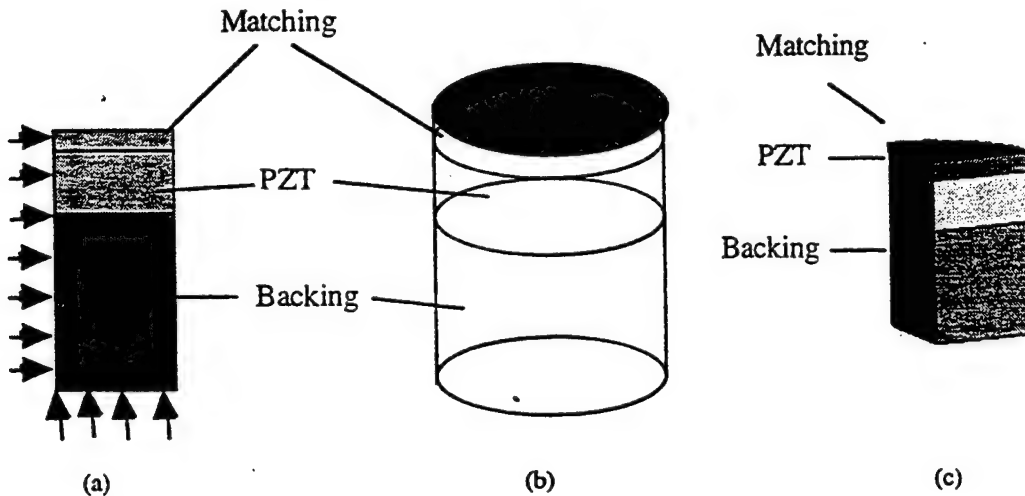


Fig. 1 Modeling scheme for a single element transducer. (a) Axial symmetry 2-D model; (b) Outline of a simple single element 3-D transducer structure and (c) 1/4 3-d model.

It is of course a better approximation to use a partial 3-D model if one could find certain symmetry of the structure to be simulated. For example, a 1/4 of the cylindrical structure shown in Fig. 1(c) would certainly be a reasonable choice for calculating beampattern if the computational size is not excessive. For a square 1-3 composite transducer, one could use 1/8 of the 3-D model as shown in Fig. 2(a). Although a unit cell 3-D modeling shown in Fig. 2(b) could be another good choice, it could not take into account the edge effects in a finite size transducer. Such edge effects are important for calculating the near field beampattern but may not be as important to calculate the fundamental resonance and impedance spectrum. The price to pay for 3-D modeling is the computation time, which could be increased orders of magnitude compared to a 2-D model. Therefore, depending on the objective of the modeling, certain simplification could be ideal while others may not give the correct answer due to over simplification.

The next important item is to apply appropriate boundary conditions to the simplified (idealized) finite element model. The three most commonly used boundary conditions are:

(1) Free boundary condition. This is a default boundary condition, which is appropriate for study a finite system and boundary effects. There will be severe wave reflection at the boundaries and the energy is pretty much trapped in the structure.

(2) Fixed boundary condition. The idea is to fix one or more degrees of freedom in the model at certain boundaries. A rule of thumb is to have at least one side in each degree of freedom to be fixed so that the translation mode can be eliminated. This is particularly important for the frequency domain algorithm since the translational degree of freedom will confuse the definition of the displacement if not causing any divergence.

(3) Buffer layer boundary condition. This condition is used to simulate semi-fixed boundary conditions, for example the bounding material, which is much softer than the ceramics or metals. The buffer layer is also needed for connecting materials having different degrees of freedom, for example solid-liquid interface, as we know that liquid has no shear restoring forces. The buffer layer is necessary to consolidate the difference in terms of the degrees of freedom.

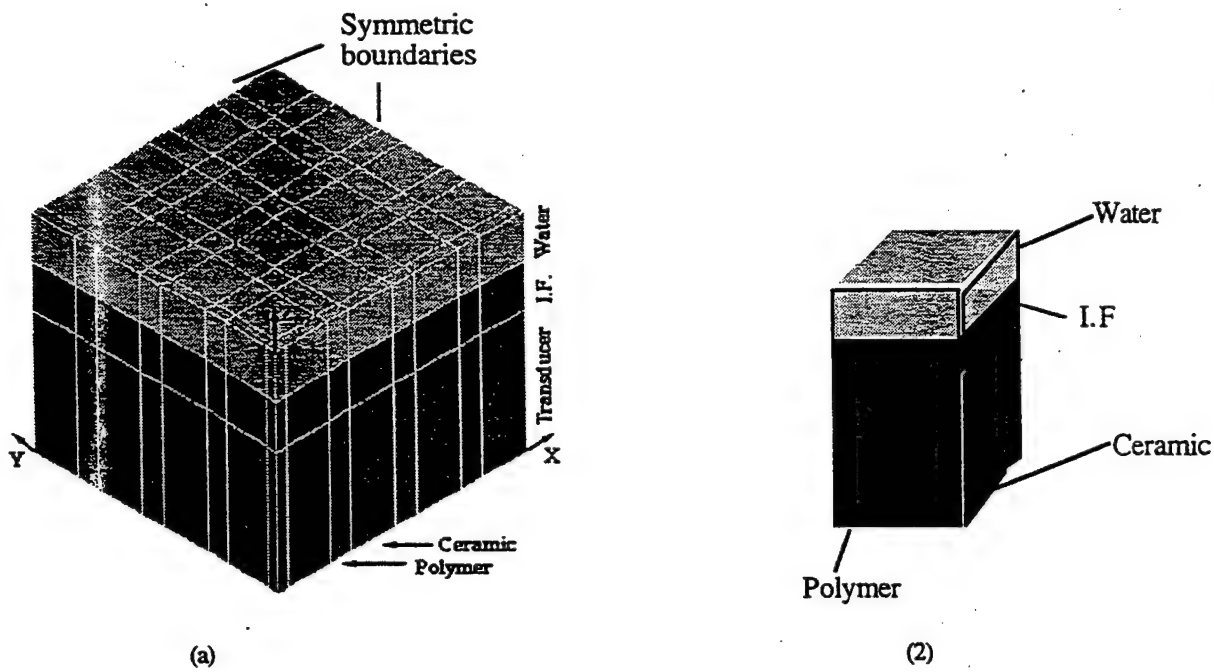


FIG. 2. Finite element models for 1-3 composite transducer. (a) 1/8 of the 36 element transducer, three unseen surfaces are prescribed symmetric; (b) 1/4 of a unit cell; only the top surface is free all other faces are prescribed symmetric.

Sometimes, symmetry boundary condition is specified in certain commercial packages, which plays similar role as the fixed boundary condition (2) mentioned above in the direction normal to the surface. Symmetry boundary condition defines a fixed line or plane which can eliminate one translational degree of freedom. One important point needs to be mentioned is that symmetry is only for mechanical boundary conditions, the electrical boundary conditions are not affected by the symmetry command.

3. VIBRATIONAL ANALYSIS

After the basic model being constructed and appropriate boundary conditions applied, one can perform several kinds of analyses using finite element methods by solving the coupled dynamical equations. In transducer design, the most useful analysis is the vibrational characteristics of the structure, including the mechanical resonance and the dynamical response to external electric and acoustic fields.

3.1 Resonance frequencies

The purpose of this analysis is to find all the resonance frequencies and the corresponding deformation shape. This includes the fundamental resonance and other mechanical resonance that may affect the operation of this mode. One could

also calculate the amplitude distribution for these modes. Showing in Fig. 3 is the calculated resonance frequency for a 2-2 composite transducer with different aspect ratio.⁶ One can see that the finite element calculation is the only one that can accurately describe the aspect ratio dependence.

We found that the simulation results are quite different for transducer in air and in water. Without loading, the polymer has higher amplitude than the ceramic due to the trapped energy in the structure. While in the case of water loading, the amplitude of the polymer becomes smaller than the ceramic since the energy is transmitted to the medium more efficiently from the polymer than from the ceramics, and only the piezoceramic elements get direct energy supply from the electric source.

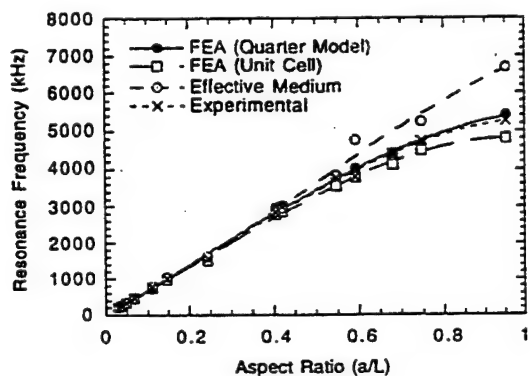


Fig. 3. Comparison of modeling and experimental results for the change of resonance frequency with the aspect ratio of the ceramic element, where L and a are the height and width of the ceramic plates in a 40% ceramic 2-2 composite transducer.

3.2 Harmonic analysis

This analysis is to see how the transducers respond to an external drive, for example, electric AC field. From this analysis, we can obtain information about the modal shape and the electrical impedance spectrum. The electrical impedance curve is one of the better modeled quantity which can be compared fairly well with experiments as shown in Fig. 4. After knowing the resonance frequency from the procedure described in Sec. 3.1, one can drive the transducer at this particular frequency and calculate the nonuniform displacement and velocity distributions at the transducer surface. The merit of the simulation is that it can take into account all the modes affecting the transducer operation and pinpoint at any spot of interest.

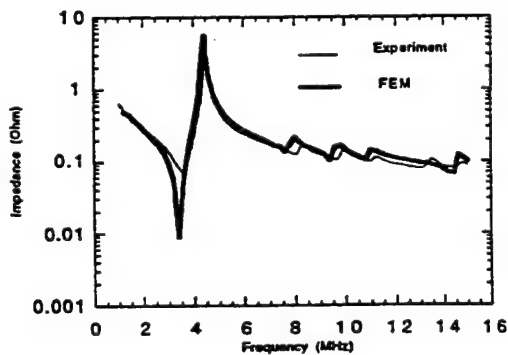


Fig. 4. Calculated and measured electrical impedance of a 80% ceramic 2-2 composite transducer.

3.3 Transient Analysis

This is to simulate the pulse response of a transducer. Experimentally, one can measure the collective pulse response using the test transducer for both sending and receiving acoustic signals. While in simulation, it is not convenient to allow the acoustic pulse to travel long time in the medium (size limitation), however, one could pinpoint the response of any component at any given position in the transducer structure.

The transient analysis under a single pulse driven condition is the most important measure for the performance of a broadband transducer, which can tell us the bandwidth, sensitivity and ringdown characteristics. However, this function in simulation is still limited to relative unit due to the lack of precise input material parameters for the frequency dependent attenuation. We found that the most convenient way to study the element cross-talk is to directly calculate the electrical response of the neighbors and then use the ratio of the neighbor response to the element response as the measure. Such a definition and procedure has been used to study the dicing effects of matching layers in a 1-D array design and provided satisfactory explanation to the commonly used design strategy.⁹ There are some differences between the transient analysis and experimental methods used to characterize pulse response, because the simulation can not duplicate the effects of frequency response of the electrical circuits in the test set-up. In order to directly compare to the experimental measured pulse response, one need to construct frequency filters in the simulation routine to address this problem.

4. RADIATION FIELD

Virtual testing refers to the simulated performance for an FEA model transducer, such as the impedance spectrum and the pulse response mentioned above. More importantly, one needs to know the radiation beampattern, both in the nearfield and in the farfield. Such beampattern calculations are based on the information provided by the vibrational analysis mentioned above. Experimentally, the transducer beampattern characterization is one of the most time consuming tasks, and is often limited in the nearfield because of the probe interference. Such interference problem can be easily overcome in simulation since no physical probe is needed. We have used two different ways to perform this computation: (1) finite element method and (2) boundary element method. The latter is the best choice for a homogeneous medium.

From our experience, the best way to calculate the beampattern is to use a combined finite element and boundary element method. Showing in Fig. 5 is the calculated beam pattern for a 1-3 composite single element transducer using this combined method. The beampattern can give us information about the directivity, focusing capability and sidelobe information, which are important parameters to evaluate the resolution of a transducer. We have evaluated a series of aperiodic 2-2 composite transducers and found out that the vanishing of lateral resonance peaks in the impedance spectrum does not guarantee a good performance of a transducer. The irregularity introduced into the structure, although can suppressed the lateral modes, may also destroy the focusing capability of the transducer.⁷

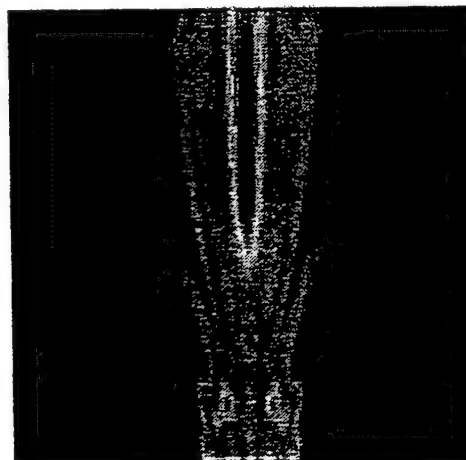


Fig. 5. The radiation beampattern of a 1-3 composite transducer in water calculated by the combined method.

5. ERROR ANALYSIS

There are still many limitations in numerical methods and one must understand them well in order to make a meaningful virtual design model for transducers. As we have emphasized that catastrophic failure is easy to detect since it will lead to divergence of the solutions, however, if the solution exists but erroneous, it is very difficult to detect. One has to use some basic knowledge to evaluate the solutions. Showing in Fig. 6 is a transducer beampattern calculated using a 3-D 1/4 model (ANSYS®). The near field pressure is accurate while the far field pattern becomes erroneous since it produced a secondary focal point which should not appear in a linear medium. Two main contributions to this problem is error accumulation for large size model and incomplete absorbing boundary conditions at the liquid boundary.

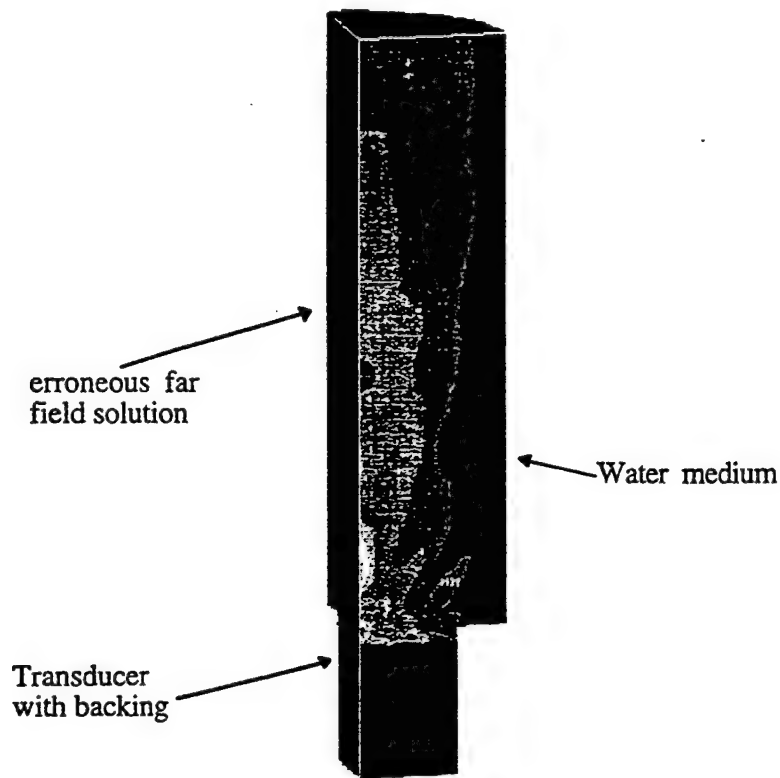


Fig. 6. A 3-D beampattern of a single element transducer calculated using finite element 1/4 model. The near field solution is good while the far field solution is erroneous.

From our experience, attentions need to be paid to the following few points while performing the simulation in order to minimize the errors in simulation design:

- 1). **Boundary conditions.** Specified boundary conditions may not be executed accurately during computations, for example, absorbing boundary condition represents non-reflection only in the case of normal incidence waves. If the wave vector has a dominant tangential component in certain region of the boundaries, the solution will contain strong influence from the boundary reflections. For transducer beampattern calculation, one should try to build a larger size fluid in the model to avoid tangential incidence condition. It is also important to eliminate the translational degree of freedom, which may not be so easy if there is no symmetry in the structure. In this case, one must define a fixed point, or a fixed line, or a fixed plane so that all the displacement will be relative to the fixed reference coordinates associated with the fixed point.
- 2). **Limit the size of the model.** There are two major purposes for limiting the size of the model. One is to reduce the computation time and the other is to reduce error accumulation. As a common knowledge, numerical variables have truncation errors which are intrinsic to numerical methods. There are also errors in all numerical algorithms which are a function of step size in time and space. Both types of errors will propagate and accumulate with the increase of the number of computation steps. Therefore, the fundamental policy is that the model size should be as small as possible while the step size as big as it allows. For example, 10-15 nodes per wavelength for time domain FEA and 3-5 nodes per wavelength

for a frequency domain FEA should be a reasonable choice in dynamical simulations. More advanced finite element methods can use even lesser nodes per wavelength to get accurate results. The errors propagate with wavefront, therefore, far field would become unreliable as shown in Fig. 6.

3). Define good aspect ratio. As stated in the theory of finite element method that the most accurate mesh shape is a cube in 3-D and square in 2-D. However, in many cases, one of the dimensions in the simulated structure is much smaller than the others, for example, the matching layer in a high frequency transducer, making the requirement of aspect ratio one very difficult to be satisfied. In such a case, one must to balance the accuracy and computation time. However, one must remember to mesh at least three nodes in any given dimension if there is a change of material property across the boundary. Nodes at the interface do not represent any of the materials in contact. Less than three nodes means no representation for the material in the computation.

4). Using correct material constants. This has been one of the most difficult issues in 3-D simulation modeling. Many of the published results are either inconsistent or incomplete. Numerical solution could be very sensitive to certain input parameters, in some cases, inaccurate material constants could totally distort the solution. Another important point is that material properties change with frequency and loading. For example, piezoelectric materials can be partially depoled during transducer fabrication and under stress. Using the room temperature ambient pressure measurement data will not give satisfactory simulation results. We found that some of the resonance techniques are also not accurate. Some strategies have been worked out to get more reliable data for piezoelectric materials.^{10,11}

5). Damping of materials. The amplitude of impedance spectrum and displacement are strongly dependent on the material damping. The 3-D simulation requires more parameters than the 1-D equivalent circuit models because it takes into account the anisotropy, while such data are often not available in the literature. Damping is frequency dependent but the equations have constant parameter input therefore can not cover the entire frequency range of interest. A damping constant measured at a given frequency can not guarantee its validity at other frequencies, which makes the modeling of broadband transducer very challenging. What we have been doing is to derive the proper damping constant from one set of measured values, for example, the impedance spectrum, then use it to calculate the other quantities.

6. CONCLUSION AND FUTURE WORKS

The advance of computer speed and algorithm efficiency make it realistic and attractive to perform virtual design of complex transducers. One could simulate many aspects of transducer design and obtain fairly good agreement with experiments. Several examples were given in this review which outlined some of the basic analyses in transducer designs. Through direct visualization one can gain much better understanding on some the problems pertinent to the 3-D nonuniform nature of vibration. For example, 3-d simulation can reveal some of the nonpiezoelectric modes which do not show up in the impedance spectrum measurements but could be excited due to nonsymmetric boundary constraints. More importantly, the 3-D simulation gives us an effective way to obtain the transducer beampattern, both for the near-field and for the far-field. The study on the beampattern distortion versus randomization showed the advantage of the 3-D modeling over 1-D circuit modeling: the disappearance of the lateral modes in the frequency spectrum does not guarantee the quality of transducer.⁷

Because of the size limitation, it may be necessary to perform layered simulation from coarse mesh to fine mesh using submodels. Such procedure has already been used in many simulation designs to find more detailed local changes without having to use fine mesh in the whole structure. In calculating the beampattern, we found that the combination of finite element and boundary element methods is a good solution to overcome error accumulation problem in large size finite element models if the medium is homogeneous.

There are still many challenges in this exciting arena in terms of more stable and efficient numerical algorithms. There is also an urgent need to characterize more accurately all the material properties including damping, and their frequency dependence.

For very high frequency transducer modeling, the current virtual design procedure needs to be further extended to integrate the 3-D Maxwell equation since the quasi-static approximation of uniform electric field will not hold. There is also a need to study nonlinear effects since many transducers, particularly very high frequency ones and therapeutic ultrasound transducers, are being driven out of the linear regime.

ACKNOWLEDGMENTS

The research was supported by the NIH under the Grant # P41 RR11795-01A1 for the National Resource Center for Medical Transducer Engineering.

REFERENCES

1. R. Krimholtz, D. A. Leedom and D. L. Mathaei, New equivalent circuits for elementary piezoelectric transducers, *Electr. Lett.*, **6**, pp. 398-399, 1971.
2. Hossack, J. A., and Hayward, G., Finite-element analysis of 1-3 composite transducers, *IEEE Trans. Ultrason. Ferroelec. Freq. Contr.* **38**, pp. 618-629, 1991.
3. Hladky-Hennion, A., and Decarpigny, J., Finite element modeling of active periodic structures: application to 1-3 piezocomposites, *J. Acoust. Soc. Am.* **94**, pp. 621-635, 1993.
4. Lerch, R., Simulation of piezoelectric devices by two- and three-dimensional finite elements, *IEEE Trans. Ultrason. Ferroelec. Freq. Contr.* **37**, pp. 233-246, 1990.
5. W. K. Qi and W. Cao Finite element analysis of periodic and random 2-2 piezocomposite transducers with finite dimensions", *IEEE Trans. Ultra. Ferro. and Frequency Control*, **44**, pp.1168-1171, 1997.
6. W. K. Qi and W. Cao Finite element analysis and experimental studies on the thickness resonance of pizocomposite transducers, *Ultrasonic Imag.*, **18**, pp. 1-9, 1996.
7. W. K. Qi and Wenwu Cao, Finite element study on random design of 2-2 composite transducer, *Proceedings of SPIE Imaging '97*, **3037**, pp. 176-180, 1997.
8. Draheim and Wenwu Cao, "Finite element and experimental study of impedance matching layer optimization, *Proceedings of SPIE Imaging '97*, **3037**, pp. 135-139, 1997.
9. W. K. Qi and W. Cao, Finite element and experimental study of compiste and 1-D array transducers, *Proc. SPIE '98*, 1998.
10. W. Cao, S. N. Zhu and B. Jinag, Analysis of shear modes in a piezoelectric vibrator, *J. Appl. Phys.*, (in press) 1998.
11. S. N. Zhu, B. Jinag and W. Cao, Characterization of piezoelectric materials using ultrasonic and resonant techniques, *Proceeding of SPIE Imaging '98*, 1998.

APPENDIX 61

ELASTIC PROPERTY CHARACTERIZATION IN THIN SAMPLES OF SUB-WAVELENGTH IN THICKNESS

WENWU CAO

*Department of Mathematics and Materials Research Laboratory, The Pennsylvania
State University, University Park, PA 16802*

(Received 24 February 1997)

A conflict exists in ultrasonic measurements between the resolution which requires higher frequency, and the penetration depth which requires long wavelength. Traditional pulse-echo method for elastic property measurements fails when the sample becomes too thin to allow the separation of repeated echoes. A data processing technique is described here which may provide a solution to this conflict. Elastic properties were successfully measured in samples as thin as 5% of the wavelength λ .

Keywords: Ultrasonic; thin layers; sub-wavelength; high resolution; penetration depth

INTRODUCTION

One of the most powerful techniques for elastic property characterization is ultrasonic method. The pulse-echo technique^[1–4] has been well developed and widely used in characterizing solid materials. Sound velocity, which directly reflect the elastic property, can be measured through the time delay between consecutive echoes. Ultrasound is also a major tool in medical diagnosis in which the elastic properties are known and the pulse-echo pattern is used to form the imaging of an object inside a body. Because pulse-echo technique is to send a tone-burst ultrasonic signal into the structure and measure the time lagging between consecutive echoes, its resolution is limited by the pulse-width. Using a good broadband short ringdown transducer, one can achieve an axial resolution of $1–2\lambda$, where λ is the wavelength. Both transmission and reflection mode operations in

ultrasonic measurements will produce similar echo patterns but different amplitudes depending on the acoustic impedance matching between the medium and the sample. A pair of parallel surfaces of the sample will serve as the reflection planes so that a series of echoes will be generated as shown in Figure 1. The time delay between the adjacent echoes is the time for an acoustic pulse to go through the sample one round trip.

It is hard to achieve sub-wavelength resolution as one can imagine from Figure 1. The pulse separation reflects the sample thickness. If the sample is too thin, these consecutive echoes will overlap to produce a global profile. As demonstrated in Figure 2, when the delay time of two consecutive echoes is less than the ringdown time of the transducer, they cannot be distinguished. The overlapping problem becomes worse for materials with low attenuation because the third echo, the fourth echo, and so on, will all contribute to the measured echo profile, making the measurement impossible.

Although the resolution of ultrasonic technique can be increased through increasing operating frequency, the attenuation increases even faster with frequency. Generally speaking, the attenuation is proportional to f^β , with $1 < \beta < 2$ for ordinary materials and $\beta > 2$ for lossy materials. In other words, higher frequency ultrasonic waves would have much shallower penetration depth, which makes the detection of bonding layer or any imbedded thin object almost impossible using ultrasonic technique, because low frequency waves do not see it while high frequency signals cannot penetrate the structure.

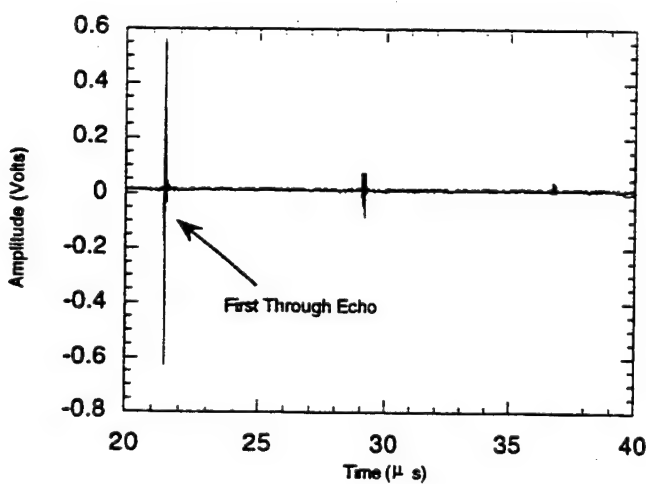


FIGURE 1 The echoes caused by the repeated reflections inside the sample. The signal is obtained from a through mode operation using a 2 MHz center frequency broadband transducer.

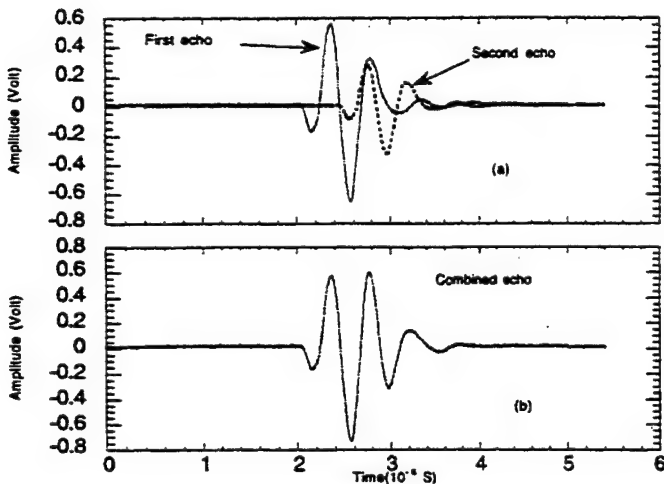


FIGURE 2 Echo overlapping in a thin sample. (a) The two consecutive echoes if not interfere with each other. (b) The actually observed overlapped signal.

The challenge is how to achieve high resolution and deep penetration at the same time. Obviously, the only way to address this problem is to use low frequency signal and achieve sub-wavelength resolution. A method is described in this paper which can be used to measure samples as thin as 5% of λ .

DATA PROCESSING SCHEME

For a thin sample, the received signal from transmission ultrasonic measurement will be a mixture of consecutive transmitted signals due to the multiple reflections within the sample. If we do not consider the attenuation of the sample, the received signal, $x(r, t)$, can be written in terms of the input signal function $s(r, t)$ in the following form:

$$x(r, t) = T_{21} T_{12} \sum_{i=0}^{\infty} R_{21}^{2i} s\left(t - \frac{(r - l)}{V_m} - \frac{(2i + 1)l}{V_s}\right) \quad (1)$$

where T_{21} and T_{12} are the transmission coefficients from the medium to the sample and from the sample to the medium, respectively, R_{21} is the reflection coefficient from sample to the medium, l is the thickness of the sample, V_m and V_s are the sound velocities of the medium and the sample, respectively.

Although the multi-reflections within the sample are not desired in the traditional ultrasonic measurement, such multi-reflections do actually carry

strong signature of the sample. One can obtain the desired information using more elaborate signal processing schemes.

A simple and direct way to abstract the time of flight inside the sample is to find the response function, $h(t)$, so that the transmitted signal $x(t)$ becomes the convolution of the input signal $s(t)$ and $h(t)$,

$$x(t) = \text{conv}[h(t), s(t)] = \int_{-\infty}^{\infty} h(\tau)s(t - \tau)d\tau \quad (2)$$

For simplicity, we have shifted the time reference and set the space variable to be zero at the exit surface of the sample.

For an ideal case, the response function of the sample is simply a series of δ -functions:

$$h(t) = \sum_{j=0}^{\infty} A^j \delta(t - \Delta t), \quad (3)$$

where

$$A = T_{21} T_{12} R_{12}, \quad \Delta t = \frac{2l}{V_s}. \quad (4)$$

In principle, if one can derive the response function $h(t)$ from the measured signals, the round trip time Δt for wave to travel inside the sample can be easily obtained from the peak separation of the δ -function series. Unfortunately, there is no easy way to get "clean" data in practical measurements. All the signals are convoluted by instrumental response functions and being added to certain level of noises, both acoustically and electronically.

In transmission mode operation, the input signal $s(t)$ and the transmitted signal $x(t)$ can be obtained by removing and placing the sample in the acoustic pathway, respectively. The experimentally observed signals (quantities with an over-bar) are not clean and may be written in the following forms:

a) Observed input signal:

$$\overline{s(t)} = \text{conv}[g(t), s(t)] + n_s(t) \quad (5)$$

b) Observed transmitted signal:

$$\overline{x(t)} = \text{conv}[g(t), \text{conv}[h(t), s(t)]] + n_x(t) \quad (6)$$

where $g(t)$ is the response function of the experimental set-up, $n_s(t)$ and $n_x(t)$ represent the noises that are being added to the true signals.

In order to develop a universal method, we like to avoid the task of having to characterize each instrument for its response function $g(t)$. This can be done by defining a new function $k(t)$ to be the modified signal input,

$$k(t) = \text{conv}[g(t), s(t)], \quad (7)$$

and utilizing the property of convolution integral:

$$\text{conv}[g(t), \text{conv}[h(t), s(t)]] = \text{conv}[h(t), \text{conv}[g(t), s(t)]] \quad (8)$$

Hence, the input and transmitted signals become

$$\overline{s(t)} = k(t) + n_s(t) \quad (9)$$

$$\overline{x(t)} = \text{conv}[h(t), k(t)] + n_x(t) \quad (10)$$

The response function can be formally written in the frequency domain as^[5]:

$$H(f) = \frac{\overline{X(f)}}{K(f)} \phi(f) = \frac{\overline{X(f)} K^*(f)}{|K(f)|^2} \phi(f) \quad (11)$$

where $\phi(f)$ is a Weiner optimal filtering factor^[5] which can be written in terms of the power spectra of $\overline{x(t)}$ and $n_x(t)$.

In order to derive the power spectrum of the noise $n_x(t)$, we can perform multiple sampling, i.e., taking the average of m_1 times measurements of the transmitted signal $\langle \overline{x(t)} \rangle_{m_1}$ and then taking another average of m_2 times measurements $\langle \overline{x(t)} \rangle_{m_2}$, with $m_2 > m_1$. It can be shown that the noise power spectrum may be replaced by these averages and the Weiner optimal filtering factor $\phi(f)$ can be written as the following^[6],

$$\phi(f) = 1 - \frac{m_1 m_2}{(m_1 - m_2) |X(f)|^2} (|\overline{X_{m_1}(f)}|^2 - |\overline{X_{m_2}(f)}|^2) \quad (12)$$

From Eqs. (11) and (12), the spectrum of the sample response function $h(t)$ is given by

$$H(f) = \frac{\overline{X(f)} \overline{S^*(f)}}{|K(f)|^2} \phi(f) \quad (13)$$

Then the response function of the specimen, $h(t)$, can be obtained from $H(f)$ using inverse Fourier Transform. We have implemented the FFT

algorithm in the data processing program so that the analysis is almost real time.

RESULTS

This signal processing scheme described above has been applied to a set of brass shims purchased from Precision Brand, Downers Grove, Illinois. The thickness of the shims ranges from 0.004"–0.025". Figures 3 and 4 show the measurement results on a 0.004" and a 0.008" thick brass shims, respectively. Figures 3(a) and 4(a) are the input and transmitted signals, which were

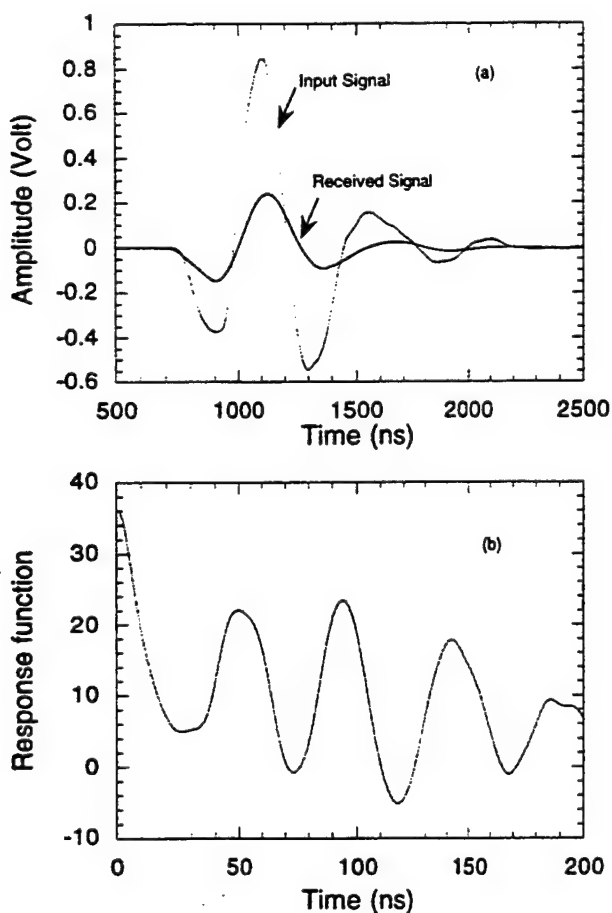


FIGURE 3 (a) The input signal to the sample and the received signal after the pulse went through the sample and (b) The response function derived from (a). The sample thickness is 0.004".

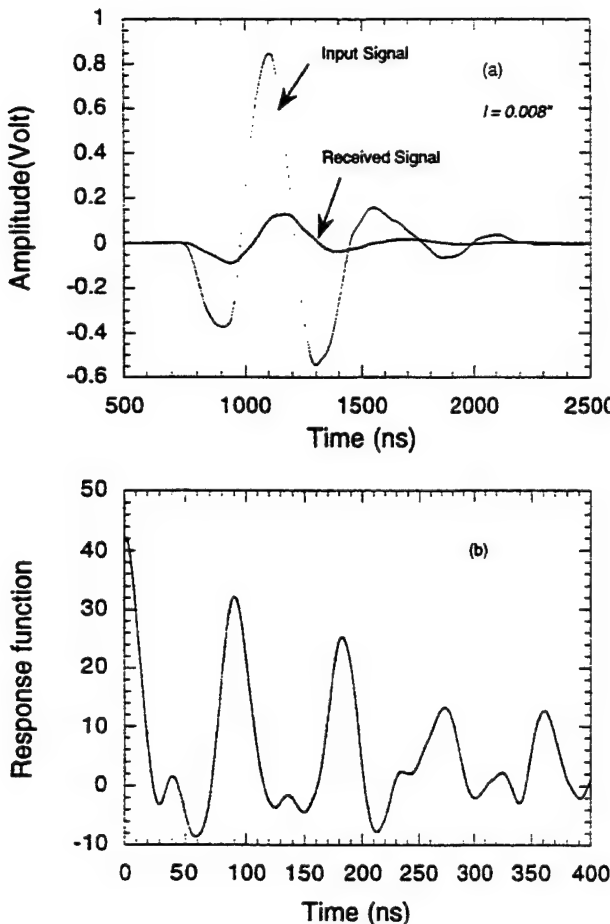


FIGURE 4 (a) The input signal to the sample and the received signal after the pulse went through the sample and (b) The response function derived from (a). The sample thickness is 0.008".

observed independently. The time shift between the input and the transmitted signals cannot be measured directly because the time difference is too small. Figures 3(b) and 4(b) are the calculated corresponding response functions for the two cases. The separation between the peaks of the response function is the time lagging between consecutive reflections inside the sample.

The sound velocity calculated using time difference between the peaks of the response function is given in Table I. One can see that the measurements are very consistent and accurate. The average sound velocity is 4480.4 m/s which gives a value for the elastic constant $c_{11} = 17.0 \times 10^{10}$ N/m². No obvious change of the elastic property with size was observed in this thickness range as shown in Table I.

TABLE I Longitudinal velocity and elastic constant c_{11} for brass shims. (70% Brass, 30% Zinc; $\rho = 8.4697 \text{ g/cm}^3$)

Sample Thickness (inch)	Longitudinal Velocity (m/s)	$c_{11}(10^{10} \text{ N/m}^2)$
0.004"	4431.8	16.635
0.005"	4519.6	17.301
0.006"	4456.1	16.818
0.008"	4490.6	17.080
0.015"	4526.7	17.355
0.025"	4457.7	16.830

During measurements, the number of observations used for noise spectrum calculation are: $m_1 = 5$ and $m_2 = 10$. Minor changes were found when the averages were taken at different m_1 and m_2 number of observations but is well within the experimental error. Using the center frequency of the transducer as a measure, the 0.004" thick sample is less than 5% of the wavelength $\lambda = 2.24 \text{ mm}$.

As shown in Figures 3 and 4 the response function is far from a δ -function series, however, one can clearly distinguish the peak positions. It is found that the response function becomes less sensitive as the thickness decreases. The peaks of the response function are sharper in the case of the 0.008" thick sample than in that of the 0.004" thick sample as shown in Figures 3 and 4. Using the 2 MHz transducer, the method reaches its limit at 0.003". All the peaks got smeared out when the sample becomes thinner than 0.002".

SUMMARY AND CONCLUSIONS

A data processing scheme is introduced here to extend the resolution of the ultrasonic pulse-echo method. Using the filtered response function and a 2 MHz broadband transducer, the sound velocity was measured for a set of brass samples and the thinnest sample is less than 5% λ of the center frequency. This result is very encouraging since the sub-wavelength resolution is the only way to resolve the intrinsic conflict of high resolution and deep penetration in ultrasonic technology. This technique may be used to study the bonding layer in composite structures and interfaces. Further extension of the method to higher frequencies and multi-layer structure is under investigation.

Acknowledgment

This research is sponsored by the Office of Naval Research under grant #N00014-96-1-1173.

References

- [1] Papadakis, E. P. (1976). "Ultrasonic Velocity and Attenuation: Measurement Methods with Scientific and Industrial Applications", in *Physical Acoustics Principles and Methods*, XII, Edited by W. P. Mason and R. N. Thurston (Academic, New York), 277-374.
- [2] Bolef, D. I. and Menes, M. (1960). "Measurement of Elastic Constants of RbBr, RbI, CsBr and CsI by an Ultrasonic C. W. Resonance Technique", *J. Appl. Phys.*, **31**, 1010-1017.
- [3] Mcskimin, H. L. (1961). "Pulse Superposition Method for Measuring the Velocity of Sound in Solids", *J. Acoust. Soc. Am.*, **33**, 12-16.
- [4] Cao, W. and Barsch, G. R. (1988). "Elastic Constants of KMnF₃ as Functions of Temperature and Pressure", *Phys. Rev. B*, **38**, 7947-7958.
- [5] Press, W. H., Flannery, B. P., Saul A., Teukolsky and Vetterling, W. T. (1986). in *Numerical Recipies*, University Press.
- [6] Cao, W. and Yuan, X. (1998). "A Signal Processing Scheme for Sound Velocity Measurement in Thin Samples", to be published.

APPENDIX 62

Analysis of shear modes in a piezoelectric vibrator

Wenwu Cao,^{a)} Shining Zhu,^{b)} and Bei Jiang

Materials Research Laboratory, The Pennsylvania State University, University Park, Pennsylvania 16802

(Received 31 October 1997; accepted for publication 5 January 1998)

A shear piezoelectric vibrator has been analyzed in detail. There are two types of shear motion associated with the same shear stain deformation. It is found experimentally that the lower frequency mode among the two has lower strength and its vibration amplitude continuously decreases as the long dimension of the vibrator increases. A nearly pure shear mode may be obtained with the aspect ratio greater than 20, but the influence of the other low frequency mode could not be totally eliminated even at such a large aspect ratio. We found that such phenomena can be understood by the conservation of angular momentum and the shared origin of these two types of shear motion. The ratio of the driving forces for these two types of shear motion is related directly to the aspect ratio of the vibrator. Formulas for calculating k_{15} from the resonant and antiresonant frequencies using both type of shear modes are given. © 1998 American Institute of Physics. [S0021-8979(98)02908-9]

I. INTRODUCTION

Piezoelectric materials have been widely used in various ultrasonic devices. One of the basic parameters used to describe the quality of piezoelectric materials is the electromechanical coupling factor, which is a measure of the effectiveness of electromechanical energy conversion. Accurately determining the shear coupling coefficient k_{15} is of practical importance for making shear transducers and for parameter input in theoretical modeling. It can also affect the accuracy of many derived material properties for a piezoelectric material.

In piezoceramics, such as lead zirconate-titanate (PZT), the symmetry is cm after poling, the shear coupling coefficient k_{15} can be related to the following material constants:

$$\epsilon_{11}^S = \epsilon_{11}^T (1 - k_{15}^2), \quad (1a)$$

$$d_{15} = k_{15} \sqrt{\epsilon_{11}^T \epsilon_{55}^E}, \quad (1b)$$

$$c_{55}^E = c_{55}^D (1 - k_{15}^2), \quad (1c)$$

where ϵ_{11}^S and ϵ_{11}^T are the clamped and free dielectric permittivities perpendicular to the poling direction, respectively. d_{15} is the shear piezoelectric constant, c_{55}^E and c_{55}^D are shear elastic stiffness constants under constant electric field and constant electric displacement, respectively.

This shear coupling coefficient k_{15} is usually measured using the thickness-shear resonance following the Institute of Electrical and Electronic Engineers (IEEE) standards.^{1,2} However, the measurement cannot be easily made with high accuracy due to the coupling of the thickness-shear mode with other unwanted modes. The coupling effect is usually more pronounced for the antiresonant frequency. For this reason, the method of using electrical resonance and the antiresonance to determine k_{15} is not recommended by the IRE

and IEEE standards.^{1,3} Instead, a dielectric measurement method was given according to Eq. (1a).^{3,4} It is easy to obtain the free permittivity ϵ_{11}^T value by measuring the capacitance at a low frequency (<1 kHz) which is well below the fundamental resonance, however, the clamped permittivity ϵ_{11}^S at very high frequencies is not easily accessible because of the influence of those mechanical resonances and/or their higher harmonics. Moreover, many piezoelectric ceramics also have fairly large capacitance relaxation which affects high frequency measurements.⁵

An alternative method to determine k_{15} is to measure values of the fundamental and overtone resonant frequencies instead of the fundamental resonant and antiresonant frequencies.^{6,7} The idea is that the unwanted modes have lower frequencies so that the influence becomes smaller for the overtones at high frequencies. Although this method is more convenient, experiments show that it gives lower values than those obtained by other techniques. In addition, if the aspect ratio of the vibrator is not large enough, the coupling effect will be extended to the overtones of the thickness-shear mode making this method invalid. Up to now, the reason for this shear mode to have such an unusual strong coupling was not fully understood.

More interestingly, the thickness-shear is *not* the lowest resonance of the structure recommended for the resonance technique, yet has the largest amplitude, which itself is a puzzle. Generally speaking, in most resonance structures, the lowest resonance usually has the largest amplitude. Our goal here is to find out the nature of this puzzle and to define quantitatively the required dimensions of the vibrator to perform a dependable measurement.

It is well known that the impedance-frequency characteristic of a vibrator used for determining k_{15} strongly depends on its geometry. However, the recommended ratios among the length l , width w , and thickness t are inconsistent in the literature. Experimentally, we could not obtain satisfactory results using some of those recommended dimensions.

^{a)}Electronic mail: wcao@sun01.mrl.psu.edu

^{b)}Permanent address: Physics Department, Nanjing University, Nanjing 210093, P. R. China.

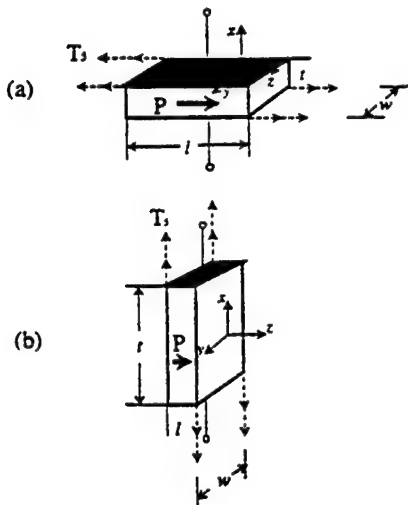


FIG. 1. (a) Thickness-shear vibrator. (b) Length-shear vibrator. The shaded areas are the electrodes and the dashed arrows represent the direction of displacement at given points. The polarization direction is indicated by an arrow on the front face of the sample.

Through detailed analysis, we have established the optimized dimensions for which the k_{15} value can be accurately determined using the resonance technique. More importantly, we have given an explanation to the cause of this strong mode coupling and the explained the amplitude relationship.

II. EXPERIMENTAL ANALYSIS OF THICKNESS-SHEAR VIBRATOR

For a thickness-shear mode piezoelectric ceramic vibrator under free boundary conditions, the following equation^{8,9} holds,

$$\tan \Xi = \frac{\Xi}{k_{15}^2}, \quad (2)$$

where $\Xi = \pi f_{nr} t / v^D$ is a normalized frequency, f_{nr} is the resonant frequency of the n th mode, t is the thickness of the vibrator, $v^D = \sqrt{c_{55}^D / p}$ is the stiffened shear velocity of the elastic wave. The ratio of an overtone to fundamental frequency f_{nr}/f_r versus value of k_{15} was tabulated in Ref. 6 according to Eq. (2). In principle, one could directly obtain the values of k_{15} for any given f_{nr}/f_r ratio using this table.

For a pure mode, Eq. (2) can also be converted to

$$k_{15} = \sqrt{\frac{\pi f_r}{2 f_a} \cot \frac{\pi f_r}{2 f_a}} = \sqrt{\frac{\pi f_r}{2 f_a} \tan \frac{\pi \Delta f}{2 f_a}}, \quad (3)$$

where f_r, f_a are the fundamental resonant and antiresonant frequencies, $\Delta f = f_a - f_r$ is the resonance bandwidth. Therefore, k_{15} may also be evaluated by measuring the fundamental resonant and antiresonant frequencies from the impedance spectrum if the mode can be decoupled from others.

In our experiments, the thickness-shear mode samples are made of PZT-5H piezoelectric ceramic purchased from Morgan Matroc Inc. The typical shape of the vibrators is a rectangular bar as shown in Fig. 1(a). For a thickness-shear mode vibrator, the polarization direction is along the longest

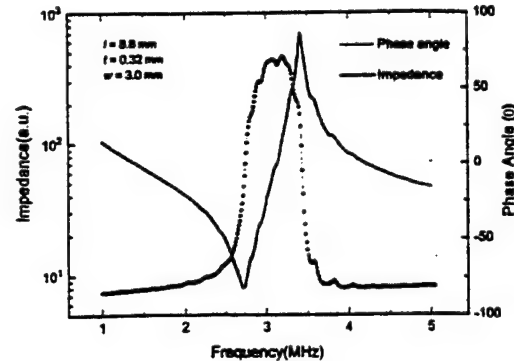


FIG. 2. Impedance-frequency spectrum of a typical thickness-shear vibrator.

dimension represented by l . The two major surfaces (top and bottom), which are parallel to each other and to the direction of polarization, were coated with gold or silver electrodes. When an AC voltage is applied across the electrodes, shear mechanical vibration can be excited in the vibrator through piezoelectric effect. Several samples with different dimensions were designed and fabricated. Considering that the dimensions, l and w , of the electrode surface are sufficiently larger than the thickness t and the relatively large permittivity of PZT-5H, edge effects of the parallel plate capacitor can be neglected in the computation of the internal electric field.

A HP-4194A impedance/gain-phase analyzer with computer interface was used for the impedance-frequency spectrum measurements. The electric field used was relatively low, typically in the range of 0.05–0.2 V/mm. The PZT samples are perfectly linear in this field range.

The impedance amplitude and phase spectra for a typical thickness-shear mode vibrator are shown in Fig. 2. This vibrator has the following dimensions: $l = 8.8$ mm, $w = 3.0$ mm, and $t = 0.32$ mm. The frequencies of the fundamental resonance and antiresonance are 2.70 MHz and 3.41 MHz, respectively. Using Eq. (3), one can easily calculate the shear electromechanical coupling coefficient to be: $k_{15} = 0.650$.

In all other vibrators used for measuring material parameters, such as the plates and bars for the measurement of k_1 , k_{33} , etc., mode coupling could be eliminated as long as the dimension corresponding to the desired fundamental mode is larger than four times of the other dimensions. It is very difficult, however, to obtain a clean thickness-shear mode. We found that the thickness-shear mode suffers mode coupling even when the aspect ratio l/t is more than 10. In order to find the origin of such an unusual behavior, a series of samples with the same thickness but different length were made and measured. Figure 3 shows the comparison of the impedance-frequency spectra of these samples near the thickness-shear resonance. The same spectra with wider frequency region are shown in Fig. 4 to demonstrate the overtone frequencies. Based on these measurements, k_{15} was calculated and the results are summarized in Table I.

Figures 3 and 4 show that the impedance-frequency spectra of the thickness-shear mode depends strongly on the ratio of l/t but nearly independent of the ratio l/w . Since these measured vibrator samples have identical thickness, the

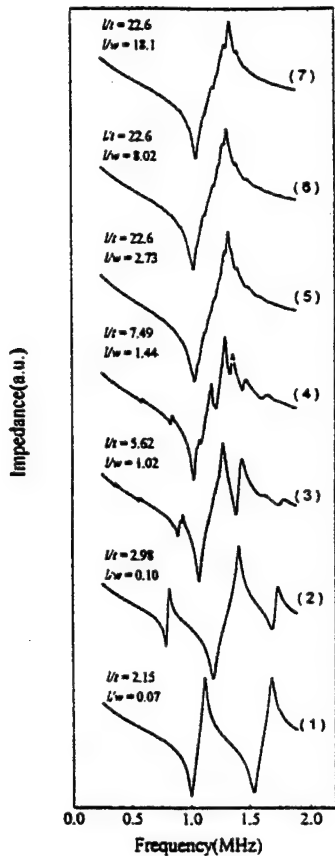


FIG. 3. Impedance-frequency characteristics near the fundamental resonance and antiresonance for thickness-shear vibrators of different aspect ratio.

above results imply that the interference mode is related to vibrator's length only. For a length to thickness ratio $l/t > 20$, although the mode is still not pure, the resonance and antiresonance frequencies can be accurately defined without any ambiguity. For the aspect ratio $l/t = 10-20$, coupling effects appear on the spectrum of the thickness-shear mode (see curve 4 in Fig. 3). However, the peaks are recognizable and k_{15} may still be determined from the minimum and maximum of the impedance curve without too much error. The mode coupling gets stronger as the ratio l/t decreases, no clearly defined thickness-shear mode can be found when the ratio $l/t < 5$. Apparently, this shear vibrator is much more demanding compared to the other types of vibrators for measuring k_1 and k_{33} , for which an aspect ratio of 4 is already sufficient to separate the modes.

In Fig. 3, curves 5-7 are for samples with identical length l and thickness t , but different width w . The three curves show that the width of the vibrator has little influence on the resonant and antiresonant frequencies if the l/t ratio is large enough. Once again, our experimental results point to the origin of the interference mode to be solely related to the sample length.

From Eq. (1c) the shear coupling coefficient k_{15} may also be determined from the ratio of the shear elastic constants under constant electric field and constant electric displacement, respectively. These elastic constants could be measured by using ultrasonic technique.^{10,11} Using the same

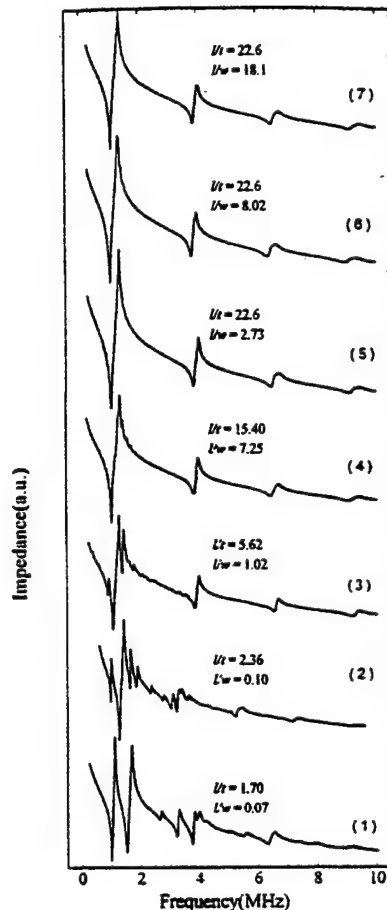


FIG. 4. Overtones for thickness-shear vibrators of different aspect ratio.

set of samples, we have measured the shear velocity with the displacement along and perpendicular to the poling direction (the wave vector is always perpendicular to the polarization), which give rise to the values for c_{35}^E and c_{35}^D , respectively. Since the ultrasonic measurements were performed at non-resonance conditions, there are no mode interference problems. The k_{15} value so obtained is geometry independent as long as the sample dimensions are not too small compared to the wavelength of the ultrasonic signal and the degree of poling is maintained the same. We have also developed a signal processing technique for measuring subwavelength thick samples so that accurate measurements on the elastic stiffness constants can be performed even for very small and thin samples.¹² The k_{15} value obtained by ultrasonic method is used as the standard to analyze the other results listed in Table I. It is found that for large l/t ratio samples, the k_{15} values obtained from the resonant and antiresonant frequencies are very close to the one obtained from the ultrasonic measurement. However, the k_{15} values calculated by using the ratio of overtone to fundamental frequencies are slightly smaller, which may due to the effects of frequency dispersion of the materials properties.

III. LENGTH-SHEAR MODE

From the above experimental analysis, the mode interference is related to the length dimension l . Looking more

TABLE I. Comparison of measured k_{15} values from different samples and different techniques.

Sample	Length l (mm)	Width w (mm)	Thickness t (mm)	$l:t$	$l:w$	Resonance f_r (MHz)	Anti-resonance f_a (MHz)	k_{15} (f_r/f_a)	k_{15} (Overtone)
1	1.43	20.17	0.84	1.70	0.07	1.54300	1.6880	0.441	
2	1.98	20.17	0.84	2.36	0.10	1.18300	1.4090	0.582	0.492
3	3.30	20.17	0.84	3.92	0.16	1.10790	1.3770	0.633	0.541
4	4.72	4.63	0.84	5.62	1.02	1.06780	1.2756	0.587	0.626
5	6.16	20.17	0.84	7.33	0.31	1.05210	1.2330	0.560	0.640
6	6.67	4.64	0.84	7.94	1.44	1.02550	1.2985	0.651	0.621
7	12.65	1.75	0.84	15.06	7.23	1.03157	1.3240	0.665	0.635
8	19.02	6.96	0.84	22.6	2.73	1.03530	1.3278	0.664	0.650
9	19.02	3.50	0.84	22.6	5.43	1.02875	1.3213	0.656	0.646
10	19.02	2.37	0.84	22.6	8.02	1.02875	1.3115	0.659	0.649
11	19.02	1.75	0.84	22.6	10.9	1.02875	1.3278	0.670	0.642
12	19.02	1.05	0.84	22.6	18.1	1.02963	1.3089	0.656	0.629
Ultrasonic	6.62	6.42	6.35					0.665	

carefully, one can find that another type of shear motion is also excited, which we call it the length-shear in contrast to the thickness-shear. In this mode, the displacement is perpendicular to the poling direction while in the thickness-shear, the displacement is parallel to the poling direction.

For a piezoelectric material, the origin of the driving force for the shear motion is an electric field induced shear strain, S_5 , which is related to the displacement components, u_1 and u_3 , in the following form:

$$S_5 = \left(\frac{\partial u_1}{\partial z} + \frac{\partial u_3}{\partial x} \right). \quad (4)$$

For the thickness-shear motion, the displacement u_3 is assumed to be zero for a long-bar shaped vibrator as shown in Fig. (1a). In this case, the shear strain is given by the first term of Eq. (4) only, and the resonance could be derived to have the form given by Eqs. (2) and (3). On the other hand, the length-shear mode, which gives rise to the same shear strain was ignored in the derivation of the formula. Due to the symmetric nature of the two shear displacement derivatives in Eq. (4), we could imagine a situation in which the thickness-shear mode may be ignored if the dimensions are designed properly. The impedance formula for this mode can be easily derived if we assume the displacement $u_1 = 0$. In this case, the shear strain is only related to the second term of Eq. (4). Using the dynamical equation and the following constitutive relations:

$$S_5 = s_{55}^E T_5 + d_{15} E_1, \quad (5a)$$

$$D_1 = d_{15} T_5 + \epsilon_{11}^T E_1, \quad (5b)$$

one can derive another relationship parallel to Eq. (2) for the length-shear mode:

$$\tan \Xi' = \left(\frac{k_{15}^2 - 1}{k_{15}^2} \right) \Xi', \quad (6)$$

where $\Xi' = (\pi f_{n_a}^r l) / v^E$ is a normalized frequency, $f_{n_a}^r$ is the antiresonant frequency in the n th mode, l is the length of the vibrator, $v^E = 1 / \sqrt{p s_{55}^E}$ is the compliance velocity of the elastic wave. In Eq. (5), s_{55}^E is the shear elastic compliance at

constant electric field, d_{15} is the piezoelectric strain constant, and ϵ_{11}^T is the dielectric permittivity at constant stress.

Using Eq. (6) and considering the fundamental resonance and antiresonance, we can get another k_{15} formula for the length-shear mode:

$$k_{15} = \frac{1}{\sqrt{1 - \frac{\tan \left(\frac{\pi f_a'}{2 f_r'} \right)}{\frac{\pi f_a'}{2 f_r'}}}} \quad (7)$$

where f_a' , f_r' are the fundamental resonant and antiresonant frequencies of the length-shear mode.

In order to verify this analysis we have made a sequence of samples with the $l:t$ ratio from 1:22 to 22:1. Here l is always the dimension along the poling direction although it may become the shorter one. Figure 5 shows the dependence of the impedance on frequency for two different aspect ratio vibrators. A nearly pure length-shear mode can be obtained when $l:t < 1/20$, which is analogous to the thickness-shear case of $l:t > 20$. The curves in Fig. 5(b) correspond to the ratio of $t:l = 27$. The shear coupling coefficient k_{15} ($= 0.650$) can be obtained using Eq. (7), which is the same as the k_{15} values measured by the nearly pure thickness-shear mode and ultrasonic method (see Table I). From this study, we concluded that the tangled modes in the shear vibrator are the thickness-shear and the length-shear modes. The fundamental reason of why it is so difficult to get rid of the mode coupling in the shear resonator is because the two shear modes share the same electric field induced shear strain. The higher harmonics of the lower frequency mode appear to decorate the higher frequency mode on the impedance spectrum.

IV. CONSERVATION OF ANGULAR MOMENTUM

For the recommended geometry in the literature, the shear vibrator is usually made with the $l:t \gg 1$. Therefore, the

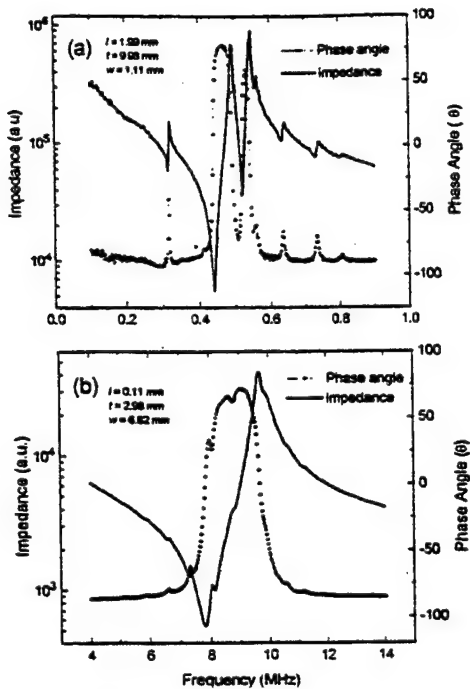


FIG. 5. Impedance spectrum of a length-shear vibrator with different geometry. (a) The ratio of $l/t=0.2$. (b) The ratio of $l/t=0.04$.

length-shear mode should be the lowest frequency mode according to the analysis above. However, experimental results show that the shear mode in the long dimension is much weaker than the shear mode in the shorter dimension. This fact is also true for the case of $l/t \ll 1$ as shown in Fig. 5. In other words, the higher frequency mode is much stronger than the lower frequency mode in the shear vibrator. This result is unusual since in most of the cases, lower frequency mode is stronger than higher frequency ones. There is no explanation in the literature for this unusual phenomenon.

Through careful analysis, we conclude that the origin of such a behavior comes from the fact that the shear deformation involves rotation but the electric drive does not provide angular moment since it is due to self-induced shear strain. Therefore, both shear motions should be involved to balance the angular momentum of the whole vibrator.

Let us look at the two special situations shown in Figs. 6(a) and 6(b) assuming only one of the modes is being excited. Figure 6(a) represents the thickness-shear mode for which the center plane along the thickness direction remains still according to symmetry. Therefore, we may analyze the upper half of the vibrator and assume a fixed boundary at the bottom. Similarly, we can analyze the length-shear mode as shown in Fig. 6(b). According to Eq. (4), the two shear displacements are connected to the same shear deformation S_5 , which was driven by the external electric field through piezoelectric effect. It is clear that both types of shear motions involve rotation and hence, the angular momentum will not be conserved if only one type of shear motion is excited. This is the intrinsic reason for the strong mode coupling observed in the shear vibrators.

According to the symmetry of the vibrator, to conserve the angular momentum of the system, the shear deformation

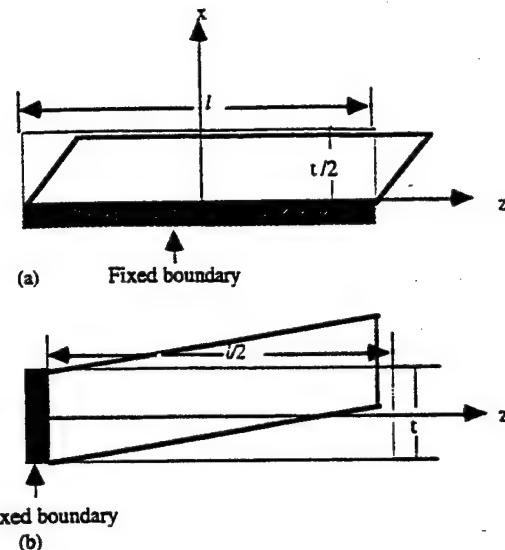


FIG. 6. Illustration of the two shear modes: (a) Thickness shear; (b) length shear. The angular momentum is not conserved in either case.

should proceed to expand along one of the diagonal direction and contract along the other as shown in Fig. 7. Therefore, the ratio of the maximum displacements for the two types of shear motion can be easily found to be

$$\frac{u_{1 \max}}{u_{3 \max}} = \frac{l}{t}. \quad (8)$$

Equation (8) can also be used to derive the ratio of the mechanical driving force for the two types of shear motion. There are three conclusions that can be drawn from the above analysis.

- (1) The mode corresponding to the shear motion along the longer dimension is always stronger than the one along the shorter dimension. The amplitude ratio between the displacements in the two directions is proportional to the ratio of their corresponding dimensions.
- (2) The two types of shear displacements will always occur in a paired fashion to conserve the angular momentum. However, the lower frequency mode can be weakened through the increase of the longer dimension.
- (3) These two shear motions are equivalent, their relative strength can be adjusted by the aspect ratio of the two relevant dimensions. Either mode could be used to measure the material properties by proper design of the vibrator dimensions to suppress the other one.

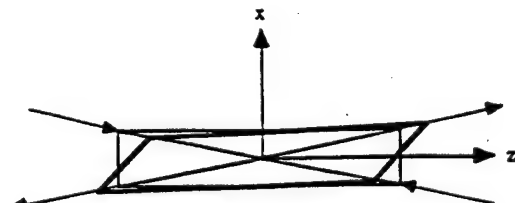


FIG. 7. The shear deformation which conserves the angular momentum. The two diagonal lines have no rotation during the shear deformation and the ratio of the two shear displacements is l/t .

The first conclusion explains the experimentally observed phenomena of weaker lower frequency mode and stronger high frequency mode because the amplitude of motion reflects the strength of the driving force, while the second conclusion can be verified from the results shown in Figs. 3 and 5. The frequency spectrum is still not smooth in the vicinity of the desired resonance even for an aspect ratio of larger than 22. The third conclusion has been verified experimentally as shown in Fig. 5(b) and Table I.

V. CONCLUSION

Our experimental results and theoretical analysis proved that the interference in the thickness-shear vibrator comes from the length-shear mode. The frequency of the length-shear mode depends on the length while its intensity is controlled by the length to thickness ratio l/t . With the increase of the l/t ratio, the length-shear mode can be weakened but could not be eliminated. Experimentally, we found that when $l/t \geq 20$, a relatively clean thickness-shear mode may be obtained. Therefore, this ratio should be used to define the dimensions if one wants to use the resonance technique to measure k_{15} . In the aspect ratio range of $10 < l/t < 20$, the impedance-frequency spectrum near the thickness-shear mode is slightly obscured by the length-shear mode. However, the resonant and antiresonant frequencies of the thickness-shear mode are still clearly shown on the spectrum and the k_{15} value calculated from the minimum and the maximum frequencies is still acceptable. When the ratio $l/t < 10$, the resonance method is not valid to determine k_{15} (see Table I).

From our experimental results, the width variation of the vibrator has no obvious influence to the spectrum of the thickness-shear mode. The effect of changing the width is only on the total capacitance which may have some influence on the precision of the effective digit in the measured values. It is recommended that the width should be at least twice as much as the thickness to reduce the edge effect of the plate capacitor.

The length-shear mode is a "twin" of the thickness-shear mode since they both share the same shear strain. We

found that k_{15} may also be measured accurately using this mode if the aspect ratio $l/t > 20$, which mirrors the situation for the thickness-shear mode. However, owing to the fact that the electrodes of the length-shear vibrator are coated on a pair of minor surfaces and the relatively large distance between the two electrodes, the measurement is more difficult than using the thickness-shear mode. The plate capacitance approximation is less accurate for the length-shear vibrator due to some degree of edge effects. This, however, was not a problem for the PZT ceramic samples we used in our experiment since the relative dielectric constant is over 1300.

Using the idea of angular momentum conservation, we have shown that the ratio of the driving forces for the thickness-shear and the length-shear is roughly proportional to l/t . This explains the fact that the lower frequency mode has much smaller amplitude than that of the high frequency one. One could arbitrarily reduce the mode interference by increasing the aspect ratio, but the influence of the lower frequency mode will always exist due to the same excitation source and the conservation of angular momentum.

ACKNOWLEDGMENTS

This research is sponsored by the Ben Franklin Partnership of Pennsylvania and the Office of Naval Research.

- ¹IRE Standard on Piezoelectric Crystal 1958. Proc. IRE 46, 764 (1958).
- ²B. Jaffe, W. R. Cook, and H. Jaffe, *Piezoelectric Ceramics* (Academic, New York, 1971).
- ³IEEE Standard on Piezoelectricity, ANSI/IEEE Std. 176-1978, New IEEE (1978).
- ⁴Proc. IRE 49, 1161 (1961).
- ⁵I. Ikeda, Fundamentals of Piezoelectricity (unpublished).
- ⁶M. Onoe, H. F. Tiersten, and A. H. Meitzler, J. Acoust. Soc. Am. 35, 36 (1963).
- ⁷H. F. Tiersten, J. Acoust. Soc. Am. 35, 53 (1963).
- ⁸A. W. Lawson, Phys. Rev. 62, 71 (1942).
- ⁹W. P. Mason and H. Jaffe, Proc. IRE 42, 921 (1952).
- ¹⁰H. J. McSkimin, J. Acoust. Soc. Am. 33, 12 (1961).
- ¹¹W. Cao and G. R. Barsch, Phys. Rev. B 12, 7947 (1988).
- ¹²W. Cao and X. Yuan (unpublished).

**MODELING
and
CHARACTERIZATION**

Relaxor Ferroelectrics

APPENDIX 63

VARIABLE STRUCTURAL ORDERING IN LEAD SCANDIUM TANTALATE-LEAD TITANATE MATERIALS

J. R. GINIEWICZ, A. S. BHALLA and L. E. CROSS*

*Materials Research Laboratory, The Pennsylvania State University,
University Park, Pennsylvania 16802 USA*

(Received 3 February 1997)

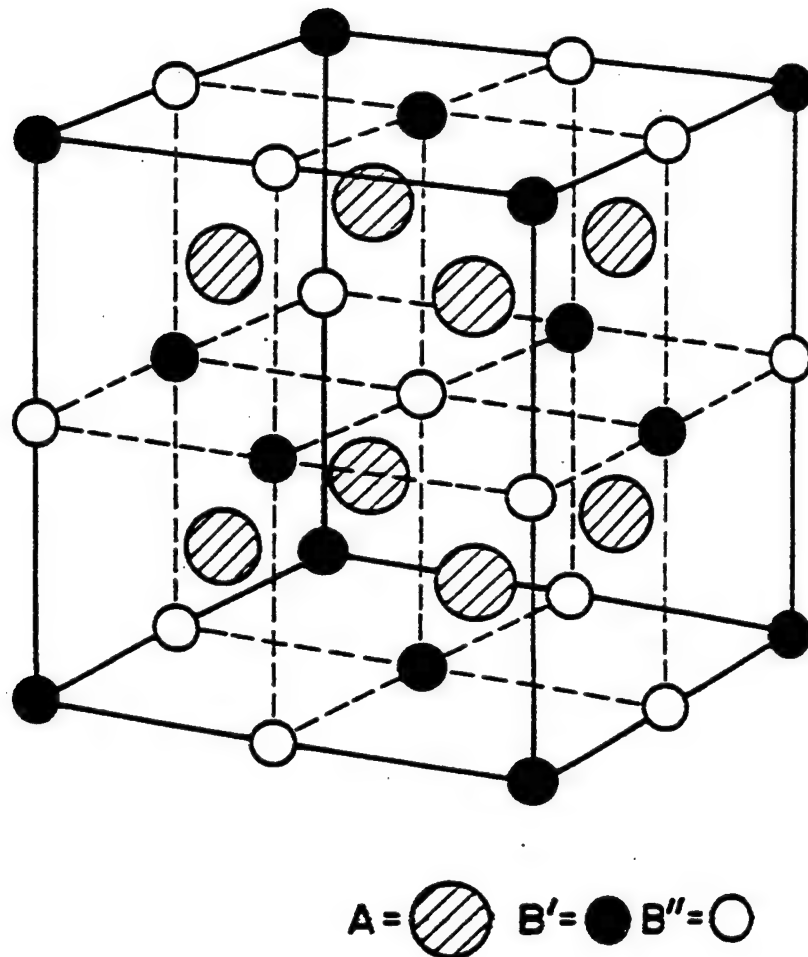
A phase region of variable order-disorder [VOD] has been identified in this study for compositions in the range [$x = 0.0-0.075$] (x : mole fraction PbTiO_3). Materials from this region retain some degree of long-range ordering of B -site cations as evidenced by x-ray and electron diffraction which is enhanced with post-sintering annealing. Annealed ceramics exhibit sharp dielectric responses [$K(T)$] and near-normal first-order ferroelectric behavior while as-fired specimens with lesser degrees of long-range ordering show the more diffuse and dispersive characteristics of a relaxor ferroelectric.

Keywords: Lead Scandium Tantalate; relaxors; ferroelectric properties

1. INTRODUCTION

The compound $\text{Pb}(\text{Sc}_{1/2}\text{Ta}_{1/2})\text{O}_3$ is a complex perovskite of the type $[A^{2+}(B_{1/2}^{3+}B_{1/2}^{5+})\text{O}_3]$. The difference in the ionic radii of the B ions [0.105 Å] and the charge difference between the two are sufficient to allow for an ordered structure and $\text{Pb}(\text{Sc}_{1/2}\text{Ta}_{1/2})\text{O}_3$ may exist in ordered states ranging from a nearly complete random distribution of B ions to nearly perfect ordering of B' and B'' in alternating planes along $\langle 111 \rangle$. The ordered structure has a double unit cell of the $(\text{NH}_4)_3\text{FeF}_6$ -type pictured in Figure 1 which consists of eight basic perovskite units. The unit cell of the superstructure is face-centered with space group $\text{Fm}3\text{m}$ in the cubic (paraelectric) phase. The ordered low-temperature (ferroelectric) phase has

*Corresponding author.

FIGURE 1 The ordered $(\text{NH}_4)_2\text{FeF}_6$ Structure.

been determined to be rhombohedral with a subcell lattice parameter of 4.072 \AA and $\alpha = 89.82^\circ$ ^[1]. The order-disorder temperature of $\text{Pb}(\text{Sc}_{1/2}\text{Ta}_{1/2})\text{O}_3$ has been reported to be $T_{OD} \approx 1470^\circ\text{C}$ ^[1, 2] and specimens with various degrees of long-range order may be produced either by quenching from temperatures above or near T_{OD} , to generate disorder in the compounds, or by annealing at elevated temperatures below T_{OD} so as to induce ordering of the B -site cations. The optimum annealing temperature range for $\text{Pb}(\text{Sc}_{1/2}\text{Ta}_{1/2})\text{O}_3$ ceramics has been determined to be $[1000 - 1100^\circ\text{C}]$ and, with the maintenance of the proper PbO atmosphere, a high degree of long-range ordering is attained in relatively short annealing periods.^[3]

The dielectric response in the radio frequency range of $\text{Pb}(\text{Sc}_{1/2}\text{Ta}_{1/2})\text{O}_3$ materials is observed to vary significantly with the degree of long-range order.^[1, 3] The temperature of the dielectric permittivity maximum ranges from $\approx -5^\circ\text{C}$ to 25°C depending upon the degree of order, with the higher transition temperatures occurring for the more highly ordered compounds.^[1, 3] In particular, there is observed a marked increase in the magnitude of $K(\text{max})$ and an overall broadening of $K(T)$ in the vicinity of the transition as shown in Figure 2b. A clear trend towards more diffuse and dispersive relaxor-type behavior occurs with decreasing long-range ordering [Figs. 3(a, b)]. The pyroelectric response of $\text{Pb}(\text{Sc}_{1/2}\text{Ta}_{1/2})\text{O}_3$ further reflects the effect long-range ordering has on the temperature dependence of the spontaneous polarization. The pyroelectric coefficients for two $\text{Pb}(\text{Sc}_{1/2}\text{Ta}_{1/2})\text{O}_3$ specimens are pictured in Figures 4(a, b). The pyroelectric coefficient peak for the highly ordered sample [Figure 4(b)] is observed to be relatively sharp while the pyroelectric peak for the more disordered sample pictured in Figure 4(a) exhibits double pyroelectric coefficient peaks. The occurrence of double pyroelectric peaks has been observed for some partially ordered $\text{Pb}(\text{Sc}_{1/2}\text{Ta}_{1/2})\text{O}_3$ materials.^[4-7] A pyroelectric doublet was reported for a partially ordered single crystal specimen.^[4, 5] transmission electron microscopy [TEM] of this specimen revealed a bimodal distribution of ordered domains consisting of ordered regions $\approx 1500\text{ \AA}$ in diameter and considerably larger ordered areas 100–1000 times the size of the smaller regions.^[4, 5]

Highly ordered $\text{Pb}(\text{Sc}_{1/2}\text{Ta}_{1/2})\text{O}_3$ has been shown to be a first-order ferroelectric by means of both dielectric and thermal measurements.^[3, 8] A latent heat effect is observed for all partially ordered and highly ordered $\text{Pb}(\text{Sc}_{1/2}\text{Ta}_{1/2})\text{O}_3$ materials which is enhanced as the degree of order is increased.^[1, 3] This is manifested in a marked increase in the magnitude and an overall narrowing of the specific heat anomaly at the transition.

A variety of versatile and interesting materials may be derived from the $(1-x)\text{Pb}(\text{Sc}_{1/2}\text{Ta}_{1/2})\text{O}_3-(x)\text{PbTiO}_3$ solid solution system. Previous investigation of this system^[9, 10] has shown that complete solid solution occurs across the entire compositional range and a morphotropic phase boundary [MPB] has been identified between rhombohedral and tetragonal phase regions over the composition range $[x = 0.4 - 0.45]$. It is anticipated for this system that some variable structural ordering such as occurs for pure $\text{Pb}(\text{Sc}_{1/2}\text{Ta}_{1/2})\text{O}_3$ will persist for compositions of low x . Assuming that the introduction of Ti^{4+} into the structure serves largely to disrupt the coherence length of long-range ordering^{*} rather than leading to a situation

^{*}The coherence length is defined in terms of the size of order domains as determined by TEM.
^[11] Short coherence length long-range order: ($20 - 800\text{ \AA}$). Long coherence length long-range order: ($> 1000\text{ \AA}$).

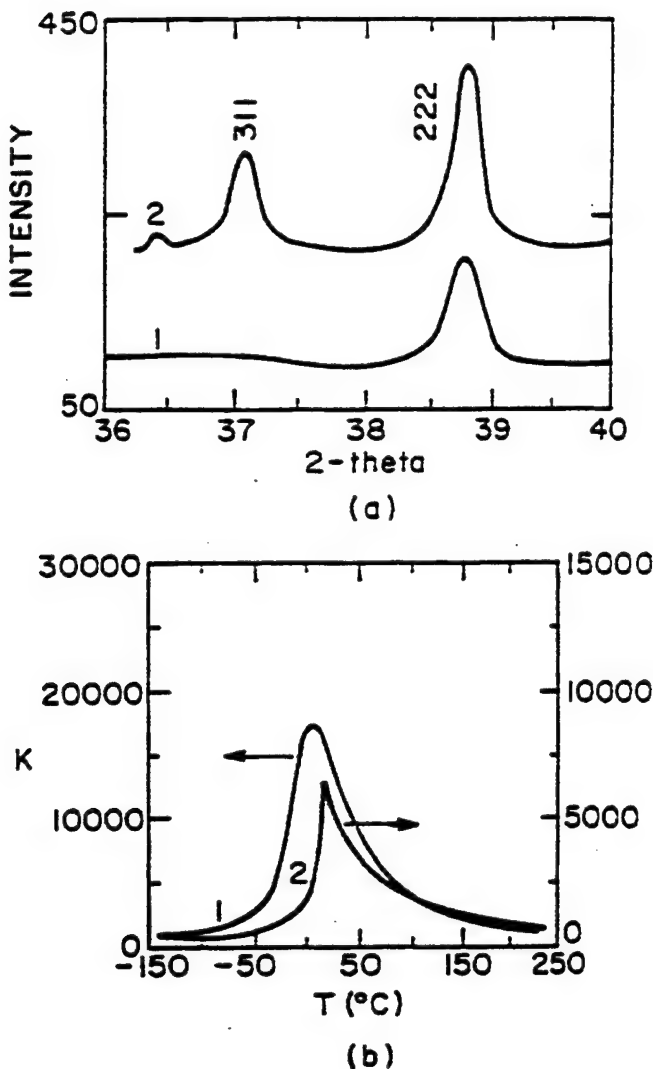


FIGURE 2 As-Fired [1] and Annealed [2] $\text{Pb}(\text{Sc}_{1/2}\text{Ta}_{1/2})\text{O}_3$ ceramics. (a) The 311/222 x-ray diffraction pair and (b) the dielectric constant as a function of temperature at 1 KHz.

where the Ti ion incorporates itself into some new ordered phase, it is expected that at some concentration of x the variable long-range ordering will disappear. Materials which do possess this particular structural characteristic are, therefore, expected to respond to high-temperature annealing in a manner similar to that of pure $\text{Pb}(\text{Sc}_{1/2}\text{Ta}_{1/2})\text{O}_3$ materials. The existence and nature of the positional ordering in these materials will be

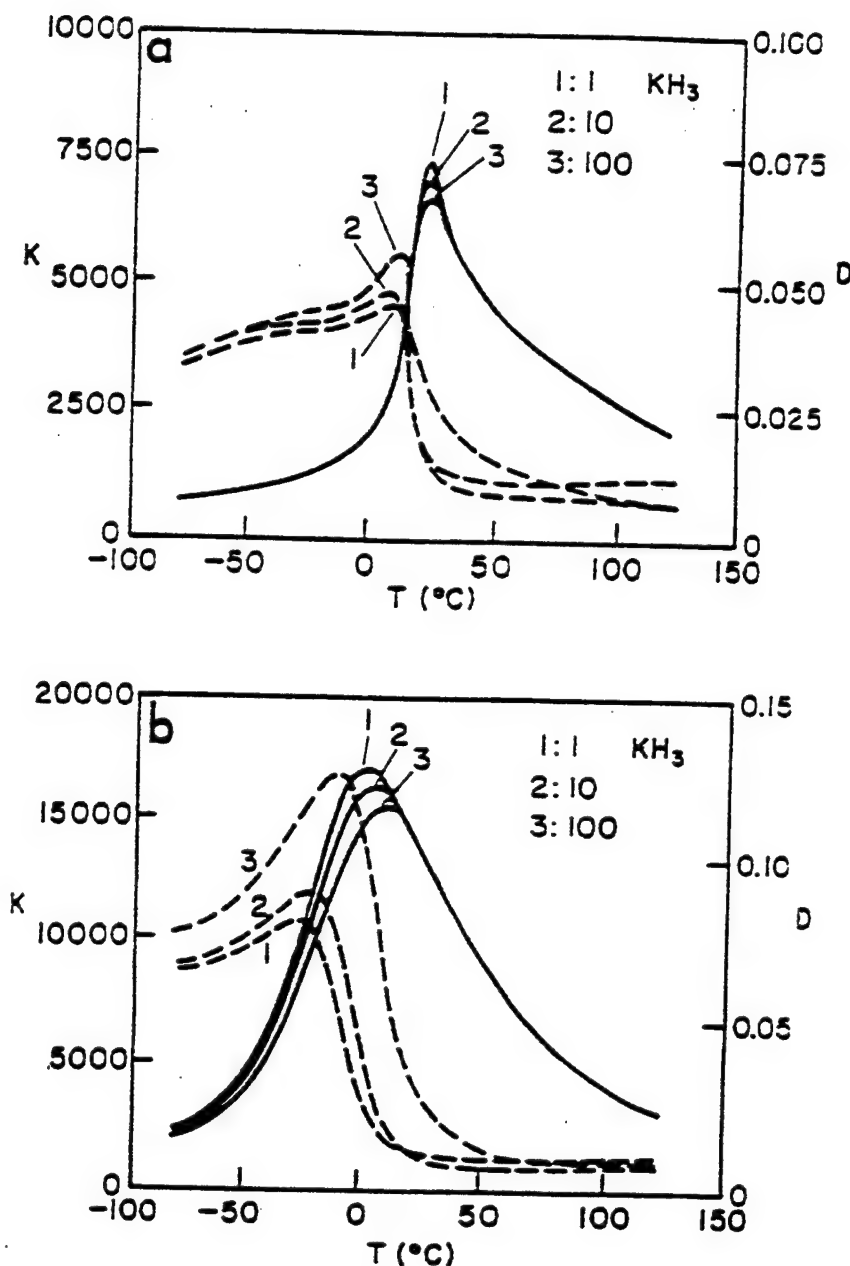


FIGURE 3 The dielectric constant and loss of $\text{Pb}(\text{Sc}_{1/2}\text{Ta}_{1/2})\text{O}_3$ as a function of temperature and frequency [7]. (a) $S = 0.87$ and (b) $S = 0.4$. (see Section III for definition of S)

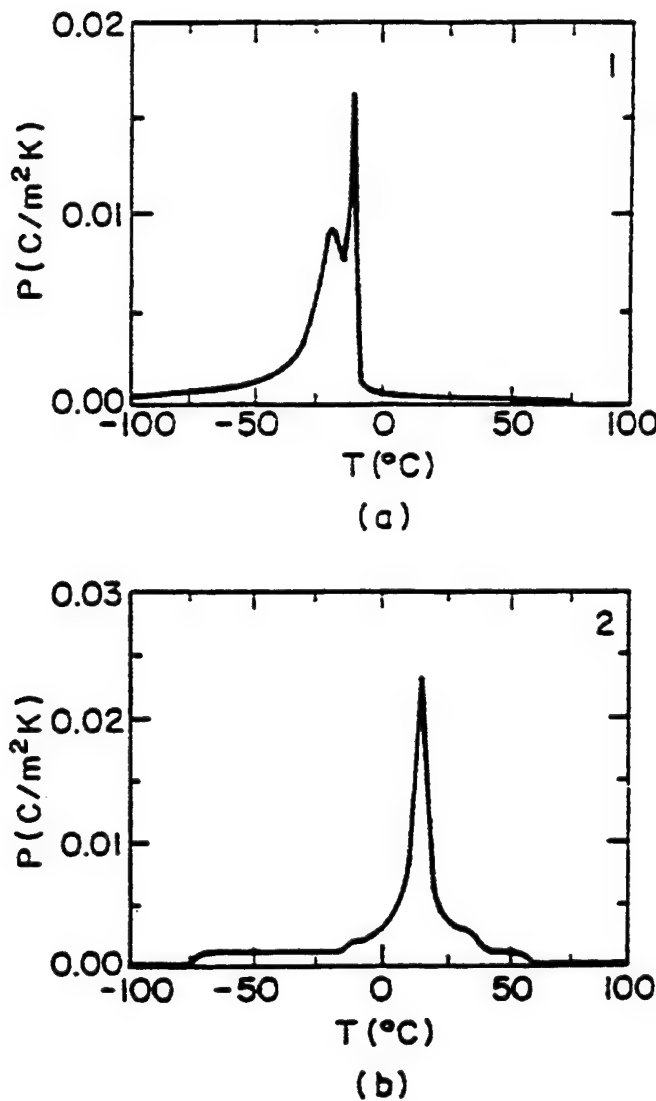


FIGURE 4 The pyroelectric coefficient for $Pb(Sc_{1/2}Ta_{1/2})O_3$ (a) As-Fired and (b) Annealed ceramics.

manifested, as for unmodified $Pb(Sc_{1/2}Ta_{1/2})O_3$, in the X-ray diffraction patterns, the dielectric and pyroelectric responses, and the specific heat characteristics of the specimens. The compositional range between these "orderable" compositions, which may possess varying degrees of long-range

order, and those which likely have an invariable, short coherence length long-range order* essentially constitute a second structural phase boundary. Examination of this variable order-disorder [VOD] region was carried out by means of x-ray diffraction, dielectric and pyroelectric measurements, and thermal analysis.

2. SAMPLE PREPARATION

The $(1-x)\text{Pb}(\text{Sc}_{1/2}\text{Ta}_{1/2})\text{O}_3-(x)\text{PbTiO}_3$ ceramics were produced by a conventional mixed-oxide method involving the use of high-purity starting compounds, a precursor-phase formulation, and controlled lead atmosphere sintering. The compositions of interest were initially prepared as powders employing a wolframite $[\text{ScTaO}_4]$ ^[1,2] precursor method^[1,3] in order to reduce the occurrence of undesirable pyrochlore phases. Starting oxides Sc_2O_3 [†] and Ta_2O_5 [†] were batched and calcined at 1400°C for 6–8 hours to form the ScTaO_4 precursor. Compositions in the range $[x \leq 0.1]$ were then formulated from PbO^\dagger , TiO_2^\dagger , and the precursor phase. Each composition was calcined at 900°C for 4 hours and at 1000°C for 1 hour with an intermediate comminution step. Compacted specimens of compositions were then subjected to firing at 1400°C for 1 hour within sealed alumina crucibles containing $\text{Pb}(\text{Sc}_{1/2}\text{Ta}_{1/2})\text{O}_3/\text{PbZrO}_3$ source powders. The specimens were then subjected to a second higher temperature sintering [1500 – 1560°C , 20 minutes] which was conducted in a molybdenum tube furnace with a relatively rapid heating and cooling schedule to avoid excessive lead-loss. The samples were 90–95% theoretical density following this second-stage sintering step. Specimens of each composition were annealed at 1000°C for 10 hours in a sealed system with a controlled lead atmosphere in order to induce structural ordering.

Specimens for X-ray diffraction, dielectric, and pyroelectric investigation were cut as plates from the sintered disks typically [0.4 cm] on edge and [0.025–0.03 cm] in thickness. The electrode surfaces were ground with 12 μm Al_2O_3 , cleaned, and sputtered with gold. Silver contact points were subsequently applied to the gold sputtered surfaces.

*See footnote on Page 283.

[†] Sc_2O_3 [Boulder Scientific Co. -99.99%]; Ta_2O_5 [Hermann C. Starck (Berlin) -Stand. Opt. Grade]; PbO [Johnson Matthey-Materials Technology UK-Grade A1]; TiO_2 [Aesar (Johnson Matthey Inc.) -99.999%].

The samples prepared for thermal analysis were all sintered at 1400°C for 1 hour and ground to a powder for measurement. The powder samples, typically 80–100 mg in size, were sealed in aluminum pans.

3. EXPERIMENTAL PROCEDURE

The degree of long-range order in the $(1-x)\text{Pb}(\text{Sc}_{1/2}\text{Ta}_{1/2})\text{O}_3-(x)\text{PbTiO}_3$ specimens was determined by x-ray diffraction using a Scintag [PADV] automated diffractometer. $\text{CuK}\alpha$ radiation was employed. The degree of structural ordering was evaluated by means of the long-range order parameter, S , which is defined in terms of the relative intensities of the superlattice and normal lattice reflections as:

$$S^2 = \left[\frac{I_{\text{super}}}{I_{\text{Normal}}} \right]_{\text{OBS}} \left[\frac{I_{\text{Normal}}}{I_{\text{Super}}} \right]_{\text{CALC}} \quad (1)$$

where the superlattice/normal reflection pairs employed are 111/200 and 311/222.^[1, 3, 8] The long-range order parameter, S , describes of B' and B'' ions on the B -site of $\text{Pb}(\text{B}'_{1/2}\text{B}''_{1/2})\text{O}_3$ as expressed by:

$$S = \frac{n - F_{B'}}{1 - F_{B'}} \quad (2)$$

where $F_{B'}$ is the fraction of B' ions in the compound and n is the fraction of the B' sites actually occupied by a B' ion. This expression reduces to:

$$S = 2n - 1 \quad (3)$$

for a 1:1 arrangement of B -site cations. A completely ordered arrangement of ions has $S=1$ while a completely disordered arrangement is denoted by $S=0$. The calculated ratio in Equation (1) has been determined for the completely ordered condition [$S=1$] and has, for $\text{Pb}(\text{Sc}_{1/2}\text{Ta}_{1/2})\text{O}_3$, values 1.33 and 0.59 for the 111/200 and 311/222 pairs respectively.^[1] The 311/222 pair (Fig. 2a) was used in this investigation to evaluate the degree of long-range order present for the $(1-x)\text{Pb}(\text{Sc}_{1/2}\text{Ta}_{1/2})\text{O}_3-(x)\text{PbTiO}_3$ materials.

Assuming that the ordering that occurs for these specimens is essentially a 1:1 ordering of Sc^{3+} and Ta^{5+} on the B -site interrupted by the presence of Ti^{4+} , the long-range order parameter as defined above may still be applied to evaluate the degree of long-range ordering present. The result of the present study tend to support this assumption; however, it is acknowledged

that a more thorough investigation is required to verify the actual position of the Ti ions in the structure and, in the event that some type of ordering occurs in which the Ti ion itself is incorporated, that the long-range order parameter must be redefined in order to accurately quantify the degree of long-range ordering that exists. In the light of these considerations, however, it should still be feasible to monitor the devolution of the variable structural ordering with composition in terms of the long-range order parameter, S , as defined so as to provide some gauge by which to assess the relative degree of ordering present throughout the compositional range of interest.

The dielectric constant, K , and dissipation factor, D , were measured as a function of temperature and frequency using an automated system consisting of an oven [Model 2300, Delta Design, Inc.], an LCR meter [Model 4274A, Hewlett Packard, Inc.], and a digital multimeter interfaced with a desk top computer [Model 9816, Hewlett Packard, Inc.]. Dielectric runs were made at 1 KHz over a temperature range of [-150-260°C].

The pyroelectric response was measured by a modified Byer-Roundy^[14] method. The specimens were initially poled in air within a temperature chamber [Model 2300, Delta Design, Inc.] in the vicinity of the transition temperature under a poling field of [20 (KV/cm)] for 15 minutes and cooled with the field applied to $\approx -100^{\circ}\text{C}$. The poling field was then removed. A desk top computer [Model 9816, Hewlett Packard, Inc.] was used to record the pyroelectric current data collected by the picoammeter [Model 4140B, Hewlett Packard, Inc.]. The pyroelectric coefficients were subsequently calculated from the pyroelectric current data.

Thermal analysis was conducted by means of differential scanning calorimetry [Model DSC-2, Perkin Elmer]. The specific heat, $C_p(T)$, was determined by referring the thermal curve of the specimen to that of a similarly contained sapphire standard.

4. RESULTS AND DISCUSSION

A series of sample was assembled comprised of as-fired and annealed specimens of compositions [$x = 0.025, 0.05, 0.075$ and 0.1]. The x-ray diffraction peaks appearing in the 2θ range [34-42°] are pictured in Figure 5(a-d). The as-fired specimens [1], for all compositions, exhibit only the fundamental reflection 222, with, at most, only a very subtle increase in intensity in the vicinity of the 2θ range over which the superlattice reflection,

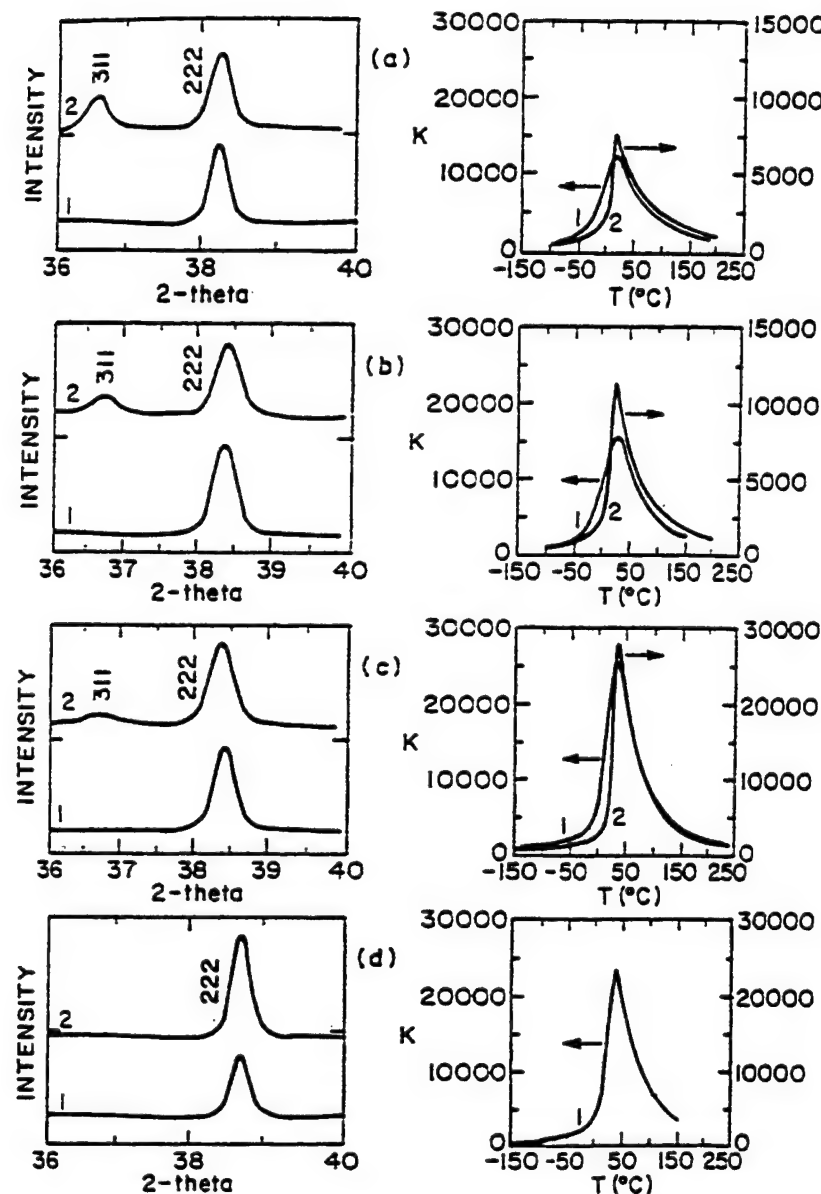


FIGURE 5 The 311/222 X-ray diffraction pair and 1 KHz $K(T)$ response of As-Fired [1] and Annealed [2] $(1-x)\text{Pb}(\text{Sc}_{1-x}\text{Ta}_{1-x})\text{O}_3-(x)\text{PbTiO}_3$ ceramics: (a) $x=0.025$, (b) $x=0.05$, (c) $x=0.075$, and (d) $x=0.1$.

311, should appear. The 311 reflection does appear for annealed specimens [2], however, decreasing in magnitude with increasing x up to $[x=0.1]$ for which no superlattice reflection is observed. The S parameters evaluated for the annealed specimens are plotted as a function of composition over the range $[x=0-0.1]$ in Figure 6. The degree of long-range ordering present for these specimens is seen to decrease steadily up to $[x=0.1]$ where long-range ordering is no longer detectable by x-ray diffraction.

Dielectric data collected at 1 KHz are given in Table I and the dielectric constant is shown as a function of temperature [1 KHz] in Figure 5(a-d) for as-fired [1] and annealed [2] specimens. A marked sharpening of the dielectric constant peak with annealing is observed for all compositions $[x \leq 0.075]$ similar to what is typically observed for pure $\text{Pb}(\text{Sc}_{1/2}\text{Ta}_{1/2})\text{O}_3$, where a very sharp peak indicates a highly ordered state and the normal ferroelectric behavior generally associated with such a specimen. The development of a more normal ferroelectric response upon annealing is also evident for the $[x \leq 0.075]$ specimens in the marked decrease of the temperature interval between the dielectric constant and the dielectric loss

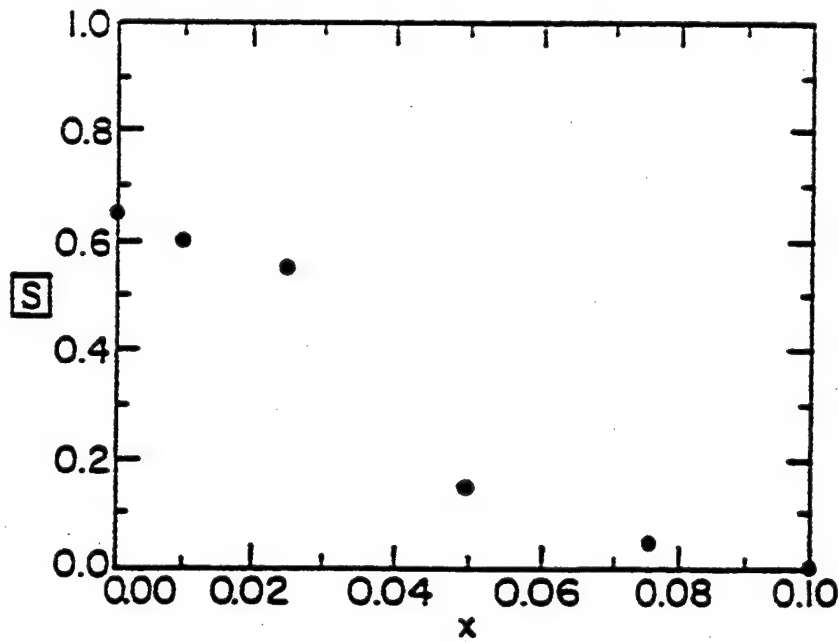


FIGURE 6 The S parameters evaluated for annealed specimens $[x=0-0.1]$.

TABLE I Dielectric data for As-Fired [1] and Annealed [2] VOD compositions [$x=0-0.1$]

x	†	$K(\max)$	$T^{\circ}\text{C}$	$D/\max)$	$T^{\circ}\text{C}$	$\delta^{\circ}\text{C}$	$\Delta T(\max)$
0.0	1	17700	5	0.08	-12	35	17
0.0	2	6400	20	0.05	9		11
0.025	1	11000	18	0.07	-25	40	42
0.025	2	7400	18	0.05	4		14
0.05	1	14600	25	0.06	-20	35	42
0.05	2	11300	25	0.07	10		14
0.075	1	26300	35	0.07	15	35	16
0.075	2	27600	35	0.06	25		11
0.1	1	22900	38	0.07	25	35	13

†: 1. As-Fired 2: Annealed

δ: Defined according to the relationship^[13]: $[(1/K) - (1, K_{\max})] = (T - T_{\max})^2/(2K_{\max}\delta^2)$ $\Delta T(\max)$: difference between the temperatures of the dielectric constant and dielectric loss maxima

maxima [$\Delta T(\max)$] (Tab. I). A strong frequency dependence of both the dielectric constant and the dielectric loss for all as-fired specimens, similar to that pictured in Figure 3b for the pure $\text{Pb}(\text{Sc}_{1/2}\text{Ta}_{1/2})\text{O}_3$ material with a low degree of structural ordering, was observed over the frequency range considered in this study.

Typical of pure $\text{Pb}(\text{Sc}_{1/2}\text{Ta}_{1/2})\text{O}_3$ is a decrease in the dielectric constant maximum upon ordering [Fig. 2b]. This tendency is also observed for the modified compositions with the difference between the maxima of as-fired and annealed specimens at a given composition showing a steady decrease on approaching the [$x=0.075$] composition. Some grain-growth upon annealing for compositions [$x \geq 0.05$] was apparent in this study which is expected to contribute, at least in part, to the enhanced response of the annealed specimens in this composition range.

The pyroelectric coefficients for as-fired [1] and annealed [2] specimens are shown as a function of temperature in Figure 7(a-d). Distinctive double peaks were observed for all of the as-fired compositions [$x < 0.1$]. A maximum separation of the two peaks occurs at [$x=0.025$] followed by a steady decrease in the separation up to [$x=0.1$]. The existence of a second peak is barely discernible for the as-fired [$x=0.075$] composition, appearing more as an asymmetry in the peak response in the form of a "shoulder" on the high-temperature side of the peak. Pyroelectric doublets such as these have been observed for partially ordered $\text{Pb}(\text{Sc}_{1/2}\text{Ta}_{1/2})\text{O}_3$ material which have been associated with the existence of bimodal size distribution of well-defined ordered regions within the specimen as evidenced by TEM images.^[4] Assuming that this type of response may be associated with the variable nature of the structural ordering that is evident for these compositions, the occurrence of a doublet and the disappearance of such a feature in the

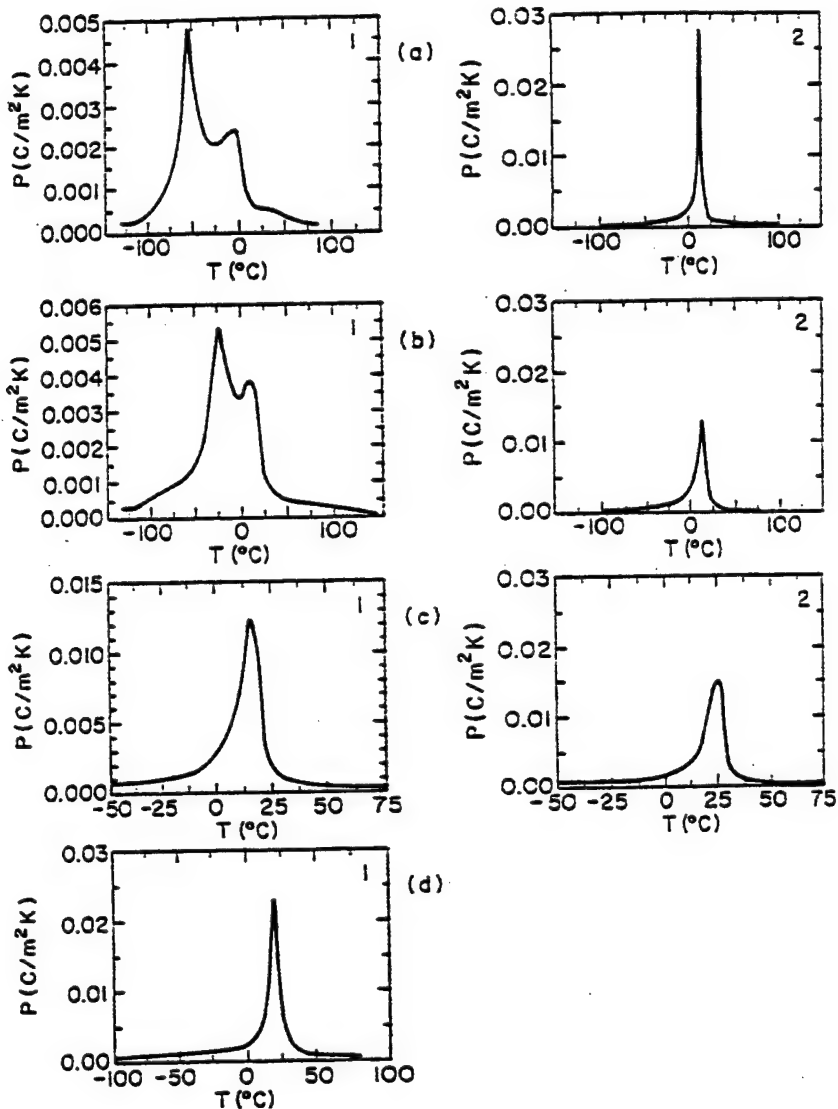


FIGURE 7 The pyroelectric coefficient for As-Fired [1] and Annealed [2] $(1-x)$ $Pb(Sc_{1-x}Ta_{1-x})O_3-(x)PbTiO_3$ ceramics: (a) $x=0.025$, (b) $x=0.05$, (c) $x=0.075$, (d) $x=0.1$.

response may be correlated with the existence of a variable long-range ordering and the compositional limit to which such ordering can be retained. Such an assumption is further supported by the consistent change in the pyroelectric coefficient doublet to a single peak response with annealing, which has already been shown to enhance the degree of long-

range ordering in specimens with compositions in this range. Further, the comparative sharpness and intensity of the peaks associated with the annealed samples with respect to the as-fired ceramics suggests that a nearly optimum and reasonably homogeneous state of ordering is achieved for these specimens.

The specific heat, $C_p(T)$, of as-fired and annealed samples are shown in Figure 8(a-d) and the onset temperatures, T_o , and enthalpies, ΔH , are recorded in Table II. These powdered specimens were all fired only under the first-stage sintering conditions previously described and, hence, the as-fired specimens were already partially ordered with the S parameter values indicated in Table II. The degrees of long-range ordering of the annealed powders were thus somewhat higher than what was achieved for samples which had been densified at higher temperatures and annealed as solids under the same conditions. In all cases, there is observed an enhancement in the maximum specific heat with annealing for a given composition, similar

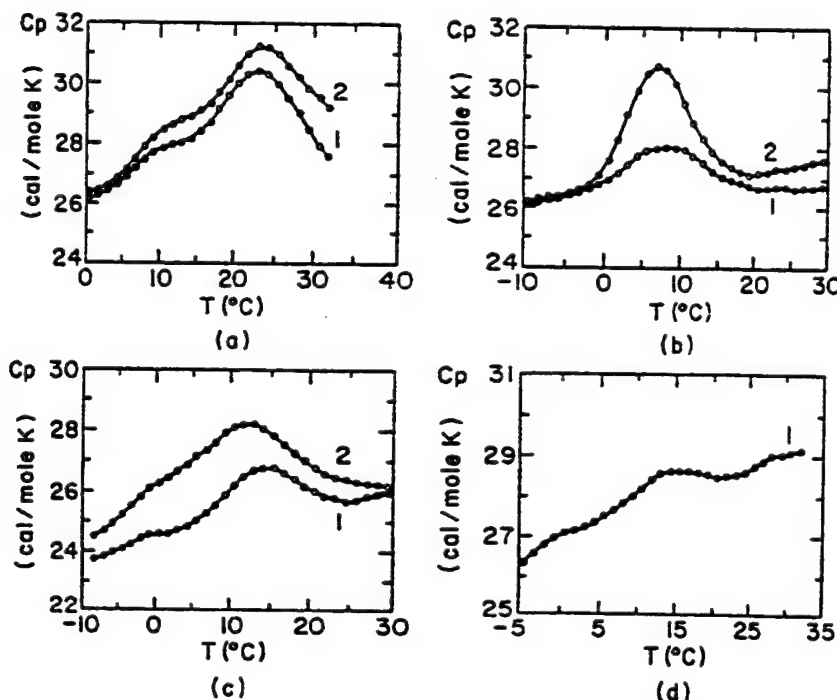


FIGURE 8 The specific heat, $C_p(T)$, of As-Fired [1] and Annealed [2] $(1-x)\text{Pb}(\text{Sc}_{1/2}\text{Ta}_{1/2})\text{O}_3-(x)\text{PbTiO}_3$ ceramics: (a) $x=0.0$, (b) $x=0.05$, (c) $x=0.075$, (d) $x=0.1$.

TABLE II The enthalpies [ΔH] and onset temperatures [T_i] of selected As-Fired [1] and Annealed [2] VOD compositions

x	†	S	$T_i^{\circ}C$	ΔH (cal/mole)
0.0	1	0.80	16	40
0.0	2	0.96	18	48
0.025	1	0.60	3	22
0.025	2	0.77	3	29
0.05	1	0.50	10	7
0.05	2	0.70	8	18

† 1: As-Fired 2: Annealed.

to that occurring for pure $\text{Pb}(\text{Sc}_{1/2}\text{Ta}_{1/2})\text{O}_3$, and a general decrease for both as-fired and annealed specimens with increasing x approaching [$x=0.1$]. The onset temperatures, T_i , (Tab. II) are generally observed to increase with increasing Ti-content while the enthalpies follow an overall decreasing trend with increasing x .

The general trends observed in the thermal properties of the VOD compositions with differing degrees of long-range order are in accord with those occurring in the dielectric and pyroelectric responses of these materials. In all cases, the more ordered specimens at a given composition show a more pronounced thermal effect which becomes steadily more diffuse with increasing x .

5. SUMMARY

A preliminary depiction of the $(1-x)\text{Pb}(\text{Sc}_{1/2}\text{Ta}_{1/2})\text{O}_3-(x)\text{PbTiO}_3$ solid solution, based on the data that are currently available for ceramic specimens from this system [9] is shown in Figure 9 in which the VOD phase region [V] as determined for this particular series of samples is identified. The boundary between these compositions of variable order/disorder [VOD] and rhombohedral compositions, which on the basis of x-ray diffraction are evidently unaffected structurally by the post-sintering heat-treatment conditions applied in this study, was determined to be in the composition range [$x=0.075-0.1$]. The proposed high-temperature Mixed Cubic [XRD] region depicted in Figure 9 over this composition range represents the coexistence of ordered and disordered phases which may be detected by means of x-ray diffraction. Further definition of the VOD phase region and a thorough refinement of the exact structural nature of the materials within

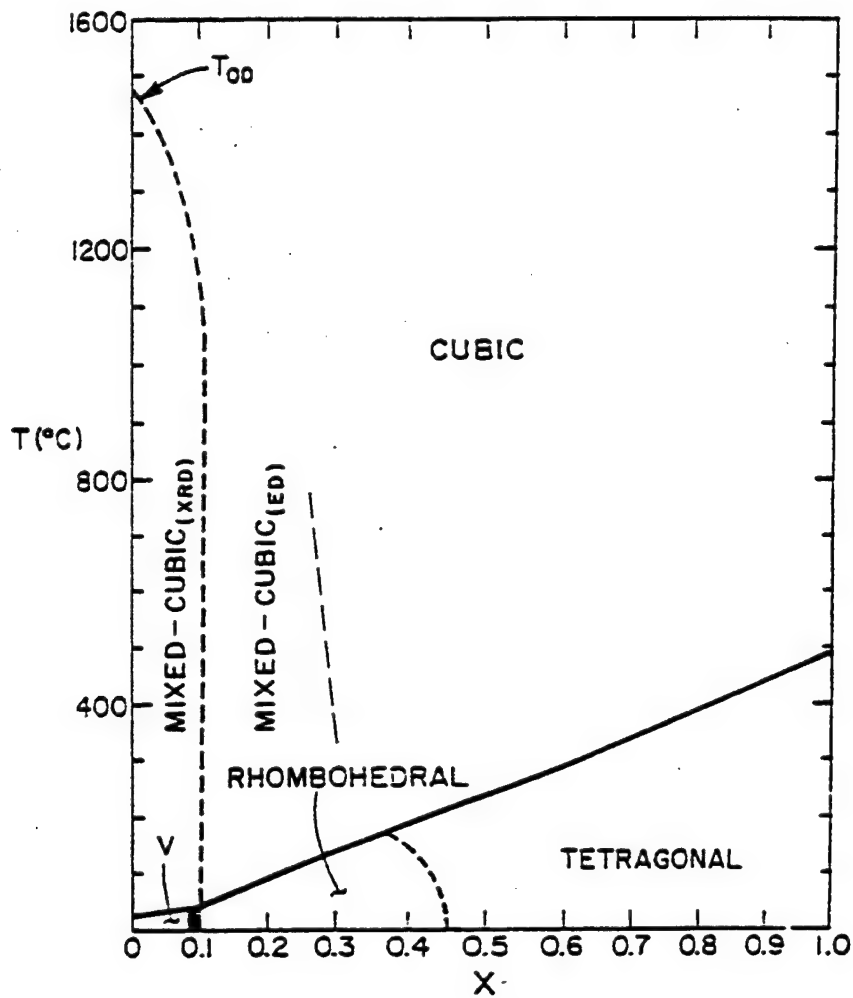


FIGURE 9 A preliminary depiction of the $(1-x)\text{Pb}(\text{Sc}_{1/2}\text{Ta}_{1/2})\text{O}_3-(x)\text{PbTiO}_3$ solid solution system. [x: mole fraction PbTiO_3].

it will require a systematic survey of these compositions over a broad range of annealing temperatures and periods. Such an investigation may yield results which indicate that, under different annealing conditions, the compositional range of variable order/disorder [VOD] is extended somewhat beyond the boundary determined in this study.

Also indicated in Figure 9 is a range of compositions [$x \approx 0.1-0.3$] for which, on the basis of electron diffraction, it has been determined that some

short coherence length long-range ordering does exist as evidenced by the *F*-type superlattice spots appearing in the electron diffraction patterns. It is suggested in this initial depiction of the system that this coexistence of ordered and disordered phases, similar to what is shown for the $[x=0-0.1]$ compositions, likely extends well into the high-temperature cubic phase region (Mixed Cubic [ED]). Materials with compositions $[x \geq 0.4]$ show no evidence of any long or short coherence length long-range ordering by means of x-ray or electron diffraction and, hence, on the basis of these observations, are regarded as completely disordered. The structural characteristics and associated ferroelectric behaviors of these compositions beyond the VOD region are presented in greater detail elsewhere.^[16]

References

- [1] Stenger, C. G. F. and Burggraaf, A. J. (1980). "Order-disorder reactions in the ferroelectric perovskites $\text{Pb}(\text{Sc}_{0.5}\text{Nb}_{0.5})\text{O}_3$ and $\text{Pb}(\text{Sc}_{0.5}\text{Ta}_{0.5})\text{O}_3$. I. Kinetics of the ordering process," *Phys. Stat. Sol.(a)*, **61**, 275.
- [2] Groves, P. (1985). "Low-temperature studies of ferroelectric lead scandium tantalate," *J. Phys. C.*, **18**, L1073.
- [3] Setter, N. (1980). "The role of positional disorder in ferroelectric relaxors." Ph.D. Thesis, The Pennsylvania State University.
- [4] Randall, C. A. and Bhalla, A. S. (1988). "Anomalously large order domains in the $\text{Pb}(\text{Sc}_{1/2}\text{Ta}_{1/2})\text{O}_3$ single crystals." *Ferroelectr. Lett.*, **9**, 47.
- [5] Randall, C. A. (1987). "A transmission electron microscopy study of normal and relaxor perovskite ferroelectric materials." Ph.D. Thesis, University of Essex.
- [6] Zhihi, C., Xi, Y. and Cross, L. E. (1983). "Depolarization behavior and reversible pyroelectricity in lead scandium-tantalate ceramics under DC biases." *Ferroelectrics*, **49**, 213.
- [7] Zhihi, C., Xi, Y. and Cross, L. E. (1983). "Reversible pyroelectric effect in $\text{Pb}(\text{Sc}_{1/2}\text{Ta}_{1/2})\text{O}_3$ ceramics under DC bias." *Ferroelectr. Lett.*, **44**, 271.
- [8] Stenger, C. G. F., Scholten, F. L. and Burggraaf, A. J. (1979). "Ordering and diffuse phase transitions in $\text{Pb}(\text{Sc}_{0.5}\text{Ta}_{0.5})\text{O}_3$ ceramics." *Solid State Commun.*, **32**(11), 989.
- [9] Giniewicz, J. R. (1991). "An investigation of the lead scandium tantalate-lead titanate solid solution system," Ph.D. Thesis, The Pennsylvania State University.
- [10] Giniewicz, J. R., Bhalla, A. S. and Cross, L. E. (submitted to Mat. Lett.).
- [11] Randall, C. A. and Bhalla, A. S. (1990). "Nanostructural-property relations in complex lead perovskites", *Jpn. J. Appl. Phys.*, **29**(2), 327.
- [12] JCPDS #24-1017 (ScTaO₄).
- [13] Shrout, T. R. and Halliyal, A. (1987). "Preparation of lead-based ferroelectric relaxors for capacitors", *Am. Ceram. Soc. Bull.*, **66**(4), 704.
- [14] Byer, R. L. and Roundy, C. B. (1972). "Pyroelectric coefficient direct measurement technique and application", *Ferroelectrics*, **3**, 333.
- [15] Smolenskii, G. A. (1970). "Physical Phenomena in Ferroelectrics with Diffused Phase Transitions", *J. Phys. Soc. Japan*, **28**(suppl.), 26.
- [16] Randall, C. A., Giniewicz, J. R., Bhalla, A. S. and Cross, L. E., "An electron diffraction study of lead scandium tantalate-lead titanate ceramics," (to be published).

APPENDIX 64

Quantitative Comparison of Transmission Electron Microscopy Techniques for the Study of Localized Ordering on a Nanoscale

Xiaoqing Pan,^{*†} Wayne D. Kaplan,^{*‡} and Manfred Rühle^{*}

Max-Planck-Institut für Metallforschung, Institut für Werkstoffwissenschaft, D-70174 Stuttgart, Germany

Robert E. Newnham^{*}

Materials Research Laboratory, The Pennsylvania State University, University Park, Pennsylvania 16802

Different transmission electron microscopy techniques have been compared for the detection and size measurements of ordered regions on a nanometer scale in a disordered matrix phase. As a model system, the perovskite lead magnesium niobate doped with varying amounts of La has been chosen for the present study. While selected area electron diffraction can reveal the existence of ordered structures, dark-field contrast micrographs are usually used to reveal the spatial distribution and the size of ordered regions. However, for small ordered regions, a few nanometers in diameter, the measurements are no longer accurate because of superposition in projection. High-resolution transmission electron microscopy (HRTEM) combined with image processing is shown to be a suitable technique to provide a quantitative measurement of such localized ordering. The detection limit of this method is discussed in detail, using the experimental results and HRTEM image simulations.

I. Introduction

IN RECENT years much interest has centered on ferroelectric compounds with diffuse phase transitions. With these so-called relaxor materials, the transition does not occur at a well-defined temperature (the Curie point), but over a temperature span which is referred to as a Curie range. Within the Curie range there exists a temperature for which the electrical permittivity is a maximum. The maximum in relaxors is, however, frequency dependent (within the radiofrequency spectrum), with the maximum displacing to higher temperatures as the applied frequency is increased. This behavior gives rise to a dispersion in the curve relating permittivity and temperature. Since relaxor materials have broad ferroelectric transitions coupled with high permittivity, they are very attractive for use in capacitors.

Oxide compounds with the perovskite structure are the best-known relaxors. The broad or diffuse transition exhibited by relaxors is attributed to the existence of fluctuations in composition, as well as to the polar microregions in the materials.¹⁻³ Previous studies revealed the existence of phase separation on a nanometer scale due to localized chemical ordering in relaxor materials, such as $\text{Pb}(\text{Sc}_{1/2}\text{Ta}_{1/2})\text{O}_3$ (PST), $\text{Pb}(\text{Mg}_{1/3}\text{Nb}_{2/3})\text{O}_3$ (PMN), and their solid solutions.⁴⁻¹⁰ To understand the properties of relaxor materials, it is important to know the size and distribution of such ordered nanoregions. Transmission electron microscopy (TEM) provides a useful tool to resolve these questions.^{4,5,10-13} The superstructure resulting from chemical ordering can be revealed by selected area electron diffraction (SAED). The nanosized ordered regions can be observed directly by dark-field (DF) contrast imaging and by high-resolution transmission electron microscopy (HRTEM).

The model system chosen for the present study was perovskite lead magnesium niobate (PMN), which is a typical example of a relaxor from the complex lead perovskite family with the general formula $\text{Pb}(\text{B}_x\text{B}'_{1-x})\text{O}_3$. The disordered phase

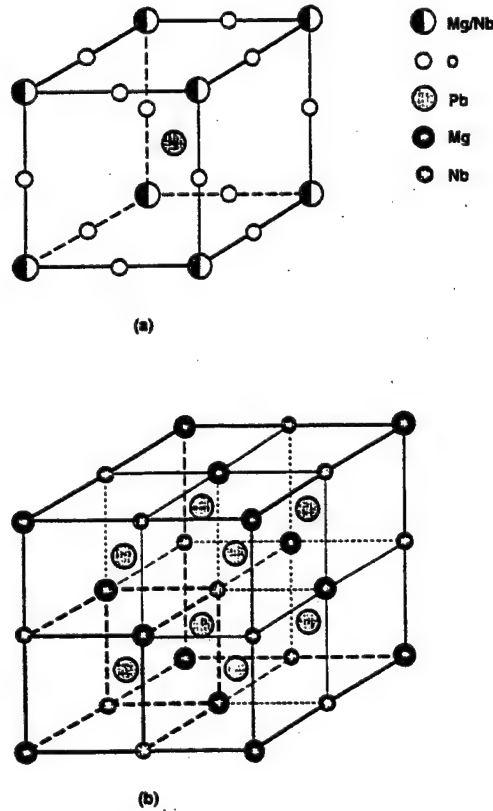


Fig. 1. (a) Schematic model for the atomic structure of disordered PMN, which is a simple perovskite structure. (b) Proposed model for the structure of ordered PMN.¹⁴ Oxygen atoms are not shown in (b). Note that the nearest neighbors on the B-sublattice are unlike and the next-nearest neighbors are similar, which results in an F-centered lattice.

T. E. Mitchell—contributing editor

Manuscript No. 191740. Received June 14, 1996; approved July 2, 1997.
Supported by the Humboldt Foundation and the National Science Foundation.

Member, American Ceramic Society.

Present address: Department of Materials Science and Engineering, University of Michigan, Ann Arbor, Michigan 48109.

Present address: Department of Materials Engineering, Technion-Israel Institute of Technology, Haifa 32000, Israel.

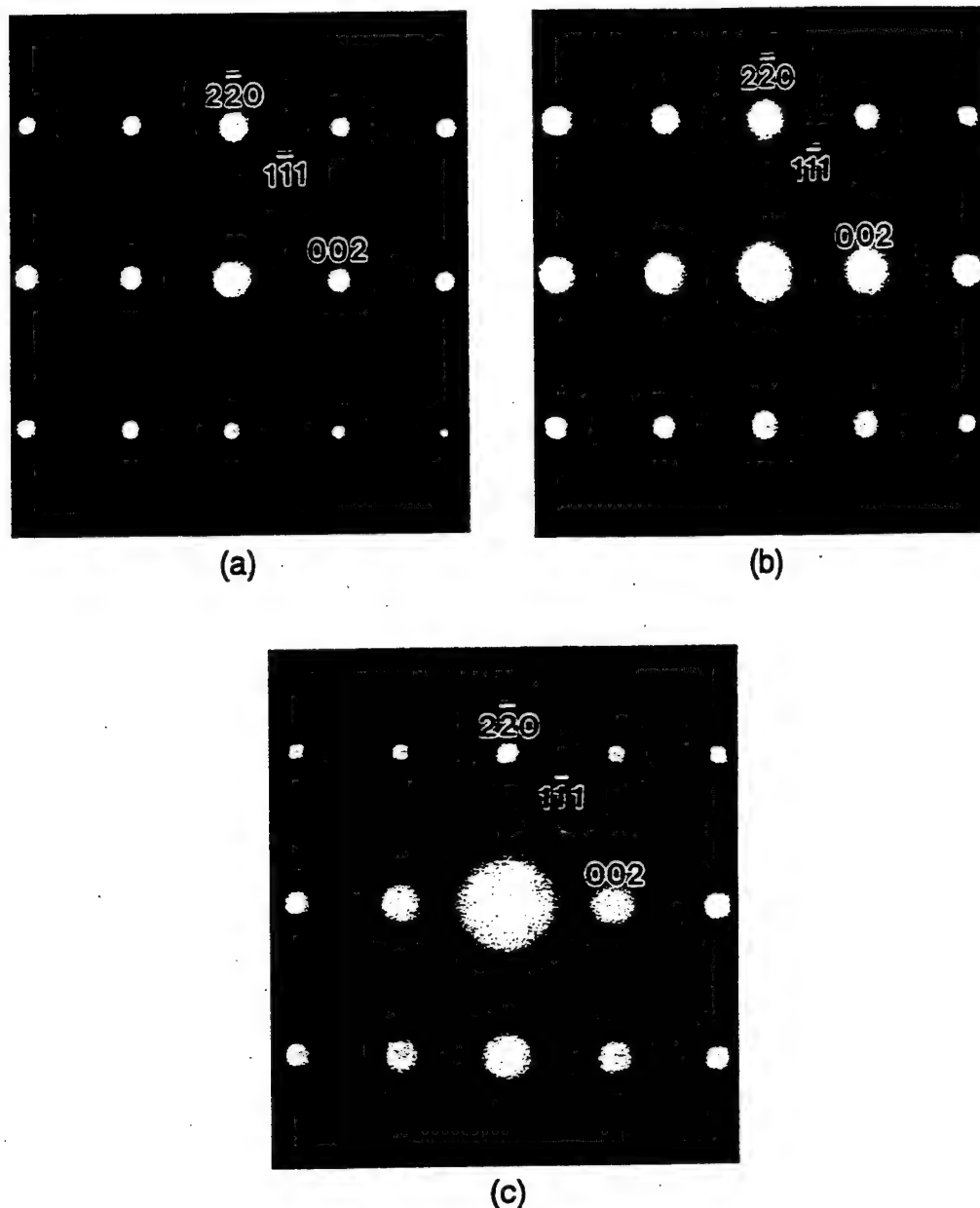


Fig. 2. SAED patterns recorded from the PMN samples doped with (a) 5 at.% La, (b) 3 at.% La, and (c) 1 at.% La. Note that the intensity of superlattice reflections relative to disordered reflections decreases with a decrease in La concentration.

of the relaxor PMN has a simple cubic perovskite structure. In the ideal perovskite structure A-cations occupy the corner positions of the lattice, B-cations occupy the body-center position, and oxygen anions are situated at the face-centered positions. In the disordered PMN phase the B-sites are randomly occupied by Mg and Nb ions, as shown in Fig. 1(a). Since two types of ions (Mg^{2+} and Nb^{5+}) with different valences and ionic radii occupy the same crystallographic position (B-site), chemical ordering can occur, which has been directly revealed by TEM investigations.⁸⁻¹⁵ In the ordered structure the nearest neighbors on the B-sublattice are unlike and the next-nearest neighbors are similar, which results in a distinct F-centered $2a_0 \times 2a_0 \times 2a_0$ superlattice (where a_0 is the lattice parameter in the disordered perovskite structure), as shown in Fig. 1(b). The diffuse, but distinct, superlattice F-spots were revealed by SAED, and ordered regions of 2–5 nm in diameter were also observed in DF images formed by superlattice reflections.¹⁰ In order to understand the ordering characteristics in PMN, La- and Na-doped PMN and solid solutions of $Pb(Mg_{1/3}Nb_{2/3})O_3$ – $PbTiO_3$ (PMN–PT) were investigated by use of conventional

DF microscopy.^{7,14,15} They found that the size of the ordered regions increases with increasing La concentration, but decreases with an increasing content of Na or PT, and based on these observations concluded that the ordering in PMN results in a deviation from stoichiometry to $Pb(Mg_{1/2}Nb_{1/2})O_3$ ($Mg:Nb = 1:1$). However, most of the samples studied were doped with high La concentrations (5–30 at.%) where inhomogeneity of the La causes large variations in the size of the ordered regions.¹⁴ PMN doped with lower amounts of La (0 and 2 wt% La_2O_3),¹⁵ but their DF microscopy does not allow for quantitative size measurements, only a qualitative comparison. Thus, a quantitative comparison of the size of the ordered regions as a systematic function of La doping is still required.

As mentioned above, the accuracy to which the size of the nano-ordered regions can be measured from DF micrographs is limited, probably because of the superposition of ordered regions in the direction of the electron beam. It is the purpose of this paper to present a systematic comparison of different TEM techniques (SAED, DF, HRTEM) for the size determination of nanosized ordered regions. It will be shown that HRTEM lat-

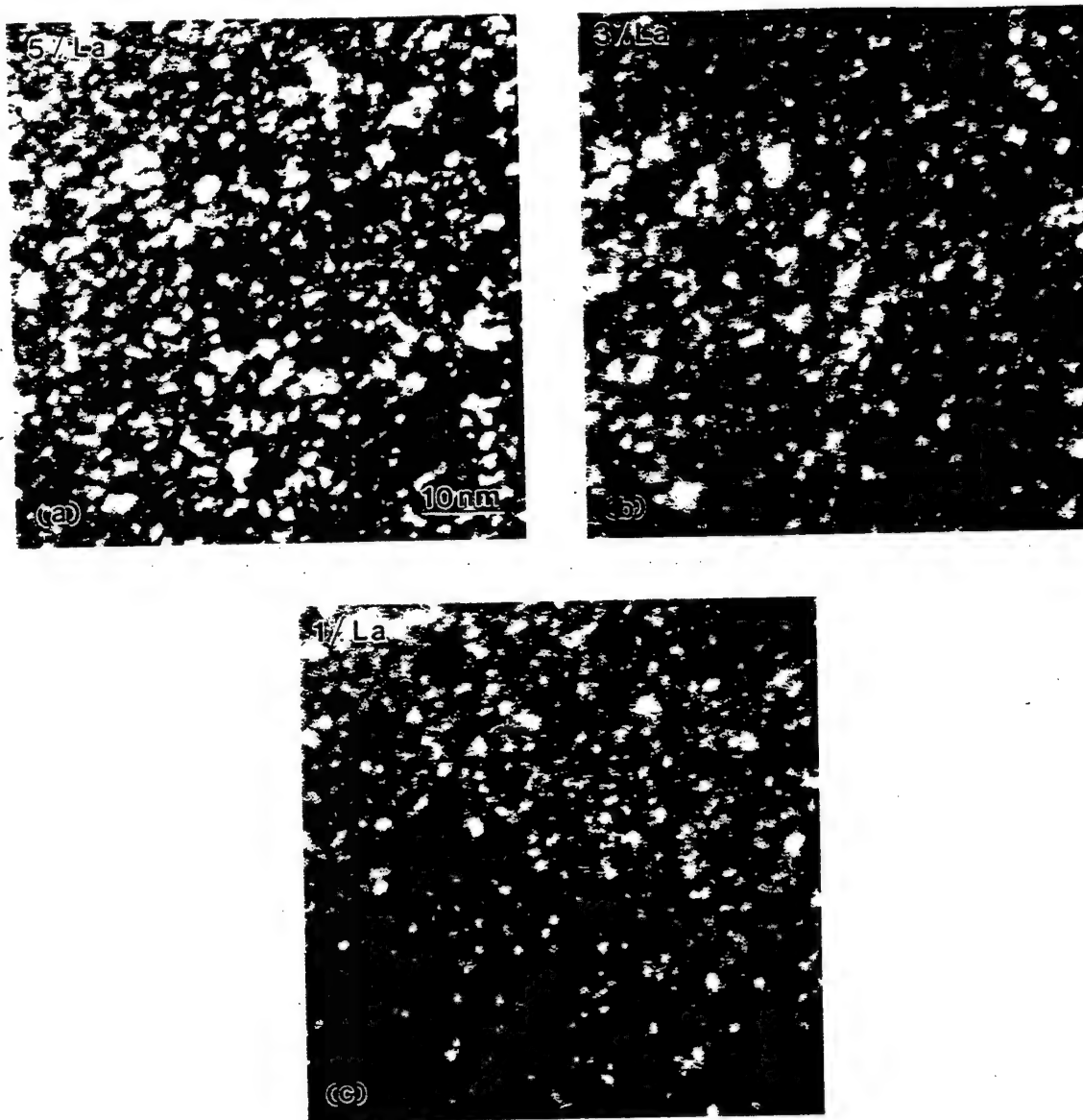


Fig. 3. DF contrast micrographs corresponding to the SAED patterns in Figs. 2(a-c), using the superlattice reflection (333). Regions of high intensity (bright) correspond to the ordered regions.

tice images in combination with image processing provide an accurate measurement of nanosized ordered regions, while DF microscopy does not.

II. Experimental Methods

Bulk samples were produced by mixing stoichiometric mixtures of PbCO_3 , La_2O_3 , MgCO_3 , TiO_2 , and Nb_2O_5 by ball-milling in distilled water for 12 h. After drying, the mixture was calcined for 4 h at 700°C and again ball-milled for 12 h. The milled powders were then pressed into 13 mm diameter disks under 140 MPa, sintered between 1100° and 1200°C for 2–4 h, and then annealed at 900°C for 4–6 h.^{16–18}

Thin disks with a diameter of 3 mm were cut from the bulk PMN ceramic materials. The disks were mechanically ground to a thickness of 100 μm and further thinned to ~20 μm by mechanical dimpling, followed by ion-milling (at 6 kV and 4°, BalTek) until perforation. In order to minimize charging under the electron beam, the TEM specimens were coated with a thin layer of carbon, and glued to a copper ring using a conducting silver paste.

Conventional TEM studies by SAED and DF micrograph

were conducted with a JEOL 200CX electron microscope equipped with a side-entry double-tilting specimen holder. The smallest objective aperture (~5 μm) was used for selecting a superlattice reflection to form DF images. HRTEM investigations were conducted using a JEM-4000EX microscope with a point resolution of 0.17 nm. HRTEM micrographs were recorded through a Gatan Slow Scan CCD camera (1024 \times 1024 pixels). Image filtering and processing were conducted using the software package DigitalMicrograph (Gatan), and the size of ordered nanoregions was determined using the computer program NIH-Image (Wayne Rasband).

III. Experimental Results and Discussion

(1) Electron diffraction

SAED patterns along the $\langle 220 \rangle$ zone axes⁸ were obtained from the studied samples. Figures 2(a–c) show three examples,

⁸In the following, an index system corresponding to the F-centered ordered structure with a lattice parameter $\frac{1}{2}a_0$ ($a_0 = 0.404$ nm) is used.

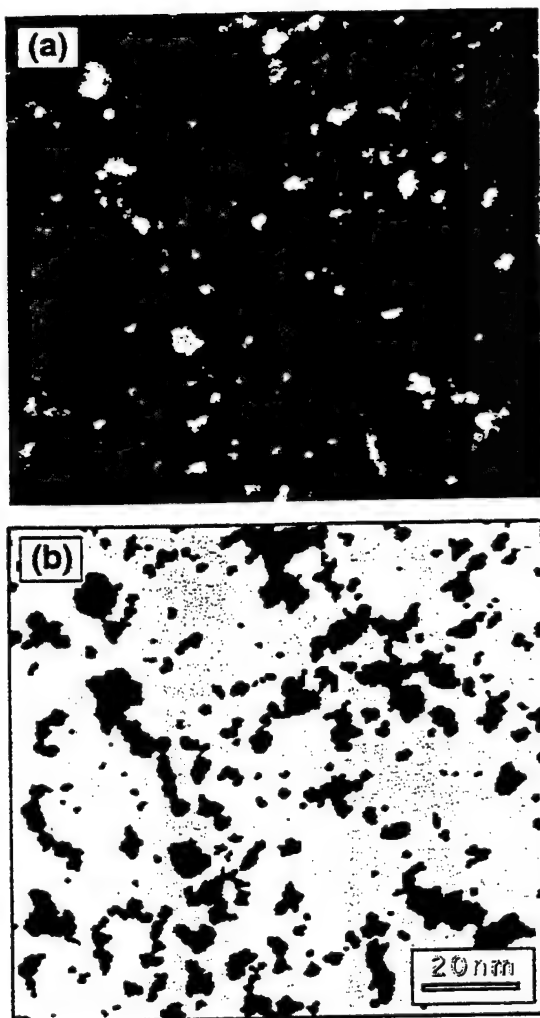


Fig. 4. (a) Digitized micrograph of a DF contrast image formed by using the superlattice reflection (333). (b) Black/white image obtained after computer processing of micrograph (a).

which were recorded from the PMN samples doped with (a) 5 at.-% La, (b) 3 at.-% La, and (c) 1 at.-% La. All of the diffraction patterns show the existence of {111} superlattice reflections, resulting from F-centered ordering. The intensity of superlattice reflections relative to disordered reflections decreases with a decrease in La concentration. Furthermore, the superlattice reflections become more diffuse (but still distinct) from Fig. 2(a) to (c). These results show that ordering in the samples becomes weak, and/or the size of ordered regions becomes smaller as a function of dopant concentration. Since the degree of ordering within the ordered regions is not known, SAED cannot be used to unambiguously discern between the degree of ordering and the size of ordered regions.

(2) Dark-Field Imaging Using a Superlattice Reflection

DF images were recorded by selecting a superlattice reflection.¹ The micrographs in Figs. 3(a–c) present DF contrast micrographs corresponding to the SAED patterns in Figs. 2(a–c), using the superlattice reflection (333). Bright regions of high intensity correspond to the ordered regions. Qualitative inspection of these micrographs does not show an unambiguous increase in ordered region size with an increase in La content.

In order to determine the size of nanosized ordered regions,

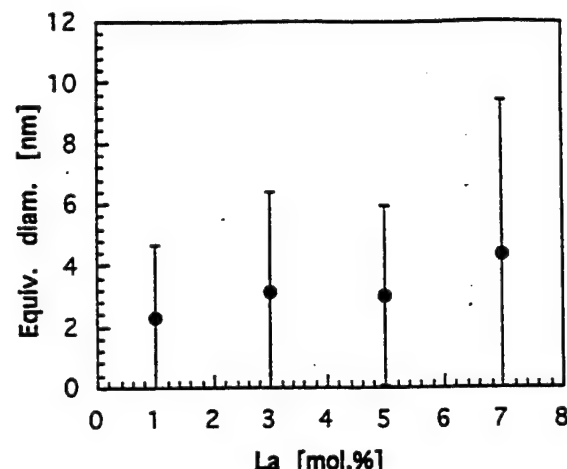


Fig. 5. Measured size and first standard deviation of the nanosized ordered regions plotted as a function of La concentration for the various specimens (determined from DF micrographs).

the DF micrographs were digitized and processed using a computer program. First, the mean intensity of the disordered matrix (the threshold intensity) was measured. This intensity value was used to distinguish between the disordered and ordered regions in the image analysis process, where the ordered regions were redefined as black, and the disordered matrix as white. Figure 4(a) shows a digitized micrograph, and Fig. 4(b) shows a black/white image after computer processing. The size of the ordered regions were determined using this method. In Fig. 5 the measured size and first standard deviation are presented as a function of La concentration for the various specimens.¹¹

Because of the varying threshold intensities across the original micrograph in Fig. 4(a), some ordered regions are not included in the processed image in Fig. 4(b). Furthermore, the superposition of ordered regions in the beam direction results in large black regions in the processed image, which also introduces a large error in the size measurement. Thus no quantitative conclusion can be made from DF micrographs concerning the relationship between domain size and La concentration, because the standard deviation is too large. Such errors will always exist in measurements taken from DF micrographs, due to the large specimen thickness (~100 nm) relative to the ordered region size, and the varying background intensity. The source and magnitude of these errors will be compared to HRTEM results in the next section.

(3) HRTEM Observations and Image Processing

It is well known that the periodicity and contrast in HRTEM lattice images depend not only on the specimen crystal structure, but also on the microscope contrast transfer function (CTF), the objective aperture size, the value of objective lens underfocus, and the specimen thickness.¹⁹ In order to detect the ordered regions, the microscope operating conditions must be such that the intensities of the superlattice reflections are maximum in the real-space lattice image. Assuming a weak-phase object (thin specimen), this condition can be reached by analysis of the CTF following the technique developed by Hutchinson *et al.*²⁰ As shown in Fig. 2, chemical ordering results in {hkl} superlattice reflections with hkl all odd. For the objective aperture used in this work (6.7 nm^{-1}), most of the intensities of the diffracted beams contributing to the [110] lattice image are from {202}, {222}, and {004} planes. The intensities of the

¹¹All of the DF micrographs were obtained by tilting the incident beam such that the {111} reflection remained on the opticaxis, creating a centered dark-field image.

¹¹For both DF and HRTEM micrographs (next section) the measured values of the size of the ordered regions are average values taken from more than 200 ordered regions in at least four different grains, for each La concentration.

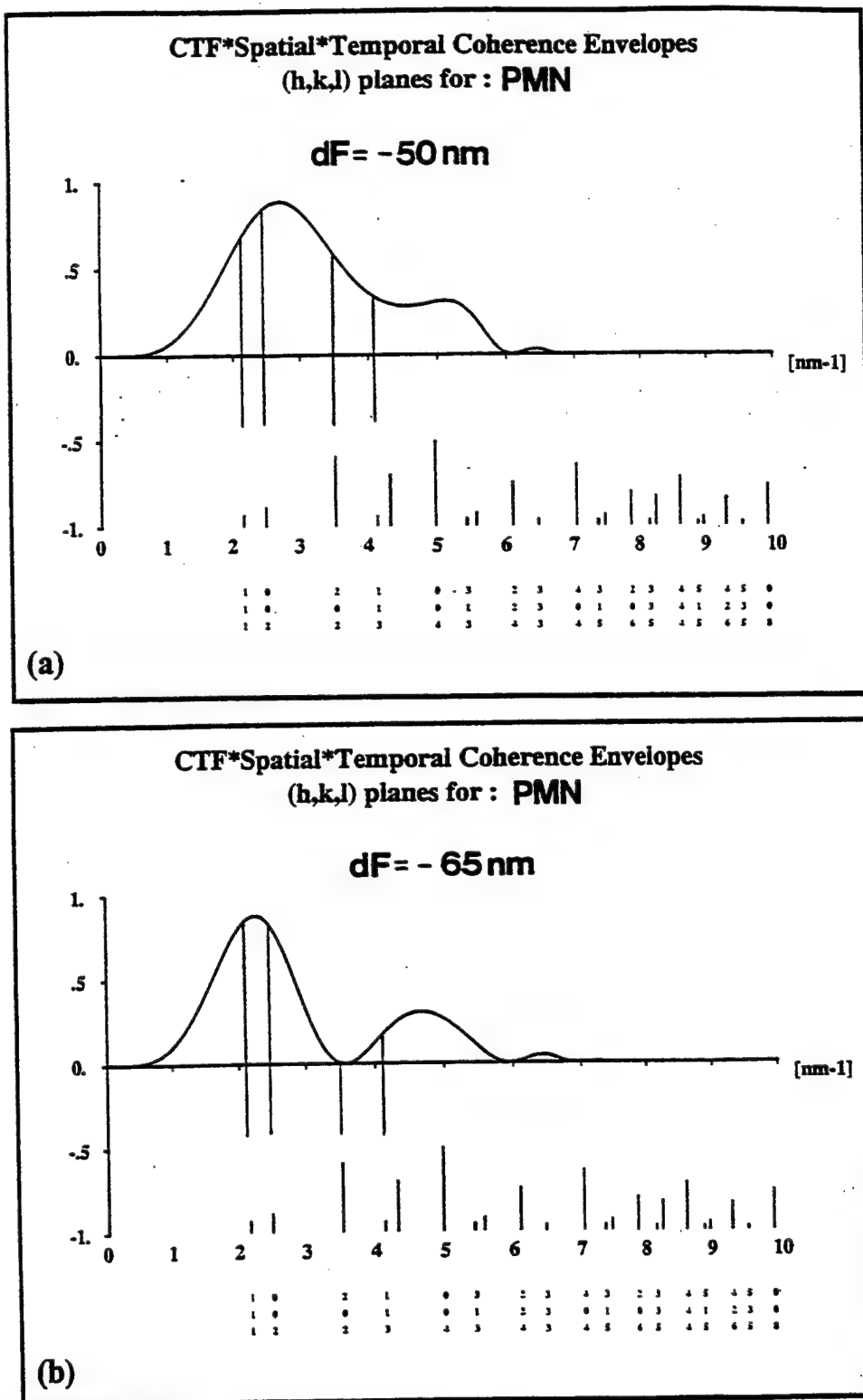


Fig. 6. Two CTFs at a defocus of (a) -50 nm (Scherzer defocus) and (b) -65 nm for the JEM-4000EX. Note that the intensity of lattice planes in the real-space image strongly depends on the defocus value of the objective lens.

superlattice reflections $\{111\}$ and $\{113\}$ are much lower than that of other reflections. Figure 6 shows two CTFs at a defocus of -50 nm (Scherzer defocus) and -65 nm, respectively, for the JEM-4000EX. It is clear that the intensity of lattice planes in the real-space image will strongly depend on the defocus value of the objective lens. At Scherzer defocus (Fig. 6(a)), optimal resolution can be obtained. However, both the disordered matrix reflections and the superlattice reflections strongly contribute to the image. To obtain optimal contrast to detect the or-

dered regions in the disordered matrix, a defocus value which will reduce the intensity of disordered lattice planes should be obtained. Figure 6(b) shows the CTF at a defocus of -65 nm, where the strong $\{202\}$ reflection is reduced to zero and the superlattice reflection $\{111\}$ has an intensity maximum. Therefore, at this defocus the ordered regions in PMN should be distinguished from the disordered matrix.

This optimal defocus value is correct only for a weak-phase object (a very thin specimen). The objective lens defocus can

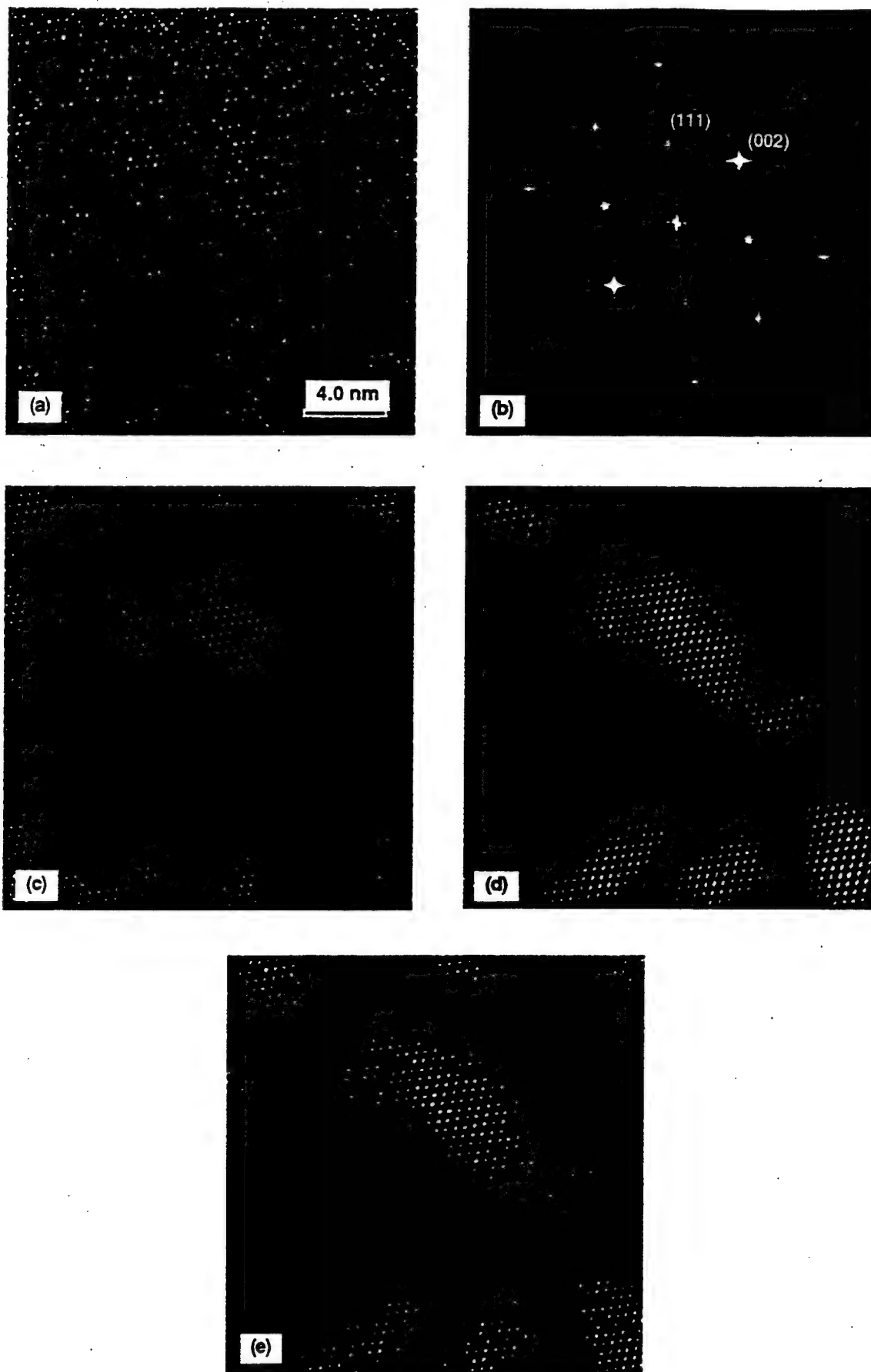


Fig. 7. Demonstration of the process used to automatically differentiate between the nanosized ordered regions and the disordered matrix: (a) A HRTEM micrograph recorded from the PMN specimen doped with 5 at. % La. (b) A Fourier transformation of image (a), where superlattice {111} reflections are evident. (c) A Fourier-filtered image using a periodic (Bragg) filter to include intensities from both ordered and disordered reflections. (d) A Fourier-filtered image, where only superlattice {111} reflections were included in the Bragg filter. (e) Intensity slice of image (d), which clearly shows the ordered regions.

be optimized for a nonidealized specimen (non-weak-phase object) in two ways. First, the intensity of lattice planes in simulated images can be evaluated as a function of defocus and specimen thickness (see Section III (4)). Second, on-line Fourier transformations of experimental images can be used to experimentally obtain relative ordered/disordered reflection intensities from HRTEM lattice images. Quantification of $\{111\}/\{002\}$ intensity ratios as a function of objective lens defocus can then be used to find the optimal defocus for a specific region of the specimen (constant thickness). The second method was applied during acquisition of the images presented in this work, and a defocus range of -65 to -70 nm was found to be optimal for the specimen thickness obtained after conventional ion-milling.

Figure 7 demonstrates the process used to automatically differentiate between the nanosized ordered regions and the disordered matrix. The HRTEM micrograph in Fig. 7(a) was recorded from the PMN specimen doped with 5 at.% La. Nanosized ordered regions can be distinguished from the disordered matrix. Figure 7(b) shows a Fourier transformation of this image. Superlattice $\{111\}$ reflections are evident. Figure 7(c) is a Fourier-filtered image of Fig. 7(a). The filtering process included the use of a periodic (Bragg) filter to include intensities from both ordered and disordered reflections. At the same time a "difference" image was obtained using the same Bragg filter to discriminate against all periodic reflections. The accuracy of the filter process was then carefully checked in order to ensure no loss of information by searching for residual periodic contrast in the "difference" image.²¹ The shape and size of the Bragg filter were adjusted such that no loss of information occurred. Figure 7(d) is also a filtered image, where only superlattice $\{111\}$ reflections were included in the Bragg filter. This process results in an image where the contrast resulting from the ordered regions is clearly distinguishable from the background intensity (the disordered matrix).

The intensity of the disordered matrix (the threshold intensity) was then measured from the filtered images (Fig. 7(d)). In this way an intensity slice was defined where the minimum was the threshold intensity, and the maximum was the intensity from the ordered regions. Application of the intensity slice to Fig. 7(d) resulted in Fig. 7(e), which is then ready for automated computer measurements of the ordered regions.

Figure 8 demonstrates the final step in automated measurements of the ordered regions. Figure 8(a) is a micrograph showing the configuration of nanosized ordered regions, obtained using the image processing described above. Figure 8(a) was then converted to a black/white image as shown in Fig. 8(b), where the perimeter of the ordered regions is distinguished using the background intensity. Figure 9 shows the measured size of the ordered regions from HRTEM micrographs plotted as a function of La concentration. The standard deviations are also shown by error bars in the figure.

The main source of error in the measurements conducted on the HRTEM micrographs is overlap of ordered regions in the electron beam direction. This can be concluded from the increase in error with an increase in ordered region size (an increase in La concentration). Also, a larger distribution of ordered region size may exist for higher La concentrations, which in turn should increase the measurement errors. These two sources of error cannot be separated by a simple histogram analysis.

Overlap of the ordered regions will cause a larger error in the analysis of DF images due to the larger specimen thickness, and thus the higher probability of superposition of ordered regions, as compared to HRTEM images which are recorded from very thin regions. HRTEM micrographs are always recorded at higher magnifications than DF images. Thus the specimen thickness in HRTEM images varies less than in DF images. This is the reason for the varying background intensity of the DF images, which does not exist to the same degree in the application of HRTEM images, and is a clear advantage of HRTEM for size measurements of ordered nanoregions.

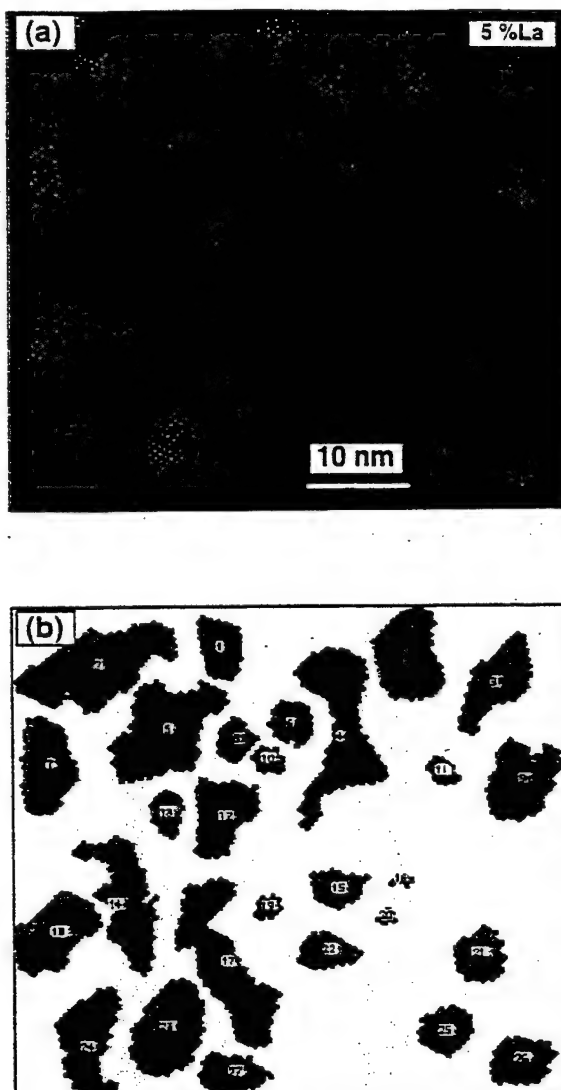


Fig. 8. Demonstration of the automated computer measurements of the ordered regions from HRTEM images: (a) A micrograph showing the configuration of nanosized ordered regions, obtained using the image processing shown in Fig. 7. (b) A black/white image converted from the image in (a) was used for the size determination of ordered nanoregions.

(4) Detection of the Ordered Regions by HRTEM

Based on the experimental results just presented, one can conclude that for the size determination of nanosized ordered regions in PMN, the combination of HRTEM lattice images and related image processing provides a higher accuracy than DF microscopy. However, it should be noted that the measured regions in the HRTEM micrographs may not be the same area as the projection of the domains in the electron beam direction, because the detectability depends on the relative thickness of the ordered region to the total specimen thickness (in the electron beam direction). Assuming a spherical shape of the ordered region, the edge of the ordered region, where its thickness in the beam direction is less than the center of the ordered region, may be undetectable in the lattice image. In other words, the area measured from the HRTEM micrograph may be less than the real projected area of the ordered domain. This will give an additional error in the measured size. To understand the importance of this error, HRTEM image simulations were conducted using the computer program EMS.²²

Figure 10 shows a schematic representation of how the simulated images in Fig. 11 were calculated. Simulated images were calculated for a PMN specimen with an ordered region of vary-

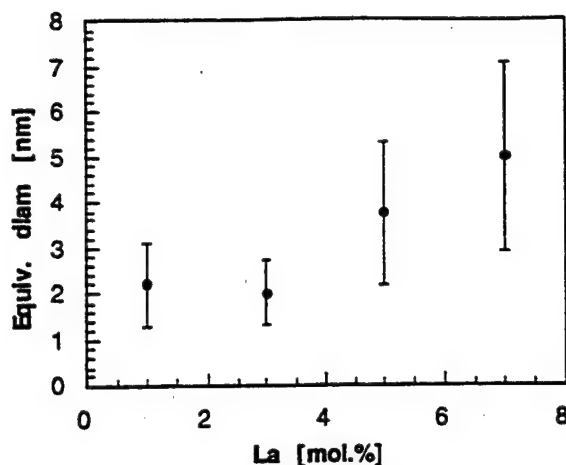


Fig. 9. Measured size of the ordered regions from HRTEM micrographs plotted as a function of La concentration. The standard deviations are shown by error bars in the figure.

ing thickness embedded in a disordered matrix, using different objective lens defocus values. The ordered slice is located in the middle of the model specimen. In the simulation the total thickness of the specimen remained the same (10 nm). However, the thickness of the ordered region increases from zero for the completely disordered simulation (a), to 10 cells for the completely ordered simulation (f). Each cell is 1.1 nm thick, which is the thickness of the ordered unit cell in the [110] direction. According to this simulated image map,²² one finds that the ordered structure can be distinguished from the disordered matrix even in Fig. 11(b), where the thickness of an ordered slice is only 2 nm (see Fig. 10(b)). In fact, from the image simulations this holds true even when the thickness of an ordered region is as thin as 1 nm (not shown in Fig. 10). However, a direct quantitative assessment of the detection limit (the minimum detectable thickness of the ordered region) can-

²²The simulated image map in Fig. 11 was produced using invariant contrast; i.e., during printing no changes were made to the contrast of the separate images. Should the maximum or minimum intensity between the different images be normalized, then the contrast would change and the apparent detectability of the ordered region would change.

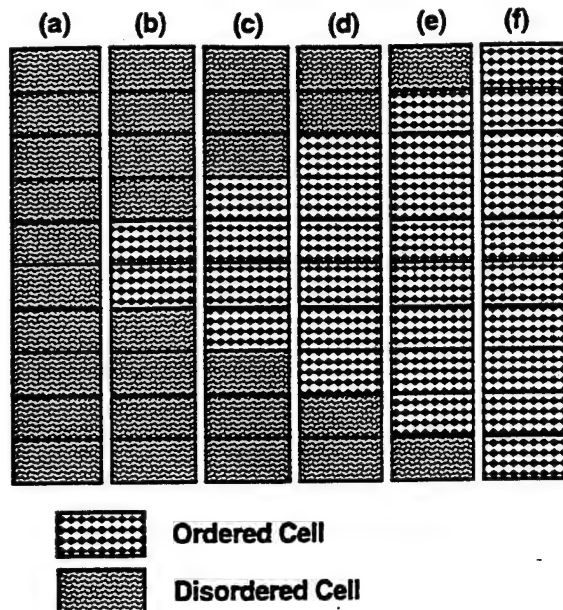


Fig. 10. Schematic representation of the structural model used for the image simulation of a PMN specimen with an ordered region of varying thickness embedded in a disordered matrix, at different objective lens defocus values. In the simulation the total thickness of the specimen remained the same (10 nm). The thickness of the ordered region increases from 0 for the completely disordered simulation (a), to 10 cells for the completely ordered simulation (f). Each cell is 1.1 nm thick, which is the thickness of the ordered unit cell in the [110] direction.

not be determined because experimental values of inelastic electron scattering are not known. One would assume that this detection limit would become worse as a function of increasing specimen thickness. For the limiting case of a very thin specimen, which applies to the images recorded from the edge of the specimen perforation, the detection limit from HRTEM does not seem to be a limiting factor, and is certainly less than the errors introduced from overlap of the ordered regions. These errors result in the standard deviation in Fig. 9. From the image map in Fig. 11 one can also conclude that the detectability of the ordered structure at defocus values between -60 and -70 nm is much higher than at other defocus values. This is in agreement with the calculated CTFs mentioned previously.

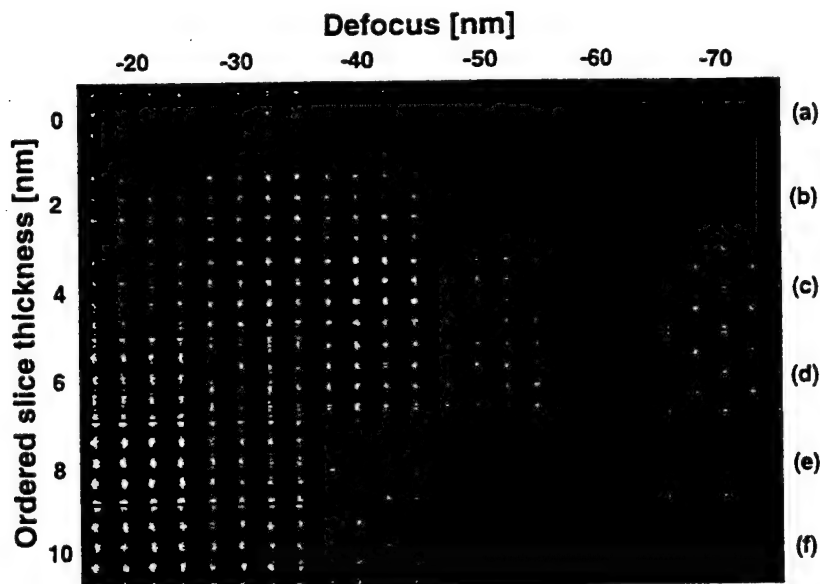


Fig. 11. Computer simulated image using the structural model presented in Fig. 10.

(5) Role of La in Ordering

Previous investigations^{14,15} have suggested that ordering in PMN includes a change in the Mg:Nb ratio from 1:2 to 1:1. The deviation from stoichiometry results in a charge imbalance in the ordered regions, which has been postulated as the main limit to the size of the ordered regions. If La is introduced into PMN as a substitutional ion on the A-sites (Pb-sites), the charge imbalance in the ordered region will be reduced.

The driving force for ordering is a reduction in free energy. In the case of PMN, ordering is assumed to result in a charge imbalance due to the deviation from stoichiometry, thus limiting the size of the ordered regions. While doping with La should cause an increase in elastic energy due to the difference in cation radii between La and Pb, it will also reduce the charge imbalance in the ordered regions. The present results show a systematic increase in the size of the ordered nanoregions with an increase in La concentration. Thus one can conclude that the reduction in free energy due to charge reduction is larger than the increase in free energy due to elastic strain. This interpretation is based on the assumption that the degree of ordering in the ordered regions is 1.0. HRTEM observations by Park *et al.*²³ combined with image simulations have concluded that the long-range order parameter for the ordered regions ranges between 0.2 and 0.8. However, even if the ordered regions do not have a long-range order parameter of 1.0, some charge imbalance would exist, and La would still serve to reduce this effect, and allow for larger ordered nanoregions.

IV. Conclusions

Different transmission electron microscopy techniques have been compared for the detection and size measurements of ordered nanoregions in disordered PMN. SAED can reveal the existence of ordered structure. However, the intensity of diffracted electron beams varies with the change of both ordering parameter and the size of the ordered regions. DF microscopy directly shows the presence of the ordered regions, but does not provide accurate size measurement for ordered nanoregions, because of the overlap of the ordered regions in projection. HRTEM combined with image processing is a more suitable technique in providing a quantitative measurement of the size of ordered nanoregions. Thus HRTEM was applied to measure the size of ordered nanoregions in PMN as a function of La concentrations. It was found that La increases the average size of the ordered regions in agreement with previous models where La is assumed to counter the charge imbalance caused by deviation from stoichiometry during ordering.

Acknowledgments: We are grateful to Dr. J. T. Fielding at the Pennsylvania State University for providing the samples.

References

- ¹G. A. Smolenskii, "Physical Phenomena in Ferroelectrics with Diffused Phase Transition (Review)," *J. Phys. Soc. Jpn.*, **28**, 26-37 (1970).
- ²B. N. Rolov, "Effect of Composition Fluctuations on Unsharp Ferroelectric Phase Transition," *Sov. Phys.: Solid State (Engl. Transl.)*, **6** [7] 1676-78 (1965).
- ³L. E. Cross, "Relaxor Ferroelectrics," *Ferroelectrics*, **76**, 241-67 (1987).
- ⁴M. P. Harmer, A. Bahalla, B. Fox, and L. E. Cross, "Electron Microscopy of Ordered Domains in Lead Scandium Tantalate $Pb(Sc_{0.5}Ta_{0.5})O_3$," *Mater. Lett.*, **2** [4A] 278-80 (1984).
- ⁵H. M. Chan, M. P. Harmer, A. Bahalla, and L. E. Cross, "TEM of the Relaxor Material $Pb(Sc_{0.5}Ta_{0.5})O_3$," *J. Appl. Phys.*, **54**, 550-52 (1985).
- ⁶H. M. Chan and M. P. Harmer, p. 739 in Materials Research, Vol. 21, *Ceramic Microstructures '86: Role of Interfaces*, Edited by J. A. Pask and A. G. Evans, Plenum, New York, 1987.
- ⁷M. P. Harmer, J. Chen, P. Peng, H. M. Chan, and D. M. Smyth, "Control of Microchemical Ordering in Relaxor Ferroelectrics and Related Compounds," *Ferroelectrics*, **97**, 263 (1989).
- ⁸C. A. Randall, D. J. Barber, R. W. Whatmore, and P. Groves, "Short-Range Order Phenomena in Lead-Based Perovskites," *Ferroelectrics*, **76**, 277 (1987).
- ⁹C. A. Randall and A. S. Bhalla, "Nanostructural-Property Relations in Complex Lead Perovskites," *Jpn. J. Appl. Phys.*, **29**, 327-33 (1990).
- ¹⁰A. D. Hilton, C. A. Randall, D. J. Barber, and T. R. Shroud, "TEM Studies of $Pb(Mg_{1/3}Nb_{2/3})O_3$ -PbTiO₃ Ferroelectric Relaxors," *Ferroelectrics*, **93**, 379-86 (1989).
- ¹¹C. A. Randall, D. J. Barber, and R. W. Whatmore, "In Situ TEM Experiments on Perovskite-Structured Ferroelectric Relaxor Materials," *J. Microsc.*, **145**, 275 (1987).
- ¹²H. B. Krause, J. M. Cowley, and J. Wheatley, "Short-Range Ordering in $PbMg_{1/3}Nb_{2/3}O$," *Acta Crystallogr.*, **A35**, 1015-17 (1979).
- ¹³E. Husson, M. Chubb, and A. Morell, "Superstructure in $PbMg_{1/3}Nb_{2/3}O$ Ceramics Revealed by High Resolution Electron Microscopy," *Mater. Res. Bull.*, **23**, 357-61 (1988).
- ¹⁴J. Chen, H. M. Chan, and M. P. Harmer, "Ordering Structure and Dielectric Properties of Undoped and La/Na-Doped $Pb(Mg_{1/3}Nb_{2/3})O_3$," *J. Am. Ceram. Soc.*, **72** [4] 593-98 (1989).
- ¹⁵A. D. Hilton, D. J. Barber, C. A. Randall, and T. R. Shroud, "On Short Range Ordering in the Perovskite Lead Magnesium Niobate," *J. Mater. Sci.*, **25**, 3461 (1990).
- ¹⁶F. S. Galasso, p. 12 in *Structure, Properties and Preparation of Perovskite-Type Compounds*, Edited by R. Sinoluchowski and N. Kurti, Pergamon Press, New York, 1969.
- ¹⁷S. L. Swartz and T. R. Shroud, "Fabrication of Perovskite Lead Magnesium Biobate," *Mater. Res. Bull.*, **17**, 1245-50 (1982).
- ¹⁸J. T. Fielding, Ph.D. Dissertation, Pennsylvania State University, University Park, PA, 1992.
- ¹⁹J. C. H. Spence, *Experimental High-Resolution Transmission Electron Microscopy*, Clarendon Press, Oxford, U.K., 1981.
- ²⁰J. L. Hutchison, C. T. Chou, M.-J. Casanove, D. Cherns, J. W. Steeds, D. A. Ashenford, and B. Laurence, "HREM of Ga₂Te₃: Imaging of an Ordered Vacancy Superlattice with Enhanced Contrast," *Ultramicroscopy*, **53** [1] 91-96 (1994).
- ²¹G. Möbus, G. Necker, and M. Rühle, "Adaptive Fourier-Filtering Technique for Quantitative Evaluation of High-Resolution Electron Micrographs of Interfaces," *Ultramicroscopy*, **49**, 46-65 (1993).
- ²²P. A. Stadelmann, "EMS a Software Package for Electron Diffraction Analysis and HRTEM Image Simulation in Materials Science," *Ultramicroscopy*, **21**, 131-46 (1987).
- ²³K. Park, L. Salamanca-Riba, M. Wuttig, and D. Viehland, "Ordering in Lead Magnesium Niobate Solid Solutions," *J. Mater. Sci.*, **29**, 1284-89 (1994). \square

APPENDIX 65

Change in electromechanical properties of 0.9PMN:0.1PT relaxor ferroelectric induced by uniaxial compressive stress directed perpendicular to the electric field

J. Zhao, A. E. Glazounov, and Q. M. Zhang^a

Materials Research Laboratory, The Pennsylvania State University, University Park, Pennsylvania 16802

(Received 12 October 1998; accepted for publication 11 November 1998)

It was shown that the uniaxial compressive stress applied perpendicular to the electric field strongly changes the dielectric and electromechanical properties of relaxor ferroelectric 0.9PMN:0.1PT at temperatures around its dielectric constant maximum, T_m . This includes: (i) a shift of the temperature of the electric field induced phase transition into the ferroelectric state and a depoling temperature to higher values which brings a large hysteresis in the material response to the electric field, and (ii) the symmetry breaking in the plane perpendicular to the direction of the electric field (3-axis). Using this symmetry breaking, from the ratio of the effective piezoelectric coefficients in the field biased state, d_{32}/d_{31} , the size of the micropolar regions at temperatures near T_m was estimated. © 1999 American Institute of Physics. [S0003-6951(99)04503-9]

In recent years, the electrostrictive properties of relaxor ferroelectrics (relaxors) have been the focus of intensive studies in view of their application in actuators and transducers. This is because at temperatures around the dielectric constant maximum, T_m , relaxors exhibit large electrostrictive strain, the strain-field relationship is practically free of hysteresis,¹ and the effective piezoelectric coefficient can be tuned by changing the magnitude of the dc bias field.² These features are highly desirable for actuators used in precise micropositioning and for applications in smart structures.

The material selected for this study was solid solution (1-x)PMN:xPT, with $x=0.10$, because it exhibits the highest strain around room temperature among other relaxor compositions. The goal was to characterize the change in its electromechanical properties with external stress, since in most actuator and transducer applications, the material is often subjected to high external mechanical load. In addition to these purely practical issues, we also demonstrate results which are of interest from a fundamental point of view. It is shown that by using the stress dependence of the piezoelectric coefficients of 0.9PMN:0.1PT one can deduce the size of the micropolar regions.

The ceramic samples were fabricated using a route described in Ref. 3. The uniaxial stress was applied to the specimen using an apparatus developed recently.⁴ In the studied temperature range around T_m , the electric field induced strain of 0.9PMN:0.1PT is electrostrictive,^{1,2} and therefore, a direct current (dc) electric bias field was applied in order to characterize the stress dependence of the effective piezoelectric coefficients of this material.

During the experiments, the induced strain was measured using a strain gauge ("KYOWA").⁴ In the dc electric field biased state, the longitudinal, S_3 , and transverse, S_j ($j=1,2$), strain responses of the material can be described by⁵

$$S_3 = d_{33}E_3 + s_{31}^E\sigma_1 \quad \text{and} \quad S_j = d_{3j}E_3 + s_{1j}^E\sigma_1, \quad (1)$$

^aCorresponding author; electronic mail: qxzl@psu.edu

where d_{ij} is the effective piezoelectric coefficient, s_{ij}^E is the elastic compliance, and the coordinate system is chosen such that the 3-axis is parallel to the applied electric field, the 1-axis is along the compressive stress, and the 2-axis is perpendicular to the 1- and 3-axes, respectively. Under the constant stress condition, we apply a weak alternating current (ac) electric field E_{ac} (< 100 V/cm) to induce ac strains S_3 , S_1 , and S_2 , parallel and perpendicular to E_{ac} , from which the effective piezoelectric coefficients $d_{33} (= S_3/E_{ac})$ and $d_{3j} (= S_j/E_{ac}, j=1,2)$ can be determined. In order to ensure that σ_1 was uniformly applied to the specimen, two strain gauges attached to opposite faces of the specimen were utilized. Adjustments were made before acquiring the data so that the strain readings from the two strain gauges were the same within 5%. The dielectric constant, ϵ , was measured by using a calibrated small resistor connected in series with the specimen, and monitoring the voltage drop across the resistor, which is related with the current flowing through the specimen. The polarization level at each electric bias field and constant stress state was measured by a Sawyer-Tower circuit. All the measurements of d_{ij} , ϵ and the polarization were performed using a frequency of 10 Hz.

Since the material is operated at temperatures near the dielectric constant maximum, where there is a large change in material properties with temperature, it is necessary to characterize them over the temperature range around T_m . In stress-free conditions and without a dc bias 0.9PMN:0.1PT has $T_m \approx 35$ °C at 10 Hz. Thus to have a systematic picture, three points were chosen: 25 °C (below T_m), 50 °C (slightly above T_m), and 80 °C (above T_m).

Unlike normal ferroelectrics, in relaxors the maximum in $\epsilon(T)$ at T_m does not correspond to the spontaneous structural phase transition to the polar state.^{6,7} In the (1-x)PMN:xPT system, with $x < 0.3$, the phase transition occurs at lower temperatures and only under a large electric field,⁸⁻¹⁰ which is represented by the electric field-temperature phase diagram.⁸ Once induced, the macropolar state will remain stable at temperatures below T_d , above

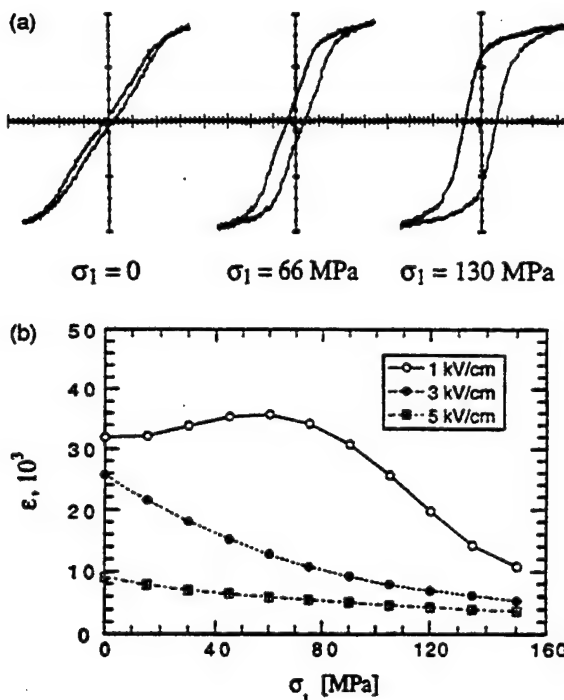


FIG. 1. Polarization and dielectric data measured at 25 °C at frequency 10 Hz. (a) Change in the polarization-electric field hysteresis loop with the compressive stress σ_1 from slim loop (micropolar state) to square loop characteristic of regular ferroelectric state. The axis scale is 1.5 kV/cm per division for electric field and 0.14 C/m² per division for polarization. (b) Stress dependence of small-signal dielectric constant measured at different dc bias field. Symbols show experimental data and the lines are drawn to guide the eye.

which the thermal depoling of the material occurs. According to the phase diagram, the depoling temperature, T_d , shifts to higher values under the dc bias field. The thermal depoling of the material above T_d manifests itself, for example, in the change of the shape of the polarization-field dependence from a rectangular loop below T_d to the so-called slim loop without hysteresis around T_m .^{6,7} On a microscopic level, the depoling is described as breaking of the macropolar state into small, nanometer scale size, regions with the local spontaneous polarization (micropolar state).⁷

In a normal ferroelectric the electrostrictive coupling in the material shifts the Curie temperature, T_c , under the external stress according to^{5,11}

$$\Delta T = 2\epsilon_0 C Q_{11} \sigma_3 \quad \text{and} \quad \Delta T = 2\epsilon_0 C Q_{12} \sigma_1, \quad (2)$$

where $\Delta T = T_c(\sigma_j) - T_c(0)$, $\epsilon_0 = 8.854 \times 10^{-12}$ F/m, C is the Curie-Weiss constant, Q_{11} and Q_{12} are the longitudinal and transverse electrostrictive coefficients, respectively, and we use a conventional sign notation that the compressive stress is of negative sign. The trend should be the same for relaxor 0.9PMN:0.1PT, where one should expect that the depoling temperature will be shifted by the external stress. For example, a compressive σ_1 stress should shift T_d to higher values, since in 0.9PMN:0.1PT $Q_{12} < 0$.¹¹

Indeed, as shown in Fig. 1(a), at 25 °C, there is a transformation of the polarization-field dependence from a slim loop under the stress free condition to a nearly square hysteresis loop under a high compressive stress, σ_1 . This implies that the macropolar state induced by the electric field becomes stable at room temperature after the field is turned

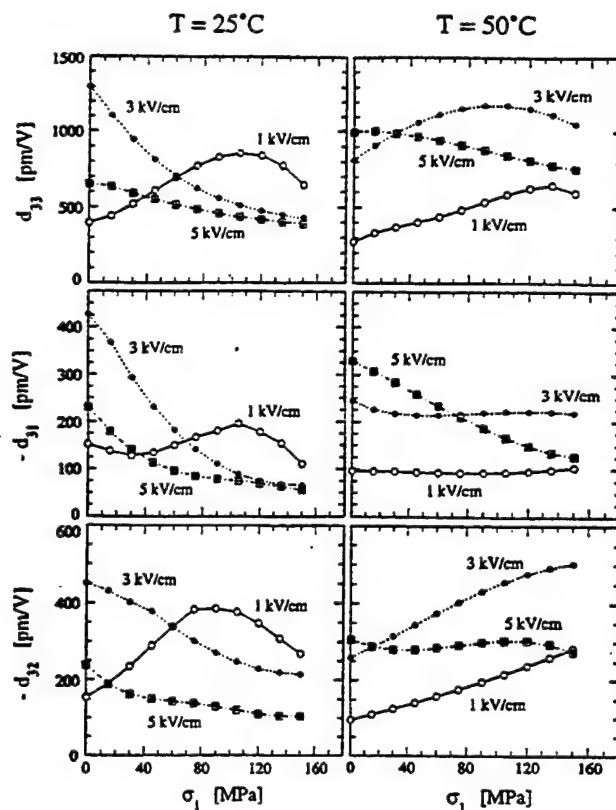


FIG. 2. Effective piezoelectric coefficients, d_{33} , d_{31} , and d_{32} , of 0.9PMN:0.1PT in the electric field biased state measured as a function of compressive stress, σ_1 , and dc bias at two temperatures: 25 °C (left column) and 50 °C (right column). The frequency of small ac probing field is 10 Hz. Symbols show experimental data, and the lines are drawn to guide the eye.

off. In other words, the compressive stress shifted the depoling temperature from $T_d \approx 10$ °C, Ref. 2, to higher values so that now $T_d(\sigma_1) > 25$ °C.

The stress dependence of the dielectric constant measured at different dc bias fields at 25 °C also presents evidence that the external stress, σ_1 , moves the depoling temperature to higher values, only that now T_d is a function of both the dc bias field, E_b , and σ_1 . In the plot in Fig. 1(b), the anomalous change in ϵ measured at $E_b = 1$ kV/cm around $\sigma_1 = 80$ MPa can be explained in terms of the phase transition from the micropolar state to the macropolar state. This corresponds to the shift in the depoling temperature from $T_d \approx 15$ °C at the stress free condition,¹² to 25 °C at $\sigma_1 = 80$ MPa, at the same value of the dc bias, $E_b = 1$ kV/cm. Furthermore, since T_d increases with increasing dc bias,⁸ one should expect that at larger E_b , a lower stress level will be required to induce the macropolar state. Indeed, this can be seen in Fig. 1(b), where at $E_b = 3$ and 5 kV/cm, the gradual decrease in $\epsilon(\sigma_1)$ indicates that the material is in the macropolar state already at $\sigma_1 = 0$. Similar gradual change is also observed in $\epsilon(\sigma_1)$ measured at 1 kV/cm at high stress levels, Fig. 1(b).

For the effective piezoelectric coefficients, the phase transition to macropolar state manifests itself in the form of the maximum in $d_{ij}(\sigma_1)$, as shown in Fig. 2 at 25 °C at $E_b = 1$ kV/cm. Using the equation for the effective piezoelectric coefficients of the electrostrictive material, for example,² $d_{33} = 2Q_{11}\epsilon_0\epsilon P(E_b)$, the maximum can be explained as a result of competition between the increase in the macro-

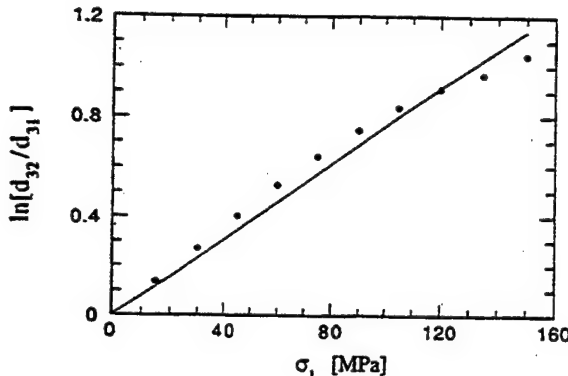


FIG. 3. Stress, σ_1 , dependence of $\ln(d_{32}/d_{31})$ calculated from the data measured at 50 °C at dc bias field of 1 kV/cm. In these conditions, the effective piezoelectric coefficients represent the strain response of the material due to reorientation of the micro-polar regions. Closed circles show the experimental data, and the solid line corresponds to the fit of Eq. (3) to the data.

scopic polarization, $P(E_b)$, during the phase transformation and the drop of the dielectric constant, shown in Fig. 1(b).

Besides the fundamental interest that an external stress can affect the electric field-temperature phase diagram of relaxors,¹³ the results presented in Fig. 1(a) raise an important issue for practical application of these materials. Namely, even though at zero stress the material does not exhibit hysteresis in the polarization-field and strain-field relationships, application of high mechanical load can transform it into a state with a large hysteresis, which will significantly affect the performance of the device.

Another interesting issue revealed by this study is a large difference between d_{31} and d_{32} , which means that the external stress σ_1 breaks the symmetry between the 1- and 2-axes. The difference includes numerical values and even the shape of the stress dependence (at 50 °C) of both coefficients, Fig. 2. For the piezoelectric response from the intrinsic contribution, i.e., from the induced lattice strain, based on the phenomenology and known experiment data, one would not expect such a large difference between d_{32} and d_{31} . On the other hand, for extrinsic contributions, such as domain wall motion or reorientation of the micropolar regions, which are thermally activated processes, the stress σ_1 can induce a large difference between d_{31} and d_{32} .

We can demonstrate that using the data measured at $E_b = 1$ kV/cm at 50 °C. At 1 kV/cm, no evidence for the phase transition to the macropolar state was observed within the whole studied range of stress σ_1 . Therefore, the material can be described as an ensemble of the micropolar regions, and for temperatures near T_m its response to small ac field is dominated by their reorientation.¹⁴ Since these regions are also ferroelastic and generate strain response, the measured d_{31} and d_{32} represent the strain related with the reorientation of the polar regions in the direction of ac probing field, i.e., along 3-axis. In $(1-x)$ PMN: x PT family, the micropolar regions have a rhombohedral structure,¹⁵ and therefore, the measured strain is related with the polar vector reorientation on 71° and 109°. For a ceramic specimen consisting of randomly oriented crystallites, the largest contribution to the strain S_1 and S_2 will be from the polar regions whose polar axis is initially close to 1- and 2-axes, respectively.

When an external static stress is applied to the specimen,

the initial orientation of individual micropolar region will depend also upon extra energy term $\sigma_1 S_1 V_r$, resulting from the coupling of stress σ_1 to the local strain S_1 in the polar region (V_r is the volume of the polar region). Thus, the difference between the population of the polar regions oriented along 1- and 2-axes will depend upon the elastic energy difference between these two orientation states. Therefore, one can write

$$\frac{d_{32}}{d_{31}} = \exp\left(\frac{\Delta S_1 V_r}{k_B T} \sigma_1\right), \quad (3)$$

where k_B is the Boltzmann constant, and ΔS_1 is the difference in the strain S_1 for polar region oriented along 1-axis and 2-axis, respectively. We stress again that we assume that all the strain response of 0.9PMN:0.1PT is from the micro-polar region reorientation, which is a good approximation for the relaxor ferroelectric at temperatures near T_m .¹⁴

Indeed, as shown in Fig. 3, the plot of $\ln(d_{32}/d_{31})$ vs σ_1 yields nearly a straight line, as predicted by Eq. (3). From the average slope of the line, we evaluated the volume V_r of a single micropolar region, using $\Delta S_1 = 0.1\%$ based on the lattice constant data of the rhombohedral polar phase for close composition, PMN, which were obtained using a high-resolution neutron powder diffraction.¹⁶ The estimate yielded $V_r \approx 100 \times 10^3 \text{ \AA}^3$, which corresponds to the size of the polar region approximately equal to 46 Å, assuming that the region has a spherical shape. This estimate is consistent with the value of 100 Å derived using other experimental techniques,^{15,17} indicating that the polar regions existing in the material indeed have a nanometer scale size.

The authors wish to thank the Office of Naval Research for the financial support of this work.

- K. Uchino, S. Nomura, L. E. Cross, R. E. Newnham, and S. J. Jang, *J. Mater. Sci.* **16**, 569 (1981).
- J. Zhao, Q. M. Zhang, N. Kim, and T. Shrout, *Jpn. J. Appl. Phys., Part 1* **34**, 5658 (1995).
- S. L. Swartz and T. R. Shrout, *Mater. Res. Bull.* **17**, 1245 (1982).
- Q. M. Zhang, J. Zhao, K. Uchino, and J. Zheng, *J. Mater. Res.* **12**, 225 (1997).
- F. Jona and G. Shirane, *Ferroelectric Crystals* (Dover, New York, 1993).
- G. A. Smolensky, *J. Phys. Soc. Jpn.* **28**, 26 (1970).
- L. E. Cross, *Ferroelectrics* **76**, 241 (1987).
- R. Sommer, N. K. Yushin, and J. J. van der Klink, *Phys. Rev. B* **48**, 13230 (1993).
- O. Noblanc, P. Gaucher, and G. Calvarin, *J. Appl. Phys.* **79**, 4291 (1996).
- E. V. Colla, N. K. Yushin, and D. Viehland, *J. Appl. Phys.* **83**, 3298 (1998).
- V. Sundar and R. E. Newnham, *Ferroelectrics* **135**, 431 (1992).
- D. J. Taylor, D. Damjanovic, and A. Bhalla, *Ferroelectrics* **118**, 143 (1991).
- G. A. Samara, *Phys. Rev. Lett.* **77**, 314 (1996).
- Q. M. Zhang and J. Zhao, *Appl. Phys. Lett.* **71**, 1649 (1997).
- N. de Mathan, E. Husson, C. Calvarin, J. Gavarri, A. Hewat, and A. Morell, *J. Phys.: Condens. Matter* **3**, 8159 (1991).
- J. Zhao, A. E. Glazounov, Q. M. Zhang, and B. Toby, *Appl. Phys. Lett.* **72**, 1048 (1998).
- S. B. Vakhrushev, B. E. Kvyatkovsky, A. Naberezhnov, N. Okuneva, and B. P. Toperverg, *Ferroelectrics* **90**, 173 (1989).

APPENDIX 66

The influence of the external stress on the electromechanical response of electrostrictive $0.9\text{Pb}(\text{Mg}_{1/3}\text{Nb}_{2/3})\text{O}_3-0.1\text{PbTiO}_3$ in the dc electrical field biased state

J. Zhao, Volkmar Mueller, and Q. M. Zhang^{a)}

Materials Research Laboratory and Electrical Engineering Department, The Pennsylvania State University, University Park, Pennsylvania 16802

(Received 16 January 1998; accepted 22 July 1998)

The influence of uniaxial compressive stress, T_3 , applied parallel to the electrical field, on the electromechanical parameters of $0.9\text{Pb}(\text{Mg}_{1/3}\text{Nb}_{2/3})\text{O}_3-0.1\text{PbTiO}_3$ ceramics in the dc electrical field biased state and at temperatures near the dielectric constant maximum T_m was investigated. It was found that T_3 reduces both the dielectric constant and polarization level, which results in a reduction of the piezoelectric coefficient with stress. However, the compliance of the material does not show much change with stress. As a consequence, the coupling factor k_{33} is also reduced with stress. On the other hand, the existence of the local micropolar region in the material causes anomalous changes in the aforementioned properties when the material is subjected to a high electric field, which induced a macropolar state. The transformation of this macropolar state back to a micropolar state under stress involves a large volume strain and results in an enhancement of the hydrostatic piezoelectric response.

I. INTRODUCTION

Lead magnesium niobate-lead titanate (PMN-PT) based electrostrictive materials exhibit many attractive features such as high dielectric constant, high electrical and elastic energy density, and low hysteresis, for actuator and transducer applications. In these applications, the materials are often subjected to high external stresses due to a prestress or high external load. In order to properly use the materials under different external conditions, it is necessary to understand how the electromechanical properties are influenced by those conditions.

In PMN-PT used in the electrostrictive regions (at temperatures near or above the dielectric constant maximum T_m), the material is composed of two phases: micropolar regions embedded in a nonpolar matrix.^{1,2} And as has been demonstrated in a recent study, the polarization response, and hence the dielectric and electric field induced strain behaviors, at temperatures near T_m are mainly controlled by the response of the micropolar regions, rather than by the so-called "intrinsic" contribution from the change of the unit cell dimension and polarization level.^{2,3} This is somewhat similar to another widely used electromechanical material, the piezoceramic lead zirconate titanate (PZT), where the material properties are largely controlled by the macrodomain configuration and the movements of the domain boundaries.⁴ One difference between the two systems is that in PMN-PT the response of the micro-

polar region exhibits only weak hysteresis while in PZT, large irreversibility occurs when external fields cause depoling of the piezoceramic.⁵ The influence of external stresses on the response of micropolar region is still unclear at this stage.

In this paper, we report the results of an experimental investigation on the effect of uniaxial compressive stress (T_3), which is parallel to the applied electric field direction (defined as the 3-direction), on various electromechanical parameters of PMN-PT with the composition of 10% PT (0.9PMN-0.1PT). As has been demonstrated by many early studies, for electrostrictive applications at near room temperature, the composition of PMN-PT is near 0.9PMN-0.1PT whose weak field dielectric constant is presented in Fig. 1.⁶⁻⁸ In addition, by applying a dc bias electric field to the material, an effective piezoelectric state can be induced, as shown schematically in Fig. 2. For an electrostrictive material such as the one investigated here, the material is often operated in the field biased state. In this investigation, therefore, all the parameters are also characterized under different dc electric bias fields to simulate this operation mode.

II. EXPERIMENTAL

All the specimens used in this investigation were made using conventional mixed oxides processing following the columbite B-site precursor method.⁹ Most of the specimens were sintered at a temperature of 1250 °C for 2–6 h followed by annealing in an oxygen-rich

^{a)}Address correspondence to this author.

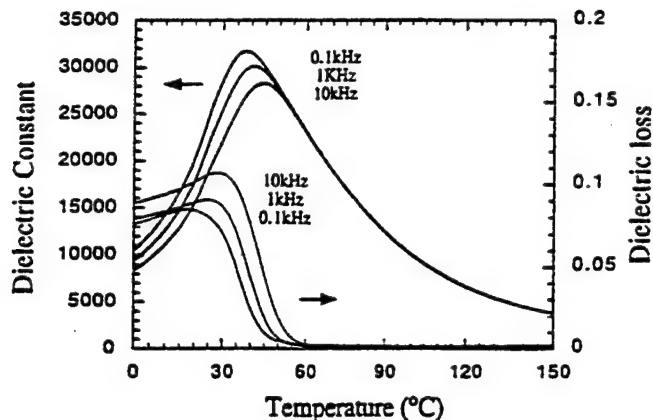


FIG. 1. The dielectric constant K and dielectric loss D as a function of temperature for 0.9PMN-0.1PT ceramics without external stress. The measuring frequency is 0.1, 1, and 10 kHz.

atmosphere at 900 °C for 6–24 h. The typical dielectric constant of the specimens is shown in Fig. 1.

In this investigation, the uniaxial stress applied to the specimens is provided by an apparatus developed recently which has been described in an early publication.⁵ Making use of this apparatus, the effective piezoelectric coefficient, the elastic compliance, and the dielectric constant in the dc electric field biased state can be characterized under well-defined boundary conditions.

In this apparatus, the strain response was measured by a strain gauge (KYOWA KFR-02-120-C1-11). In the dc electric field biased state, the strain response of the specimen is described by¹⁰

$$S_3 = d_{33}E_3 + s_{33}^E T_3 \quad \text{and} \quad S_1 = d_{31}E_3 + s_{13}^E T_3.$$

Hence, in the dc electric field biased state, a weak ac electric field E_{ac} (< 100 V/cm) induces ac strains S_3 and S_1 (under constant stress condition), parallel and perpendicular to E_{ac} , respectively, from which the piezoelectric coefficients d_{33} ($= S_3/E_{ac}$) and d_{31} ($= S_1/E_{ac}$) can be determined (see Fig. 2). In analogy, by measuring the strains S_3 and S_1 induced by a weak ac stress field T_{ac} (about 0.1 MPa) under constant electric field condition, the elastic compliance s_{33}^E and s_{13}^E can be determined. In this investigation, the strain was acquired at a frequency of 10 Hz. In order to improve the signal-to-noise ratio, the voltage signal from the strain gauge amplifier was measured by a lock-in amplifier. Furthermore, to ensure that T_3 was uniformly applied to the specimen, two strain gauges attached to opposite faces of the specimen were utilized. Adjustment was made before the data acquisition so that the strain readings from the two strain gauges were the same within 5%. From repeated measurements, it was found that this adjustment was not very crucial to the determination of piezoelectric coefficients. However, for the elastic compliance, any nonuniformity in T_3 can result in a large error. Hence, the

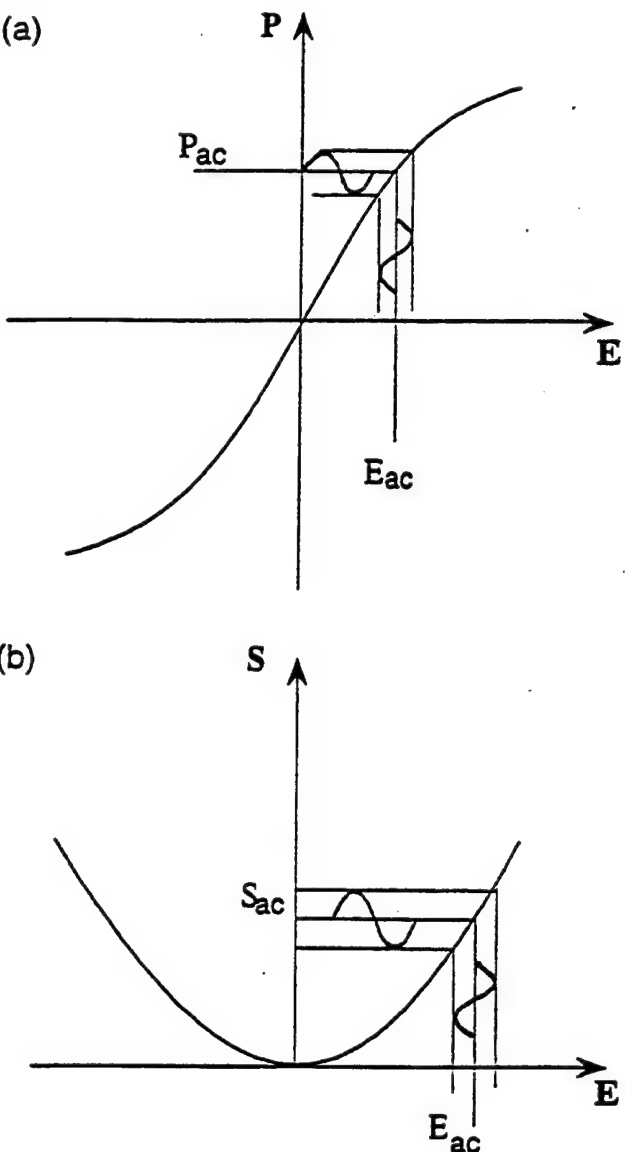


FIG. 2. Schematic drawing of (a) the polarization P and (b) strain S responses of 0.9PMN-0.1PT in the dc electric field-biased state where the effective dielectric constant is defined as P_{ac}/E_{ac} and the effective piezoelectric coefficient as S_{ac}/E_{ac} , respectively. S_{ac} can be S_1 and S_3 and E is the electric field.

error in the piezoelectric coefficient determined is within 5% while error in the elastic compliance is about 10%.

The dielectric constant was determined using either a multifrequency LCR meter (HP model 4192A), or a calibrated small resistor in series with the specimen. In the later method, the voltage across the resistor, which is directly proportional to the current flowing through the specimen, was measured using a lock-in amplifier. From the data, the complex dielectric constant can be determined. The frequency range for the dielectric constant measurement is from 10 Hz to 1 MHz. The polarization level at each electric bias field and dc stress state was measured by a Sawyer-Tower circuit.

Since the material is operated at a temperature near the dielectric constant maximum T_m where there is a large change in the dielectric constant (see Fig. 1) and the polarization level in the field biased state, it is necessary to characterize the electromechanical parameters over a temperature region about T_m . In this investigation, three temperatures were chosen: 25 °C ($< T_m$), 50 °C (near above T_m), and 80 °C ($> T_m$).

III. THE DIELECTRIC RESPONSES

Presented in Fig. 3 is the dielectric constant acquired at 25 °C, which is below the dielectric constant maximum ($T_m = 37$ °C at 1 kHz). Without dc electric bias fields, the data in Fig. 3 show that the dielectric constant decreases as the compressive stress T_3 increases, a trend generally expected for a dielectric material with a positive electrostrictive coefficient Q_{11} .^{11,12} On the other hand, at high dc bias fields, for instance, at 5 kV/cm, an increase of the dielectric constant with the compressive stress was observed. For the pressure range investigated, a dielectric maximum was observed near 60 MPa, which seems to be inconsistent with conventional electrostrictive behavior. This could be understood from the fact that because of the existence of micropolar regions, a high dc bias field can induce a macropolar state in the material. As the compressive stress increases, which tends to reduce the macropolarization level in the material, a "transformation" of the macropolar domain state to micropolar state occurs, resulting in the observed broad dielectric constant anomaly.¹³

It is well known that for a dielectric material, the change of the dielectric constant K with external stress can be a result of the electrostrictive coupling in the material. In fact, for many nonferroelectric materials, the electrostrictive coefficient can be determined conveniently from the slope of $1/K$ versus the applied stress T .^{11,12} However, for a ferroelectric based electrostrictive material such as PMN-PT, the change in the dielectric constant can also be a result of the changes in the local polarization state as has been pointed out in an early publication (shifting of the local Curie temperatures).¹² Moreover, the polarization response near T_m is mainly from the reorientation process of the micropolar regions to the external electric field. These so-called "extrinsic" contributions to the dielectric response can be affected by external stress. As a consequence, the $1/K$ versus T_3 relation even for the data without dc electric field exhibits a strong nonlinear behavior and the slope of the curve is far below Q_{11} measured directly from the strain-polarization relationship.

For the data at temperatures above the dielectric constant maximum, the dielectric constants all show monotonic decrease with the compressive stress for the dc bias fields investigated (up to 5 kV/cm), although at

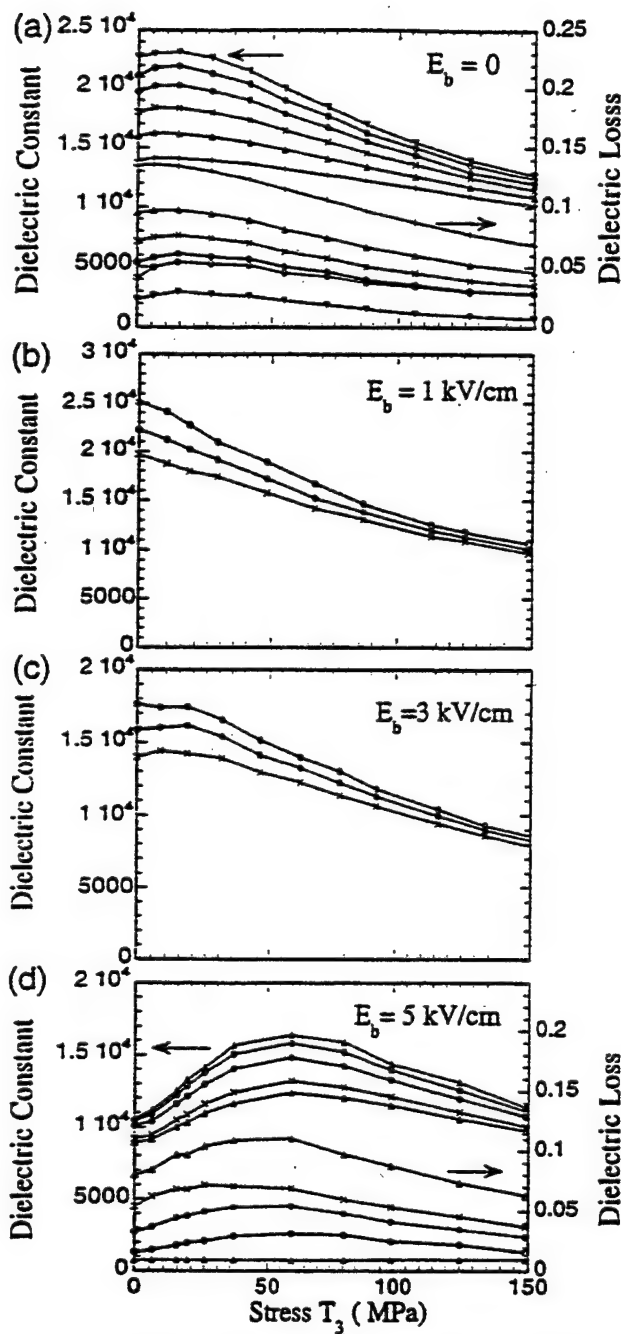


FIG. 3. The dielectric constant K and dielectric loss D as a function of the compressive stress T_3 measured at 25 °C and different dc bias electric fields: (a) $E_b = 0$, (b) $E_b = 1$ kV/cm, (c) $E_b = 3$ kV/cm, and (d) $E_b = 5$ kV/cm. The measuring frequency of the data: 10 Hz (\blacktriangle), 0.1 kHz (\circ), 1 kHz (\bullet), 10 kHz (\times), 100 kHz (Δ), and 1 MHz ($+$).

50 °C, the dielectric constant under 5 kV/cm dc electric bias field exhibits a plateau at $T_3 < 50$ MPa, which is presented in Fig. 4. The existence of this plateau is reminiscent of the transformation of the material from a macropolar state to a micropolar state, analogous to that observed at 25 °C. Because of the existence of the micropolar regions, even for the data at 80 °C (shown in

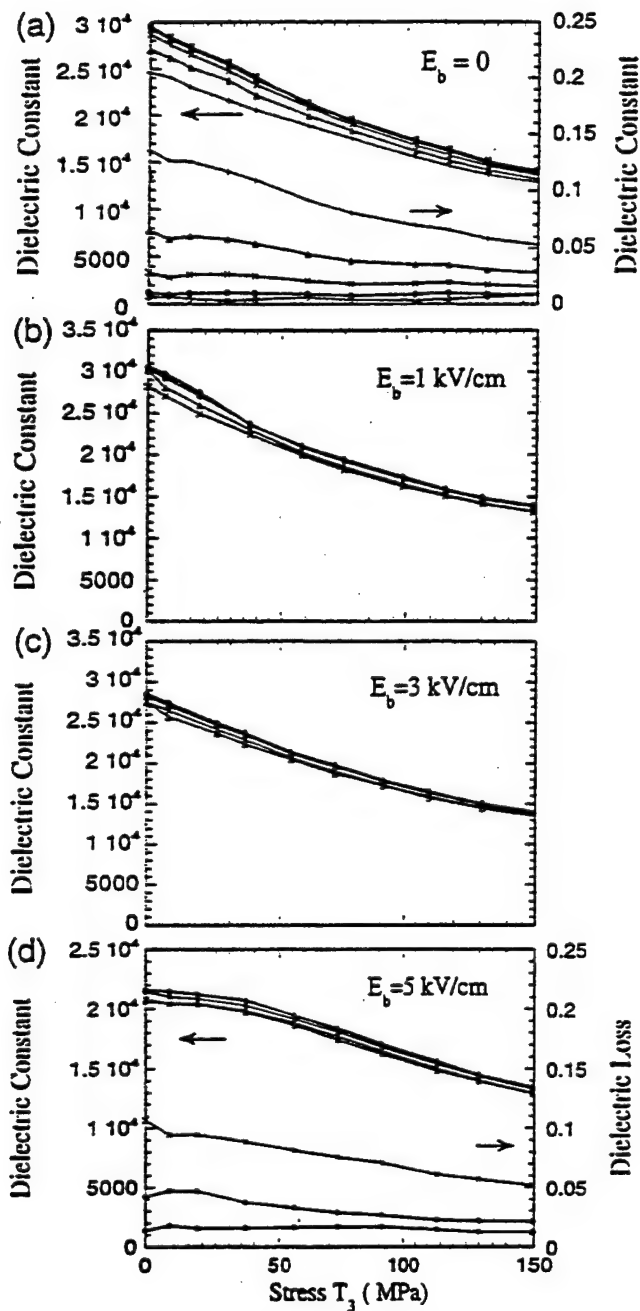


FIG. 4. The dielectric constant and dielectric loss as a function of the compressive stress T_3 measured at 50 °C. (a) $E_b = 0$, (b) $E_b = 1 \text{ kV/cm}$, (c) $E_b = 3 \text{ kV/cm}$, and (d) $E_b = 5 \text{ kV/cm}$. The measuring frequency: 10 Hz (▲), 0.1 kHz (○), 1 kHz (●), 10 kHz (×), 100 kHz (Δ), and 1 MHz (+).

Fig. 5), the slope of the dielectric stiffness versus stress is still far below that determined by the electrostrictive coefficient despite the curve of $1/K$ versus T_3 exhibiting a nearly linear relationship in the stress range investigated. In addition, the slope of the curve decreases as the dc bias field increases, a signature of increased ferroelectric activity in the material when subjected to high electric fields.

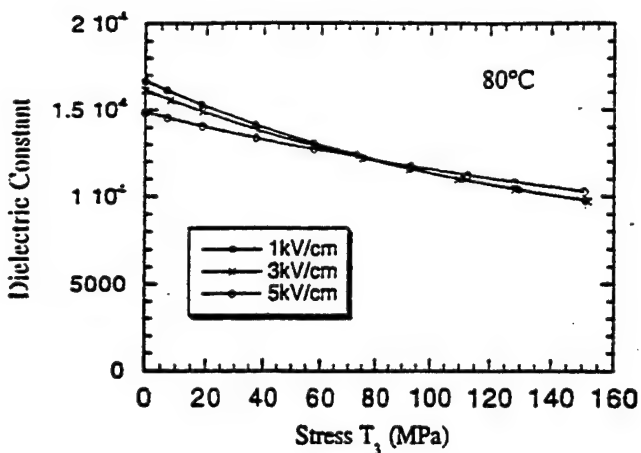


FIG. 5. The dielectric constant as a function of the compressive T_3 at 80 °C, 1 kHz, and under different dc bias fields. The dielectric constant at this temperature exhibits very little dispersion.

At 25 and 50 °C, the dielectric data exhibit strong frequency dispersion. For that reason the data were collected at frequencies from 10 Hz to above 100 kHz to probe the influence of this dispersion by the applied stress T_3 . Apparently, the external stress T_3 reduces the dielectric dispersion significantly, and accompanying this reduction in the dispersion the dielectric loss is also reduced. The results reveal that the compressive stress T_3 reduces the response of the micro-polar regions and hence the degree of the relaxor behavior in the material. The data at 80 °C was acquired at a single frequency of 1 kHz because of a very weak frequency dispersion at the temperature.

IV. THE ELASTIC COMPLIANCE AS A FUNCTION OF THE COMPRESSIVE STRESS AT DIFFERENT BIAS FIELDS

Elastic compliances s_{33}^E and s_{13}^E were characterized as a function of compressive stress at different electric bias fields and temperatures are presented in Figs. 6 and 7, respectively. The general features revealed from the data are as follows: (i) the elastic compliance increases with dc bias fields and, hence, the polarization level in the material; (ii) the compliance exhibits a slight decrease with the compressive stress; (iii) the compliance decreases with temperature for the three temperatures measured. For the data at 25 °C under 5 kV/cm, an anomaly is observed which is apparently related to the phase transformation from a macropolar state to a micropolar state as has been discussed in the dielectric data. In the temperature and stress range investigated, the ratio of $-s_{13}^E/s_{33}^E$ remains near 1/3.

In an early investigation by Cao and Evans,¹⁴ it was found that in soft PZT, Poisson's ratio can reach near 0.5 when there is a stress depoling of the samples which is a direct consequence of the domain reorientation during

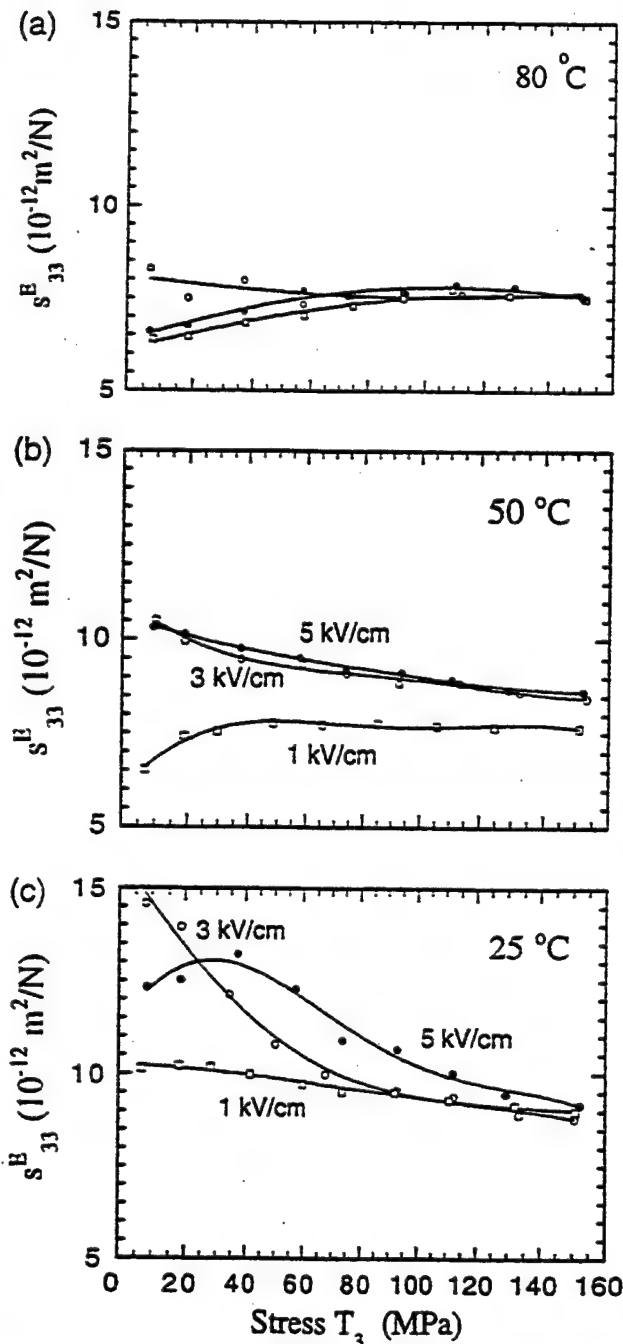


FIG. 6. The elastic compliance s_{33}^E as a function of the compressive T_3 at different temperatures: (a) 80 °C, (b) 50 °C, and (c) 25 °C, and dc electric bias fields: zero bias (X), 1 kV/cm (□), 3 kV/cm (○), and 5 kV/cm (●).

the depoling process. If there is a significant contribution from the reorientation of the micropolar regions to the elastic process in the material, one would expect similar results, since this process will not generate volume strain. Therefore, the relatively small ratio of $-s_{13}^E/s_{33}^E$ implies that the reorientation process of micropolar regions, which is responsible for the large dielectric constant near T_m , is not contributing significantly to the elastic process.

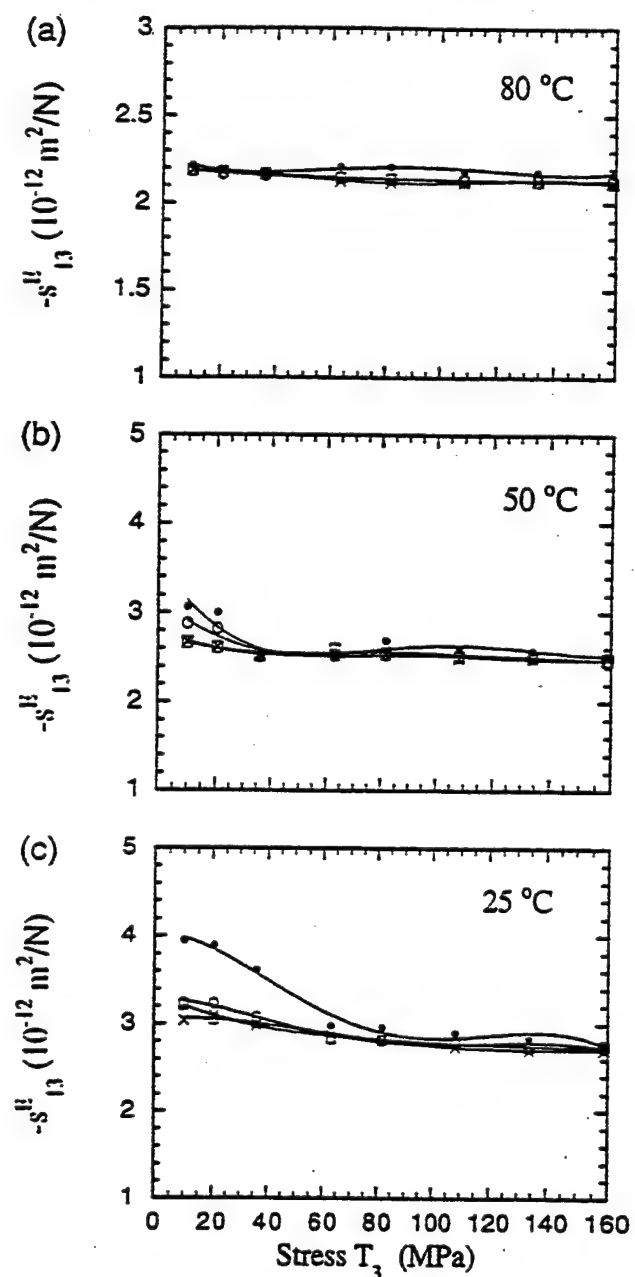


FIG. 7. The elastic compliance s_{13}^E as a function of the compressive T_3 at different temperatures: (a) 80 °C, (b) 50 °C, and (c) 25 °C, and dc electric bias fields: zero bias (X), 1 kV/cm (□), 3 kV/cm (○), and 5 kV/cm (●).

Indeed, there is only a very weak elastic compliance peak at temperatures near T_m .¹⁵

V. THE EFFECTIVE PIEZOELECTRIC RESPONSES IN DC FIELD BIASED STATES

The effective piezoelectric coefficients d_{33} and d_{31} in the electric field biased state were characterized and are presented in Figs. 8 and 9. Analogous to the dielectric

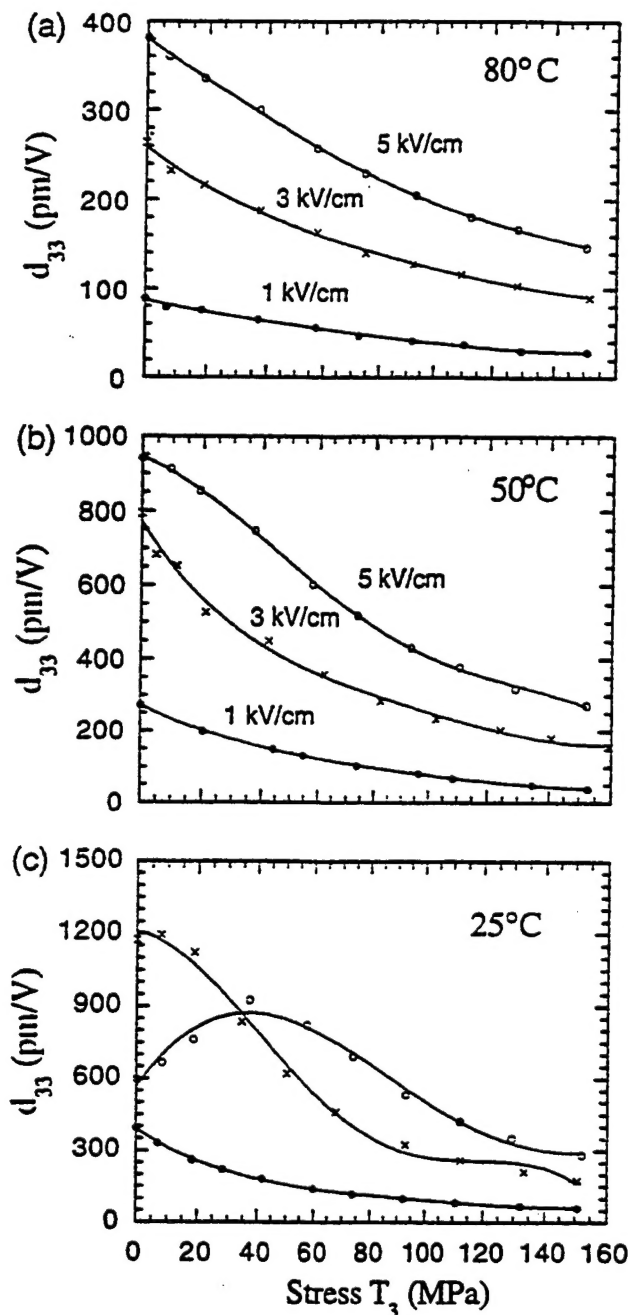


FIG. 8. The effective piezoelectric coefficient d_{33} at the dc field-biased states as a function of the compressive T_3 at different temperatures: (a) 80 °C, (b) 50 °C, and (c) 25 °C; and dc electric bias fields: 1 kV/cm (•), 3 kV/cm (×), and 5 kV/cm (○).

constant and elastic compliance data, a broad peak of d_{33} at the bias field of 5 kV/cm data was observed. In addition, there is also a weak peak at 3 kV/cm, while at 1 kV/cm d_{33} decreases monotonically with the stress. As pointed out earlier, this anomalous behavior observed at 3 and 5 kV/cm bias fields is associated with the phase transformation in the material in the dc field biased state from a macropolar state to a micropolar

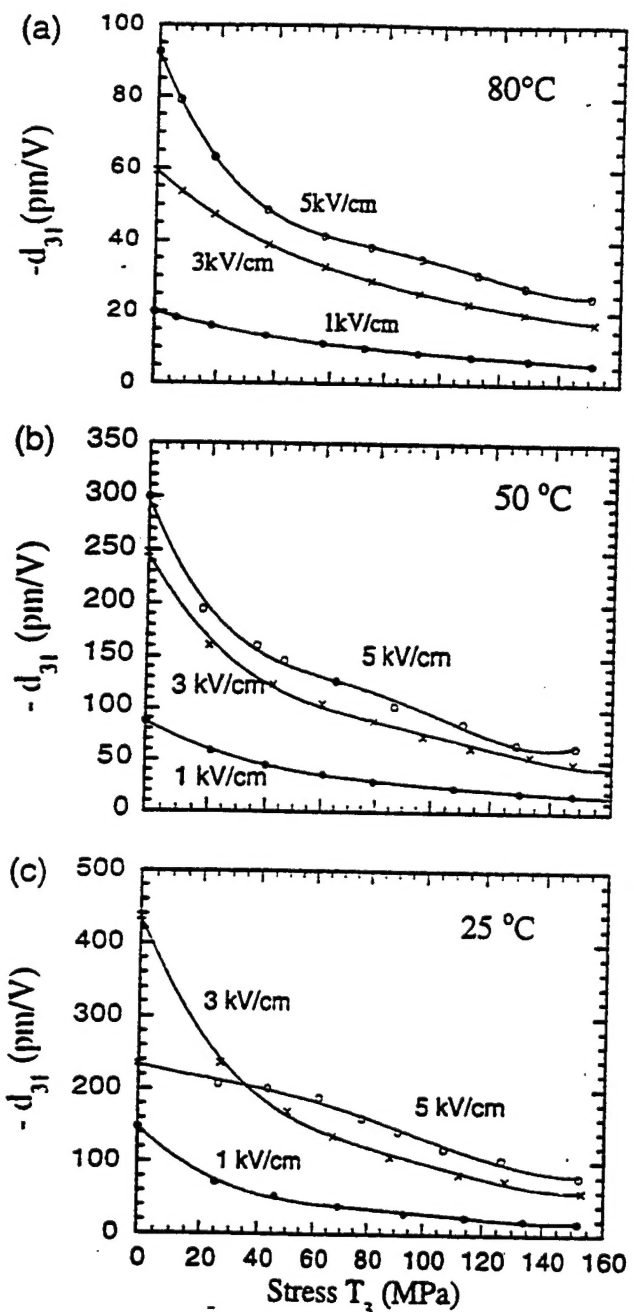


FIG. 9. The effective piezoelectric coefficient d_{31} at the dc field-biased states as a function of the compressive T_3 at different temperatures: (a) 80 °C, (b) 50 °C, and (c) 25 °C; and dc electric bias fields: 1 kV/cm (•), 3 kV/cm (×), and 5 kV/cm (○).

state. The peak is much less pronounced in the data of d_{31} . At higher temperatures, both d_{33} and d_{31} exhibit a monotonic decrease with the compressive stress. The decrease of d_{33} and d_{31} with the compressive stress at higher temperatures is a result of the reduction of the polarization level P_3 and the dielectric constant K at the dc field biased state with the stress. In fact, the ratio of d_{33} (or d_{31}) to $P_3 K$, which is directly proportional to

the effective electrostrictive coefficients of the ceramic sample, does not show marked change with stress.

Based on d_{33} and d_{31} data, the hydrostatic piezoelectric coefficient d_h ($d_h = d_{33} + 2d_{31}$) in the dc field biased state is evaluated and presented in Fig. 10. One of the interesting features of the data in Fig. 10 is that a very pronounced peak in d_h is observed at 25 °C under a 5 kV/cm bias field. For the data at higher temperatures, a weaker but clear peak is observed under 5 kV/cm bias

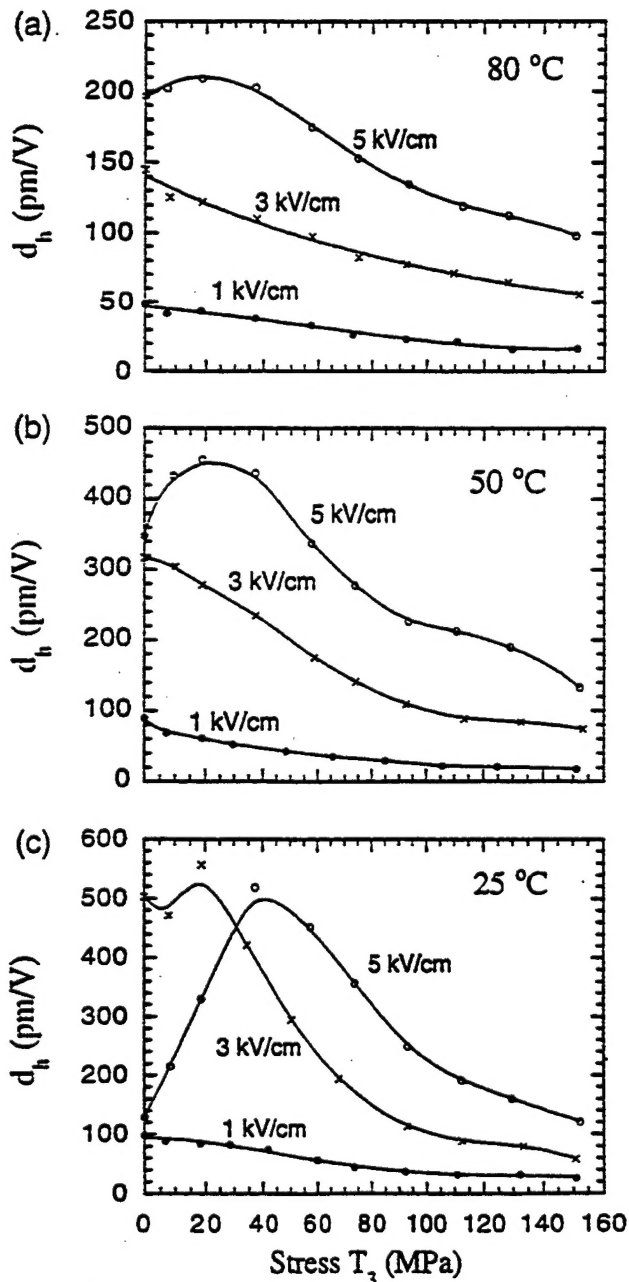


FIG. 10. The effective hydrostatic piezoelectric coefficient d_h at the dc field-biased states as a function of the compressive T_3 at different temperatures: (a) 80 °C, (b) 50 °C, and (c) 25 °C; and dc electric bias fields: 1 kV/cm (●), 3 kV/cm (×), and 5 kV/cm (○).

field. This is in sharp contrast to the dielectric, elastic compliance, and piezoelectric d_{33} and d_{31} coefficients where the peak associated with the anomaly is much weaker. As has been pointed out, the anomaly is due to the transformation from a macropolar state to a micropolar state due to the applied stress. The result reveals that this transformation involves a large volume change which yields a large change in d_h in the broad transition region.

In a recent study of the electrostrictive coefficients of prototype cubic phase of PMN, it was found that the hydrostatic electrostrictive coefficient is about $0.08 \text{ m}^2/\text{C}^4$.³ This value is more than 10 times higher than that determined directly from a field-induced strain measurement.² The difference between the two results lies in the fact that at temperatures near T_m , the material has a high population of micropolar regions and the reorientation of these polar regions does not generate volume change. Consequently, the Q_h measured from the volume strain-polarization relationship at temperatures near T_m has a much smaller value than the intrinsic Q_h value of the material. (Q_h for the prototype cubic phase of 0.9PMN-0.1PT is nearly the same as that of PMN.) In this paper, this low value of Q_h measured from field-induced volume strain S_v at temperatures near T_m is named as the apparent Q_h (Q_h^a) of the material to distinguish it from the intrinsic Q_h which is determined from the change in the lattice constant of the unit cell due to the change in polarization.

For 0.9PMN-0.1PT, $Q_h^a = 0.006 \text{ m}^4/\text{C}^2$ at room temperature without external field. From the electrostrictive relation $S_v = Q_h^a P^2$, where P is the total polarization response in the sample, and also $S_v = Q_h P_v^2$, where P_v is the polarization response which generates volume strain, the ratio $P_v/P = \sqrt{Q_h^a/Q_h}$ can be determined. For PMN-PT near T_m , this ratio is about 0.27, which implies that about 70% of the weak field polarization response in 0.9PMN-0.1PT at temperatures near T_m is due to the reorientation of the micropolar regions, which does not generate the volume change of the material.

This observation raises an interesting issue on how to improve the hydrostatic response of the material, which is important for many underwater applications. By reducing the polarization response related to the micropolar region reorientation, even if this may not increase d_h in the case that P_v in the material does not change (from the electrostrictive relation, $d_h = 2Q_h P_v \Delta P_v$ in the field biased state), the reduction of the dielectric constant will improve the hydrostatic figure of merit $d_h g_h$ since g_h is equal to d_h/K . The $d_h g_h$ for the samples investigated is presented in Fig. 11. As can be seen from the figure, in spite of the fact that the material possesses a relatively high d_h ($> 400 \text{ pm/V}$, about 10 times higher than that of PZT piezoceramics), the relatively high dielectric constant due to the micropolar region reorientation results

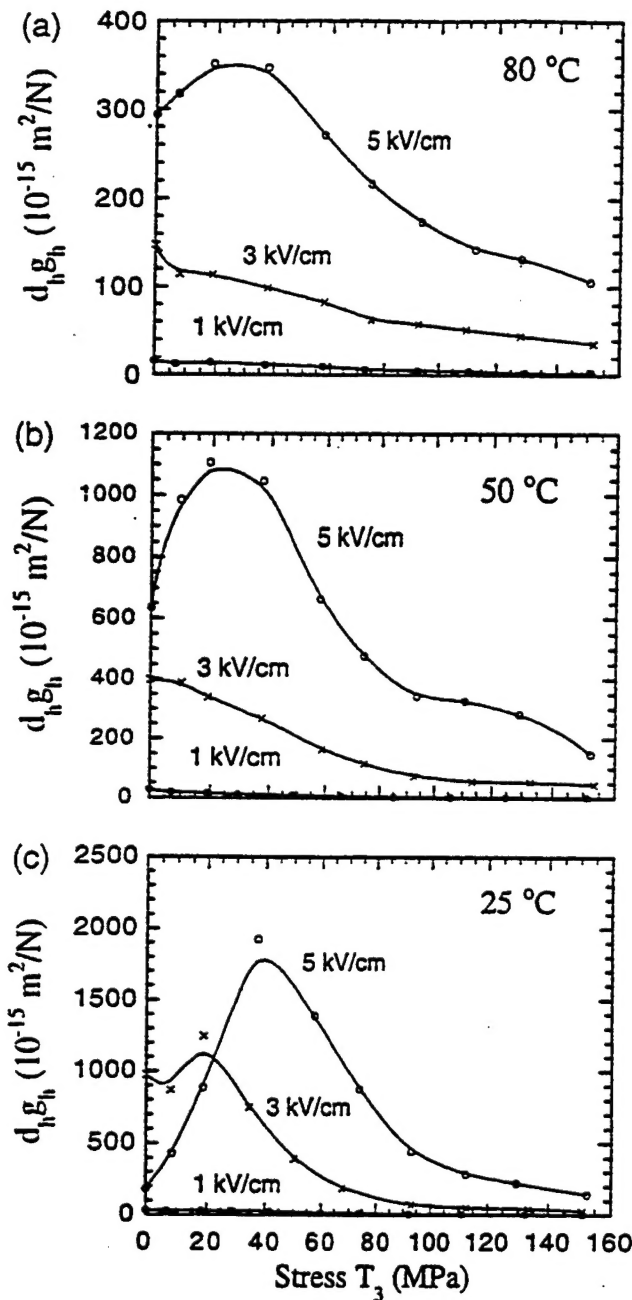


FIG. 11. The hydrostatic figure of merit $d_h g_h$ at the dc field-biased states as a function of the compressive T_3 at different temperatures: (a) 80 °C, (b) 50 °C, and (c) 25 °C; and dc electric bias fields: 1 kV/cm (●), 3 kV/cm (×), and 5 kV/cm (○).

in a figure of merit which is only about 20 times higher than that of PZT piezoceramics and is nearly the same as that of the piezopolymer PVDF.¹⁶

VI. THE ELECTROMECHANICAL COUPLING FACTOR k_{33} UNDER UNIAXIAL STRESS T_3

From the data presented in the preceding sections, the electromechanical coupling factor k_{33} , defined as

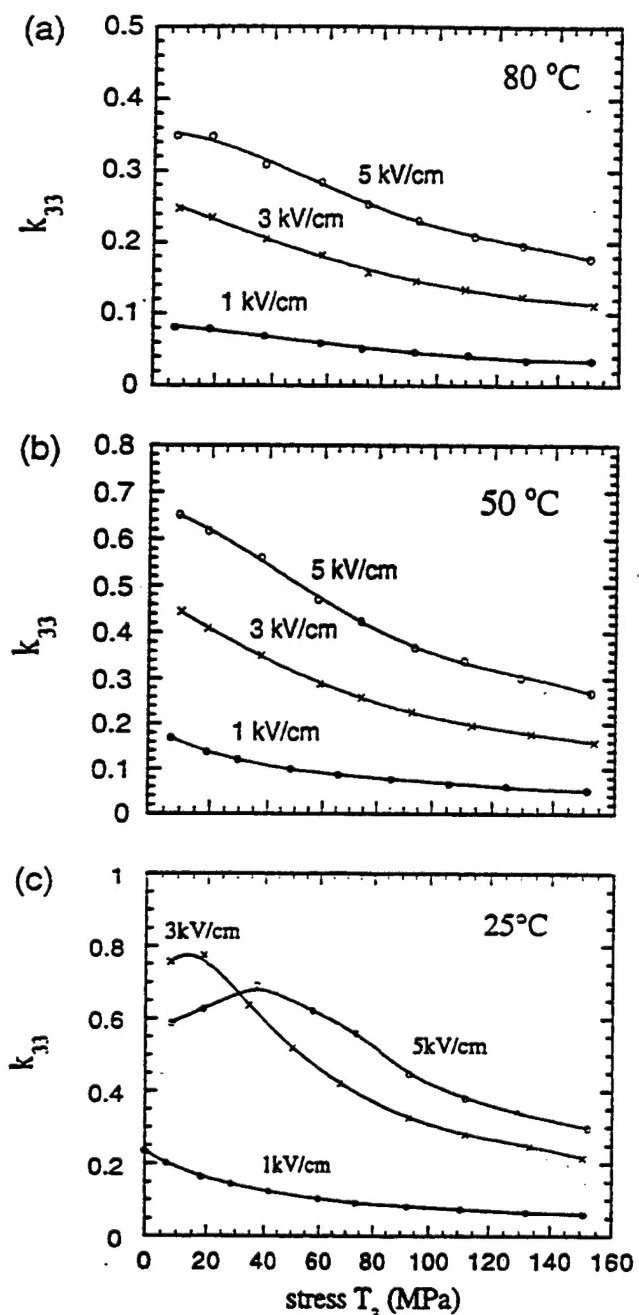


FIG. 12. The electromechanical coupling factor k_{33} (calculated at 10 Hz) as a function of the compressive T_3 at different temperatures: (a) 80 °C, (b) 50 °C, and (c) 25 °C; and dc electric bias fields: 1 kV/cm (●), 3 kV/cm (×), and 5 kV/cm (○).

$k_{33}^2 = d_{33}^2 / (K \epsilon_0 s_{33}^E)$, where ϵ_0 is the vacuum permittivity, can be derived.¹⁰ The coupling factor as a function of T_3 is presented in Fig. 12. Apparently, at high dc bias electric fields and without external stress, k_{33} of 0.9PMN-0.1PT at temperatures near T_m is near that of soft PZT, i.e., above 0.7. A disappointing feature of this material is that k_{33} drops quite significantly as the material is subjected to external compressive stress. This seems inevitable from the data presented in the

preceding sections since the reduction of the piezoelectric coefficients with stress is due to the reduction in both the dielectric constant and the polarization level in the field-biased state while the elastic compliance does not show a marked reduction with stress. As a result, k_{33} is reduced with stress. In order to improve the material performance with stress, one may need to develop materials with a broader dielectric peak so that the reduction of the polarization and dielectric constant with stress can be reduced.

VII. SUMMARY

The influence of uniaxial compressive stress on the electromechanical behavior of $0.9\text{PMN}-0.1\text{PT}$ ceramics under dc bias electric fields at temperatures near T_m was investigated. The compressive stress T_3 reduces the responses of the micropolar regions, which results in a decrease in the dielectric constant, dielectric dispersion, dielectric loss, and effective piezoelectric coefficients. Our results also show that the response of the micropolar regions contributes far less to the elastic process compared with the dielectric process. Hence, the elastic compliance does not exhibit a marked change with stress and the ratio of $-s_{13}^E/s_{33}^E$ remains near 1/3. By combining the data of the piezoelectric coefficient, the dielectric constant, and elastic compliance, the longitudinal electromechanical coupling factor k_{33} was derived and was shown to decrease with the compressive stress T_3 .

For electrostrictive PMN-PT at temperatures near T_m , the material can be converted into a macropolar state by applying a high dc electric field. Compressive stress will force the material back into a micropolar state, and the experimental results reveals that there is a broad transformation region between the two states instead of a smooth process. This transformation involves a change in part of the material between a rhombohedral phase and a cubic phase which involves a large volume strain as revealed by a pronounced peak in the hydrostatic piezoelectric coefficient d_h . This phenomenon could be

used to enhance the hydrostatic piezoelectric response of the material if the bias stress level is properly adjusted. Furthermore, for a given external prestress level, the material composition may be adjusted so that this transformation will occur at the given stress.

ACKNOWLEDGMENT

This work was supported by the Office of Naval Research.

REFERENCES

1. L. Eric Cross, *Ferroelectrics* **76**, 241-267 (1987).
2. Q. M. Zhang and J. Zhao, *Appl. Phys. Lett.* **71** (12), 1649-1651 (1997).
3. J. Zhao, A. E. Glazounov, and Q. M. Zhang, *Appl. Phys. Lett.* (1998, in press).
4. Q. M. Zhang, H. Wang, N. Kim, and L. E. Cross, *J. Appl. Phys.* **75**, 454 (1994).
5. Q. M. Zhang, J. Zhao, K. Uchino, and J. Zheng, *J. Mater. Res.* **12**, 226-234 (1997).
6. J. Zhao, Q. M. Zhang, N. Kim, and T. Shrout, *Jpn. J. Appl. Phys.* **34** (10), 5658-5663 (1995).
7. S. M. Pilgrim, M. Massuda, J. D. Prodey, and A. P. Ritter, *J. Am. Ceram. Soc.* **75** (7), 1964-1969 (1992).
8. C. L. Horn, S. M. Pilgrim, N. Shankar, K. Bridger, M. Massuda, and S. R. Winzer, *IEEE Trans. Ultrason., Freq. Cont.* **41** (4), 542-551 (1994).
9. S. L. Swartz and T. R. Shrout, *Mater. Res. Bull.* **17**, 1245-1250 (1982).
10. *IEEE Standard on Piezoelectricity*, IEEE, Ultrason., Ferroelect., and Freq. Contr. Soc., ANSI/IEEE Std. 176-1897 (1987).
11. V. Sundar and R. E. Newnham, *Ferroelectrics* **135**, 431-446 (1992).
12. Q. M. Zhang, W. Y. Pan, S. J. Jang, and L. E. Cross, *Ferroelectrics*, **88**, 147-154 (1988).
13. G. A. Samara, *Phys. Rev. Lett.* **77**, 314-317 (1996).
14. H. Cao and A. G. Evans, *J. Am. Ceram. Soc.* **76** (4), 890-896 (1993).
15. Dwight D. Viehland, Ph.D. Thesis, The Pennsylvania State University (1991).
16. Hong Wang, Ph.D. Thesis, The Pennsylvania State University (1994).